ISBN 978-82-326-2610-6 (printed version)
ISBN 978-82-326-2611-3 (electronic version)
ISSN 1503-8181

NTNU
Norwegian University of
Science and Technology

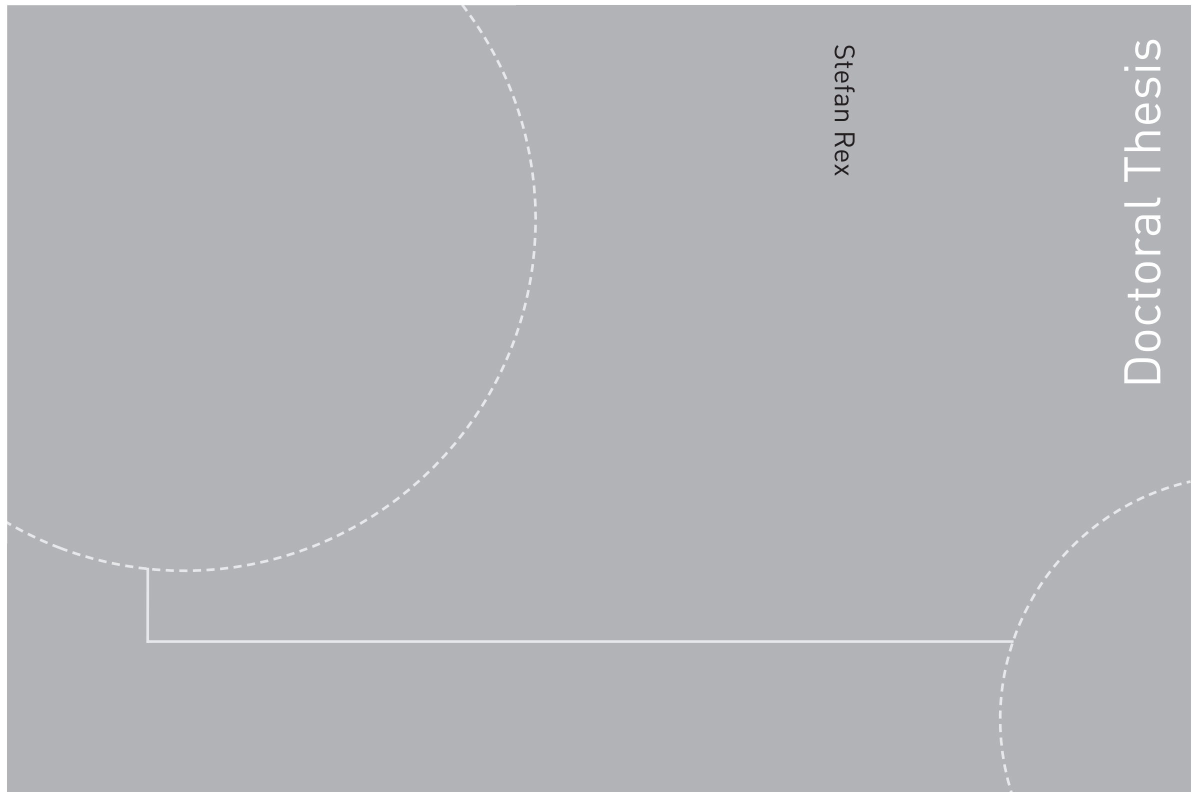

Stefan Rex

Doctoral Thesis

Doctoral theses at NTNU, 2017:271

NTNU
Norwegian University of
Science and Technology
Faculty of Natural
Sciences and Technology
Department of Physics

NTNU

Doctoral theses at NTNU, 2017:271

Stefan Rex

Electric and magnetic signatures of boundary states in topological insulators and superconductors

NTNU
Norwegian University of
Science and Technology

Stefan Rex

Electric and magnetic signatures of boundary states in topological insulators and superconductors

Thesis for the degree of Philosophiae Doctor

Trondheim, August 2017

Norwegian University of Science and Technology
Faculty of Natural
Sciences and Technology
Department of Physics

NTNU
Norwegian University of
Science and Technology

NTNU
Norwegian University of Science and Technology

Thesis for the degree of Philosophiae Doctor

Faculty of Natural
Sciences and Technology
Department of Physics

ISBN 978-82-326-2610-6 (printed version)
ISBN 978-82-326-2611-3 (electronic version)
ISSN 1503-8181

Doctoral theses at NTNU, 2017:271

Printed by Skipnes Kommunikasjon as

Abstract

This thesis is based on original research that was carried out in the field of topological phases in quantum condensed matter physics. The results have been published in five papers in Physical Review B, which form the core of the thesis.

Three of these papers are concerned with magnetic order at the surface of a three-dimensional topological insulator, more precisely phenomena related to the so-called topological magnetoeletric effect (TME). This effect causes an electric field to induce a magnetic polarization. The first paper explores the role of Coulomb interaction at an interface of a ferromagnetic insulator with a topological insulator. The main finding is that the long-range interaction causes a nonlocal contribution to the TME. This is further investigated by deriving the Landau-Lifshitz equation describing the magnetization dynamics at the interface. In the second paper, the system is extended to a multilayer heterostructure. It is shown that the effect of the Coulomb interaction can effectively be described as a topological magnetic dipole-dipole interaction. Furthermore a setup is proposed where a magnetic texture can be manipulated nonlocally by means of an electric voltage. The third paper represents a generalization of the bilayer system to bipartite magnetic insulators. The main finding is a topological staggered-field-electric effect in ferrimagnetic insulators. All these three papers are based on completely analytical calculations within effective continuum models.

The other two papers deal with topological superconducting systems. The first one is about a so-called Majorana wire, a spin-orbit coupled semiconductor nanowire with proximity-induced superconductivity in an external magnetic field. Such a system can host localized Majorana zero modes at the wire ends under certain conditions, when it is in a topologically nontrivial phase. One aspect of this condition, namely the allowed range of magnetic field orientations, is analytically derived in the paper. This is supplemented by calculating the conductance spectra of a Majorana wire-trivial conductor junction, which show the decay of the prominent zero-bias peak at the predicted critical angle. The last paper resulted from an external collaboration, where nodal noncentrosymmetric superconductors are studied. For certain crystallographic orientations, the surface of such a material features Majorana zero modes as flat-band states that are restricted to bounded regions in the surface Brillouin zone. By self-consistent numerical computation of the superconducting gaps, it is shown that the surface spontaneously breaks time-reversal symmetry for sufficiently low temperatures. The surface states become weakly dispersive and are no longer Majorana modes.

Sammendrag

Denne avhandlingen består av fem vitenskapelige artikler med arbeid innenfor teoretisk faste stoffers fysikk, nærmere bestemt såkalte topologiske materialer. De første tre artiklene dreier seg om magnetisme på overflaten til en topologisk isolator. Det finnes en topologisk magnetoelektrisk effekt (TME) i slike systemer. Det betyr at elektriske og magnetiske felt er koplet, noe som kan være nyttig i nanoteknologi. I to artikler beskrives det hvordan denne effekten kan få en lengre rekkevidde når Coulomb-vekselvirkninger tas i betraktning. Dette innebærer en ny effekt, nemlig en topologisk vekselvirkning mellom magnetiske dipoler. Den tredje artikkelen utleder en variant av TME der et elektrisk felt kan indusere mer kompliserte former av magnetiske felt.

De to siste artiklene tar for seg topologiske superledere. I disse er det mulig å finne Majorana fermioner, eksotiske kvante-tilstander som kan beskrives som sine egne antipartikler. Det beregnes i den fjerde artikkelen når Majorana fermioner er tilstede i en nano-tråd, som bare er topologisk når flere komponenter kombineres på en spesiell måte. I den siste artikkelen blir det slått fast at Majorana fermionene kan forsvinne i en viss slags topologiske superledere når temperaturen blir veldig lav.

List of papers

Paper [1] Stefan Rex, Flavio S. Nogueira, and Asle Sudbø
Nonlocal topological magnetoelectric effect by Coulomb interaction at a topological insulator-ferromagnet interface
Physical Review B **93**, 014404 (2016)

Paper [2] Stefan Rex, Flavio S. Nogueira, and Asle Sudbø
Topological magnetic dipolar interaction and nonlocal electric magnetization control in topological insulator heterostructures
Physical Review B **94**, 020404(R) (2016)

Paper [3] Stefan Rex, Flavio S. Nogueira, and Alse Sudbø
Topological staggered field electric effect with bipartite magnets
Physical Review B **95**, 155430 (2017)

Paper [4] Stefan Rex and Asle Sudbø
Tilting of the magnetic field in Majorana nanowires: Critical angle and zero-energy differential conductance
Physical Review B **90**, 115429 (2014)

Paper [5] Carsten Timm, Stefan Rex, and P. M. R. Brydon
Surface instability in nodal noncentrosymmetric superconductors
Physical Review B **91**, 180503(R) (2015)

My contribution to the papers

Paper [1]

I did the analytical calculations and wrote most of the article text. I also created the figure.

Paper [2]

I performed the calculations and created the figures. I suggested the specific multi-layer structure shown in Fig. 1. I also wrote the major portion of the manuscript.

Paper [3]

I set up the model of the interface on which this project is based. I derived all analytical results and substantially contributed to their interpretation. I wrote the main part of the manuscript and prepared the figures.

Paper [4]

I performed the analytical and numerical calculations. I created the figures and wrote the major part of the article.

Paper [5]

This paper was motivated by preliminary work I did in my diploma project. As a PhD student, I was involved in the discussion of the numerical results obtained by the first author and participated in writing the final manuscript.

Acknowledgements

I would like to express my gratitude to several people who have been important during the four years of my PhD studies in Trondheim.

Naturally I am thankful to Prof. Asle Sudbø. Thank you for being an inspiring and motivating supervisor, also at times when progress on some project was not immediate, and for always having a supportive attitude. In addition, I am grateful to Dr. Flavio Nogueira, who collaborated with us on all three papers devoted to topological insulators and magnetism. I thank Prof. Carsten Timm and Dr. Philip Brydon for the joint work on nodal noncentrosymmetric superconductors. Carsten also gave me the opportunity to give talks on my work at TU Dresden.

I thank Prof. Ronny Thomale and Dr. Anton Akhmerov for taking the time to evaluate this thesis and join the assessment committee for my defense along with Assoc. Prof. Jon Andreas Støvneng.

There are many people at the physics department who significantly enriched my time at NTNU. Within the Sudbø-group, I initially enjoyed company by Troels Bojesen and Peder Galteland. Later, Fredrik Nicolai Krohg and Henning Hugdal joined not only the group but also my, by then, sparsely populated office. It was also great to have all the other (mostly) theorists in the section around: Eirik, Therese, Marina, Niklas, Jeroen, Hans, Erlend, Lars, Camilla, William, Vegard, Øyvind, Sverre, Sol, Ali, Vetle, Arnau, Dag-Vidar, André, Manu, Cecilia, Alireza. Thanks to everyone for not only scientific discussions, but also all our joint lunch and coffee breaks including both inspiring and absurd conversations.

Special thanks to Peder, who was a great room mate at the Winter School at Nordita and the March Meeting in San Antonio. I will also keep good memories from New Orleans, where I spend some enjoyable evenings with Nicolai and Jeroen, and from Baltimore with Sol, Vetle and Ali.

In Trondheim, many of you also contributed to social life outside the university, by frequently joining – or letting me join – for a run (or race), barbecue, some games of chess, a nice dinner, “studying”[1]

---

[1] in rare cases the quotations marks were unjustified

at some café in the weekend, and many other nice activities.

Speaking about non-academic life, thanks also to all my fellow musicians in Heimdal Storband and in Betel Brass. I enjoyed the many hours I spent with you at numerous rehearsals and concerts. Furthermore, I was happy to be part of Betel Pinsemenighet in Trondheim, were I met plenty of appreciated people.

Thanks to my friends and former study mates from Germany, Marco, Julius, and Tim, who came far up north to visit me.

Of course, I have to devote a special thanks to my parents and brothers, who were, despite the distance, supportive and motivating throughout these past four years.

To those who feel unable to identify with any of the aforementioned names: including everyone I had the pleasure to meet here in Trondheim would undoubtedly exceed the space available on this page. Feel thanked anyway!

Preface

This thesis presents the results of the research that I have conducted during my PhD term at NTNU from 2013 to 2017. The scientific outcome of my work is represented by the five papers that are included in their final published form. They are not ordered chronologically. Instead, the three papers on magnetism on topological insulator surfaces are placed first, as this subject had most weight in my PhD studies.

The research papers are preceded by five chapters that serve as an introduction to the general field of topological condensed matter and to the specific systems that will be encountered in the papers. This introductory part hence does not represent original research or ideas of my own, unless where a reference to my papers is made. Rather, it provides background knowledge that has been collected from many other publications. Some sources that have been particularly useful are the review articles by Hasan and Kane [6] and Qi and Zhang [7], which are standard references for topological insulators and supercondctors, lecture notes by Tong [8] that I consulted concerning the quantum Hall effect and some general aspects, and a review by Schnyder and Brydon [9] on nodal superconductors.

Although the introduction part is meant to provide the necessary background to understand the purpose and findings of the research papers, it is clearly not a textbook. Thus, many important facts and relations are simply cited from the literature. Derivations, or parts of them, are only shown where I found them useful, which is of course a matter of taste[2]. Occasionally heuristic arguments are given to convey some intuition for the objective at hand.

Towards the end of the Chapters 4 and 5 there are sections that summarize and briefly explain the results of the papers. As the complete papers are included in the thesis, I did not intend to merely repeat their content in these sections. Instead, I tried to highlight aspects that are not expanded on in the papers and keep it short otherwise. The results of my research projects have also been presented and discussed at several conferences and seminars (cf. Tab. 1) after publication, which helped me to broaden my understanding and some-

---

[2] and perhaps my individual learning process

times to see the results from a different angle. For that reason, the thesis also contains a few remarks that cannot be found at all in the papers.

The five chapters are organized in the following manner. Chapter 1 provides a very basic introduction. Chapter 2 reviews notions of topology that are important in condensed matter theory, before concrete systems are discussed in Chapter 3: the Su-Schrieffer-Heeger model as one of the simplest topological models that can be found, the quantum Hall effect in some detail due to its tremendous importance in the development of the field, and then topological insulators, which are dealt with in three of the five papers. The heterostructures that are investigated in these papers are explained more specifically in Chapter 4. The last chapter is directed at topological superconductors and introduces the other two papers.

All copyrighted material in the thesis is reprinted with permission. Specifically, this applies to the five research papers and in addition Figs. 3.3(b) and 4.2. This content was originally published by APS in the Physical Review journals. Figure 5.6 is reprinted under the Creative Commons Attribution 3.0 licence.

Table 1: Events (outside NTNU) where I presented results from the papers in this thesis.

Year	**Event**	**Papers**
2014	Workshop SHYNED: Physics and application of superconducting hybrid nano-engineered devices, Santa Maria di Castellabate (Italy)	[4]
2015	APS March Meeting, San Antonio (USA)	[4]
2015	CNTQC Workshop Top-Spin: Spin and topological phenomena in nanostructures, Salerno (Italy)	[4]
2015	Condensed matter theory seminar, Dresden (Germany)	[1]
2016	APS March Meeting, Baltimore (USA)	[1, 2]
2016	ToCoTronics Workshop: Correlated electrons at surfaces and interfaces, Würzburg (Germany)	[1, 2]
2016	34th Jerusalem Winter School: New Horizons in Quantum Matter, Jerusalem (Israel)	[1, 2]
2017	TKM institute seminar, Karlsruhe (Germany)	[1–3]
2017	APS March Meeting, New Orleans (USA)	[3]
2017	Nordita conference: Frontiers of topological quantum matter, Stockholm (Sweden)	[3]
2017	Condensed matter theory seminar, Dresden (Germany)	[1–3]

Contents

Chapter 1

Introduction

The work presented in this thesis [1–5] is located within the broad field of condensed matter physics, which is (mostly) the science of electrons in a crystal (thus, in a solid material). A relatively young and vivid subfield is concerned with so-called topological quantum matter, comprising the prominent material class of topological insulators and superconductors [6, 7]. These novel materials are fascinating states of matter: By virtue of extraordinary – "topologically nontrival" – features of the bulk material, exotic quantum states can emerge at the surface. For instance, despite being insulating in the bulk, a topological insulator (TI) becomes metallic at the surface, where it exhibits electrons for which the term "relativistic" suits although they move at only 0.2 % of the speed of light. Topological superconductors (TSCs) host quantum states that act like Majorana fermions. Such fermions are their own antiparticles, which is, at least most likely, not the case for any known elementary particle. Furthermore, such topological surface properties are robust against a variety of perturbations, as they are protected by topology. Unsurprisingly, topological materials have attracted much attention, both for being of fundamental interest and for their potential technological use in nanodevices with envisioned applications ranging from spintronics to quantum-computation. The relevance of topological quantum matter in general was also acknowledged by the Nobel Prize in Physics in 2016, which was awarded to Thouless, Haldane, and Kosterlitz "for theoretical discoveries of topological phase transitions and topological phases of matter" [10].

The papers at the end of this thesis deal with topological surface states: Papers [1–3] explore the interplay of TIs and magnetism, while Papers [4] and [5] are concerned with the existence of Majorana states in superconducting systems. Clearly, topology plays a superior role in the entire thesis. The next section is therefore devoted to explain what topology is about. This will be followed by some introductory remarks on topology in condensed matter.

1.1 What is topology?

Topology [11,12] is a subfield of mathematics that aims at classifying objects[3] (one may think of geometric shapes in two or three dimensions) according to essential properties that do not depend on details. Such essential properties are identified on the basis of continuous deformations[4]. Every property that is not affected by any continuous deformation is topological, otherwise it is not. We illustrate the kind of properties that topology is concerned with, also called topological invariants, by three examples.

1. *Connectedness.* Consider the two areas shown in Fig. 1.1. Apart from differences in their shapes, which are details, they are different on a fundamental level because the dark area is connected whereas the light one is not. Any deformation merging the two light "pieces" would be discontinuous. Mathematically speaking, the light area is not connected because it can be written as the union of two disjoint open[5] sets.

2. *Winding number.* A closed path in two dimensions that is not allowed to cross a given defect in the plane, can be topologically characterized by the number of times it winds around that point. This number must be an integer (Actually, this yields a topological invariant of the punctured plane – its fundamental group $\pi_1 = \mathbb{Z}$.). Three simple examples are shown in Fig. 1.2.

---

[3] In general so-called topological spaces, often equipped with an additional algebraic structure.

[4] in the sense of homeomorphisms

[5] relative to its own topology, not the $\mathbb{R}^2$

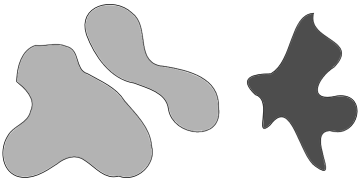

Figure 1.1: The light area is not connected, in contrast to the dark area, which makes them topologically distinct.

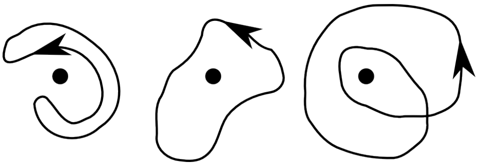

Figure 1.2: Three closed paths with different winding number ν with respect to a given point (black dot). From left to right, $\nu = 0$, 1, and 2, respectively.

3. The *genus* g is a topological invariant characterizing a closed two-dimensional surface[6] S, like the surface of a finite three-dimensional object. Pictorially, it counts the number of holes in (or handles attached to) the object (see Fig. 1.3): if S is the surface of a cube, $g = 0$. The same is true for the sphere, hence the two are topologically equivalent (continuously deformable into one another). However, if a handle is attached to the sphere or a hole is drilled through the cube, their genus changes to $g = 1$ – the topology has been altered as such operations are not continuous. On the other hand, the latter two surfaces share their topological features with the torus, which also has one hole ($g = 1$).

In the third example, topology can be linked to geometry. The connection is made by the Gauss-Bonnet theorem [11], which states that the genus can be calculated by integrating the Gaussian curvature G over the entire surface:

$$g = 1 - \frac{1}{2} \int_S G(\mathbf{r})\, \mathrm{d}^2 r \tag{1.1}$$

This is remarkable, because geometry accurately maintains all the details that topology discards. One can also say that geometry describes local properties, while topology is only sensitive to global properties.

---

[6] more precisely: compact, orientable, and without a boundary

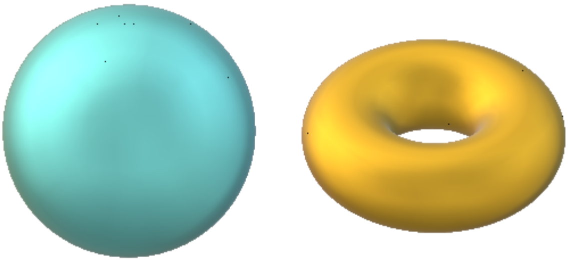

Figure 1.3: Two closed surfaces with genus $g = 0$ (left) and $g = 1$ (right).

1.2 Topology and condensed matter

Under certain conditions, topological invariants not unlike the ones above can be assigned to solid materials when they are described in terms of their band structure. These bands indicate which states of an electron in the material are allowed by quantum mechanics. As a precondition to make use of topological concepts, it turns out that the occupied and empty states should be disconnected, like the light shape in Fig. 1.1. Then, the occupied states (filled bands) can in some cases be characterized by winding numbers. In other cases, the Gauss-Bonnet theorem can be generalized to calculate an analogue of the genus: the Chern number. For the TIs, the relevant topological invariant can only have two different values and is said to be in $\mathbb{Z}_2$.

Whenever a material exhibits a topological invariant with nonzero value, one can expect physical features that remain completely unaffected by a broad range of perturbations, as long as those do not lead to a discontinuous alteration, because topology is by definition independent of any local details. For instance, in the quantum Hall effect (QHE), which was the first system that was understood to be of a topological nature, Klitzing [13] discovered a conductance that takes certain quantized values regardless of material parameters or geometric characteristics of the sample. The quantization in the QHE has such a stunning precision that the effect is nowadays used as the definition of the unit Ohm. Klitzing also received the Nobel Prize in 1985.

The QHE historically started the interest for topological effects in condensed matter. Meanwhile, topology seems ubiquitous and has become a significant guiding scheme in the search for novel phases of matter. The questions that one can investigate when dealing with topological quantum matter can be sorted in three categories:

1. How can topology be applied? What types of topologically nontrivial systems (i.e. Hamiltonians) are in principle possible? How can they be classified and which topological invariants characterize the different classes?

2. Which physical systems are realizations of the cases identified in 1.? Which microscopic mechanisms are responsible for the topological properties? Which materials are good candidates to look for nontrivial topology?

3. By which observables can a specific topological phase be identified? What are the unique signatures and how can they be applied in novel quantum devices?

The first question is mainly a mathematical one. The aspect of how to apply topological concepts has lead to several different branches within the field of topological quantum matter. The TIs and TSCs that have already been mentioned belong to the symmetry-protected topological (SPT) phases, which is maybe the most important branch. For the SPT phases, a comprehensive classification of the possible topological phases exists. In other cases, the classification can be very difficult, for instance for strongly correlated topological systems.

The second question involves both physics and chemistry. Having identified Hamiltonians where mathematics allows for the presence of nontrivial topological invariants, it is in general still a difficult task to find a material, or sometimes even a toy model, for which a certain Hamiltonian provides the correct (effective) description. At times it may require to scan over large families of compounds, hoping to discover one that realizes the desired topological phase. Alternatively, one can try to engineer topological systems by combining the properties of known materials in heterostructures or artificial meta-materials.

The third question is linked to the second: If a material is believed to be topological, how can this assumption be verified unambiguously in experiments? Finally, it also adds practical relevance to the field as applications can be proposed. Usually topologically protected boundary states are the centerpiece in such considerations.

The structure of the thesis approximately follows these questions, culminating in the research papers, which all deal mainly with questions of the third kind[7]. The next chapter will deal with the classification of SPT phases and demonstrate how topological invariants can be defined. Afterwards, Chapter 3 introduces systems that realize such phases. Chapter 4 is focused on phenomena related to TIs. The questions 2 and 3 are then revisited in the last chapter for the case of superconductors.

---

[7] partly also with the existence of a topological phase

Chapter 2

Topological concepts in condensed matter

This chapter serves to clarify general notions of topology, while specific physical systems will be discussed in the next chapter. The TIs and TSCs can be understood within the framework of SPT phases. As there are several other kinds of topological systems, a brief overview is given in the first section. Afterwards, the classification of SPT phases is presented. The remaining sections define some of the relevant topological invariants (the $\mathbb{Z}$ invariants), whereby the formal link between topology and physics becomes visible. The equally important $\mathbb{Z}_2$ invariants are deferred to Chapter 3. We close the chapter with some remarks on the bulk-boundary correspondence.

2.1 Overview

As topology has become a very fashionable theme in condensed matter physics during the past decade, several different kinds of systems are now labeled as "topological", which can sometimes cause confusion. Although the terminology is not always completely congruent throughout the literature and the field keeps growing rapidly, there are some main concepts and terms that can be mentioned[8] to put this thesis in a broader context:

---

[8] The list is not meant to be exhaustive, though, and the items are not completely disjoint.

- SPT phases [14, 15] with a full bulk energy gap, typically described at zero-temperature and with (at most) short-range interactions. The topological classification depends on generic symmetries in the system. This comprises TIs and TSCs.
- Nodal topological materials where the bulk energy gap has point or line nodes. The concepts of SPT phases can be applied in a weaker sense to a sub-Hamiltonian that is restricted to the co-dimension of the nodes minus one [16]. Examples are Dirac and Weyl semimetals [17] and nodal SCs [9].
- Topological crystalline insulators (TCIs) [18] and higher-order TIs [19], where the SPT classification is extended by certain crystallographic symmetries.
- Topological order: in contrast to the SPT (and related) phases, topologically ordered phases are characterized by long-range entanglement, strong correlations, and fractional excitations [20]. Prominent examples are the fractional quantum Hall effect (FQHE) [21], quantum dimer models [22], and spin liquids [23]
- Topological defects: The defect itself is topological, rather than the bulk system hosting it, e.g. skyrmions [24] in spin systems or crystal dislocations [25].

The QHE [13,26,27] can be mentioned in its own right. It can be seen as the parent system for all of the first four categories above.

In this thesis, Papers [1–4] are concerned with phenomena related to “classical” SPT phases. Paper [5] deals with a nodal system that can be seen as a generalized SPT phase. In the next section, the general classification of the SPT phases by generic symmetries [28] is introduced.

2.2 Periodic table of SPT phases

Let a system of noninteracting fermions be described by a Hamiltonian $\mathcal{H}$ in matrix form in a suitable basis of states, taking into account all present quantum numbers. Assume further that $\mathcal{H}$ is irreducible in the sense that there is no other (orthonormal) basis in which $\mathcal{H}$ would be block-diagonal – it would then be sufficient to consider these blocks separately. Formally speaking, there is no unitary matrix U that commutes with $\mathcal{H}$.

However, the Hamiltonian can still have *anti*-unitary symmetries of the form $\mathcal{K}U$, with the operator $\mathcal{K}$ of complex conjugation [29]. The unitary transformation of $\mathcal{H}$ with U then yields a relation to the complex conjugate Hamiltonian $\mathcal{H}^*$. By hermiticity of $\mathcal{H}$, there are only two possible symmetries of that kind, denoted $\mathcal{T} = \mathcal{K}U_\mathcal{T}$ and $\mathcal{C} = \mathcal{K}U_\mathcal{C}$, with

$$U_\mathcal{T}^\dagger \mathcal{H}^* U_\mathcal{T} = \mathcal{H}, \tag{2.1}$$

$$U_\mathcal{C}^\dagger \mathcal{H}^* U_\mathcal{C} = -\mathcal{H}. \tag{2.2}$$

The physical interpretation of Eq. (2.1) is time-reversal symmetry (TRS), while Eq. (2.1) describes invariance under charge inversion, or particle-hole symmetry (PHS). If TRS is present, the operator $\mathcal{T}$ of time reversal (TR) squares to either $\mathbb{1}$ or $-\mathbb{1}$. The same is true for $\mathcal{C}$ in the case of PHS. In addition, the joint effect of TRS and PHS has to be considered. If both are present, there is a symmetry $\mathcal{S} = \mathcal{T}\mathcal{C} = U_\mathcal{T} U_\mathcal{C} = U_\mathcal{S}$ with

$$U_\mathcal{S}^\dagger \mathcal{H} U_\mathcal{S} = U_\mathcal{C}^\dagger \mathcal{H}^* U_\mathcal{C} = -\mathcal{H}. \tag{2.3}$$

This symmetry is called chiral symmetry. It must be absent if a Hamiltonian has only exactly one of the symmetries $\mathcal{T}$ or $\mathcal{C}$, but a unitary matrix $U_\mathcal{S}$ satisfying Eq. (2.3) can still exist if both TRS and PHS are absent. Thus, all possible combinations of $\mathcal{T}^2 = 0, \pm\mathbb{1}$, $\mathcal{C}^2 = 0, \pm\mathbb{1}$, and $\mathcal{S}^2 = 0, \mathbb{1}$ (where zero denotes the absence of the symmetry) yield ten different classes of Hamiltonians as listed in the first four columns of Tab. 2.1. This classification is known as the "tenfold way" and was introduced by Altland and Zirnbauer [30] in expansion of the previously known Wigner-Dyson classes [31,32]. It is based on mathematical work by Cartan [33].

Remarkably, there is a close link between the tenfold way and topology [16]. Schnyder *et al.* [28] and Kitaev [34] have demonstrated that for non-interacting Hamiltonians with a gapped energy spectrum the number of possible topologically distinct phases is determined by the

Table 2.1: The classification of Hamiltonians according to TRS $\mathcal{T}$, PHS $\mathcal{C}$, and chiral symmetry $\mathcal{S} = \mathcal{T}\mathcal{C}$ into ten classes [30] allows to catalogue the topological invariants [16, 28, 29, 34] that can be defined in n (mod 8) dimensions.

Symmetry				Topological invariant							
Class	$\mathcal{T}^2$	$\mathcal{C}^2$	$\mathcal{S}^2$	1D	2D	3D	4D	5D	6D	7D	8D
A	0	0	0	0	$\mathbb{Z}$	0	$\mathbb{Z}$	0	$\mathbb{Z}$	0	$\mathbb{Z}$
AIII	0	0	$\mathbb{1}$	$\mathbb{Z}$	0	$\mathbb{Z}$	0	$\mathbb{Z}$	0	$\mathbb{Z}$	0
AI	$\mathbb{1}$	0	0	0	0	0	$\mathbb{Z}$	0	$\mathbb{Z}_2$	$\mathbb{Z}_2$	$\mathbb{Z}$
BDI	$\mathbb{1}$	$\mathbb{1}$	$\mathbb{1}$	$\mathbb{Z}$	0	0	0	$\mathbb{Z}$	0	$\mathbb{Z}_2$	$\mathbb{Z}_2$
D	0	$\mathbb{1}$	0	$\mathbb{Z}_2$	$\mathbb{Z}$	0	0	0	$\mathbb{Z}$	0	$\mathbb{Z}_2$
DIII	$-\mathbb{1}$	$\mathbb{1}$	$\mathbb{1}$	$\mathbb{Z}_2$	$\mathbb{Z}_2$	$\mathbb{Z}$	0	0	0	$\mathbb{Z}$	0
AII	$-\mathbb{1}$	0	0	0	$\mathbb{Z}_2$	$\mathbb{Z}_2$	$\mathbb{Z}$	0	0	0	$\mathbb{Z}$
CII	$-\mathbb{1}$	$-\mathbb{1}$	$\mathbb{1}$	$\mathbb{Z}$	0	$\mathbb{Z}_2$	$\mathbb{Z}_2$	$\mathbb{Z}$	0	0	0
C	0	$-\mathbb{1}$	0	0	$\mathbb{Z}$	0	$\mathbb{Z}_2$	$\mathbb{Z}_2$	$\mathbb{Z}$	0	0
CI	$\mathbb{1}$	$-\mathbb{1}$	$\mathbb{1}$	0	0	$\mathbb{Z}$	0	$\mathbb{Z}_2$	$\mathbb{Z}_2$	$\mathbb{Z}$	0

symmetry class and the dimension of the system (modulo eight), cf. Tab. 2.1. Only two kinds of topological invariants that distinguish the different phases are possible (if there are nontrivial phases at all), namely either $\mathbb{Z}$ or $\mathbb{Z}_2$ invariants. When nontrivial topology is found in such systems, it is protected by the presence (or absence) of the symmetries in its respective class, hence the name SPT phases. Table 2.1 is often referred to as the periodic table of SPT phases, and is an important guide in the search for novel topological phases.

As a precursor to the following chapters, we already mention where the systems discussed there are placed in the periodic table:

- Su-Schrieffer-Heeger model (Section 3.1): class BDI in 1D, $\mathbb{Z}$ invariant protected by chiral symmetry
- QHE (Section 3.2): class A in 2D, $\mathbb{Z}$ invariant from TRS breaking
- TIs (Section 3.3 ff.): class AII in 2D and 3D, $\mathbb{Z}_2$ invariant pro-

tected by TRS

- Majorana wires (Section 5.4): class D in 1D, $\mathbb{Z}_2$ invariant protected by PHS
- Nodal noncentrosymmetric superconductors (Section 5.5): gapless, but weak topology via class AIII in 1D, $\mathbb{Z}$ invariant

A further remark about the periodic table is at hand. If a nonzero entry appears for a Hamiltonian of given class and dimension, it only means that mathematics would allow for at least one nontrivial topological phase. However, the physical system does not *have to* realize such a phase. For example, for any BDI Hamiltonian in 1D a $\mathbb{Z}$-invariant ν taking integer values can be defined. For a specific instance of such a Hamiltonian, ν may still happen to be always zero, or assume only 2 different values. A nonzero entry in the periodic table is thus a necessary but not sufficient condition to find a nontrivial phase.

In cases where there is a $\mathbb{Z}$ invariant, it can be written in terms of a winding number about the origin of the 2D plane (if there is chiral symmetry) or as a Chern number (otherwise). These invariants will be explained in Sections 2.3 to 2.5. The $\mathbb{Z}_2$ invariants for the topological insulators with TRS will be discussed at the end of the next chapter.

2.3 Berry phase

The Berry phase [35] is a quantum analogue of the geometric phase that is known from classical mechanics [36]. For instance, a Foucault pendulum that is transported along a triangular path on the globe formed by two meridians and one quarter of the equator is rotated by $\frac{\pi}{2}$. In quantum mechanics, a Hamiltonian that is adiabatically transported along a closed path in a curved parameter space gives rise to a phase shift of the eigenstates. Such a phase difference can have a physical meaning, in contrast to the global phase of wavefunctions. The geometric phase of the Foucault pendulum can be related to the Gaussian curvature – the fact that the pendulum is rotated is a manifestation of the curved surface of the globe. As mentioned in the introduction, the Gaussian curvature can in turn be used to calculate the genus, which is an integer topological invariant. Similarly, the Berry phase is related to a (generalized) curvature from which one can calculate an integer topological invariant of the quantum-mechanical system. This invariant is called Chern number.

Consider a Hamiltonian H that depends on a set of parameters $\{p_i\}$, whereby a path in parameter space can be parametrized as $p_i(t)$. The system may be in an eigenstate $|\Psi\rangle$ at $t = 0$. We assume furthermore that t can be varied in an adiabatic manner, meaning that if $|\Psi\rangle$ is the n-th eigenstate of $H(p_i(t = 0))$, than for any t the system will be in the n-th eigenstate of $H(t) \equiv H(p_i(t))$, which we call $|n(t)\rangle$. This is only possible if for any t, the n-th eigenenergy $\varepsilon_n(t)$ is non-degenerate, i.e. no level crossings occur in the process of changing t. In that sense, one can call H a "fully gapped" Hamiltonian with respect to the path $p_i(t)$.

The evolution of the eigenstate is given by the Schrödinger equation [37],

$$i\hbar\partial_t|\Psi(t)\rangle = H(t)|\Psi(t)\rangle. \tag{2.4}$$

The solution to this equation is [11]

$$|\Psi(t)\rangle = e^{i\eta(t)-\frac{i}{\hbar}\int_0^t \varepsilon_n(t)\mathrm{d}t}|n(t)\rangle, \tag{2.5}$$

with the phase

$$\eta(t) = i\int_0^t \mathrm{d}t'\langle n(t')|\partial_{t'}n(t')\rangle. \tag{2.6}$$

If $p_i(0) = p_i(T)$, then $\eta \equiv \eta(T)$ is called the Berry phase. It is often rewritten in the form

$$\eta = i\int_{\mathcal{C}} \mathrm{d}\mathbf{p}\,\langle n(\mathbf{p})|\boldsymbol{\nabla}_{\mathbf{p}}|n(\mathbf{p})\rangle, \tag{2.7}$$

where $\mathcal{C}$ is the closed loop in parameter space, $\mathbf{p}$ is the vector of parameters p_i, and the i-th component of $\boldsymbol{\nabla}_{\mathbf{p}}$ is ∂_{p_i}.

This formal solution of the Schrödinger equation has a geometric interpretation. One can directly link the Berry phase to the mathematical framework of differential forms on fibre bundles [11,12], which will not be reviewed here, by defining the Berry connection

$$\mathcal{A} = -i\langle n(\mathbf{p})|\boldsymbol{\nabla}_{\mathbf{p}}|n(\mathbf{p})\rangle \tag{2.8}$$

and the corresponding Berry curvature[9]

$$\mathcal{F}_{ij} = \frac{\partial \mathcal{A}_i}{\partial p_j} - \frac{\partial \mathcal{A}_j}{\partial p_i}. \tag{2.9}$$

In principle, one could attach arbitrary phases to the eigenvectors at each parameter point, $|n(\mathbf{p})\rangle \mapsto \exp(i\varphi(\mathbf{p}))|n(\mathbf{p})\rangle$. By Eq. (2.8) it is clear that $\mathcal{A}$ will depend on $\varphi(\mathbf{p})$. In contrast, the specific choice of phases cancels in $\mathcal{F}$, which is thus gauge-independent. The Berry phase is evidently the negative integral of $\mathcal{A}$ along the loop $\mathcal{C}$ in parameter space. However, as $\mathcal{C}$ is closed, it can be rewritten by Stokes' theorem as an integral of $\mathcal{F}$ over the area enclosed by $\mathcal{C}$. Therefore, the Berry phase is also gauge-independent and it is plausible that it can have a physical meaning.

2.4 Chern number and Bloch sphere

Let us now consider the special case where the parameter space is a two-dimensional closed surface S. If there is a loop $\mathcal{C}$ in S, then because S is closed, it is divided in two areas A_1, A_2 that are both bounded by $\mathcal{C}$: traveling along the loop, it is arbitrary which side is defined as "inside" or "outside" of $\mathcal{C}$. Consequently, the Berry phase, which is a physical quantity, must not depend on this choice up to an integer multiple of 2π:

$$-\eta = \int_{A_1} \mathcal{F}_{ij} \mathrm{d}p^i \wedge \mathrm{d}p^j = 2\pi C - \int_{A_2} \mathcal{F}_{ij} \mathrm{d}p^i \wedge \mathrm{d}p^j \tag{2.10}$$

with $C \in \mathbb{Z}$. The sign in front of the last integral appears because $\mathcal{C}$ winds in opposite direction relative to A_1 and A_2. The immediate conclusion is that the integral over $S = A_1 \cup A_2$ must be quantized:

$$C = \frac{1}{2\pi} \int_S \mathcal{F}_{ij} \mathrm{d}p^i \wedge \mathrm{d}p^j. \tag{2.11}$$

---

[9] In general, the relation between the curvature (a two-form) and the connection (a one-form) is $\mathcal{F} = \mathrm{D}\mathcal{A} = \mathrm{d}\mathcal{A} + \mathcal{A} \wedge \mathcal{A}$, with the covariant derivative D, the exterior derivative d, and the wedge product $\wedge$ [11].

The integer C is the Chern number. More precisely, it is the *first* Chern number $C^{(1)}$ – one can generalize the argument above to any even dimension [29]. This leads to the n-th Chern number $C^{(n)}$ in $2n$ dimensions. In analogy to the genus g in the Gauss-Bonnet theorem, $C^{(n)}$ is a topological invariant. This can be understood heuristically by the fact that C cannot change its value in a continuous manner by the restriction to integers.

Why is the case of closed parameter spaces important? In condensed matter physics, the wavefunctions of non-interacting electrons in a lattice potential have the Bloch form [38] $\Psi_{\mathbf{k}}(\mathbf{r}) = \exp(i\mathbf{k}\cdot\mathbf{r})u(\mathbf{r})$, where u is periodic with respect to the lattice vectors $a_i\hat{\mathbf{e}}_i$: $u(\mathbf{r}+a_i\hat{\mathbf{e}}_i) = u(\mathbf{r})$. This allows to describe the system by its band structure in momentum space. The momentum $\mathbf{k}$ is only defined modulo the reciprocal lattice vectors and can be restricted to the first Brillouin zone (BZ), where k_i and $k_i + 2\pi/a_i$ are identified. By virtue of this periodicity, the BZ in 1D can be mapped onto the circle S_1. In n dimensions, it is the product space of n circles, $S_1 \times \ldots \times S_1 \equiv T_n$ which is the n-torus. Hence, momentum space is always a closed manifold. If we treat $\mathbf{k}$ like the parameter $\mathbf{p}$ above, we can assign a Chern number to a band of the Hamiltonian if two conditions are satisfied:

1. The number of dimensions is even as required to define $C^{(n)}$.
2. The band structure is compatible with the assumption of adiabatic parameter change which underlies the derivation of the Berry phase.

While the first condition is clear, the second one means that (i) there is no crossing of bands and (ii) the band is completely filled. Physically, this restricts the topological classification of bands in terms of Chern numbers to materials where the Fermi level E_F lies inside an energy gap – in other words, band insulators.

Condition (i) can be loosened by neglecting features of the band structure outside the gap. Technically, one can continuously transform the original Hamiltonian to a flat-band Hamiltonian where all filled bands have some energy $E_1 < E_F$ and all empty bands $E_2 > E_F$ (for details see [28]). This reduces the Hamiltonian to the two-level form

$$H(\mathbf{k}) = s(\mathbf{k})\mathbb{1}_{2\times 2} + \mathbf{d}(\mathbf{k}) \cdot \boldsymbol{\sigma} \tag{2.12}$$

with the Pauli matrices $\boldsymbol{\sigma} = (\sigma_x, \sigma_y, \sigma_z)^{\mathrm{T}}$, and the restrictions $s(\mathbf{k}) = (E_1 + E_2)/2$, $|\mathbf{d}(\mathbf{k})| = (E_2 - E_1)/2$. Then the unit vector

$$\hat{\mathbf{e}}_{\mathbf{d}}(\mathbf{k}) = \frac{\mathbf{d}(\mathbf{k})}{|\mathbf{d}(\mathbf{k})|} \tag{2.13}$$

defines a mapping from the BZ to the unit sphere (called the Bloch sphere). The Chern number has the following visual interpretation [8]: it counts how often the mapping $\mathbf{k} \mapsto \hat{\mathbf{e}}_{\mathbf{d}}(\mathbf{k})$ wraps the Bloch sphere as $\mathbf{k}$ runs over the entire BZ.

2.5 Winding number

The Chern number cannot be defined in odd dimensions. However, the mapping to the Bloch sphere still exists. In a system with chiral symmetry, $\mathbf{d}(\mathbf{k})$ is restricted to a plane [16]. This allows for the definition of a winding number of $\mathbf{d}(\mathbf{k})$ around the origin, as $|\mathbf{d}(\mathbf{k})| = 0$ is forbidden by the energy gap. The winding number was already introduced pictorially in Chapter 1. Here, we just augment this with a formal definition in the 1D case[10]. When k runs once over the BZ the winding number is

$$\nu = \frac{1}{2\pi} \int_{\mathrm{BZ}} \mathrm{d}k\, \theta(k) = \theta\left(\frac{\pi}{a}\right) - \theta\left(-\frac{\pi}{a}\right), \tag{2.14}$$

where $\theta(k)$ is the polar angle of $\mathbf{d}(\mathbf{k})$ as a continuous function of k.

Chern and winding numbers are sufficient to describe the SPT phases with $\mathbb{Z}$ invariant: every $\mathbb{Z}$ entry in the periodic table Tab. 2.1 occurs either in an even dimension or in a class with chiral symmetry.

2.6 Bulk-boundary correspondence

The interest in topological materials is largely owed to the existence of the exotic quantum states at their boundaries that were mentioned

---

[10] The more complicated definition in $2n + 1$ dimensions can be found in [29], but is not relevant for the following chapters.

in the introduction. They are found at the ends of a 1D system, the edges of a 2D system, or the surfaces of a 3D system. Examples for each case will be given in the next chapter. The reason why these states emerge can be heuristically explained in the following manner: At the interface between two topologically distinct phases[11] there is a topological invariant ν that takes a different value on the two sides of the interface. In consequence, the value of ν must change as one crosses the interface. This is not possible without closing the energy gap, though, and therefore an in-gap (zero energy) state must exist that is localized at the interface and persists as long as the bulk topology remains unchanged. Mathematically, this is often described using the 1D Jackiw-Rebbi (JR) model [39]. We do not review it here because a closely related model is discussed in Section 3.1. The relation of the bulk topology to the existence of zero-energy boundary states is called the bulk-boundary correspondence[12] [43–45].

However, the simple line of thought above does not provide a rigorous proof of the bulk-boundary correspondence as it makes assumptions that are not always justified. Specifically, if the interface is characterized by different symmetries than the bulk, the topological index as a function of the spatial coordinate may simply be ill-defined at the interface, such that there is no reason for a gap closure[13]. This situation is relevant in the Papers [1–3], that deal with a TI surface where TRS is explicitly broken, and Paper [5], which provides an example of spontaneous symmetry breaking. Generally speaking, one has to check the bulk-boundary correspondence for each given topological system, e.g. by transforming it to the JR model in the direction perpendicular to the boundary. Using more advanced field-theoretic methods, one can show that the bulk-boundary correspondence is a generic property of the SPT phases [43–45] as long as none of the defining symmetries is violated.

---

[11] One of them might be trivial, e.g. the vacuum.

[12] Apparently the term originated from string theory [40–42] and was later adopted in condensed matter.

[13] There may still be localized surface states, but not necessarily at zero energy.

Chapter 3

Topological Insulators: From one to three dimensions

Having reviewed the general framework of SPT phases, we will now consider physical systems in which such topological phases materialize. Here, the focus is solely on bulk insulators – superconductors are devoted their own chapter. While the research Papers [1–3] deal with heterostructures involving 3D TIs, it is beneficial to begin with lower-dimensional systems, and then see how the 3D TI can be obtained by generalizing the simpler models. We will start in 1D with the Su-Schrieffer-Heeger (SSH) model, followed by the QHE[14] in 2D. The quantum spin Hall effect (QSHE), a 2D TI, will only be discussed in a brief manner. Finally, the 3D TIs are introduced, including their $\mathbb{Z}_2$ invariants which had not been presented in Chapter 2.

3.1 Su-Schrieffer-Heeger model

The Su-Schrieffer-Heeger (SSH) model [46, 47] is perhaps the simplest example of a topological condensed matter system. It provides a two-band description of a bipartite crystal in one dimension. It exhibits two distinct phases that can be distinguished by a topological invariant

---

[14] Always in the sense of integer QHE, unless noted otherwise.

and illustrates the generic features of an SPT phase, in particular the existence of exponentially localized zero-energy modes at the boundary.

Originally, the SSH model was proposed to describe polyacetylene, which basically is a chain of carbon atoms. Each carbon atom has bonds to the neighboring two carbon atoms and one bond to a hydrogen atom, which localizes three valence electrons. The fourth valence electron determines the electronic transport properties of the molecule. This is represented by a nearest-neighbor hopping term in the SSH model. It turns out that the free energy is minimized when the carbon atoms are not equidistant but slightly displaced, such that each atom has one neighbor that is a bit closer than the other. Thus, the chain can be decomposed in two sub-chains ($i = 1, 2$) forming a bipartite lattice with a staggered hopping amplitude. We write α, β for the hopping within and in between unit cells, respectively. With the operator $\phi^\dagger_{i,n}$ of electron creation, where n runs over the unit cells, it is straight-forward to write down the lattice Hamiltonian for electron hopping in a molecule of length N:

$$H_{\text{SSH}} = \alpha \sum_{n=1}^{N} \left(\phi^\dagger_{2,n}\phi_{1,n} + \text{h.c.} \right) + \beta \sum_{n=1}^{N-1} \left(\phi^\dagger_{1,n+1}\phi_{2,n} + \text{h.c.} \right) \tag{3.1}$$

Note that H_{SSH} does not account for the spin degree of freedom, therefore two copies of the model must be employed to adequately describe a real molecule, or the molecule must be subject to a strong magnetic field. However, we will not discuss polyacetylene in further detail and instead simply consider the spinless SSH Hamiltonian as a “toy model” to demonstrate the topological features. Although there is no spin degree of freedom, the sublattice index takes the role of a pseudospin (in analogy to graphene), and the Hamiltonian can conveniently be expressed using spinors $\Phi^\dagger_n = (\phi^\dagger_{1,n}, \phi^\dagger_{2,n})$ and the Pauli matrices $\boldsymbol{\sigma} = (\sigma_x, \sigma_y, \sigma_z)$. Let us first look at the bulk of a long chain, where momentum is a good quantum number:

$$\begin{aligned} H_{\text{bulk}} &= \alpha \sum_n \Phi^\dagger_n \sigma_x \Phi_n + \frac{\beta}{2} \sum_n \Phi^\dagger_{n+1}(\sigma_x + i\sigma_y)\Phi_n + \Phi^\dagger_n(\sigma_x - i\sigma_y)\Phi_{n+1} \\ &= \frac{1}{N} \sum_k \Phi^\dagger_k \mathcal{H}(k) \Phi_k, \end{aligned} \tag{3.2}$$

where

$$\Phi_n^\dagger = \frac{1}{N}\sum_k e^{inka\Phi_k^\dagger}, \tag{3.3}$$

a is the distance between two unit cells and

$$\begin{aligned}
\mathcal{H}(k) &= \begin{pmatrix} 0 & \alpha+\beta e^{ika} \\ \alpha+\beta e^{-ika} & 0 \end{pmatrix} && (3.4)\\
&= \mathbf{d}(k)\cdot\boldsymbol{\sigma}, && (3.5)\\
\mathbf{d}(k) &= (\alpha+\beta\cos ka, -\beta\sin ka, 0) && (3.6)
\end{aligned}$$

The dispersion relation is readily read off:

$$\varepsilon(k) = \pm\sqrt{\alpha^2+\beta^2+2\alpha\beta\cos ka}. \tag{3.7}$$

As there is a gap $\Delta\varepsilon = 2|\alpha-\beta|$ between the upper and the lower band, which are at half filling empty and filled, respectively, the chain is a band insulator whenever $\alpha \neq \beta$. Although $\varepsilon(k)$ is symmetric under exchange of α, β, the two insulating phases with $\alpha > \beta$ and $\alpha < \beta$ are not identical.

The difference between these phases is based on the topology of the bulk. The Hamiltonian Eq. (3.6) is periodic in momentum, thus the vector $\mathbf{d}(k)$ describes a closed loop as k is varied from 0 to $\frac{2\pi}{a}$ in an adiabatic manner (actually a circle in the $d_x - d_y$ plane around $(\alpha, 0)$ with radius β). This loop cannot be contracted to a point if it encloses the origin, as the gapped state requires $\alpha \neq \beta$. Without the gap, k can no longer be changed adiabatically. Hence, it is meaningful to define the winding number ν of the loop with respect to the origin. Clearly, $\nu = 1$ if $\alpha < \beta$, and $\nu = 0$ if $\alpha > \beta$. The existence of a winding number perfectly fits into the periodic table, Tab. 2.1. The SSH model has chiral symmetry with $U_{\mathcal{S}} = \sigma_z$, which transforms $\mathcal{H}(k)$ to $-\mathcal{H}(k)$:

$$\sigma_z d_x\sigma_x\sigma_z + \sigma_z d_y\sigma_y\sigma_z = -id_x\sigma_z\sigma_y + id_y\sigma_z\sigma_x = -d_x\sigma_x - d_y\sigma_y \tag{3.8}$$

The model has also TRS and PHS, placing it in class BDI. However, it is the chiral symmetry that protects the winding number because all 1D Hamiltonians with chiral symmetry have a $\mathbb{Z}$ invariant. Note that although the SSH model has a $\mathbb{Z}$ invariant, it exhibits only two topologically distinct phases.

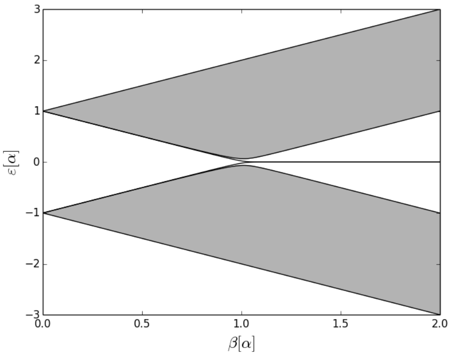

Figure 3.1: The eigenenergies of the SSH model in units of the intra-cell hopping α for $N = 70$ as the inter-cell hopping β varies from 0 to 2α. The grey regions are filled with bulk states. A state close to $\varepsilon = 0$ appears when $\beta > \alpha$.

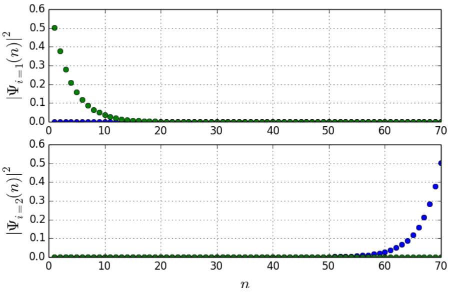

Figure 3.2: The weight of the wavefunctions Ψ_+ (green dots) and Ψ_- (blue dots) at each unit cell for $N = 70$ and $\beta = 1.15\alpha$, upper plot: sublattice $i = 1$, lower plot: sublattice $i = 2$.

The nontrivial phase $\nu = 1$ is accompanied by the existence of localized boundary states at zero energy inside the bulk band gap because of the bulk-boundary correspondence that was introduced in the previous chapter. This can be verified by exact diagonalization of the real-space Hamiltonian for a finite chain. There are two states with eigenenergy $\varepsilon \to 0$ as $N \to \infty$ if $\alpha < \beta$. Figure 3.1 shows how the eigenenergies change as β varies for a SSH chain of length $N = 70$. As the bulk has an energy gap, it is clear that the zero-energy eigenstates must be located at the boundary of the system. Indeed, the two wavefunctions $\Psi_{a,b}(n)$ of these states decay exponentially in the bulk. In Fig. 3.2, the weight of $\Psi_\pm = \Psi_a \pm \Psi_b$ at each site is shown for the two sublattices. One can see that $\Psi_+(n)$ and $\Psi_-(n)$ each describe a state that is localized at one end of the wire, where sublattice 1 contributes only to the state at the left end, while sublattice 2 contributes only at the right end. This can be understood from the limiting case $\beta \ll \alpha$. If we set $\alpha = 0$, then an electron at the outermost atom at one end of the chain cannot hop anywhere and is thus localized. As there is no on-site potential in the model, the energy of this state is zero. The same happens at the other end, where the outermost atom belongs to the other sublattice.

3.2 The quantum Hall effect

When a current is running through a metal, the moving electrons will be deflected if a magnetic field perpendicular to the direction of the current is applied. Therefore one can measure a voltage U_H between the lateral edges of the sample. This is known as the Hall effect, named after Edwin Hall [48]. In 1980, von Klitzing *et al.* [13] observed a surprising deviation from the classical effect in a quasi-two-dimensional electron gas (2DEG), for which he was awarded the Nobel Prize just five years later. In a high magnetic field and at sufficiently low temperature[15], the Hall conductance σ_{xy} becomes quantized to integer multiples of $\frac{e^2}{h}$. At the same time, the longitudinal resistance drops to zero. This is the QHE and was the first physical phenomenon in a condensed matter system where a direct link to topology was established. It can thus be seen as the origin of the field of topological phases of quantum matter. We will first briefly review the classical Hall effect and then explain its quantized version.

3.2.1 Classical Hall effect

Consider the Drude model for a 2DEG [8], which is given by the equation of motion

$$m\partial_t^2\mathbf{r} = -e(\mathbf{E} + \partial_t\mathbf{r} \times \mathbf{B}) - \frac{m}{\tau}\partial_t\mathbf{r} \tag{3.9}$$

for electrons with mass m and charge $-e$ subject to the Lorentz force and velocity-dependent friction. The scale of the latter is set by the typical time τ between dissipative scattering events. We assume the magnetic field is pointing out of plane, $\mathbf{B} = B\hat{\mathbf{e}}_z$, while the electric

---

[15] $\approx 15\,\mathrm{T}$ and $1.5\,\mathrm{K}$ in the original experiment [13], but up to room temperature in more recent experiments [49]

field **E** is in the plane. The equilibrium state of the system, where $\partial_t^2 \mathbf{r} = 0$, is then given by Ohm's law,

$$\mathbf{E} = \rho\,\mathbf{j} \tag{3.10}$$

$$\rho = \frac{m}{ne^2\tau}\begin{pmatrix} 1 & \omega_c\tau \\ -\omega_c\tau & 1 \end{pmatrix} \tag{3.11}$$

where the current density is $\mathbf{j} = -ne\partial_t\mathbf{r}$, n is the electron density, and $\omega_c = eB/m$ the cyclotron frequency. As $(\rho_{ij})_{i,j=x,y}$ is not diagonal if $B \neq 0$, **E** will have a component orthogonal to the current. The off-diagonal entries $\rho_\mathrm{H} = \rho_{xy} = -\rho_{yx}$ represent the Hall effect. The Hall resistivity and thus the Hall voltage will increase linearly with B, while the longitudinal resistivity ρ_{xx} is constant.

Remarkably, $\rho_\mathrm{H} = m\omega_c/ne^2$ is, in contrast to ρ_{xx}, independent of dissipation in the system, as it does not include τ. This is a first sign that the Hall effect is of a rather fundamental nature.

3.2.2 Landau quantization

For Hall experiments in the quantum limit, the Drude model is insufficient to describe both the Hall and the longitudinal resistivity, see Fig. 3.3. The QHE is a consequence of the quantization of electron states into Landau levels [37], which becomes important at high fields.

For an electron restricted to two dimensions in a perpendicular magnetic field as above, the Hamiltonian is

$$H = \frac{1}{2m}\left[\mathbf{p} + e\mathbf{A}(\mathbf{r})\right]^2, \tag{3.12}$$

where **p** is the canonical momentum. It is convenient to use Landau gauge with the vector potential is $\mathbf{A}(\mathbf{r}) = Bx\hat{\mathbf{e}}_y$, such that the Hamiltonian does not depend on the y component. Then, the momentum component k_y will be a good quantum number and the remaining Hamiltonian describes a harmonic oscillator with displacement in x direction,

$$H = \frac{1}{2m}p_x^2 + \frac{m}{2}\omega_c^2\left(\frac{\hbar k_y}{eB} + x\right)^2, \tag{3.13}$$

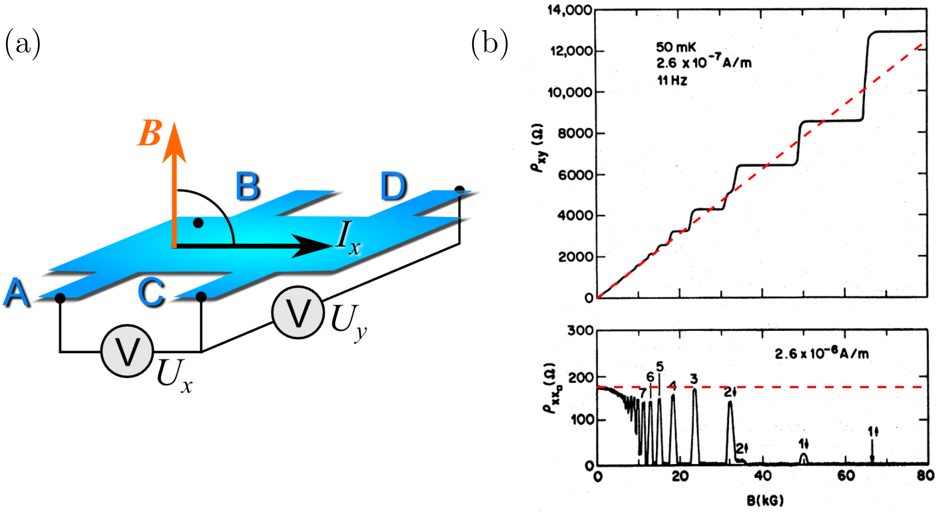

Figure 3.3: (a) A typical setup for a Hall effect experiment, where the voltage is measured both parallel and orthogonal to the current in a perpendicular magnetic field. (b) Measured data for the Hall resistance ρ_{xy} (upper panel) and the longitudinal resistance ρ_{xx} (lower panel) as a function of the magnetic field strength by M. A. Paalanen *et al.* [50], where ρ_{xy} has plateaus at quantized values, while ρ_{xx} drops to zero simultaneously. The original figure (in black) is adopted from [50] (©APS, 1982). The red dashed lines are added to indicate the behavior expected from the classical Hall effect.

with the eigenenergies given by

$$\varepsilon_{\mathrm{i}} = \hbar\omega_c \left(i + \frac{1}{2}\right), \quad i \in \mathbb{N}. \tag{3.14}$$

These Landau levels are degenerate, as they do not depend on k_y. This defines a very simple "band structure" with equidistant flat bands[16]. The density of states depends on the magnetic flux: For a sample of size $L_x \times L_y$, k_y will be quantized in units of $\Delta k_y = 2\pi/L_y$. Thus, the displacement of the x component in Eq. (3.13) is quantized by $\Delta x = \frac{\hbar}{eB}\Delta k_y$. The number of states is then $L_x/\Delta x = eL_xL_yB/h$.

Assume that η of the Landau levels are filled at a certain Fermi

---

[16] Note that the electron spin has not been taken into account. Each of the bands will actually be split in two by the Zeeman effect.

energy. Then the total density of states is $n = \eta eB/h$. If we insert this expression into the Drude formula for the Hall resistance, we find

$$\rho_{\mathrm{H}} = \frac{h}{e^2}\frac{1}{\eta} \quad \text{or} \quad \sigma_{xy} = \eta\frac{e^2}{h}. \tag{3.15}$$

These are exactly the experimentally observed quantized values. Every filled Landau level contributes one quantum of conductivity to σ_{xy}.

This argument still has a severe drawback. Namely, the assumption that there are only filled Landau levels is unjustified. The density n in a given sample will be a material constant and coincide with the density of states in the Landau levels only for some discrete field strengths $B_\eta = nh/\eta e$. In contrast, the key feature of the QHE are plateaus where σ_{xy} takes a quantized value over a range of field strengths. In fact, the existence of the plateaus requires the presence of localized states in between the Landau levels, as induced by disorder in the sample. Such states do not contribute to the conductivity, but can to some extent compensate for the incongruous number of electrons if B does not exactly match any B_η. Thus, the amount of disorder controls the width of the plateaus. We will not discuss disorder in further detail, though, as it is not necessary to understand to the topology of the QHE, which we will focus on next.

3.2.3 Hall conductivity and topology

The quantized Hall conductivity can be identified with an abstract mathematical topological invariant of the Hamiltonian system, meaning that the system undergoes a topological transition each time a new plateau is reached. This is a very deep inside, which has been established in seminal works by Laughlin [26] and Thouless, Kohomoto, Nightingale, and den Nijs (TKNN) [27][17]. It means that σ_{xy} is not just an observable that happens to be restricted to discrete values by quantum mechanics, but rather expresses very fundamental properties of the geometry that is underlying the mathematical description of the Hall system.

---

[17] Laughlin's argument is less general than the TKNN paper, as it relies on a specific real-space geometry.

For simplicity, consider a 2D system of electrons on a square lattice with spacing a, where the Hamiltonian is defined in momentum space on the BZ, which forms a 2-torus. The conductivity can be calculated by means of the Kubo formula [51]. This leads to the correct quantum-mechanical answer, whereas the derivation of Eq. 3.15 still involved the Drude model. For σ_{xy}, the relevant correlation function appearing in the Kubo formula is the one of the currents in x and y direction. At zero temperature, and expressed in a suitable basis of eigenstates in Bloch form, $\Psi^n_{\mathbf{k}}(\mathbf{r}) = e^{i\mathbf{k}\cdot\mathbf{r}} u^n_{\mathbf{k}}(\mathbf{r})$ (band index n), it can be written as [8]

$$\sigma_{xy} = i\hbar \int\limits_{\mathrm{BZ}} \frac{\mathrm{d}^2k}{(2\pi)^2} \sum_{\substack{m,n:\\ \varepsilon_m < E_\mathrm{F} < \varepsilon_n}} \frac{\langle u^m_{\mathbf{k}}|j_y|u^n_{\mathbf{k}}\rangle\langle u^n_{\mathbf{k}}|j_x|u^m_{\mathbf{k}}\rangle - \langle u^m_{\mathbf{k}}|j_x|u^n_{\mathbf{k}}\rangle\langle u^n_{\mathbf{k}}|j_y|u^m_{\mathbf{k}}\rangle}{(\varepsilon_m(\mathbf{k}) - \varepsilon_n(\mathbf{k}))^2} \tag{3.16}$$

Here, we have also assumed that the band structure has an energy gap, and that E_F is inside the gap. The indeces m, n run thus over the filled and empty bands, respectively. This resembles the precondition of the semi-classical calculation, where no partly filled Landau levels had been allowed. To act with the current operator on the wavefunctions, it is practical to replace it by the group velocity in terms of the Hamiltonian,

$$\mathbf{j} = \frac{e}{\hbar}\boldsymbol{\nabla}_{\mathbf{k}} H(\mathbf{k}). \tag{3.17}$$

Then, using $H(\mathbf{k})|u^m_{\mathbf{k}}\rangle = \varepsilon_m(\mathbf{k})|u^m_{\mathbf{k}}\rangle$, Eq. (3.16) becomes

$$\begin{aligned}\sigma_{xy} \;=\; & \frac{ie^2}{\hbar} \int\limits_{\mathrm{BZ}} \frac{\mathrm{d}^2k}{(2\pi)^2} \sum_{\substack{m,n:\\ \varepsilon_m < E_\mathrm{F} < \varepsilon_n}} \\ & \left\langle \frac{\partial u^m_{\mathbf{k}}}{\partial k_y} \middle| u^n_{\mathbf{k}} \right\rangle \left\langle u^n_{\mathbf{k}} \middle| \frac{\partial u^m_{\mathbf{k}}}{\partial k_x} \right\rangle - \left\langle \frac{\partial u^m_{\mathbf{k}}}{\partial k_x} \middle| u^n_{\mathbf{k}} \right\rangle \left\langle u^n_{\mathbf{k}} \middle| \frac{\partial u^m_{\mathbf{k}}}{\partial k_y} \right\rangle\end{aligned} \tag{3.18}$$

As the eigenstates form a complete basis, the summation in the equation above can be reduced to the filled bands using

$$\sum_{n:\,\varepsilon_n > E_F} |u^n_{\mathbf{k}}\rangle\langle u^n_{\mathbf{k}}| = \mathbb{1} - \sum_{m:\,\varepsilon_n < E_F} |u^m_{\mathbf{k}}\rangle\langle u^m_{\mathbf{k}}|. \tag{3.19}$$

In addition, $\partial^2/\partial k_x \partial k_y = \partial^2/\partial k_y \partial k_x$. Thus, we have the final expression [8,27]

$$\sigma_{xy} = \frac{ie^2}{\hbar} \int_{\mathrm{BZ}} \frac{\mathrm{d}^2 k}{(2\pi)^2} \sum_{m:\, \varepsilon_m < E_\mathrm{F}} \left\langle \frac{\partial u^m_\mathbf{k}}{\partial k_y} \middle| \frac{\partial u^m_\mathbf{k}}{\partial k_x} \right\rangle - \left\langle \frac{\partial u^m_\mathbf{k}}{\partial k_x} \middle| \frac{\partial u^m_\mathbf{k}}{\partial k_y} \right\rangle . \tag{3.20}$$

In this form, the Hall conductivity can be given a topological interpretation, because the term that is summed over is identical to the Berry field strength [compare to Eqs. (2.8) and (2.9)]. Therefore, the integration over the BZ yields

$$\sigma_{xy} = -\frac{e^2}{h} \sum_{m:\, \varepsilon_m < E_F} C_m, \tag{3.21}$$

with C_m being the first Chern number of the m-th band. This proves the integer quantization of the Hall conductivity. The sum of the Chern numbers in Eq. (3.21) is also referred to as the TKNN integer [27]. If the TKNN integer vanishes, the system is in a topologically trivial state with no Hall conductivity, otherwise the mapping of the toroidal momentum space onto the Bloch sphere describes a nontrivial wrapping of the sphere.

We make three remarks: First, the formula above is strikingly general, which reflects its topological nature. The actual Hamiltonian has not been used, the only assumption was that the bands are separated into filled and empty bands by the Fermi level. Thus, the system must be an insulator. Details of the Hamiltonian and, consequently, the precise shape of the bands, are not important. The bare flat Landau levels lead to the same result as wildly curved bands.

Second, TRS is explicitly broken by the magnetic field. In the absence of restrictions on the Hamiltonian, it will in general also have no other symmetries. The QHE is thus placed in class A, and the TKNN integer is the $\mathbb{Z}$ invariant predicted by the periodic table. The $\mathbb{Z}$ invariant remains even if PHS is included.

Third, although we have explained the quantization of σ_{xy} on topology grounds, the actual value of the TKNN integer for a 2DEG in a magnetic field remains to be calculated. This will not be presented

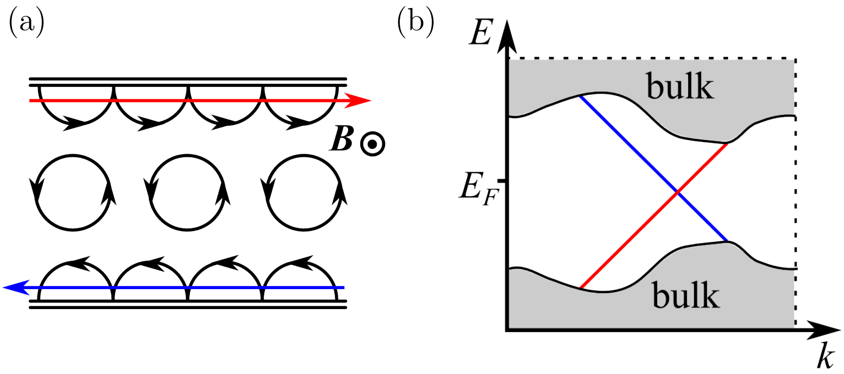

Figure 3.4: (a) Cartoon of the bouncing electron orbit along the quantum Hall sample edges. (b) Qualitative band structure with a bulk energy gap and chiral edge states.

here, but leads to a rich diagram of topological phases (i.e., parameter regions with different TKNN integer) known as the Hofstadter butterfly [8,27,52].

3.2.4 Chiral edge states

The TKNN formula Eq. (3.21) requires an insulator. In consequence, if we set $y \to x$ in the Kubo formula, we find $\sigma_{xx} = 0$, in apparent conflict with the observation $\rho_{xx} = 0$. To understand how the Hall effect works physically, it is crucial to turn to a finite system. As in the SSH model, the bulk-boundary correspondence gives rise to zero-energy boundary modes. These are now one-dimensional edge states. Without rigorous derivation, they can be understood intuitively from the classical picture. Nontrivial topology, i.e. $\sigma_{xy} \neq 0$, requires a nonzero magnetic field which forces the states onto circular cyclotron orbits. Electrons that are very close to the edge cannot complete their orbit, but will bounce back when they hit the edge. This leads to a "bouncing" orbit with a net velocity along the edge, as shown in Fig 3.4(a). The edge state allows electrons to move in only one direction, which depends on the orientation of the magnetic field. It is therefore called a *chiral* mode. This property forbids backscattering: there are no available reversely moving states to scatter into, except at the opposite side of the sample. Thus, the edge of the quantum Hall sample is a perfect conductor, although the bulk is insulating. Figure 3.4(b) shows the qualitative band structure where the chiral edge modes lead to lines crossing the bulk energy gap.

3.3 Quantum spin Hall effect

The key property of the QHE is the breaking of TRS by the external magnetic field. One may wonder whether an intrinsic analogue of this effect exists, i.e., a quantum Hall state that does not require external fields (first envisioned by Haldane [53]) or even remains TRS[18]. Roughly speaking, one can imagine two copies of the quantum-Hall system with reversed sign on top of each other [7]. The resulting magnetic field cancels, and the edge modes come in pairs with opposite chirality. Such a scenario can be realized in the presence of spin-orbit coupling (SOC), which preserves TRS, but makes electrons experience an effective magnetic field which depends on their momentum. The net charge current at the edge of this system vanishes. However, in each pair of counter-propagating edge modes the spin polarization of the modes will be opposite, giving rise to a *helical* edge mode, such that an edge spin current occurs. This is known as the quantum spin Hall effect (QSHE). It displays the main features of TIs: an insulating bulk respecting TRS and helical edge states with linear dispersion (close to zero energy).

In contrast to the QHE, in the QSHE the experimental discovery [54] was preceded by theoretical predictions [55–57]. Without going into the details of realizations of the QSHE, like HgTe/CdTe quantum wells [54], an effective model developed by Bernevig, Hughes, and Zhang (BHZ) [57] is presented in the following. The research Papers [1–3] in this thesis only deal with 3D TIs, such that we review the two-dimensional case only as far as necessary to understand its generalization to three dimensions. The BHZ Hamiltonian $\mathcal{H}_{\mathrm{BHZ}}$ is defined on a space of two bands (labeled $1, 2$) which are each split by SOC in two helicity branches (labeled $\pm$). In the basis $(|1+\rangle, |2+\rangle, |1-\rangle, |2-\rangle)$,

---

[18] This shifts the system to class AII. $\mathcal{T}^2 = -\mathbb{1}$ for spin-$\frac{1}{2}$ fermions.

$\mathcal{H}_{\mathrm{BHZ}}$ [7, 57] is written as

$$\mathcal{H}_{\mathrm{BHZ}}(\mathbf{k}) = \begin{pmatrix} h(\mathbf{k}) & 0 \\ 0 & h^{*}(-\mathbf{k}) \end{pmatrix}, \tag{3.22}$$

such that TRS is explicitly taken into account, where the 2×2 block h is

$$h(\mathbf{k}) = \left(C - D\mathbf{k}^2\right) \mathbb{1}_{2\times 2} + A\left(k_x\sigma_x - k_y\sigma_y\right) + \left(M - B\mathbf{k}^2\right)\sigma_z. \tag{3.23}$$

A, B, C, D, M are model parameters that depend on material properties and the geometry of the sample, and $\mathbf{k}^2 = k_x^2 + k_y^2$. The form of h is obtained from basic symmetry considerations, where all allowed terms are represented to second order in momentum[19].

From the simple picture relating the QSHE to two QH systems, one would expect a number of helical edge states equal to the corresponding TKNN integer of the subsystems. It turns out, though, that any even number of helical edge states is unstable, as arbitrarily weak disorder will essentially remove a pair of helical states by backscattering [7, 58]. Therefore, the QSHE has only one topological and one trivial state, indicating a $\mathbb{Z}_2$ topological index[20]. The BHZ model has the advantage that the edge state wavefunctions $\Psi^{\mathrm{BHZ}}_{\mathrm{edge},\pm}$ can be derived explicitly for a semi-infinite system in the half-plane $x > 0$ with open boundary conditions [7], where the term $C - Dk_x^2$ can be neglected for simplicity [59]. It turns out that the condition to find helical edge states is $M/B > 0$, where the helicity is determined by the sign of A/B and the wavefunctions are exponentially localized at the edge [7, 59]:

$$\Psi^{\mathrm{BHZ}}_{\mathrm{edge},+}(x) = \left(\psi_{\mathrm{edge}}(x), 0\right)^{\mathrm{T}} \quad \Psi^{\mathrm{BHZ}}_{\mathrm{edge},-}(x) = \left(0, \psi_{\mathrm{edge}}(x)\right)^{\mathrm{T}}, \tag{3.24}$$

$$\psi_{\mathrm{edge}}(x) = C\left(e^{-s\lambda_1 x} - e^{-s\lambda_2 x}\right) v_s, \tag{3.25}$$

with a normalization constant C, $s = \pm 1$, the eigenvectors v_s of the Pauli matrix σ_y, and

$$\lambda_{1,2} = \frac{A \pm \sqrt{A^2 - 4MB}}{2B}. \tag{3.26}$$

---

[19] apart from an inversion-symmetry-breaking term, which is not required to obtain a topologically nontrivial state

[20] The $\mathbb{Z}_2$ index will be explained in Sec. 3.5.

Projecting $\mathcal{H}_{\mathrm{BHZ}}$ onto the space of edge states $(\Psi^{\mathrm{BHZ}}_{\mathrm{edge},+}, \Psi^{\mathrm{BHZ}}_{\mathrm{edge},-})$, the effective low-energy Hamiltonian $\mathcal{H}_{\mathrm{edge}}(k_y) = Ak_y\sigma_z$ is obtained. The two states with opposite spin are thus both linearly dispersing with opposite velocity.

The condition $M/B \equiv \zeta > 0$ is very insightful when the bulk spectrum of the BHZ model [7] is considered:

$$\varepsilon(\mathbf{k}) = C - D\mathbf{k}^2 \pm \sqrt{A^2\mathbf{k}^2 + B^2\left(\zeta - \mathbf{k}^2\right)^2} \tag{3.27}$$

At $\mathbf{k} = 0$, the bulk gap closes when $\zeta = 0$. If one imagines ζ being tuned from negative to positive values, the gap closes and opens again. In the final state, the order of the bands is inverted at $\mathbf{k} = 0$ compared to the initial state. This twist in the band structure is the reason why the BHZ Hamiltonian becomes topologically nontrivial. Physically, it is the strength of the SOC that determines whether the band structure is inverted or not. Therefore, topological materials or heterostructures usually involve heavy elements. In the HgTe/CdTe quantum wells, for instance, the SOC of mercury is responsible for the formation of a topological phase [57]. However, any other mechanisms than SOC that causes band inversion would in principle also lead to a topological phase [60].

3.4 Three-dimensional topological insulators

The SOC-induced band inversion as found in the BHZ model can be generalized to three dimensions. The generic importance of band inversion will become clearer in the next section. Here, we focus on an effective model by Zhang *et al.* [61] which allows for a derivation of the topological surface states. It is valid for $\mathrm{Bi_2Se_3}$, $\mathrm{Bi_2Te_3}$, and $\mathrm{Sb_2Te_3}$ upon fitting of the parameters to *ab initio* band structure calculations. These materials are known as second-generation 3D TIs [6][21]. By the combined effect of chemical bonding, the crystal field, and atomic SOC, the energetically lowest states descending from the valence p orbitals

---

[21] The first TIs were $\mathrm{Bi}_{1-x}\mathrm{Sb}_x$ alloys for a certain range of x [62].

of Bi or Sb are shifted below the originally lower-lying states stemming from the p orbitals of Se or Te, causing band inversion at the Γ point (i.e., the center of the BZ) [7]. The effective model accounts for crystal symmetries in addition to TRS and contains only terms up to second order in momentum. This leads to the following generic form [61] in the basis of the four relevant low-energy bands close to the Γ point, ordered by spin $(\uparrow, \downarrow)$ and parity $(\pm)$ according to $(|\uparrow +\rangle, |\uparrow -\rangle, |\downarrow +\rangle, |\downarrow -\rangle)$:

$$\begin{aligned}\mathcal{H}_{\mathrm{3DTI}}(\mathbf{k}) &= \left(C + D_1 k_z^2 + D_2\right) \mathbb{1}_{4\times 4} \\ &\quad + \begin{pmatrix} \mathcal{M}(\mathbf{k}) & A_1 k_z & 0 & A_2 k_- \\ A_1 k_z & -\mathcal{M}(\mathbf{k}) & A_2 k_- & 0 \\ 0 & A_2 k_+ & \mathcal{M}(\mathbf{k}) & -A_1 k_z \\ A_2 k_+ & 0 & -A_1 k_z & -\mathcal{M}(\mathbf{k}) \end{pmatrix}, \end{aligned} \tag{3.28}$$

where $k_\perp^2 = k_x^2 + k_y^2$, $k_\pm = k_x \pm i k_y$, and $\mathcal{M}(\mathbf{k}) = M - B_1 k_z^2 - B_2 k_\perp^2$. There are 8 model parameters: $M, C, A_1, A_2, B_1, B_2, D_1, D_2$. The anisotropy in z direction is present because the surface will be assumed to lie in the xy plane. Similarly to the BHZ model, band inversion occurs at $\mathbf{k} = 0$ if M, B_1, and B_2 have the same sign. Then, exponentially localized surface states can be derived in analogy to the two-dimensional case. The projection of the Hamiltonian onto these surface states provides an effective low-energy theory of the TI surface [6, 7], $H^{\mathrm{sur}} = \sum_{\mathbf{k}_\shortparallel} \Psi^\dagger(\mathbf{k}_\shortparallel) \mathcal{H}^{\mathrm{sur}}(\mathbf{k}_\shortparallel) \Psi(\mathbf{k}_\shortparallel)$ with

$$\mathcal{H}^{\mathrm{sur}}(k_x, k_y) = C + A_2 \left(\sigma_x k_y - \sigma_y k_x\right) \tag{3.29}$$

and $\Psi^\dagger = (\psi_\uparrow, \psi_\downarrow)$. The constant C will be neglected from now on, which practically amounts to fine-tuning of the chemical potential. The constant A_2 can be replaced by the Fermi velocity, $A_2 = \hbar v_F$. For later reference, we transform the Hamiltonian into a Lagrangian density:

$$\mathcal{L}^{\mathrm{sur}}(\mathbf{k}_\shortparallel) = \Psi^\dagger(\mathbf{k}_\shortparallel) \left[i\hbar \partial_t - \hbar v_F \left(\sigma_x k_y - \sigma_y k_x\right)\right] \Psi(\mathbf{k}_\shortparallel) \tag{3.30}$$

In two dimensions[22], the Pauli matrices coincide with Dirac's γ matrices via the relations $\gamma_0 = \sigma_z$, $\gamma_1 = -i\sigma_x$, $\gamma_2 = -i\sigma_y$. Therefore, it

---

[22] In the $(2+1)$-dimensional Minkowski space-time we use the metric tensor with the signature $(+,-,-)$.

is convenient to use the notation of quantum electrodynamics (QED) where $\overline{\Psi} = \Psi^\dagger \gamma_0$ and the Feynman-slash $\not{Q} = \gamma^\mu Q_\mu$. Replacing $k_{x,y}$ by $-i\partial_{x,y}$ and $\partial = (\partial, v_F \partial_x, v_F \partial_y)$ then yields the Lagrangian

$$\mathcal{L}^{\mathrm{sur}}(\mathbf{r}) = \overline{\Psi}(\mathbf{r})\, i\not{\partial}\, \Psi(\mathbf{r}), \tag{3.31}$$

where we also switched to natural units ($\hbar = 1$, $c = 1$). This is the well-known massless Dirac equation, whereby the Fermi velocity has taken over the role of the speed of light. In that sense, the TI surface states are referred to as Dirac fermions. In other words, they imitate relativistic particles at a non-relativistic velocity range, $v_F \approx 5 \times 10^5\,\mathrm{m/s}$ [61]. Given Eq. (3.31), it is natural to apply field-theoretic methods to evaluate the low-energy properties of the TI surface, which is utilized in the Papers [1], [2], and [3].

The low-energy spectrum is also referred to as the Dirac cone. Notably, the 3D TIs have only one Dirac cone per surface. The TI surface is therefore distinct from strictly 2D Dirac materials with TRS, in particular graphene [63], where the Dirac states have to come in pairs as dictated by the Nielson-Ninomiya theorem [64,65] of fermion doubling. In a 3D TI, two opposite surfaces together satisfy the theorem, such that an odd number of Dirac cones on each surface is allowed [6]. The fact that the TI surface could not exist as an independent 2D system, but must be attached to a topological 3D bulk, is also called the holographic principle[23] [7]. The linear dispersion and helicity of the surface states has been directly observed by angle-resolved photoemission spectroscopy (ARPES) in $\mathrm{Bi}_{1-x}\mathrm{Sb}_x$ [62], $\mathrm{Bi}_2\mathrm{Se}_3$ [67], $\mathrm{Bi}_2\mathrm{Te}_3$ [68, 69], and $\mathrm{Sb}_2\mathrm{Te}_3$ [69] after they had been predicted to be TIs.

Another important property of the surface states that is readily seen from Eq. (3.29) is the helicity. As in the QSHE, the motion of the topological states is linked to their spin. This property is known as spin-momentum locking and is a major reason for the technological interest in TIs. In principle, it allows to manipulate magnetic moments by electric currents and makes TIs interesting constituents for future spintronics devices [70].

The equivalence of the surface theory and the Dirac equation raises one further question: Is it possible to obtain a mass term in the TI

---

[23] Again, this term goes back to string theory [66].

surface theory? From Eq. (3.31), it is clear that a Dirac mass term would be of the form $m\sigma_z$, indicating that the mass is coupled to the spin in z direction. Thus, an external magnetic field (alternatively: magnetic order) orthogonal to the TI surface can open a gap in the spectrum of the surface states. This gapped surface phase has many interesting properties that will be elucidated in Chapter 4.

3.5 $\mathbb{Z}_2$ invariant of topological insulators

A relatively simple way to characterize TR-symmetric insulators by topological invariants arises from topological band theory (TBT) [6, 71]. TRS relates the states at momenta $\mathbf{k}$ and $-\mathbf{k}$. A special role is played by the n points in the BZ that are mapped onto themselves under TR, where $n = 4, 8$ in 2D and 3D, respectively. At these TR-invariant momenta, all states must be Kramers-degenerate, while the degeneracy can be lifted by SOC everywhere else in the BZ. The topological features of the band structure are then completely described by the way in which the states at the TR-invariant momenta are connected to each other. In the trivial case, the two degenerate states at a TR-invariant momentum are also connected to degenerate states at any other TR-invariant momentum, such that each state has a well-defined partner across the entire BZ. However, if the splitting induced by SOC is strong enough, two degenerate states can also be connected to states of different energy at another TR-invariant point, leading to a nontrivial band structure.

The idea of connecting states at the TR-invariant points is directly related to the protection of boundary states inside the bulk energy gap, as such states cannot be removed by any continuous deformation if they are nontrivially connected. This is illustrated in Fig. 3.5. In the trivial case, a pair of bands inside the gap could be pushed out by a smooth perturbation. Thus, any state at the Fermi level is not protected. In the nontrivial case, the in-gap states do not come in pairs but are connected to both the valence and the conduction band. This feature will remain under any continuous deformation, leading to a topological protection of the Fermi level crossing. In fact, an odd number of states (deformable to one crossing) at E_F is guarantueed

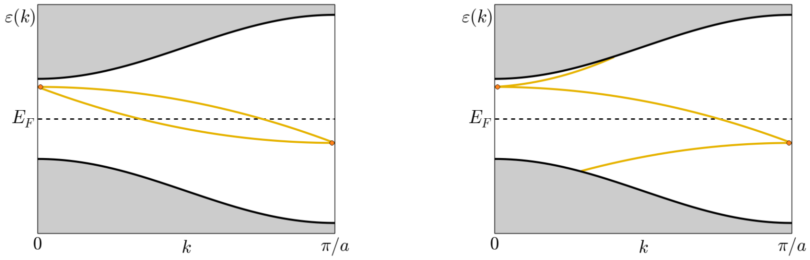

Figure 3.5: Trivially (left) and a non-trivially (right) connected states inside the gap of an insulator with TRS along a path connecting two TR-invariant points at the center ($k = 0$) and one edge ($k = \pi/a$) of the BZ. The orange dots denote Kramers-degeneracies of states. The yellow lines are boundary modes, while the grey areas are the bulk bands. Only in the non-trivial case the crossing of the Fermi level is topologically protected. The figures are inspired by Fig. 3 in [6].

by topology, while there is an even number of crossings (deformable to none) in the trivial case. A band crossing E_F can be linearized in an effective low-energy theory, leading to the Dirac cone discussed in the previous section.

One can construct a $\mathbb{Z}_2$ topological invariant ν of the band structure from the matrix representation of the TR operator $\mathcal{T}$ in the basis of Bloch states with conjugated momenta [58, 72–74]. The matrix elements are

$$T_{mn}(\mathbf{k}) = \langle -\mathbf{k}, m | \mathcal{T} | \mathbf{k}, n \rangle \tag{3.32}$$

and the properties of $\mathcal{T}$ dictate that $T(\mathbf{k})^{\mathrm{T}} = -T(-\mathbf{k})$. Consequently, at the TR-invariant momenta Λ_i ($i = 1, \ldots, n$), $T(\Lambda_i)$ is skew-symmetric and its Pfaffian [75] $\mathrm{Pf}[T(\Lambda_i)]$ is well-defined. Because $\mathrm{Pf}[T(\Lambda_i)]^2 = \det[T(\Lambda_i)]$, the quantity

$$\delta_i = \frac{\mathrm{Pf}[T(\Lambda_i)]}{\sqrt{\det[T(\Lambda_i)]}} \tag{3.33}$$

can only take the values ±1. Fu and Kane [72] have shown that the topology of the band structure is characterized by the topological index

$\nu \in \mathbb{Z}_2$ defined by

$$(-1)^{\nu} = \prod_{i=1}^{n} \delta_i, \tag{3.34}$$

where ν is even in the trivial and odd in the topological case. This corresponds to the previously discussed concept of band inversion as follows: $\delta_i = 1$ describes normal band ordering (compared to atomic orbitals) at Λ_i, while $\delta_i = -1$ for an inverted band structure. If bands are inverted twice (or an even number of times), such that there is an even number of negative factors in Eq. (3.34), they can be unraveled continuously, while they cannot if band inversion occurs an odd number of times.

For completeness we mention that in 3D TBT, an insulator can be *weakly* topological even if ν is even. In addition to Eq. (3.34), also all products of four δ_i are topological invariants if the corresponding Λ_i lie in a plane [6, 73, 74]. From the three independent planes in 3D one can define three independent invariants ν_1, ν_2, ν_3. If ν is even, but any of ν_1, ν_2, ν_3 is odd, the system is called a weak TI. All possible combinations of even or odd ν, ν_1, ν_2, ν_3 amount to a total of 16 topologically distinct phases. However, weak TIs turn out to be not robust against disorder [73]. They can be viewed as stacked QSH layers, where the vector (ν_1, ν_2, ν_3) can be related to the stacking direction. Only if ν is odd (strong TI), a natively 3D topological state is found.

3.6 Chern-Simons action of topological insulators

One drawback of TBT is that it is restricted to non-interacting systems. A more general approach to the topological classification is topological field theory (TFT) [76], which is equivalent to TBT in the non-interacting limit. TFT formulates a generalization of the QHE to four spatial dimensions, from which one can subsequently derive the $\mathbb{Z}_2$ insulators in three and finally two dimensions by a procedure called dimensional reduction [7]. We do not review the entire TFT here, but include some key expressions.

Some years after the explanation of the QHE in terms of the TKNN integer [27], it was discovered [77] that the quantum Hall state could also be described by means of Chern-Simons (CS) field theory [11] with the CS action[24]

$$S_{\mathrm{QHE}} = \frac{C_1}{4\pi} \int \mathrm{d}^{(2+1)}x\, \epsilon^{\mu\nu\rho} A_\mu \partial_\nu A_\rho \tag{3.35}$$

in $(2+1)$ dimensions in covariant form with the electromagnetic potential A. The coefficient C_1 can in general be calculated from the single-particle Green's functions [7, 78], even in the presence of interactions, but reduces exactly to an integral over the Berry curvature in the absence of interactions and is thus equal to the TKNN integer. From the transformation of A under TR, where A_0 is even while the vector potential $\mathbf{A} = (A_1, A_2)$ is odd, one finds that the action S_{QHE} does not have TRS.

The CS theory can be generalized to systems of arbitrary even spatial dimension [11], which can be interpreted as higher-dimensional descendents of the QHE [79]. In $(4+1)$ dimensions, the action reads

$$S_{\text{4D-CS}} = \frac{C_2}{24\pi^2} \int \mathrm{d}^{(4+1)}\, \epsilon^{\mu\nu\rho\sigma\tau} A_\mu \partial_\nu A_\rho \partial_\sigma A_\tau \tag{3.36}$$

and is, in contrast to S_{QHE}, invariant under TR [7]. Again, the coefficient is an integer[25], $C_2 \in \mathbb{Z}$ [78]. Although this generalization seems like a purely mathematical gimmick, it is physically meaningful because the 3D TI can be derived from $S_{\text{4D-CS}}$. If one restricts the theory to the special cases where $A_{(3+1)} = (A_0, \ldots, A_3)$ depends only on the first three out of four spatial coordinates, the last coordinate x_4 can be integrated out if the spacetime is compactified ("rolled up") in the respective dimension [7, 76]. The surplus field A_4 may cause a magnetic flux ϕ through this compactified dimension, given by the integral of A_4 over x_4. The resulting field theory in three spatial dimensions takes the form of a so-called theta term

$$S_\theta = \frac{\alpha}{32\pi^2} \int \mathrm{d}^{(3+1)}x\, \theta(x) \epsilon^{\mu\nu\rho\sigma} F_{\mu\nu}(x) F_{\rho\sigma}(x) \tag{3.37}$$

---

[24] here in atomic units $\hbar = 1$, $e = 1$

[25] C_2 can be identified with the second Chern number $C^{(2)}$.

with $\theta = C_2\phi$, the fine structure constant α, and the electromagnetic tensor $F_{\mu\nu} = \partial_\mu A_\nu - \partial_\mu A_\nu$. Interestingly, such field theories had been studied before in quantum chromodynamics (QCD), where θ was dubbed the axion field [80]. However, no elementary axionic particles are known to date. In the context of TIs, the field θ must be further restricted such that the symmetries of the original field theory $S_{\text{4D-CS}}$ are maintained – in particular TRS. Under TR, $A_4 \to -A_4$, thus ϕ and θ must also be odd. In addition, a 2π shift of the flux ϕ must leave the physics unaffected and hence θ and $\theta + 2\pi C_2$ are equivalent. In consequence, to respect TRS, θ can take only one of the two values 0 or πC_2. This implies as well that θ cannot vary smoothly and must be a constant rather than a field. For simplicity, one can assume[26] $C_2 = 1$ [7]. The TR-invariant insulator in 3D can only be in one of two states, reflecting the $\mathbb{Z}_2$ classification already found in TBT: Either $\theta = 0$, where the TFT vanishes and only a trivial insulator without a CS action remains. The action is then basically given by an ordinary Maxwell term. Or $\theta = \pi$, where the effective field theory contains the topological theta term S_θ with a quantized coefficient. This state of matter is a 3D TI.

One can further reduce the dimensionality to obtain the QSHE, which is again $\mathbb{Z}_2$ quantized. However, reducing to one spatial dimension in the same manner leads to a state that is always topologically trivial – there is no one-dimensional TI in class AII.

---

[26] Strictly speaking, $C_2 \in \mathbb{Z}$ leaves a mod 2π ambiguity in the value of θ.

Chapter 4

Magnetic topological insulator heterostructures

Having introduced 3D TIs and reviewed some of their properties, we will now consider surfaces of 3D TIs in the presence of magnetic order. Such surfaces turn out to have several remarkable properties related to the TME. In this chapter, we will first explain their general electromagnetic features. Afterwards, we turn to the results of the Papers [1] and [2], which examine the influence of Coulomb interaction on layered ferromagnetic insulator (FMI)-TI systems via the topological terms. The last section summarizes the findings of Paper [3], where the interface of a TI with a bipartite magnetic insulator (BMI) is investigated.

4.1 The TRS-broken surface

The electromagnetic theory of the 3D TI, Eq. (3.37), can also be written as [76, 81, 82]

$$\begin{aligned} S_\theta &= \frac{\theta\alpha}{4\pi^2}\int \mathrm{d}^{(3+1)}x\,\mathbf{E}\cdot\mathbf{B} \\ &= \frac{\theta\alpha}{8\pi^2}\int \mathrm{d}^{(3+1)}x\,\epsilon^{\mu\nu\rho\sigma}\partial_\mu(A_\nu\partial_\rho A_\sigma). \end{aligned} \tag{4.1}$$

The first line reveals a coupling of the electric and magnetic field in the TI bulk with a quantized coefficient. This is the (bulk) TME, which is a hallmark feature of the TI state. The second line insinuates that one can transform the equation into a surface integral by Stokes' theorem for a finite TI, which would give rise to a surface CS term:

$$S_\theta = \frac{\theta\alpha}{8\pi^2} \int_{\text{surf.}} \mathrm{d}^{(2+1)}x \, \epsilon^{\mu\nu\rho} A_\mu \partial_\nu A_\rho. \tag{4.2}$$

However, there is a subtlety that is again related to symmetry. The surface CS term breaks TRS, which is intuitively clear from the formal similarity of Eq. (4.2) to the QHE expressed by S_{QHE}, Eq. (3.35). In fact, S_θ in Eq. (4.1) is only valid for the infinitely extended TI bulk. In the presence of a surface there are Dirac boundary modes, as discussed in the previous chapter. The contribution from these delocalized gapless modes is missing in the bulk electromagnetic theory. Appropriate analysis of the entire system [82–85] shows that the surface states exactly cancel S_θ, such that the CS term is actually absent.

Eq. (4.2) can only be restored if the surface states are gapped out. We have seen in Section 3.4 that a mass term can be introduced in the surface Dirac equation by a magnetic field or a magnetization m_z orthogonal to the surface. In the latter case, the Lagrangian Eq. (3.31) becomes

$$\mathcal{L}(\mathbf{r}) = \overline{\Psi}(\mathbf{r}) \left[i\partial\!\!\!/ + J m_z \right] \Psi(\mathbf{r}), \tag{4.3}$$

with an effective exchange coupling constant J. The Dirac cone with and without m_z is shown in Fig. 4.1. The magnetic term also breaks TRS explicitly, in agreement with a CS term. It is therefore the TRS-broken TI surface where the TME can be observed. We make two further remarks on such systems:

1. It is only the out-of-plane component of the magnetic field or magnetization that opens a gap. Any in-plane component only shifts the position of the Dirac cone in momentum space.

2. The nontrivial bulk topology is protected by TRS, and one may wonder if this is in conflict with having a magnetic field at the surface, which will inevitably also invade the bulk. Strictly speaking, this breaks TRS in the TI. Yet such fields are not strong enough

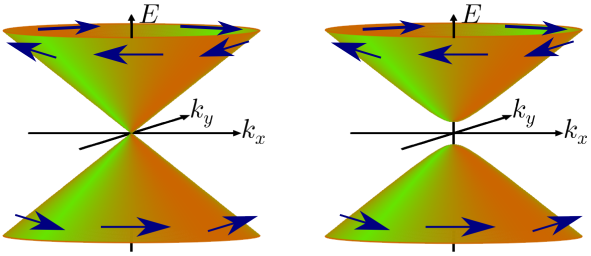

Figure 4.1: The Dirac cone without (left) and with (right) mass term. The arrows indicate the spin to visualize the spin-momentum locking.

> to undo the SOC-induced band inversion up to considerable field strengths [7, 82] and therefore the surface states will be gapped but not completely removed. This situation is called *local* TRS breaking at the surface.

Magnetic order at TI surfaces can be achieved by magnetic doping [86, 87]. Another possibility is to induce magnetic order by proximity at an interface with a magnetic insulator [88, 89], which is assumed in the Papers [1–3]. The CS term at such interfaces causes several remarkable phenomena. In the following, some important examples are briefly presented.

4.1.1 Half-integer quantum Hall effect

As already mentioned, the surface CS term formally resembles the QHE. Yet it is rather different: with $\theta = \pi$, the coefficient corresponds to the forbidden TKNN number of $\frac{1}{2} \notin \mathbb{Z}$. One finds in that sense only *half* a QHE. The half-integer QHE is a manifestation of the holographic principle as it reflects the topology in the 3D bulk rather then a mere 2D surface. One can understand the half "Chern number" by bringing the gapped surface Hamiltonian in two-band form $\mathcal{H}(\mathbf{k}) = \mathbf{d}(\mathbf{k}) \cdot \boldsymbol{\sigma}$ (compare Eq. (2.12)), where

$$\mathbf{d}(\mathbf{k}) = (\hbar v_F k_y, -\hbar v_F k_x, m_\Psi) \tag{4.4}$$

and $m_\Psi = J m_z$ denotes the effective fermion mass. Then the unit vector $\hat{\mathbf{e}}_\mathbf{d}(\mathbf{k})$ is restricted to the upper half-space if $m_\Psi > 0$ and to the lower half-space if $m_\Psi < 0$. As the surface momentum $\mathbf{k}$ runs over[27] $\mathbb{R}^2$, one half of the Bloch sphere is covered by the mapping $\mathbf{k} \mapsto \hat{\mathbf{e}}_{\mathbf{d}}(\mathbf{k})$ [7]. This line of thought also shows that the sign of the mass term matters in the CS term although it does not in the energy spectrum. Indeed, the Hall conductance of the half-integer QHE [76] is

$$\sigma_{xy} = \frac{1}{2} \frac{m_\Psi}{|m_\Psi|} \frac{e^2}{h}, \tag{4.5}$$

which implies that σ_{xy} remains at a quantized value even in the limit of a weak mass and jumps by e^2/h at $m_\Psi = 0$.

While this effect provides in principle a smoking-gun signature of the TI state of matter, it is hardly measurable as for a real TI sample one would have to isolate the effect of a single surface [82]. If all surfaces contribute, the summed conductance would again be an integer multiple of e^2/h. The effects described in the next section are more relevant for experiments and applications.

4.1.2 Topological magnetoelectric effect

While the TI bulk is always characterized by the presence of the $\mathbf{E} \cdot \mathbf{B}$ term in Eq. (4.1), it can only be accessible to measurements in the form of the surface TME. At a magnetically gapped surface, the CS term contains a coupling of the form $\mathbf{E}^{\|} \cdot \mathbf{B}^{\|}$, where the superscript $\|$ denotes the in-plane components of the electric and the magnetic field. When the effective magnetic field is caused by magnetic order, the TME will be proportional to $\mathbf{E}^{\|} \cdot \mathbf{m}^{\|}$. The explicit derivation of such terms is the foundation of the results in the Papers [1–3]. Physically the surface TME means that an in-plane electric field induces a magnetic polarization that is either parallel or antiparallel. Recall that to gap the surface states, the magnetization should point in the out-of-plane direction[28] in the first place. The TME will then lead to a tilting of $\mathbf{m}$ by inducing in-plane components.

---

[27] As our surface Hamiltonian represents a continuum theory, the BZ is replaced by the entire plane.

[28] At least the component m_z must be sufficiently large

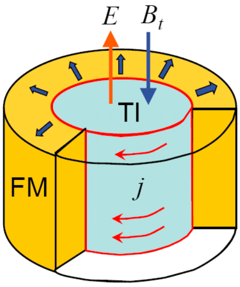

Figure 4.2: Relation of the TME to the half-integer QHE in a cylindrical TI geometry with FMI coating. Adopted from [76] (©APS, 2011).

The TME is linked to the half-integer QHE in the following way [76]: Imagine a TI in a cylindrical geometry, where the surface is covered by a FMI to ensure the local TRS breaking (Fig. 4.2). Applying a field **E** along the axis (thus in-plane with respect to the surface) leads to a half-quantized Hall current **j**, which is running around the cylinder. This current loop induces a magnetic field **B** that is again aligned with the axis, thus $\mathbf{B} \parallel \mathbf{E}$. If **B** is pointing in the same or opposite direction as **E** depands on the sign of **j**, which in turn depends on the sign of m_Ψ. Therefore, the TME has the same dependence on the sign of the mass as the half-integer QHE.

A direct consequence of the TME is a quantized Faraday rotation [76, 90]. When a polarized electromagnetic wave is transmitted through a TRS-broken TI surface, the electric component of the wave induces an aligned magnetic field and the magnetic component induces an aligned electric field. Summing up the fields, the plane of polarization is rotated by an angle ϑ, which has the quantized value $\vartheta = \alpha/4\pi$. A similar effect occurs for reflected light (Kerr rotation). Both effects have been observed experimentally [91, 92]. The existence of the TME is thereby verified. Magneto-optical effects beyond the linear response have been derived in [93], where two impinging rays can induce an AC polarization in the TI along the out-of-plane direction, if they are linearly polarized with a relative angle of $\pi/2$.

4.1.3 Magnetic monopole effect

Another consequence of the TME that is often referred to is the magnetic monopole effect [94]. From classical electrostatics it is known that the field of a point charge close to a metallic surface can be described by introducing a mirror charge [95]. A similar method can be used for a charge placed above a TRS-broken TI surface. Through the TME, the mirror charge translates into a magnetic charge, i.e. a magnetic monopole. Thus, the field outside the TI looks as if there was a monopole inside the TI. It is important to point out that this effect does not predict the presence of a physical magnetic monopole, but only a virtual one.

A related effect is that electric and magnetic charges (in the sense of an in-plane divergence) at the TI surface coincide [96]. This causes magnetic textures, for instance domain walls, to carry an electric charge. The correspondence of electric and magnetic charge is also reproduced in Paper [1].

4.1.4 Technological prospect in spintronics

Magnetic TI heterostructures are a promising novel platform for spintronics devices. The use of magnetized materials for information processing and storage depends on having efficient microscopic mechanisms to convert electric into magnetic signals and vice versa [97]. Naturally, the TME is an interesting candidate for this task. It allows for electric manipulation of the effective field in the magnetization dynamics [98, 99] or of the anisotropy field in the FMI [100]. Several studies have suggested electric control of domain wall motion in FMI-TI nano-devices, e.g. [96, 101–104]. The potential applications of the TME in spintronics have been part of the motivation for the studies presented in the Papers [1–3], besides the search for setups to directly detect the TME response.

4.2 Coulomb interaction at topological interfaces

The TME at a FMI-TI interface is mostly thought of as a coupling of the magnetization $\mathbf{m}$ to an external electric field. However, any electric potential, including intrinsic potentials as far as present, will enter into the CS term in the same way. Importantly, Coulomb interactions between the surface Dirac electrons are inevitably present. The interaction is mediated by a fluctuating electric potential. Therefore one can expect new topological terms that couple the magnetization to this Coulomb potential. Notice that the Coulomb interaction is unscreened at the gapped surface, if the Fermi level is inside the gap. Hence all interaction-related phenomena will be long-range. This will clearly have an impact on the interfacial magnetization dynamics.

The idea behind Paper [1] was to derive the topological Coulomb term that is generated via the TME and derive the modified Landau-Lifshitz equations (LLEs) [105] in a FMI-TI bilayer system. In Paper [2], this project was extended to a more complex heterostructure where also interactions between different interfaces can be studied. Below, we present the effective model on which the calculations are based and summarize the main results. Related previous work on the bilayer system was done by Nogueira and Eremin [106–108]. All equations in this section are given in units of $\hbar = 1, c = 1$.

4.2.1 Interface model

From the previous discussion of the TI surface, we have the effective Lagrangian of the Dirac states with exchange-coupling to a magnetization $\mathbf{m}$,

$$\mathcal{L}_{\text{Dirac}}(\mathbf{r}) = \overline{\Psi}(\mathbf{r}) \left[i\not{\partial} + J\mathbf{m} \cdot \boldsymbol{\sigma} \right] \Psi(\mathbf{r}). \tag{4.6}$$

In addition, the FMI layer is described by

$$\mathcal{L}_{\text{FMI}}(\mathbf{r}) = \mathbf{b}(\mathbf{r}) \cdot \partial_t \mathbf{m}(\mathbf{r}) - \frac{\kappa}{2} \left[\boldsymbol{\nabla} \mathbf{m}(\mathbf{r}) \right]^2 - \frac{n^2}{2} \mathbf{m}(\mathbf{r})^2 - \frac{u}{24} \left[\mathbf{m}(\mathbf{r})^2 \right]^2, \tag{4.7}$$

containing the following contributions:

1. A Berry phase term $\mathbf{b}$ with the property

   $$\boldsymbol{\nabla}_{\mathbf{m}} \times \mathbf{b} = -\frac{\mathbf{m}}{\mathbf{m}^2}, \tag{4.8}$$

   where $\boldsymbol{\nabla}_{\mathbf{m}}$ is the vector containing the partial derivatives with respect to the components of $\mathbf{m}$. Generally, for a spin-$\frac{1}{2}$ fermion in a magnetic field, the Berry field strength comes in the guise of a monopole in parameter space[29] [8, 11]. In the equations of motion for $\mathbf{m}$ (which are the LLEs) this term leads to the typical precession around the effective field.

2. The exchange coupling[30] in the FMI of strength κ. Written out, the short-hand notation $(\boldsymbol{\nabla}\mathbf{m})^2$ reads $\sum_{i,j=x,y,z}(\partial_i m_j)^2$.

3. The terms with the temperature-dependend coefficients n and u complete a ϕ^4 theory for the magnitude of $\mathbf{m}$. At temperatures below the Curie temperature, where FM order sets in, $n^2 < 0$, while u is always positive. Although such terms are present, they do not play a key role in our calculations, which are restricted to $T = 0$. One can then simply assume that $|\mathbf{m}|$ has a fixed nonzero value and suppress the n and u terms. They are shown in Paper [1], but not in Paper [2] for brevity.

We take it for granted that $\mathbf{m}$ is aligned in the out-of-plane direction at equilibrium, so that we obtain a gapped surface. In reality, the measurements in [109] indicate that the magnetization can also have a tilted orientation at low temperatures. In our calculations, the in-plane component of $\mathbf{m}$ is of the order of the fluctuations around the mean-field solution.

Finally, we want to include the Coulomb interaction. Even though the TI surface is described by a Dirac field theory, adding the Coulomb interaction does not require the general QED Lagrangian. The reason is that the Dirac physics happens at typical velocities of v_F, which is much smaller than the speed of light. It is therefore sufficient to treat

---

[29] where the parameter is the magnetic field

[30] Note that in the papers $\boldsymbol{\nabla}$ denotes the 2D differential operator, therefore the z component appears explicitly.

the Coulomb interaction classically. We start with the density-density interaction

$$V = \frac{1}{2}\sum_{\mathbf{k}} \rho(\mathbf{k}) v_C(\mathbf{k}) \rho(-\mathbf{k}), \tag{4.9}$$

where the density operator is $\rho(\mathbf{k}) = \sum_{\mathbf{q},s=\uparrow,\downarrow} \Psi^\dagger_{\mathbf{q}+\mathbf{k},s}\Psi_{\mathbf{q},s}$ and $v_C(\mathbf{k})$ is the $1/r$ Coulomb potential transformed to momentum space. A subtlety here is that the Fourier transformation (FT) of the 3D potential is performed in only *two* dimensions parallel to the surface. For details of the FT see Appendix A. The result is

$$v_C(\mathbf{k}) = \frac{2\pi e^2}{|\mathbf{k}|} e^{-|\mathbf{k}|d}, \tag{4.10}$$

where $d = 0$ for a single interface. If the two density operators in Eq. (4.9) describe electrons at different planes then $d > 0$ denotes the distance between them. This general expression is only relevant for Paper [2]. The interaction can be made quadratic in the fermionic operators by means of a Hubbard-Stratonovich (HS) decoupling [110, 111], which is based on the multidimensional real Gaussian integral

$$\int \mathrm{d}^N x\, e^{-\frac{1}{2}\mathbf{x}\cdot A\cdot\mathbf{x}+\mathbf{x}\cdot\mathbf{v}} = \sqrt{\frac{(2\pi)^N}{\det A}}\, e^{\frac{1}{2}\mathbf{v}\cdot A^{-1}\cdot\mathbf{v}}. \tag{4.11}$$

The interaction Eq. (4.9) appears in the exponent when the partition function is written in path-integral [111] form

$$\mathcal{Z} = \int D[\Psi^\dagger] D[\Psi]\, e^{iS}. \tag{4.12}$$

Then ρ plays the role of $\mathbf{v}$ in the right-hand side of Eq. (4.11). A term linear in ρ as in the left-hand side of Eq. (4.11) requires to introduce an auxiliary HS field φ. The decoupling leads to

$$V \to \sum_{\mathbf{q}} \varphi(\mathbf{q})\rho(\mathbf{q}) - \sum_{\mathbf{q}} \frac{1}{2}\varphi(-\mathbf{q})\frac{1}{v_C(\mathbf{q})}\varphi(\mathbf{q}) \tag{4.13}$$

in the Lagrangian. It is practical to absorb units of $1/e$ into the HS field such that it can be interpreted as an electric potential. Transformed to real space, we arrive at the Coulomb Lagrangian

$$\mathcal{L}_{\mathrm{C}}(\rho,\varphi) = -e\varphi(-\mathbf{r})\rho(\mathbf{r}) + \frac{1}{8\pi^2}[\nabla_{\mathbf{r}}\varphi(\mathbf{r})] \cdot \int \mathrm{d}^2\mathbf{r}' \, \frac{\nabla_{\mathbf{r}'}\varphi(\mathbf{r}')}{|\mathbf{r}-\mathbf{r}'|}. \tag{4.14}$$

The long range character of the interaction is now completely stored in the integral over the HS field. The other term, $\Psi^\dagger[e\varphi]\Psi$, can simply be inculded in $\mathcal{L}_{\mathrm{Dirac}}$. Finally, if an external electric field is present, this adds a fixed potential ϕ to φ. This completes the model. The full fermionic Lagrangian can be written in covariant form as described previously, where the in-plane magnetization and the electric potential can be collected in a vector $a = (e\varphi/J, m_y, -m_x)$:

$$\mathcal{L} = \overline{\Psi}\left[i\partial\!\!\!/ + m_\Psi + J\tilde{m}_z - J a\!\!\!/\right]\Psi \tag{4.15}$$

The term $J\tilde{m}_z$ describes fluctuations in the out-of-plane direction, whereas the mean-field part $\overline{m}_z$ gives rise to the mass term m_Ψ.

4.2.2 Nonlocal modification of the LLEs

By integrating out the fermions from the partition function [111], one can now derive the effective theory for the electric potential and the magnetization, as described in the papers. This calculation amounts (to leading order) to the evaluation of 1-loop vacuum polarization diagrams and is shown in detail in Appendix B. From Eq. (4.15) one obtains

$$\delta\mathcal{L} = \frac{\epsilon_{\mu\nu\lambda}a^\mu\partial^\nu a^\lambda}{8\pi} - \frac{\left(\epsilon_{\mu\nu\lambda}\partial^\nu a^\lambda\right)^2}{24\pi m_\Psi} - \frac{m_\Psi\tilde{m}_z^2}{2\pi} + \frac{(\partial\tilde{m}_z)^2}{24\pi m_\Psi}. \tag{4.16}$$

The first term is the CS term that arises from the nontrivial topology in the TI. The second one is the Maxwell term. The other terms describe fluctuation-induced anisotropy in the out-of-plane direction. Similar expressions for the CS term had been found before in [98,106]. It contains the TME term and a Berry phase. Specifically, the TME takes the form

$$\mathcal{L}_{\mathrm{TME}} = \frac{\sigma_{xy}e}{v_F J}\mathbf{m}^\parallel \cdot \boldsymbol{\nabla}^\parallel\varphi, \tag{4.17}$$

where in our units $\sigma_{xy} = J^2/4\pi$ and the superscript $\|$ marks the restriction to the in-plane components. To make the impact of Coulomb interaction visible, one has to evaluate $\delta\mathcal{L}$ together with the integral term in Eq. (4.14). It is then clear that $\mathcal{L}_{\mathrm{TME}}$ contains nonlocal terms. Specifically, in Paper [1] it is shown that the magnetization at the interface couples to the effective Coulomb field

$$\mathbf{E}(\mathbf{r}) = -\int \mathrm{d}^2 r' \, \varrho(\mathbf{r}') \frac{\mathbf{r} - \mathbf{r}'}{|\mathbf{r} - \mathbf{r}'|^3} \tag{4.18}$$

where the charge density has the topologically protected part

$$\varrho(\mathbf{r}) = \frac{\sigma_{xy} e}{v_F J} \boldsymbol{\nabla}^{\|} \cdot \mathbf{m}^{\|}(\mathbf{r}) \tag{4.19}$$

that stems from the CS term. When the LLEs are derived from the effective Lagrangian, this leads to the topological interaction-induced contribution $\sigma_{xy} e \mathbf{E}/(2 v_F J)$ to the effective field[31]. This nonlocal alteration of the LLEs is the main result of Paper [1].

4.2.3 Topological dipolar interaction

In Paper [2] we investigate how the nonlocal effects apply in a heterostructure with two parallel FMI-TI interfaces at a distance d, where the Coulomb interaction acts both within and between the interfaces (labeled with an index $i = 1, 2$). The interaction via topologically protected terms between otherwise (nearly) uncoupled interfaces provides an interesting setup to detect the TME. Note that the proposed layered structure shown in Fig. 4.3(a) has two such interfaces belonging to different TIs to avoid effects of the side surfaces.

A key insight of this paper is that the topological Coulomb-mediated effective interaction between the magnetic moments at the interfaces

---

[31] The complete LLEs are given in the paper.

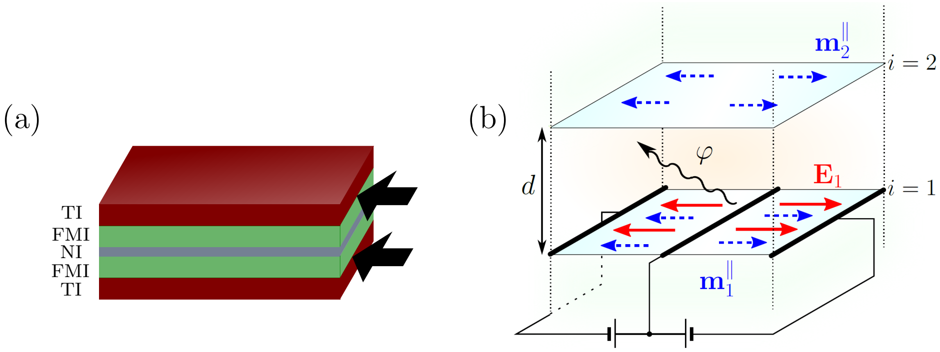

Figure 4.3: (a) A setup with two parallel FMI-TI interfaces. NI denotes a nonmagnetic insulator. (b) A configuration where the magnetization at $i = 2$ is manipulated in a topologically protected manner by an electric field at $i = 1$. From Paper [2].

can be expressed as

$$\begin{aligned}\mathcal{L}_{\rm dip}(\mathbf{r}) &= -\left(\frac{e}{2Jv_F}\right)^2 \sum_{i,j=1,2} \sigma_{xy,i}\sigma_{xy,j} \int \frac{\mathrm{d}^2 r'}{\left[(\mathbf{r}-\mathbf{r}')^2 + (1-\delta_{ij})d^2\right]^{3/2}} \\ &\qquad \left\{ \frac{3\Big[\mathbf{m}_i^{\|}(\mathbf{r})\cdot(\mathbf{r}-\mathbf{r}')\Big]\Big[\mathbf{m}_j^{\|}(\mathbf{r}')\cdot(\mathbf{r}-\mathbf{r}')\Big]}{(\mathbf{r}-\mathbf{r}')^2 + (1-\delta_{ij})d^2} - \mathbf{m}_i^{\|}(\mathbf{r})\cdot\mathbf{m}_j^{\|}(\mathbf{r}') \right\}\end{aligned} \tag{4.20}$$

This expression has the same form as the classical dipole-dipole interaction (CDI) [95]. We have thus found a topological magnetic dipolar interaction (TDI). Because of the apparent similarity of the two interactions, it is expedient to emphasize the differences:

1. The interaction Eq. (4.20) has been derived from the CS term and is therefore topologically protected. The quantization of σ_{xy} enters in the coefficient.

2. In contrast to CDI, the TDI is only concerned with the in-plane components of the magnetization, while the component orthogonal to the interface has no effect. Our calculation assumes that,

at the mean-field level, $\mathbf{m}$ is orthogonal to the interface to ensure the mass term, thus $\mathbf{m}^{\|}$ and the TDI are of the order of the fluctuations.

3. The sign of the TME depends on the sign of the mass term, corresponding to the orientation of the magnetization “into” or “out of” the TI. For the inter-plane TDI ($i \neq j$), $\sigma_{xy,i}$ and $\sigma_{xy,j}$ can have either equal or opposite sign. The overall sign of the TDI can therefore be changed by switching the magnetization at one of the interfaces. The TDI can thus favor alignment or counteralignment of $\mathbf{m}_i$ and $\mathbf{m}_j$. The latter effect is opposite to CDI.

4. The low-energy theory for the TI surface describes Dirac fermions upon replacing the speed of light by the Fermi velocity. This causes a dramatic rescaling of all subsequent effects as compared to their QED analogues[32]. In the coefficient of the TDI versus the CDI (in proper units), one has to compare $1/v_F^2$ and $1/c^2$, respectively. Assuming $v_F = 5 \times 10^5 m/s$, the velocity rescaling leads to a relative factor of 360 000 in favor of TDI.

5. Eq. (4.20) describes a purely interfacial effect, while CDI also couples magnetic moments anywhere else. Despite the previous point, the strength of the TDI depends on the magnetic proximity effect and might be reduced by experimental issues with the interface quality, in contrast to CDI. Also, as soon as one fails to gap the TI surface states, the TDI vanishes altogether.

The model of the system did not include CDI. However, it would not change the calculation and can also be added in the end. The net dipole-dipole interaction is then the sum of Eq. (4.20) and the classical term. In the paper it is proposed to detect the TDI by means of polarized neutron reflectometry motivated by the recent successful application of that technique in Bi_2Se_3-EuS structures [109]. Furthermore, it is suggested to apply the topological coupling of the interfaces in spintronics devices, where it would allow for the topologically

---

[32] Of course, CDI is obtained from QED in the classical limit.

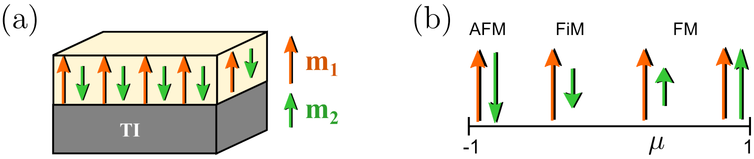

Figure 4.4: (a) Interface of the TI with a BMI. (b) The BMI can be tuned between AFM and FM order by a model parameter. From Paper [3].

protected nonlocal manipulation of the magnetization in an operating layer by applying a voltage at a separated controlling layer, see Fig. 4.3(b).

4.3 Topological staggered-field-electric effect

In Paper [3], the setting of Paper [1] is generalized in a different direction. Namely, the TME is studied at the interface of a TI with a general bipartite magnetic insulator (BMI), which can be tuned between the antiferromagnetic (AFM) and ferromagnetic configurations, see Fig. 4.4. This includes ferrimagnetic (FiM) insulators, among them e.g. the technologically relevant yttrium iron garnet (YIG). YIG-TI samples have been fabricated in recent experiments [112, 113]. In addition, in this paper more attention is paid to the proximity effect. In the beginning, the surface of the magnet and the surface of the TI are described separately and then coupled via electron hopping. Coulomb interaction is kept in the calculation, although it is not the main focus of this work, and produces similar effects as in Papers [1] and [2].

For clarity, we list the constituents of the model below. The model is again set up in the continuum limit. Nevertheless, the term sublattice is used occasionally to refer to the subsystems of $\mathbf{m}_1$ and $\mathbf{m}_2$, as a bipartite crystal is still the microscopic origin of the two magnetic moments.

- The BMI is modeled as before by Eq. (4.7) for $\mathbf{m}_1$ and $\mathbf{m}_2$ separately. The two components are then coupled by $\mathcal{L} = -\lambda \mathbf{m}_1 \cdot \mathbf{m}_2$. Both $\mathbf{m}_1$ and $\mathbf{m}_2$ are assumed to be orthogonal to the interface at mean-field, $\mathbf{m}_i = \overline{m}_i \hat{\mathbf{e}}_z$, and we define $\mu = \overline{m}_2/\overline{m}_1$ (without loss of generality, $|\mu| \leq 1$), which describes the configuration of the magnet as in Fig. 4.4(b).

- At the magnet's surface, we introduce two species of localized fermions χ_1, χ_2 with spins coupled to $\mathbf{m}_1$, $\mathbf{m}_2$, respectively:

  $$\mathcal{L}_{\text{ex}} = J \sum_{i=1,2} \chi_i^\dagger (\mathbf{m}_i \cdot \boldsymbol{\sigma}) \chi_i \tag{4.21}$$

  The same coupling constant is assumed on both sublattices. However, it could easily be generalized to staggered coupling if desired.

- In addition, these fermions are directly coupled with an amplitude t (real for simplicity), allowing them to change "flavor":

  $$\mathcal{L}_\chi = \begin{pmatrix} \chi_1^\dagger \\ \chi_2^\dagger \end{pmatrix} \begin{pmatrix} i\partial_t & t \\ t & i\partial_t \end{pmatrix} \begin{pmatrix} \chi_1 \\ \chi_2 \end{pmatrix} \tag{4.22}$$

  In a bipartite lattice model, this would correspond to a process where electrons can hop between sublattices inside each unit cell but not between unit cells. Thus this process is on-site, $\propto \delta_{\mathbf{r},\mathbf{r}'}$, in the continuum limit. It is also useful to define the dimensionless parameter $\tau = (t/J\overline{m}_1)^2$.

- The TI surface dispersion is initially the gapless Dirac cone, but already equipped with a coupling to the electric potential with both Coulomb and external-field parts,

  $$\mathcal{L}_{\text{Dirac}} = \Psi^\dagger [i\partial_t - iv_F(\sigma_y \partial_x - \sigma_x \partial_y) + e(\varphi + \phi)]\Psi. \tag{4.23}$$

- The proximity effect is included by electron hopping as already mentioned,

  $$\mathcal{L}_{\text{prox}} = h\Psi^\dagger(\chi_1 + \chi_2) + \text{h.c.} \tag{4.24}$$

- For the complete description of Coulomb interaction, the integral expression appearing in Eq. (4.14) is taken into account as well.

From this theory, the effective coupling of the Dirac fermions to $\mathbf{m}_1$ and $\mathbf{m}_2$ is derived by integrating out χ_1 and χ_2. Here we do not go into the details of this part of the calculation. Explicit expressions of all terms generated by the quantum fluctuations of χ_1 and χ_2 can be found in Paper [3], comprising anisotropy, Berry phases, and a renormalization of λ at the surface. One restriction to the model must be mentioned, though: in the way the magnet's surface is modeled, it has degenerate eigenstates at zero energy if $\tau = \mu$. This choice of parameters does not describe an insulator, and integrating out χ_i in the low-energy theory is forbidden. The line $\tau = \mu$ in parameter space has to be excluded in the following.

The effective theory for TI surface including the proximity effect now reads

$$\mathcal{L}_{\text{eff}} = \mathcal{L}_{\text{Dirac}} + \gamma\Psi^\dagger \left(t^2 - J^2\mathbf{m}_1 \cdot \mathbf{m}_2\right) \Psi + \sum_{i=1,2} \Psi^\dagger J_i \mathbf{m}_i \cdot \sigma\Psi, \tag{4.25}$$

where γ is a constant given by[33]

$$\gamma = \frac{2th^2}{t^4 + J^2(J^2\overline{m}_1^2\overline{m}_2^2 - 2t^2\overline{m}_1\overline{m}_2)} \tag{4.26}$$

and the coupling constants are

$$J_i = \frac{h^2 J}{t^4 + J^2(J^2\overline{m}_1^2\overline{m}_2^2 - 2t^2\overline{m}_1\overline{m}_2)} \left(J^2\mathbf{m}_{3-i}^2 - t^2\right). \tag{4.27}$$

The first new contribution to $\mathcal{L}_{\text{Dirac}}$ is a shift in the chemical potential. The constant part can be neglected if the chemical potential is externally tuned such that the Fermi level is close to the Dirac point. The fluctuating part depends on the dynamic angle between $\mathbf{m}_1$ and $\mathbf{m}_2$. The second new contribution in the Dirac Lagrangian contains the exchange-coupling to the magnetization that we were looking for. For each $\mathbf{m}_i$, the coupling has the same form that was assumed in the Papers [1] and [2] without explicitly computing the proximity effect, which is reassuring. This coupling leads to a mass term $m_\Psi = J_1\overline{m}_1 + J_2\overline{m}_2$ and thereby gaps the Dirac energy spectrum[34].

---

[33] Slightly deviating from the notation in the paper, here γ is rescaled by $1/J^2$.

[34] The case $J_1\overline{m}_1 = -J_2\overline{m}_2$ is equivalent to $\tau = \mu$ and already excluded.

Furthermore, we have found the expression Eq. (4.27) for the constants J_i. Interestingly, $J_1 \neq J_2$ if $|\mathbf{m}_1| \neq |\mathbf{m}_2|$[35], although we started with the same J on both sublattices.

The second part of the calculation is to integrate out the Dirac fermions Ψ as well, which is done in the same manner as for the FMI-TI interfaces. In that way, one can again derive the CS term which contains the TME:

$$\mathcal{L}_{\text{TME}} = \frac{e}{4\pi v_F}\left(J_1\mathbf{m}_1^{\|} + J_2\mathbf{m}_2^{\|}\right)\cdot\mathbf{E}. \tag{4.28}$$

In other words, the regular TME appears on both sublattices, which is not surprising. However, a novel effect arises from the net response of the entire system, because J_1 and J_2 can be different. In fact, the coupling constants can even have opposite signs. In that case, an electric field generates (mainly) a staggered field rather than a net magnetization in the plane, as $\mathbf{m}_1$ and $\mathbf{m}_2$ are tilted in opposite directions, see Fig. 4.5(a). This is the topological staggered-field electric effect (TSE). From Eq. (4.27) one readily finds the parameter regions of the model that exhibit the TME or TSE. These are shown in Fig. 4.5(b) in terms of the dimensionless parameters μ and τ. The TSE is possible within a certain range of t whenever $|\mathbf{m}_1| \neq |\mathbf{m}_2|$, in particular for FiMs. FiMs are often treated like FMs, reducing them to the net magnetization. The result of Paper [3] reveals a case where this simplification can grossly fail. On the other hand, when the BMI has pure AFM order[36] no TSE is found, which may seem unintuitive as the staggered field is maximal in the AFM configuration.

For further clarification of the diagram in Fig. 4.5(b), there are no distinct phases with a clear transition in between, but regimes where the induced in-plane net magnetization $\mathbf{m}^{\|} = \mathbf{m}_1^{\|} + \mathbf{m}_2^{\|}$ is larger (TME) or smaller (TSE) in magnitude than the in-plane staggered field $\mathbf{l}^{\|} = \mathbf{m}_1^{\|} - \mathbf{m}_2^{\|}$. Exactly at the line $\tau = \frac{1}{2}(\mu^2 + 1)$ in parameter space, $\mathbf{m}^{\|} = 0$, corresponding to a "pure" TSE. The TSE provides a novel possibility to electrically manipulate a staggered field, which is an important task in AFM spintronics [115]. A drawback is that for real materials it might

---

[35] If we take $|\mathbf{m}_i| = \text{const.}$ one can replace $\mathbf{m}_i^2$ by $\overline{m}_i^2$

[36] In that case $m_\Psi = 0$ anyway, but one can think of interfaces of magnetically doped TIs with AFMs as in [114].

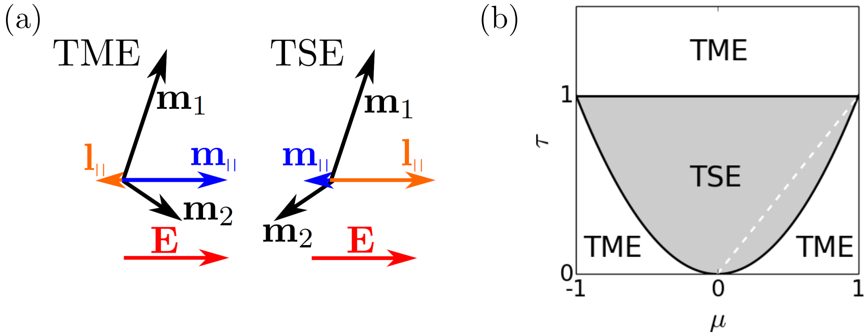

Figure 4.5: (a) Schematic depiction of the TME and TSE. (b) Parameter regions where the TME and the TSE are found. From Paper [3].

be hard to predict where they are located in the parameter space of our simple model system. More advanced models would hardly allow for explicit analytic solutions as obtained in Paper [3].

As a subordinate result, also the γ-term in $\mathcal{L}_{\text{eff}}$ contributes to the CS term after Ψ has been integrated out:

$$\mathcal{L}_\gamma = \frac{\gamma J^2}{4\pi v_F}\left(J_1\mathbf{m}_1^{\|} + J_2\mathbf{m}_2^{\|}\right)\cdot\boldsymbol{\nabla}^{\|}\left(\overline{m}_1\tilde{m}_{2,z} + \overline{m}_2\tilde{m}_{1,z}\right) \tag{4.29}$$

This term is interesting in so far as it yields a topological coupling of the in-plane and out-of-plane fluctuations in a non-homogeneous configuration where $\boldsymbol{\nabla}^{\|}\tilde{m}_{i,z} \neq 0$. Thus, it affects the dynamics of textures and domain walls. The LLEs become rather complicated, though, cf. Appendix C in [3].

Chapter 5

Topological Superconductors

In the previous two chapters, we have discussed properties of TIs, where the concepts of topology could be applied because of the energy gap in the bulk band structure. The topological classification of gapped band structures can be straight-forwardly generalized to superconductors (SCs). Like an insulator, a SC also has an energy gap, although it has a different physical interpretation. The eigenstates are Bogoliubov quasiparticles (BQPs) instead of electrons and holes, and the gap corresponds to the energy required to break up Cooper pairs rather than exciting electrons from the valence band to the conduction band. TSCs are SCs where the band structure of the BQPs has a nontrivial topological invariant [6, 7].

We relinquish a comprehensive discussion of superconductivity, but briefly review the formalism of Bogoliubov-de-Gennes (BdG) Hamiltonians in the first section. Afterwards, we explain which SCs can be topological and what kind of boundary states they have. Finally, we discuss the systems investigated in Papers [4] and [5], namely Majorana nanowires and nodal noncentrosymmetric superconductors (NCSs), respectively.

5.1 Bogoliubov-de-Gennes Hamiltonians

In general, a superconducting phase [116] is based on the pairing of electrons into Cooper pairs, which allows them to form a condensate. The two main characteristics of SCs, perfect diamagnetism (the Meißner effect) [117] and vanishing electric resistivity [118], are consequences of the condensation. The pairing of electrons requires an attractive interaction between them. Even an arbitrarily weak attractive interaction will lead to superconductivity below a certain critical temperature T_c. While the original theory of superconductivity by Bardeen, Cooper, and Schrieffer (BCS) [119, 120] is based on a phonon-mediated effective interaction, a variety of other microscopic mechanisms are possible, too.

At equilibrium, the Cooper pairs consist of electrons with opposite momentum. This leads to a term of the general form $\Delta_{\sigma,\sigma'}(\mathbf{k})c^\dagger_{\mathbf{k},\sigma}c^\dagger_{-\mathbf{k},\sigma'}$ in the Hamiltonian at the mean-field level, with the creation operator $c^\dagger_{\mathbf{k},\sigma}$ for electrons with momentum $\mathbf{k}$ and spin σ. The coefficient Δ is the superconducting order parameter, whereby $\Delta = 0$ if $T \geq T_c$. In principle, $\Delta(\mathbf{k}, \sigma, \sigma')$ can be calculated if the underlying pairing mechanism is known. For conventional BCS SCs, for instance, Δ is isotropic and pairs only electrons with opposite spin. Such calculations can be difficult, though, and moreover the pairing mechanism is still unknown or under debate in several superconducting materials.

Irrespective of the precise origin of the pairing, SCs can generically be described by an effective Hamiltonian of the form

$$H_{SC} = \frac{1}{2}\sum_{\mathbf{k}} \Psi^\dagger_{\mathbf{k}} \mathcal{H}_{\mathrm{BdG}}(\mathbf{k}) \Psi_{\mathbf{k}} \tag{5.1}$$

with the Nambu spinor [121] $\Psi_{\mathbf{k}} = (c_{\mathbf{k}\uparrow}, c_{\mathbf{k}\downarrow}, c^\dagger_{-\mathbf{k}\uparrow}, c^\dagger_{-\mathbf{k}\downarrow})^{\mathrm{T}}$ and the BdG Hamiltonian

$$\mathcal{H}_{\mathrm{BdG}}(\mathbf{k}) = \begin{pmatrix} \xi(\mathbf{k}) & \Delta(\mathbf{k}) \\ \Delta^\dagger(\mathbf{k}) & -\xi^{\mathrm{T}}(-\mathbf{k}) \end{pmatrix}. \tag{5.2}$$

We note that the number of states is doubled in the Nambu spinor compared to the physical number of states. In the BdG notation, the SC order parameter can be treated as a model parameter. In the normal state, $\Delta = 0$, the eigenstates of the BdG Hamiltonian are electrons and holes where the dispersion follows from $\xi(\mathbf{k})$. In particular, at the normal-state Fermi surface[37] $\xi(\mathbf{k})_{\mathbf{k}\in\mathrm{FS}}$ has eigenvalues equal to zero. In the presence of pairing, Eq. (5.2) is non-diagonal, and the eigenstates will be mixtures of electrons and holes – the BQPs. They describe the excitations of the condensate by pair-breaking. The eigenenergy is minimal at the Fermi surface, where $\mathcal{H}_{\mathrm{BdG}}$ has an eigenvalue that is purely determined by $\Delta(\mathbf{k})_{\mathbf{k}\in\mathrm{FS}}$ and defines the gap of the excitation spectrum. Therefore, Δ is also referred to as the superconducting gap.

The order parameter can be characterized by its dependence on $\mathbf{k}$ and its matrix structure in spin space. The momentum dependence can be expanded into spherical harmonics so that one can distinguish gaps with s, p, d, …-wave symmetry. One can also label the specific orbitals, e.g. p_x or $d_{x^2-y^2}$. In spin space, the gap can be decomposed into the singlet and triplet-pairing part according to [122]

$$\Delta(\mathbf{k}) = \left[\delta_{\mathrm{singlet}}(\mathbf{k}) + \boldsymbol{\delta}_{\mathrm{triplet}}(\mathbf{k}) \cdot \boldsymbol{\sigma}\right] i\sigma_y, \tag{5.3}$$

where $\delta_{\mathrm{singlet}}(\mathbf{k}) = \delta_{\mathrm{singlet}}(-\mathbf{k})$ and $\boldsymbol{\delta}_{\mathrm{triplet}}(\mathbf{k}) = -\boldsymbol{\delta}_{\mathrm{triplet}}(-\mathbf{k})$. Usually, the anti-symmetry of fermionic wavefunctions dictates that the order parameter is either even in momentum with singlet pairing, or odd in momentum with triplet paring. A conventional BCS SC has an s-wave singlet order parameter. However, in the presence of SOC, Δ will in general have both singlet and triplet pairing contributions [123]. This becomes important in the case of noncentrosymmetric SCs, which will be discussed further in Section 5.5.

5.2 Majorana zero modes

The BdG formalism makes it easy to translate the models of TIs to TSCs [7,28,124]. We know already how to construct 4×4 Hamiltonians with nontrivial band topology, namely exactly as in the BHZ model Eq. (3.22) and its counterpart in 3D, Eq. (3.28). In the Nambu basis[38], the matrix entries have a different meaning, though[39]. In particular,

---

[37] There may be two spin-split Fermi surfaces, e.g. in the presence of SOC.

[38] A one-to-one translation of the matrices requires that the Nambu spinor is written in the order $(c_{\mathbf{k}\uparrow}, c^\dagger_{-\mathbf{k}\uparrow}, c_{\mathbf{k}\downarrow}, c_{-\mathbf{k}\downarrow})^{\mathrm{T}}$.

[39] Note that the PHS-breaking terms proportional to the unit matrix must be discarded.

A (or A_1, A_2 in 3D) becomes the superconducting order parameter. The term $A(k_x\sigma_x - k_y\sigma_y)$ from the BHZ model then describes triplet p wave pairing. These superconducting Hamiltonians still lead to helical boundary modes as in the TIs. One can also find superconducting analogues to the QHE (the chiral $p_x \pm ip_y$ SC in 2D [125]) and the SSH model (see next section). They all share the essential property of p wave pairing, which rules out all conventional SCs. A rare example of a p wave SC is Sr_2RuO_4 [126,127]. A p wave gap also occurs in the superfluid phase of ^{3}He [128], which is conceptionally similar to a SC. Interestingly, effective p wave pairing can also be proximity-induced, for instance at a TI interface with an s wave SC [129] or a d_{xy}-wave SC [130], or in nanowires with SOC (Section 5.4).

The high interest in TSCs is owed to their exotic boundary states [131,132]. In a TI, a single Dirac cone is found on each surface. In a TSC, on the other hand, the number of states is doubled by the BdG formalism. Thus, the topologically protected surface mode corresponds to *half* of an ordinary fermionic state. In fact, these zero-energy modes are Majorana fermions [125,131]. The defining property of a Majorana fermion is being its own antiparticle, $\psi^\dagger = \psi$ [133]. This is possible in TSCs because BQPs are superpositions of electrons and holes. To date no fundamental particle with this property is known (in the absence of indications of the neutrinoless double-β decay [134–136]). Formally, every ordinary fermion operator can be decomposed in two Majorana operators. The Majorana zero modes (MZMs) in TSCs are special because they are appear spatially separated as unpaired Majorana quasiparticles on opposite boundaries. This will be made explicit in the next section on the Kitaev model [137].

The MZMs have a second remarkable property: non-Abelian braiding statistics [131,132,138], which was predicted in [125,139]. While in 3D all particles must be fermions or bosons, for which the many-particle wavefunction gains a factor of -1 or 1 under the exchange of two particles, respectively, in 2D particles can also be so-called anyons. For Abelian anyons [140], the factor is a complex phase $\exp(i\varphi)$. By changing φ, one can interpolate between fermions and bosons. Even more, the wavefunction can acquire factors that do not commute with each other. In that case, the particles are called non-

Abelian anyons [141]. The reason for the more general particle exchange relation is that the topology of $\mathbb{R}^2 \setminus \{0\}$ and $\mathbb{R}^3 \setminus \{0\}$ is very different [12]: in 2D a nontrivial winding number around the origin is possible, whereas it is not in 3D. Therefore, particle exchange in 2D can in general depend on the path of one particle around the other (which can be pinned to the origin). In 3D, all paths are homotopic. Non-Abelian exchange has also been predicted for excitations in the fractional QHE [125, 142].

Non-Abelian braiding is attracting much attention because it could be applied in topological quantum computation [138]. The non-commuting factors acquired by braiding operations would lead to different quantum states which could be used to encode information. The advantage compared to other quantum computation schemes, e.g. using spin qubits, is that a topological quantum computer would be fault-tolerant [138], because the information is stored non-locally.

5.3 The Kitaev chain

A first toy model capable of realizing MZMs was found by Kitaev [137]. He proposed a spinless p-wave SC on a 1D lattice,

$$H_{\text{Kitaev}} = -\mu \sum_{i=1}^{N} c_i^\dagger c_i - \frac{1}{2} \sum_{i=1}^{N-1} \left(t c_i^\dagger c_{i+1} + \Delta c_i c_{i+1} + \text{h.c.} \right), \tag{5.4}$$

with chemical potential μ, nearest-neighbor hopping t, and a superconducting order parameter Δ pairing fermions on neighboring sites. For $N \to \infty$, the model can be transformed into a momentum-space BdG Hamiltonian[40], which in this case is only a 2×2 matrix as spin is absent:

$$H_{\text{BdG}}(k) = \begin{pmatrix} \xi(k) & \Delta^*(k) \\ \Delta(k) & -\xi(k) \end{pmatrix}, \tag{5.5}$$

with

$$\xi(k) = -t \cos ka - \mu \tag{5.6}$$

$$\Delta(k) = -i\Delta \sin ka \tag{5.7}$$

---

[40] Constants are neglected

and the lattice spacing a. As required for a p-wave SC, $\Delta(k)$ is an odd function. For simplicity we assume that Δ is real. The energy spectrum

$$\varepsilon(k) = \pm\sqrt{\xi(k)^2 + |\Delta(k)|^2} \tag{5.8}$$

is usually gapped at any k, unless $\mu = \pm t$ or $\Delta = 0$ [131].

The next step is to decompose each fermion into two Majorana operators γ_A and γ_B,

$$c_i = \frac{1}{2}(i\gamma_{A,i} + \gamma_{B,i}). \tag{5.9}$$

Inversely, $\gamma_{A,i} = -i(c_i - c_i^\dagger)$ and $\gamma_{B,i} = c_i + c_i^\dagger$ so that evidently $\gamma_{A,i}^\dagger = \gamma_{A,i}$ and $\gamma_{B,i}^\dagger = \gamma_{B,i}$. Furthermore, $\gamma_{\alpha,i}^2 = 1$ and the anticommutator is $[\gamma_{\alpha,i}\gamma_{\beta,j}]_+ = 2\delta_{\alpha\beta}\delta_{ij}$. The Hamiltonian Eq. (5.4) then becomes

$$H_{\text{Kitaev}} = \frac{i}{2}\mu\sum_{i=1}^{N}\gamma_{B,i}\gamma_{A,i} + \frac{i}{4}\sum_{i=1}^{N-1}\left[(t+\Delta)\gamma_{A,i+1}\gamma_{B,i} + (t-\Delta)\gamma_{A,i}\gamma_{B,i+1}\right] \tag{5.10}$$

In this form, the Kitaev chain is reminiscent of the SSH model presented in Sec. 3.1. However, now we have two Majorana operators per site instead of two electron operators. One can show that two coupled Kitaev chains are equivalent two the SSH model [143]. Like the SSH model, the Kitaev chain is in class BDI and has two topologically distinct gapped phases, where the nontrivial phase has zero-energy modes that are localized at the ends of the chain. This can be seen from two limiting cases (see also Fig. 5.1):

1. $\mu \neq 0$, $\Delta = t = 0$. Only the first sum in Eq. (5.10) remains, and the Hamiltonian can as well be expressed with the ordinary fermion operators c_i. In this limit, we simply have a row of completely uncoupled fermions. This case is topologically trivial.

2. $\mu = 0$, $\Delta = t \neq 0$. All terms except $(t+\Delta)\gamma_{A,i+1}\gamma_{B,i}$ vanish. This can again be written as a row of uncoupled fermions, but not with the operators c_i. Instead, one has to introduce new fermions $d_i = (i\gamma_{B,i} + \gamma_{A,i+1})/2$ that form bound states of Majorana modes

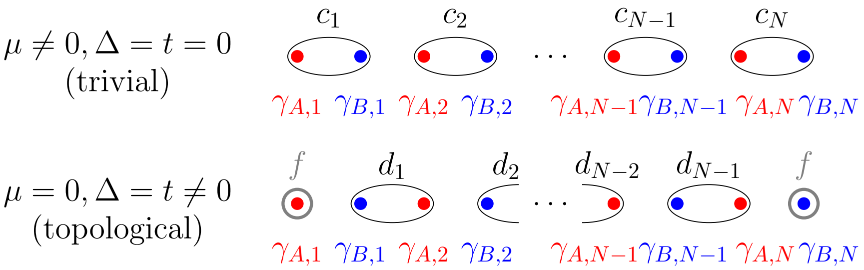

Figure 5.1: Sketch of two limiting cases of the Kitaev chain Eq. (5.10).

belonging to neighboring sites, with the Hamiltonian

$$H = \Delta \sum_{i=1}^{N-1} \left(d_i^\dagger d_i - \frac{1}{2} \right) . \tag{5.11}$$

At the ends of the chain, $\gamma_{A,1}$ and $\gamma_{B,N}$ remain as isolated Majorana modes. They can be combined into a fermion operator $f = (\gamma_{A,1} + i\gamma_{B,N})/2$ which describes a state at zero energy, as it is absent in the Hamiltonian. In constrast to the d_i's, f cannot be interpreted as an actual particle, as it is highly non-local – $\gamma_{A,1}$ and $\gamma_{B,N}$ are separated by the entire chain length. This is the non-trivial case.

All other parameter configurations (except the gapless case) can be continuously connected to one of the two cases above [131], i.e. without closing the energy gap in the bulk spectrum Eq. (5.8). Indeed, the Kitaev chain is characterized by a $\mathbb{Z}_2$ topological invariant that distinguishes the trivial from the topological case and is determined by the bulk bands. The BdG Hamiltonian can be written as $H_{\text{BdG}} = \mathbf{d}(k) \cdot \boldsymbol{\sigma}$, with the vector

$$\mathbf{d}(k) = -\Delta \sin(ka)\hat{\mathbf{e}}_y + \xi(k)\hat{\mathbf{e}}_z . \tag{5.12}$$

In analogy to the SSH model, the vector $\mathbf{d}(k)$ describes a circle in the (y, z) plane if k is running once over the BZ, $k \to k + 2\pi/a$. The circle cannot cross the origin, which would mean to close the gap, so we can define its winding number ν around $(0, 0)$. It is clear that either $\nu = 0$ or $\nu = 1$. In the two limiting cases above, case 1 has $\nu = 0$ and case

2 has $\nu = 1$. Similarly to the TIs, the topological case can also be understood as an inversion of the band structure at $k = 0$ as compared to $k = \pm\pi/a$.

The following section discusses the most prominent implementation of the Kitaev chain in semiconductor nanowires [144–147]. There are noteworthy other suggestions to construct Kitaev chains, among others based on the edge states of the QSHE [148] or on chains of magnetic atoms on a SC (Shiba chains) [149].

5.4 Semiconductor Majorana nanowires

Attempting to realize the Kitaev chain in a physical system, one is facing two problems: (i) there are no spinless fermions, and (ii) there are almost no p-wave SCs. Remarkably, both obstacles can be overcome by a cunning combination of three relatively easily accessible components, as proposed by[41] Lutchyn *et al.* [144] and Oreg *et al.* [145], namely

- strong SOC, as found e.g. in the semiconductors InAs [150] and InSb [151]
- Zeeman splitting caused by an external magnetic field
- s-wave singlet pairing, which can be induced by proximity to a conventional SC

Starting from a ballistic 1D system, the effect of these ingredients is as follows (see also Fig. 5.2): by SOC the spin degeneracy is lifted. The dispersion relation is thus split in two branches with different helicity which intersect at $k = 0$. A gap between the branches is then introduced by the Zeeman field. This allows to project out the higher-energy branch. The remaining system is effectively spinless, solving problem (i). Finally, the induced s-wave pairing restricted to that spinless system is transformed into an effective gap with p-wave symmetry by the SOC, which solves problem (ii).

---

[41] Kitaev [137] had already insinuated this option in a footnote.

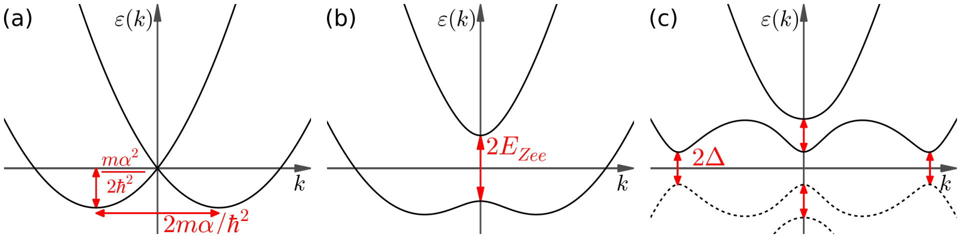

Figure 5.2: Schematic band structure of the Majorana nanowire as the three key effects are subsequently added: (a) SOC of strength α, (b) Zeeman splitting E_{Zee}, (c) s-wave SC gap Δ. The parameters are unrealistic in this plot for better visibility ($\alpha = 1.2$, $E_{\mathrm{Zee}} = 0.6$, $\Delta = 0.3$ in dimensionless units where $m = 1$ and $\hbar = 1$).

5.4.1 Model

To be precise, the wire, which we choose to be aligned along the x axis, is described by the BdG Hamiltonian Eq. (5.2) with

$$\xi(k) = \left(\frac{\hbar^2 k^2}{2m} - \mu\right) \mathbb{1}_{2\times 2} + \alpha k \sigma_z + \frac{1}{2} g \mu_B \mathbf{B} \cdot \boldsymbol{\sigma}, \tag{5.13}$$

$$\Delta(k) = -i\Delta\sigma_y, \tag{5.14}$$

where m is the effective mass, μ the chemical potential, α the SOC strength (the SOC field is along the z axis), $\frac{1}{2} g\mu_B |\mathbf{B}|$ equals the Zeeman energy E_{Zee}, with Bohr's magneton μ_B and a g-factor that can be up to ≈ 50 in the mentioned semiconductors [152,153], and the proximity-induced s-wave gap Δ. In spherical coordinates, we write the magnetic field as $\mathbf{B} = B(\cos\varphi \sin\vartheta, \sin\varphi \sin\vartheta, \cos\vartheta)^{\mathrm{T}}$.

If the Hamiltonian is diagonalized at $\Delta = 0$, the eigenenergies are

$$\varepsilon_{\rho,\tau}(k) = \rho \left(\frac{\hbar^2 k^2}{2m} - \mu\right) + \tau \sqrt{E_{\mathrm{Zee}}^2 + (\alpha k)^2 + 2\rho\alpha k E_{\mathrm{Zee}} \cos\vartheta} \tag{5.15}$$

with $\rho, \tau = \pm 1$. Superconductivity can be introduced subsequently in the eigenbasis, where the matrix elements of the gap correspond to the intraband pairing in both the high- and the low-energy band, and an interband pairing [147]. When the Hamiltonian is projected onto the low-energy bands, only the respective intraband pairing remains. This effective SC order parameter of the spinless model satisfies $\Delta_{\text{eff}}(k) = -\Delta_{\text{eff}}(-k)$ and[42]

$$|\Delta_{\text{eff}}(k)|^2 = \frac{\Delta^2}{2}\left[1 - \frac{E_{\text{Zee}}^2 - (\alpha k)^2}{\sqrt{\left[E_{\text{Zee}}^2 + (\alpha k)^2\right]^2 - 4(\alpha k)^2 E_{\text{Zee}}^2 \cos^2\vartheta}}\right]. \quad (5.16)$$

Thus, the system is indeed a realization of a 1D spinless p-wave SC as described by the Kitaev chain.

Now we retrieve the topological criterion for the semiconductor nanowire [144, 145]. As for the Kitaev chain, the transition from the trivial to the topological phase happens when the bulk energy gap closes at $k = 0$. Instead of deriving the gap closure from the projected spinless model, which is quite cumbersome in its explicit form, one can instead use the full model Hamiltonian given by Eqs. (5.13) and (5.14). At $k = 0$, the splittings induced by Δ and E_{Zee} compete (compare with Fig. 5.2). Indeed, band inversion appears when the applied magnetic field is large enough to overcome the superconducting gap. This is already the complete answer if $\mu = 0$, otherwise the condition for the topological phase is [144, 145]

$$E_{\text{Zee}} > \sqrt{|\Delta|^2 + \mu^2}, \quad (5.17)$$

and exponentially localized MZMs at the wire ends can be derived if the model is restricted to a finite length [144, 145].

5.4.2 Experimental signatures

Before we proceed to the results of Paper [4], we make some remarks about the experimental signatures by which the existence of MZMs in the topological phase can be verified. There are two main effects: a junction of a topological wire and a normal lead will show perfect Andreev reflection [154] at zero bias if a zero-energy mode is present [146, 155, 156]. This leads to a zero-bias conductance peak (ZBCP) in the differential conductance spectrum of the junction. Perfect Andreev

---

[42] The expression Eq. (5.16) reduces to the one given in [147] if θ is set to $\pi/2$.

reflection implies that the ZBCP should have the quantized value of $2e^2/h$. The second effect is the 4π Josephson effect [144, 148, 157], where the periodicity of the Josephson effect [158] is doubled by the MZMs in a topological-normal-topological wire junction.

Here we focus on the ZBCP, which has been reported in several experiments, e.g. [159–165], starting in 2012 [159]. These measurements have confirmed that a ZBCP is only present above the predicted critical magnetic field strength in Eq. (5.17). However, the quantized value of the peak was not reached. It has also been criticized that a ZBCP could be caused by other effects as well, e.g. the Kondo effect [166]. After the initial experiments, an enormous amount of work has been published in order to suggest solutions to these issues based on more comprehensive theoretical models. Such models include, among others, finite size and temperature effects [167, 168], effects of the finite cross section of the wire [169–171], an explicit treatment of the superconducting proximity effect [172, 173], disorder [172, 174], and interactions in the wire [175]. By now, the existence of MZM in semiconductor Majorana nanowires has become a widely accepted fact.

On the other hand, conclusive evidence of the zero-energy modes being non-Abelian Majorana modes is still pending. This would demand braiding experiments where the MZMs can be moved in a controlled manner, which is much more challenging than conductance spectroscopy. The same technological level would be necessary for further advances towards topological qubits and finally topological quantum computation [138, 176].

5.4.3 Tilting of the magnetic field

The appearance of MZMs requires not only a sufficient strength of the magnetic field, but also a suitable direction of the field. The commonly assumed case is that the magnetic field is applied exactly orthogonal to the SOC field ($\vartheta = \pi/2$). There will always be some uncertainty in experiments, though. For instance, by the presence of the bulk s-wave SC the magnetic field can be locally deflected because of the Meissner effect. It is therefore interesting to ask how stable the topological phase is towards changes in the field direction. In addition, the field can be rotated purposefully to check if signatures of the MZMs are restricted to the topological phase, which provides a valuable sanity check for the origin of these signatures. The ZBCP has been measured as a function of the field direction e.g. in [159, 165, 177]. The impact of the field direction on the emergence of MZMs and the ZBCP was the main objective of Paper [4]. Here, we summarize the main findings. Previously, the direction of the magnetic field had been considered numerically in [178] and briefly in [167].

The effect of tilting the magnetic field away from $\vartheta = \pi/2$ is to skew the band structure, which is displayed in Fig. 5.3. Varying the second angle, φ, has no influence on the eigenenergies, but only adds a phase factor to the eigenstates. While the energy spectrum at $k = 0$ is unaffected, the energy gap at approximately the Fermi momentum[43] k_F closes indirectly when the tilting angle reaches a critical value ϑ_c. Thus, if the field is tilted further than ϑ_c, there will be partially filled bands. In terms of band theory, this case resembles a "metal" rather than an "insulator" (in reality it is, of course, still a SC) and the system can no longer be topological. This is different from the transition into a trivial gapped state as when Eq. (5.17) is violated. Instead, the wire becomes trivial in the sense that any topological invariant becomes ill-defined as the concept of adiabatic variation of parameters breaks down. The MZMs at the ends of the wire are absorbed into bulk bands when those reach zero energy and the two MZMs recombine into an ordinary fermion.

The critical angle ϑ_c can be calculated analytically from the model presented in Section 5.4.1. In the paper, the condition $\varepsilon(k) = 0$ for the gap closure is resolved by a graphical discussion of the characteristic polynomial of the BdG Hamiltonian with the result that the wire is in the topological regime if

$$|\cos\vartheta| < \frac{\Delta}{E_{\text{Zee}}} \tag{5.18}$$

in addition to Eq. (5.17). This agrees with the numerical results found in [178] and was also confirmed in later work [179]. The critical angle can also be calculated rigorously, which we briefly sketch here as it

---

[43] k_F in the absence of superconductivity

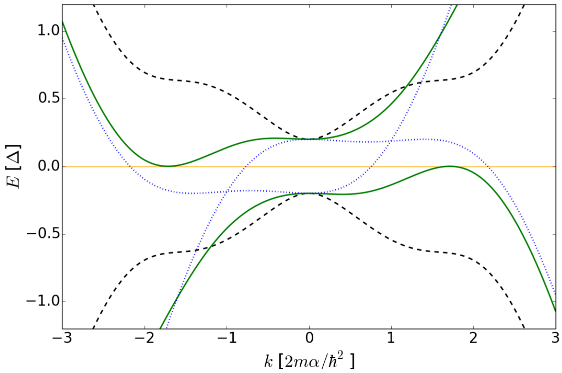

Figure 5.3: Low-energy band structure of the Majorana wire with tilted magnetic field at $\vartheta = \pi/2$ (black dashed line), $\vartheta = \vartheta_c$ (green solid line), and $\vartheta = \pi$ (blue dotted line).

is not further explained in the paper. The characteristic polynomial p at zero energy is bi-quartic in momentum, meaning that $p(\varkappa)$ is of order four with $\varkappa = k^2$. We know that exactly at ϑ_c the low energy bands touch zero energy with a local extremum, which automatically becomes a zero of $p(k)$ with double multiplicity. As there are two such points at (approximately) $\pm k_F$, $p(\varkappa)$ will also have a multiple root. A quartic polynomial has a multiple root if and only if its discriminant is zero [180]. It turns out that the discriminant is a quartic polynomial of $\cos\vartheta$. The general solution formula for quartic polynomials [181] then leads to the solution. Explicit expressions for the characteristic polynomial and the discriminant are given in Appendix C.

The result Eq. (5.18) is perhaps unintuitive. One may have expected that only the component of the magnetic field orthogonal to the SOC field matters for the topological phase. In that case, tilting the field would have no consequence as long as the orthogonal component remains large enough to satisfy Eq. (5.17). Then one could reach the topological phase for any field direction (except if $\mathbf{B}$ is exactly parallel to the SOC field) if B is just large enough. The result in Eq. (5.18) demonstrates that this intuitive reasoning is incorrect. In contrast, the stronger the applied field, the narrower becomes the allowed range of angles. The condition Eq. (5.17), on the other hand, always contains the full field and not just a certain component, because the field direction does not matter at $k = 0$. For practical purposes, the condition on the field direction implies that the magnetic field should be just as large as required by Eq. (5.18), but not too much larger than that if one wants the topological phase to be stable for a broad range of field orientations.

Having derived the desired condition, one can also study the behavior of the ZBCP as ϑ is varied from $\pi/2$ to π, thereby crossing ϑ_c. This is done for a junction of a normal lead ($x < 0$) with the Majorana wire ($x > 0$) with an intermediate delta-shaped tunnel barrier of strength V. Both sides of the junction can be described by the same BdG Hamiltonian with the spatially dependend gap $\Delta(x) = \Delta\Theta(x)$. In the paper, the differential conductance is calculated using a slightly generalized[44] Blonder-Tinkham-Klapwijk (BTK) formalism [182] at $T = 0$.

For a certain electric bias, the available states at that energy on both sides of the junction, including evanescent solutions with complex k, can be obtained by diagonalizing the BdG Hamiltonian. These solutions are then sorted by their group velocity $\propto \partial\varepsilon(k)/\partial k$ into incident and outgoing waves. Considering electrons impinging from the normal side, the following scattering processes [182] produce outgoing waves:

1. Andreev reflection [154], where an incident electron forms a Cooper pair with another electron upon entry into the SC. Conservation of charge requires a hole to be reflected into the normal lead.
2. Ordinary reflection of electrons at the junction
3. Ordinary transmission of electrons across the junction
4. Extraordinary transmission, whereby the sign of k changes

The resulting wavefunction $\Psi(x)$ is obtained by summation of the incident and all outgoing wavefunctions with coefficients a_i, b_i, c_i, d_i corresponding to the processes 1–4, respectively ($i = 1, 2$ denotes the spin degree of freedom). The coefficients follow from the continuity of the wavefunction at the junction and the condition that the derivative has a finite step proportional to the tunnel barrier. This is a linear

---

[44] to include spin and the effect of SOC

system of 8 equations from which lengthy analytical expressions could be derived. In the paper, this system of equations is instead solved numerically (with exact results).

The electric current caused by the four processes above is proportional to their respective probability currents. The probability current J must satisfy the continuity equation $\nabla J = -\partial_t \rho$, with the probability density ρ, where the Schrödinger equation [37] demands

$$\begin{aligned} \partial_t \rho &= \partial_t(\Psi^\dagger \Psi) = \left(\partial_t \Psi^\dagger\right) \Psi + \Psi^\dagger \left(\partial_t \Psi\right) \\ &= \frac{1}{i\hbar}\Big[-\left(H\Psi\right)^\dagger \Psi + \Psi^\dagger \left(H\Psi\right)\Big]. \end{aligned} \tag{5.19}$$

While the ballistic Hamiltonian $H = -\hbar^2 \nabla^2 \tau_z / 2m$ leads to the well known probability current[45]

$$J_{\text{normal}} = \frac{\hbar}{m} \mathfrak{Im}\left(\Psi^\dagger \nabla \tau_z \Psi\right), \tag{5.20}$$

the presence of SOC, $H_{\text{SOC}} = -i\alpha \nabla \sigma_z$, gives rise to the extra term

$$J_{\text{SOC}} = \frac{\alpha}{\hbar} \Psi^\dagger \sigma_z \Psi. \tag{5.21}$$

The magnetic field does not contribute to J as the system is one-dimensional. Once the scattering coefficients $a_i, \ldots, d_i$ are known, the scattering probabilities $A_i, \ldots, D_i$ are given by the incident probability current J_{in} and the probability currents $J_{a_i}, \ldots, J_{d_i}$ of the outgoing waves as the ratio $A_i = J_{a_i}/J_{\text{in}}$, and so on. The BTK formula [182] finally gives the differential conductance

$$\frac{dI}{dE} = \frac{e^2}{h}\left[1 + \sum_{i=1,2} \left(A_i - B_i\right)\right] \tag{5.22}$$

The result is displayed in Fig. 5.4 for various orientations of the magnetic field. As the critical angle is approached, the ZBCP gets very sharp and disappears at the transition, where it splits in two small peaks at finite energies. As long as the wire is in the topological regime,

---

[45] Here with an additional Pauli matrix τ_z in particle-hole space as we work in the BdG formalism

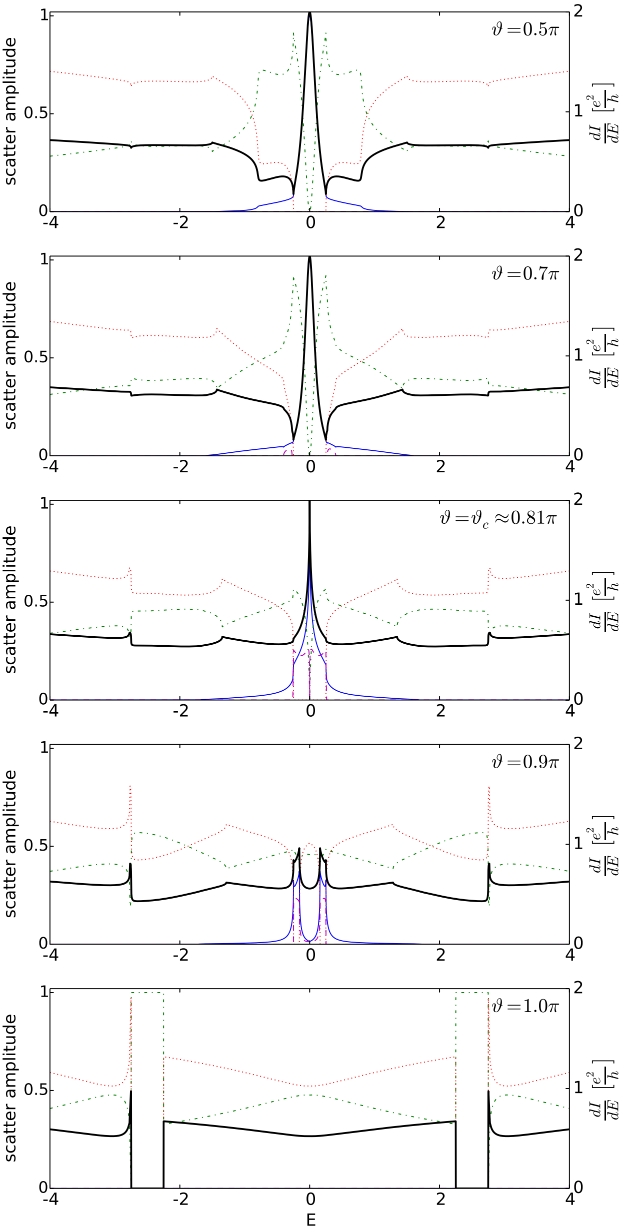

Figure 5.4: Differential conductance (black) and BTK amplitudes A (blue), B (green), C (red), and D (purple) for different ϑ with dimensionless parameters $E_{\mathrm{Zee}} = 1.5$, $\Delta = 1.25$, $\mu = 0$, $\alpha = 1/\sqrt{2}$. From [4].

the results reproduce the expected quantized peak value of $2e^2/h$, independent of the tunnel barrier strength. In contrast, the residual zero-bias conductance in the trivial regime can always be surpressed by increasing V. This is suggested in the paper as an experimental way to test the topological phase.

5.5 Nodal noncentrosymmetric superconductors

In this section, we introduce NCSs [183–186], which are the topic of Paper [5]. Such SCs have unusual gaps and exhibit interesting topological features, although they are not TSCs in the same sense as the p-wave SCs in 1D and 2D. The key difference is that NCSs (and, more generally, all nodal SCs [9,187]) are not fully gapped in the bulk, hence the usual topological invariants of SPT phases cannot be defined. The following two subsections provide a brief explanation of the characteristic properties of NCSs, mainly based on [9]. Finally, the results of Paper [5] are presented.

5.5.1 Singlet-triplet mixing

In a noncentrosymmetric SC, the crystal structure lacks inversion symmetry. Intrinsic electric crystal fields can occur by the displacement of atoms compared to the inversion symmetric unit cell. As an example, the crystal structure of $CePt_3Si$ is displayed in Fig. 5.5, which was the first NSC to be discovered [188, 189]. As a consequence of the electric field, noncentrosymmetric SCs generically exhibit strong SOC [9]. In addition, without a center of inversion, parity is not a good quantum number. Therefore, the superconducting pairing can have both singlet (even parity) and triplet (odd parity) components without violating the overall symmetry requirements of fermionic wavefunctions.

The normal-state dispersion block in the BdG Hamiltonian Eq. (5.2) takes the general form

$$\xi(\mathbf{k}) = \xi_0(\mathbf{k}) + \alpha \mathbf{l} \cdot \sigma, \tag{5.23}$$

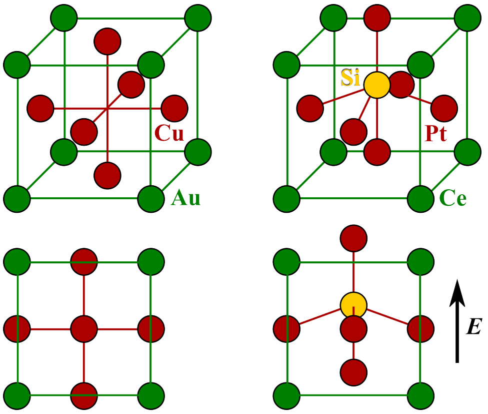

Figure 5.5: Schematic crystal structure of the centrosymmetric $AuCu_3$ lattice (left) and the noncentrosymmetric SC $CePt_3Si$ [188] (right) in 3D (top) and front view (bottom) of a unit cell. The additional atom with pyramidal coordination causes a displacement along one axis, leading to an electric field $\mathbf{E}$. The tetrahedral distortion in $CePt_3Si$ is not shown for better comparability.

where $\xi_0(\mathbf{k})$ denotes all spin-independent terms and the second term describes SOC with strength α and a vector $\mathbf{l}$ that depends on the direction of the field $\mathbf{E}$ in the crystal. The gap $\Delta(\mathbf{k})$ keeps the form of Eq. (5.3) with both $\delta_{\text{singlet}}(\mathbf{k})$ and $\boldsymbol{\delta}_{\text{triplet}}(\mathbf{k})$ being nonzero to account for the mixing of singlet and triplet pairing. A slight simplification arises from the fact that the free energy is minimized by the alignment of the triplet-pairing vector $\boldsymbol{\delta}_{\text{triplet}}$ with the SOC vector $\mathbf{l}$ if interband pairing is absent [190], thus at equilibrium one may write

$$\Delta(\mathbf{k}) = [\delta_{\text{singlet}}(\mathbf{k}) + \delta_{\text{triplet}}(\mathbf{k})\mathbf{l} \cdot \boldsymbol{\sigma}]\ i\sigma_y. \tag{5.24}$$

For instance, $CePt_3Si$ has an s+p-wave gap [189]. The typical scenario is that the coexistence of gaps with different parity leads to line nodes of the gap on the 3D Fermi surface. This feature becomes most pronounced when δ_{singlet} and δ_{triplet} are of comparable size [185]. The BdG Hamiltonian of NCSs has all TRS, PHS, and chiral symmetry and belongs to class DIII, but in the absence of a full gap the periodic table does not apply.

5.5.2 Topology with a nodal gap

Apart from engineered p-wave superconductivity in heterostructures like the Majorana nanowires, TSCs with a full bulk energy gap are very rare. However, far more unconventional (i.e., not s-wave) SCs are known which have nodal gaps. Nodal SCs comprise, apart from NCSs, the famous high-temperature cuprate $d_{x^2-y^2}$-wave SCs [191,192], some Uranium compounds, e.g. f-wave UPt$_3$ [193,194], and many others [9]. In general, nodal SCs can have point or line nodes on the Fermi surface. It turns out that nodal SCs (and other systems with nodal gaps) can be topologically characterized despite the lack of an energy gap in the bulk. We will only consider the case line nodes, which is relevant for the NCSs.

The key idea is to apply the concepts known from the SPT phases to a lower-dimensional[46] Hamiltonian that is restricted to an intersection of the 3D BZ in which no nodes appear. When the gap has line nodes, one can fix two components $(k_i, k_j) \equiv \mathbf{k}_{\shortparallel}$ of the momentum and think of them as parameters. The remaining dimension along $k_\perp$ corresponds to a line running through the 3D BZ, and the restricted BdG Hamiltonian $\mathcal{H}_{\mathbf{k}_\parallel}(k_\perp)$ describes this 1D system. For almost all choices of $\mathbf{k}_{\shortparallel}$ the line will not intersect with the nodes of the gap, thus $\mathcal{H}_{\mathbf{k}_\parallel}(k_\perp)$ is fully gapped and may have a nontrivial band structure. The price of this procedure is that the 1D Hamiltonian loses TRS and PHS, because for a momentum $\mathbf{k}$ belonging to the restricted system, the symmetry-related point $-\mathbf{k}$ will in general not have the same $\mathbf{k}_{\shortparallel}$. Nevertheless, chiral symmetry persists and the 1D Hamiltonian is therefore in class AIII, where a $\mathbb{Z}$ winding number can be defined [9]. As $\mathbf{k}_{\shortparallel}$ is varied, any topological invariant of $\mathcal{H}_{\mathbf{k}_\parallel}(k_\perp)$ can only change when the 1D cut through the BZ crosses a nodal line. In consequence, in the 2D BZ of $\mathbf{k}_{\shortparallel}$, regions where $\mathcal{H}_{\mathbf{k}_\parallel}(k_\perp)$ is in a different topological phase are separated from each other by the projections of the nodal lines onto the 2D BZ. This is illustrated in Fig. 5.6.

Nontrivial topology within the bounded areas A_n formed by the projections of the nodal lines implies the existence of MZMs at the ends of the 1D system via the bulk-boundary correspondence, similar

---

[46] This dimension is $\delta = D - d - 1$ in a system with D spatial dimensions and d-dimensional nodes [16].

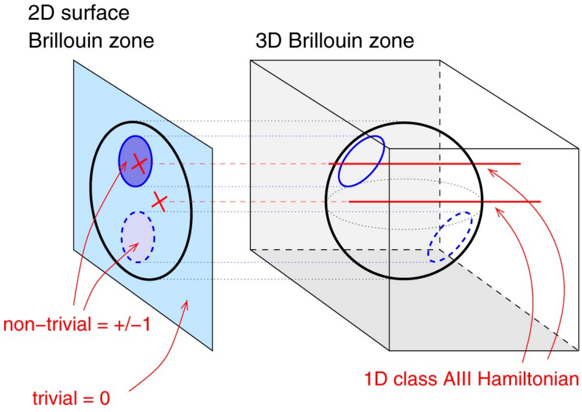

Figure 5.6: Projection of the bulk FS on the surface BZ. For surface momenta inside the projection of the line nodes (blue circles), nontrivial topology is found in the corresponding 1D Hamiltonian (visualized by the red lines). This leads to topology-protected MZMs at the surface for these momenta. Adopted from Schnyder and Brydon [9] (published under Creative Commons Attribution 3.0 licence).

to the previously discussed Majorana nanowires. Thus, on surfaces of the 3D sample that are orthogonal to the direction of $k_\perp$, MZMs are found everywhere within A_n in the surface BZ. In other words, zero-energy Majorana flat bands are formed. Evidently the projection crucially depends on the direction in which $k_\perp$ is chosen. By rotation of the projection axis, one can shrink the two highlighted projection areas in Fig. 5.6 to zero. This means that the Majorana flat bands will only be present on surfaces with proper crystallographic orientation.

Strictly dispersionless bands are a special feature, because usually the free energy can be reduced by adding (at least weak) dispersion to such bands, hence lifting the high degeneracy of states. In NCSs, the flat bands are protected by topology and cannot become dispersive unless (i) the gap closes or (ii) symmetry breaking occurs at the surface. For instance, if TRS is broken by proximity to a FMI, the surface states become chirally dispersive [195].

5.5.3 Surface instability

It turns out that, at sufficiently low temperatures, TRS can also be broken spontaneously at the topological surfaces. This is the main message of Paper [5]. Alterations of the bulk properties close to the surface are not captured by the BdG Hamiltonian as introduced in Section 5.1, where spatially uniform parameters have implicitly been assumed. In particular, it is known that the superconducting gap can be modified – in both amplitude and symmetry – close to surfaces or edges [196, 197]. The reason is, roughly speaking, that there are less electrons that participate in the pairing interaction close to a boundary. TRS-breaking surface phases have, for instance, been predicted [198] and observed [199] in certain cuprates. TRS breaking can also be favored by further interactions in addition to the pairing interaction [200]. Such studies had not been undertaken for NCSs, which motivated the work of Paper [5].

To be able to properly account for the surfaces, the NCS is considered on a lattice in slab geometry, where the Hamiltonian is transformed to a real space in one dimension as $k_\perp$ is no good quantum number. Specifically, a square lattice with (101) surfaces is considered, which is a suitable choice to obtain regions with MZMs in the surface BZ for an $s + p$ wave NCS. Instead of introducing a uniform mean-field superconducting gap, the singlet and triplet components are calculated self-consistently, starting from the attractive on-site and nearest-neighbor[47] interactions

$$H_{\text{int}} = -U_s \sum_j c^\dagger_{j,\uparrow} c^\dagger_{j,\downarrow} c_{j,\downarrow} c_{j,\uparrow} - U_t \sum_{<i,j>} \sum_{s,s'=\uparrow,\downarrow} c^\dagger_{i,s} c^\dagger_{j,s'} c_{j,s'} c_{i,s}. \tag{5.25}$$

This interaction gives rise to pairing with the singlet order parameter

$$\Delta^s_j = \frac{U_s}{2} \left\langle c_j^{\mathrm{T}} i\sigma_y c_j \right\rangle, \tag{5.26}$$

where $c_j = (c_{j,\uparrow}, c_{j,\downarrow})^{\mathrm{T}}$, and the triplet order parameter

$$\Delta^t_{i,j} = iU_t \left\langle c_j^{\mathrm{T}} i\sigma_y \boldsymbol{\sigma} c_i \right\rangle. \tag{5.27}$$

---

[47] Restricted to the plane orthogonal to the SOC field, such that the triplet order parameter will be aligned with **l**, cf. Eq. (5.24).

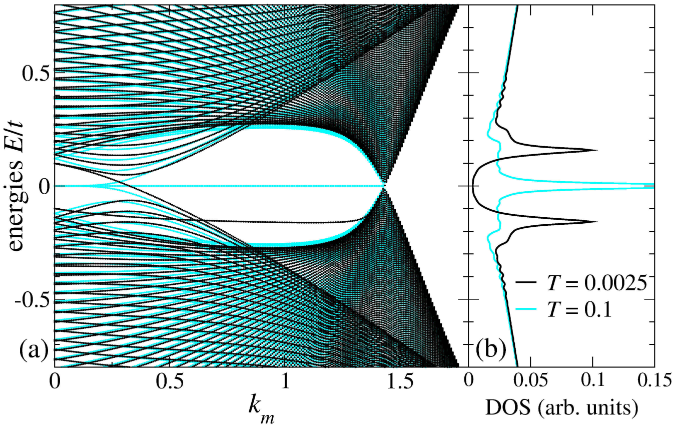

Figure 5.7: (a) Dispersion along a line cut (labeled k_m) through the (101) surface BZ and (b) density of states of the $s + p$ wave NCS considered in Paper [5]. At $T > T_c$ (light blue), TRS is preserved in the entire system and a Majorana zero-energy flat band of surface states exists for a range of momenta. At $T < T_c$ (black), TRS is broken at the surface, the surface band is shifted to finite energies and is weakly dispersive. Figure taken from [5].

Note that this calculation is done at finite temperature, in contrast to the other Papers [1–4]. The thermal average is written as $\langle \ldots \rangle$. The values of U_s and U_t are chosen such that the nodal structure of the corresponding gaps in an infinitely extended system (where uniform gaps can be assumed) would yield regions with Majorana flat bands of a decent extent in the 2D BZ.

For the slab of finite thickness, the gaps as a function of the spatial coordinate are then computed numerically by minimizing the free energy with an iterative algorithm. Details are found in the Supplemental material of Paper [5]. The result is that both the singlet and the triplet gap are indeed altered in proximity to the surfaces of the slab:

1. The amplitude of the singlet gap is enhanced, while the amplitude of the triplet gap is reduced compared to the bulk value.

2. In addition, all gap components develop a complex phase relative

to each other and to the bulk values if the temperature is below a critical value T_c.

While it is not surprising that the strength of the pairing is influenced by a surface, the second result signals the breaking of TRS. In the TRS-breaking phase, the flat bands are shifted from zero energy and acquire a weak dispersion. This lifts the high degeneracy and removes the zero-energy peak in the density of states, see Fig. 5.7. At finite energies the surface states are no longer Majorana modes. Furthermore, the TRS-broken phase is accompanied by emergent spin currents at the surface.

The critical temperature T_c below which the symmetry-breaking sets in is much lower than the superconducting transition temperature (at least for the parameters chosen in the paper). Thus, this work suggests that Majorana flat bands are present over a broad range of temperatures, while spontaneous breaking of TRS becomes energetically favorable at very low temperatures. A recent study [201] proposes that TRS breaking may even occur in the bulk.

Appendix A

2D Fourier transformation of the $1/r$-potential

Here, we show how the 3D r^{-1} potential is transformed into momentum space in the two in-plane dimensions. We make use of the general relation

$$\frac{1}{a^b} = \frac{1}{\Gamma(b)} \int_0^\infty \mathrm{d}x \, x^{b-1} e^{-ax} \tag{A.1}$$

which directly follows from the definition of the Γ-funtion. Applying this relation in the Fourier transformation (FT) with $a = \mathbf{r}^2$ and $b = \frac{1}{2}$, we get

$$\begin{aligned}
\int \mathrm{d}^2 r \frac{e^{-i\mathbf{k}\cdot\mathbf{r}}}{|\mathbf{r}|} &= \frac{1}{\Gamma\left(\frac{1}{2}\right)} \int_0^\infty \frac{\mathrm{d}\tau}{\sqrt{\tau}} \underbrace{\int \mathrm{d}^2 r \, e^{-\tau\mathbf{r}^2 - i\mathbf{k}\cdot\mathbf{r}}}_{=\frac{\pi}{\tau} e^{-\mathbf{k}^2/4\tau}} \\
&= \frac{\pi}{\Gamma\left(\frac{1}{2}\right)} \frac{2}{|\mathbf{k}|} \underbrace{\int_0^\infty \frac{\mathrm{d}u}{\sqrt{u}} e^{-u}}_{=\Gamma(1/2)} \\
&= \frac{2\pi}{|\mathbf{k}|},
\end{aligned} \tag{A.2}$$

where we substituted $u = \mathbf{k}^2/4\tau$ in the second line.

In Paper [2], we also need the transformation of the Coulomb potential acting between parallel planes of distance d (assuming $d > 0$ for simplicity). Then $|\mathbf{r}|^{-1}$ is replaced by $\left(\mathbf{r}^2 + d^2\right)^{-1/2}$. We use again

Eq. (A.1) with $a = \mathbf{r}^2 + d^2$ and $b = \frac{1}{2}$, leading to

$$\begin{aligned}
\int \mathrm{d}^2 r \frac{e^{-i\mathbf{k}\cdot\mathbf{r}}}{\sqrt{\mathbf{r}^2+d^2}} &= \frac{1}{\Gamma\left(\frac{1}{2}\right)} \int_0^\infty \frac{\mathrm{d}\tau}{\sqrt{\tau}} \int \mathrm{d}^2 r\, e^{-(\mathbf{r}^2+d^2)\tau - i\mathbf{k}\cdot\mathbf{r}} \\
&= \sqrt{\pi}\int_0^\infty \frac{\mathrm{d}\tau}{\tau^{3/2}} e^{-\left(\frac{\mathbf{k}^2}{4\tau}+d^2\tau\right)} \\
&\overset{t^2=\tau}{=} 2\sqrt{\pi}\int_0^\infty \mathrm{d}t\, \frac{e^{-\mathbf{k}^2/4t^2}}{t^3} t e^{-d^2t^2} \\
&= -\frac{4\sqrt{\pi}}{\mathbf{k}^2}\int_0^\infty \mathrm{d}t \left(1-2d^2t^2\right) e^{-\left(\frac{|\mathbf{k}|}{2t}-dt\right)^2} e^{-|\mathbf{k}|d}. \qquad \text{(A.3)}
\end{aligned}$$

The integral becomes Gaussian with the brute-force substitution $u = \frac{|\mathbf{k}|}{2t} - dt$ which yields

$$\begin{aligned}
t^2 &= \frac{u^2}{2d^2} + \frac{|\mathbf{k}|}{2d} - \frac{u}{d}\sqrt{\frac{u^2}{4d^2}+\frac{|\mathbf{k}|}{2d}} \qquad \text{(A.4)} \\
\mathrm{d}t &= \left(-\frac{1}{2d} + \frac{u}{4d^2\sqrt{\frac{u^2}{4d^2}+\frac{|\mathbf{k}|}{2d}}}\right)\mathrm{d}u. \qquad \text{(A.5)}
\end{aligned}$$

Now we split the integral in two parts corresponding to the two addends in the term $(1-2d^2t^2)$. The first part is

$$-\frac{4\sqrt{\pi}e^{-|\mathbf{k}|d}}{\mathbf{k}^2}\int_{\infty}^{-\infty} \mathrm{d}u \left(-\frac{1}{2d} + \text{odd in } u\right) e^{-u^2} = -\frac{2\pi}{d\mathbf{k}^2}e^{-|\mathbf{k}|d}, \qquad \text{(A.6)}$$

while the second one is a little more lengthy:

$$\begin{aligned}
&-\frac{4\sqrt{\pi}e^{-|\mathbf{k}|d}}{\mathbf{k}^2}\int_{-\infty}^{\infty} \mathrm{d}u\; 2d^2 \left[-\frac{1}{2d}\left(\frac{u^2}{2d^2}+\frac{|\mathbf{k}|}{2d}\right) - \frac{u^2}{4d^3} + \text{odd in } u\right] e^{-u^2} \\
&= \frac{4\sqrt{\pi}}{\mathbf{k}^2}e^{-|\mathbf{k}|d}\frac{|\mathbf{k}|}{2}\sqrt{\pi} + \frac{4\sqrt{\pi}}{d\mathbf{k}^2}e^{-|\mathbf{k}|d}\int_{-\infty}^{\infty}\mathrm{d}u\, u^2 e^{-u^2} \\
&= \frac{2\pi}{|\mathbf{k}|}e^{-|\mathbf{k}|d} + \frac{4\sqrt{\pi}}{d\mathbf{k}^2}e^{-|\mathbf{k}|d}\frac{\sqrt{\pi}}{2}. \qquad \text{(A.7)}
\end{aligned}$$

The second term cancels Eq. (A.6). In total, the result is

$$\int \mathrm{d}^2 r \frac{e^{-i\mathbf{k}\cdot\mathbf{r}}}{\sqrt{\mathbf{r}^2+d^2}} = \frac{2\pi}{|\mathbf{k}|}\, e^{-|\mathbf{k}|d} \qquad \text{(A.8)}$$

and is identical to the solution Eq. (A.2) in the limit $d \to 0$.

Appendix B

Integrating out the fermions

This appendix explicitly shows how the fermions are integrated out from the Lagrangian

$$\mathcal{L} = \overline{\Psi}\left(i\not{\partial} + m_\Psi\right)\Psi + J\overline{\Psi}\left(\tilde{m}_z - \not{\phi}\right)\Psi \tag{B.1}$$

The first part contains the mean-field terms, the second part contains the fluctuations. For further clarification of the quantities, see the main text in Section 4.2. Some steps of the calculation are also found in the appendix of Paper [1]. The integration methods applied here are adopted from quantum field theory [202]. Performing the Gaussian integral in the partition function in the standard way [111], one finds the action

$$\begin{aligned} S &= \mathrm{Tr}\ln\left[i\not{\partial} + m_\Psi + J(\tilde{m}_z - \not{\phi})\right] \\ &= S_{\mathrm{MF}} + \mathrm{Tr}\left[GJ(\tilde{m}_z - \not{\phi}) - \frac{1}{2}GJ(\tilde{m}_z - \not{\phi})GJ(\tilde{m}_z - \not{\phi}) + \ldots\right] \end{aligned} \tag{B.2}$$

whereby the first term in the square brackets vanishes close to the mean-field solution. The propagator is

$$G = (i\not{\partial} + m_\Psi)^{-1} = \frac{-i\not{\partial} + m_\Psi}{\partial^2 + m_\Psi^2} \tag{B.3}$$

and we have used the abbreviated notation

$$\mathrm{Tr}(\ldots) = \int \mathrm{d}t \int \mathrm{d}^2x \sum_\nu \langle \nu | \mathrm{tr}(\ldots) | \nu \rangle. \tag{B.4}$$

The small trace symbol is the ordinary matrix trace and ν runs over all other quantum numbers. In the plane-wave basis, $\nu = (\omega, \mathbf{k})$. In the following, we will evaluate the fluctuations δS to leading order and at $T = 0$.

Switching from Minkowski to Euclidean space by a Wick rotation $\tau = it$ [202], we find $\partial^2 \to -\partial^2$ and $i\not\partial \to -\not\partial$. Notice that the (2+1)D Euclidean γ-matrices are $(\sigma_z, \sigma_x, \sigma_y)$. To leave $\not{a}$ invariant, we have to transform a into the Euclidean vector $(a_0, ia_1, ia_2) \equiv \alpha$, hence $\not{a} \to \not{\alpha}$. Furthermore, the FT to reciprocal space is done, where we use the notation $\varkappa = \omega, \mathbf{k}$ and $\lambda = \Omega, \mathbf{q}$ with frequencies ω, Ω and momenta $\mathbf{k}, \mathbf{q}$. Then

$$\begin{aligned}&\delta S = \\ &\frac{iJ^2}{2}\int\frac{\mathrm{d}^3\varkappa}{(2\pi)^3}\int\frac{\mathrm{d}^3\lambda}{(2\pi)^3}\frac{1}{(\varkappa^2+m_\Psi^2)((\varkappa-\lambda)^2+m_\Psi^2)} \\ &\mathrm{tr}\left[(m_\Psi + i\not\varkappa)(-\not\alpha(\lambda)+\tilde{m}_z(\lambda))(m_\Psi + i(\not\varkappa-\not\lambda))(-\not\alpha(-\lambda)+\tilde{m}_z(-\lambda))\right]\end{aligned} \tag{B.5}$$

The matrix structure of the terms inside the trace is completely encoded by the Euclidean γ-matrices, for which [202]

$$\mathrm{tr}(\gamma^\mu\gamma^\nu) = 2\delta_{\mu\nu} \tag{B.6}$$

$$\mathrm{tr}(\gamma^\mu\gamma^\nu\gamma^\lambda) = 2i\varepsilon_{\mu\nu\lambda} \tag{B.7}$$

$$\mathrm{tr}(\gamma^\mu\gamma^\nu\gamma^\lambda\gamma^\rho) = 2\delta_{\mu\nu}\delta_{\lambda\rho} - 2\delta_{\mu\lambda}\delta_{\nu\rho} + 2\delta_{\mu\rho}\delta_{\nu\lambda} \tag{B.8}$$

Multiplying out Eq. (B.5), one can arrange it into four terms that contain $\alpha^\mu(\lambda)\alpha_\nu(-\lambda)$, $\tilde{m}_z(\lambda)\tilde{m}_z(-\lambda)$, $\tilde{m}_z(\lambda)\alpha_\mu(-\lambda)$, and $\alpha_\mu(\lambda)\tilde{m}_z(-\lambda)$, respectively, and correspond to four Feynman diagrams. Viewing α as a wiggly line, $\tilde{m}_z$ as a slashed line, and fermions with solid lines as in Paper [1] and [2], we will now go through these four diagrams separately.

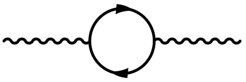 =

$$iJ^2\int\frac{\mathrm{d}^3\varkappa}{(2\pi)^3}\,\alpha_\mu(\lambda)\alpha_\nu(-\lambda)\left[\frac{\varepsilon_{\mu\rho\nu}m_\Psi\lambda_\rho}{(\varkappa^2+m_\Psi^2)((\varkappa-\lambda)^2+m_\Psi^2)} + M_{\mu\nu}(\lambda)\right] \tag{B.9}$$

where

$$M_{\mu\nu}(\lambda) = \frac{\delta_{\mu\nu}(m_\Psi^2 + \varkappa\cdot(\varkappa-\lambda)) - 2\varkappa_\mu\varkappa_\nu + \varkappa_\nu\lambda_\mu + \varkappa_\mu\lambda_\nu}{(\varkappa^2+m_\Psi^2)((\varkappa-\lambda)^2+m_\Psi^2)} \tag{B.10}$$

It is useful to prove that $\int \frac{\mathrm{d}^3\varkappa}{(2\pi)^3} M_{\mu\nu}(\lambda)$ is proportional to the operator of orthogonal projection along λ, $P_{\mu\nu}(\lambda)$, which has the defining property $\lambda_\mu P_{\mu\nu}(\lambda) = 0$:

$$\begin{aligned}
\lambda_\mu \int \frac{d^3\varkappa}{(2\pi)^3} & M_{\mu\nu}(\lambda) \\
&= \int \frac{d^3\varkappa}{(2\pi)^3} \frac{\lambda_\nu(m_\Psi^2 + \varkappa\cdot(\varkappa-\lambda)) - 2\lambda\cdot\varkappa\varkappa_\nu + \varkappa_\nu\lambda^2 + \lambda\cdot\varkappa\lambda_\nu}{(\varkappa^2+m_\Psi^2)((\varkappa-\lambda)^2+m_\Psi^2)} \\
&= \int \frac{d^3\varkappa}{(2\pi)^3} \frac{\lambda_\nu(m_\Psi^2+\varkappa^2) + \varkappa_\nu(-2\lambda\cdot\varkappa+\lambda^2)}{(\varkappa^2+m_\Psi^2)((\varkappa-\lambda)^2+m_\Psi^2)} \\
&= \int \frac{d^3\varkappa}{(2\pi)^3} \frac{\lambda_\nu}{(\varkappa-\lambda)^2+m_\Psi^2} + \int \frac{d^3\varkappa}{(2\pi)^3} \frac{\varkappa_\nu}{\varkappa^2+m_\Psi^2} \\
&\quad - \int \frac{d^3\varkappa}{(2\pi)^3} \frac{\varkappa_\nu}{(\varkappa-\lambda)^2+m_\Psi^2} \\
&= 0
\end{aligned} \tag{B.11}$$

where we used $-2\lambda\cdot\varkappa + \lambda^2 = (\varkappa-\lambda)^2 + m_\Psi^2 - (\varkappa^2+m_\Psi^2)$ and then shifted the coordinate $\varkappa \to \varkappa - \lambda$ in the last integral. Consequently, there is a scalar $S(\lambda)$ such that $\int \frac{\mathrm{d}^3\varkappa}{(2\pi)^3} M_{\mu\nu}(\lambda) = S(\lambda)P_{\mu\nu}(\lambda)$, where P has the standard form

$$P_{\mu\nu}(\lambda) = \delta_{\mu\nu} - \frac{\lambda_\mu\lambda_\nu}{\lambda^2}. \tag{B.12}$$

Hence

$$\mathrm{tr}\int \frac{\mathrm{d}^3\varkappa}{(2\pi)^3} M_{\mu\nu}(\lambda) = S(\lambda)\,\mathrm{tr}\,[P_{\mu\nu}(\lambda)] = 2S(\lambda), \tag{B.13}$$

and with Eq. (B.10) we obtain

$$S(\lambda) = \frac{1}{2}\int \frac{\mathrm{d}^3\varkappa}{(2\pi)^3} \frac{3m_\Psi^2 + \varkappa^2 - \varkappa\cdot\lambda}{(\varkappa^2+m_\Psi^2)[(\varkappa-\lambda)^2+m_\Psi^2]}. \tag{B.14}$$

With

$$\varkappa^2 - \varkappa \cdot \lambda = \frac{1}{2}[(\varkappa^2 + m_\Psi^2) + (\varkappa - \lambda)^2 + m_\Psi^2] - m_\Psi^2 - \frac{1}{2}\lambda^2 \tag{B.15}$$

and a shift $\varkappa \to \varkappa + \lambda$ in one term we can write

$$S(\lambda) = \left(m_\Psi^2 - \frac{\lambda^2}{4}\right) I(\lambda) + \frac{1}{2}\int \frac{d^3\varkappa}{(2\pi)^3} \frac{1}{\varkappa^2 + m_\Psi^2}, \tag{B.16}$$

where the integral $I(\lambda)$ is given by

$$\begin{aligned} I(\lambda) & \\ = & \int \frac{d^3\varkappa}{(2\pi)^3} \frac{1}{(\varkappa^2 + m_\Psi^2)((\varkappa - \lambda)^2 + m_\Psi^2)} \\ = & \int_0^\infty \mathrm{d}X_1 \int_0^\infty \mathrm{d}X_2 \int \frac{d^3\varkappa}{(2\pi)^3}\, e^{-(\varkappa^2 + m_\Psi^2)X_1} e^{-((\varkappa-\lambda)^2 + m_\Psi^2)X_2} \\ = & \int_0^\infty \mathrm{d}X_1 \int_0^\infty \mathrm{d}X_2 \left(\frac{1}{X_1 + X_2}\right)^{3/2} e^{-\left[m_\Psi^2(X_1+X_2) + \lambda^2 \frac{X_1 X_2}{X_1+X_2}\right]} \int \frac{d^3\tilde{\varkappa}}{(2\pi)^3}\, e^{-\tilde{\varkappa}^2} \end{aligned} \tag{B.17}$$

with the following substitution in the last line:

$$\tilde{\varkappa}^2 = (X_1 + X_2)\left(\varkappa - \frac{\lambda X_2}{X_1 + X_2}\right)^2. \tag{B.18}$$

The Gaussian integral is known. Further on, we transform the variables $(X_1, X_2) \to (\sigma, \tau) \in [0, \infty) \times [0, 1]$ with $X_1 = \tau\sigma$ and $X_2 = (1 - \tau)\sigma$. The determinant of the transformation is equal to σ. The integral now reads

$$\begin{aligned}
I(\lambda) &= \frac{1}{(2\sqrt{\pi})^3}\int_0^1 \mathrm{d}\tau \int_0^\infty \mathrm{d}\sigma\, \frac{e^{-[m_\Psi^2\sigma+\lambda^2\tau(1-\tau)\sigma]}}{\sqrt{\sigma}} \\
&= \frac{1}{(2\sqrt{\pi})^3}\int_0^1 \mathrm{d}\tau \int_0^\infty \mathrm{d}(\sqrt{\sigma})\, 2e^{-[m_\Psi^2+\lambda^2\tau(1-\tau)]\sqrt{\sigma}^2} \\
&= \frac{1}{8\pi}\int_0^1 \mathrm{d}\tau \sqrt{\frac{1}{m_\Psi^2+\lambda^2\tau(1-\tau)}} \\
&= \frac{1}{8\pi|\lambda|}\int_{-\frac{1}{2}\frac{|\lambda|}{\sqrt{m_\Psi^2+\lambda^2/4}}}^{\frac{1}{2}\frac{|\lambda|}{\sqrt{m_\Psi^2+\lambda^2/4}}} \mathrm{d}t\, \frac{1}{\sqrt{1-t^2}} \\
&= \frac{1}{4\pi|\lambda|}\arcsin\left(\frac{|\lambda|}{\sqrt{4m_\Psi^2+\lambda^2}}\right) \\
&= \frac{1}{4\pi|\lambda|}\arctan\left(\frac{|\lambda|}{2m_\Psi}\right). \qquad \text{(B.19)}
\end{aligned}$$

For small $|\lambda|$, the arctan can be Taylor-expanded to second order. The integral then takes the simple form

$$I(\lambda) = \frac{1}{8\pi m_\Psi} - \frac{\lambda^2}{96\pi m_\Psi^3}. \qquad \text{(B.20)}$$

The other integral in Eq. (B.16) is formally divergent. To solve it, we apply dimensional regularization [202]. We first show an equality for gamma functions:

$$\begin{aligned}
\Gamma(x)\Gamma(y) &= \int_0^\infty \mathrm{d}t\, t^{x-1}e^{-t}\int_0^\infty \mathrm{d}s\, s^{y-1}e^{-s} \\
&= \int_0^\infty \mathrm{d}\rho \int_0^1 \mathrm{d}\tau\, \rho(\rho\tau)^{x-1}e^{-\rho\tau}[\rho(1-\tau)]^{y-1}e^{-\rho(1-\tau)} \\
&= \int_0^\infty \mathrm{d}\rho\, \rho^{x+y-1}e^{-\rho}\int_0^1 \mathrm{d}\tau\, \tau^{x-1}(1-\tau)(y-1) \\
&= \Gamma(x+y)\int_0^\infty \mathrm{d}\sigma\, \sigma^{x-1}(1+\sigma)^{-(x+y)}. \qquad \text{(B.21)}
\end{aligned}$$

The coordinate transformation in the second line is $t=\rho\tau$, $s=\rho(1-\tau)$ and in the last line $\sigma=\tau/(1-\tau)$. With this result, a general formula for dimensional regularization can be obtained:

$$\begin{aligned}
&\int \frac{\mathrm{d}^D \varkappa}{(2\pi)^D} \frac{1}{\varkappa^2 + m_\Psi^2} \\
&= \frac{2\pi}{(2\pi)^D} \left(\prod_{k-1}^{D-2} \int_0^\pi \sin^k \vartheta_k \mathrm{d}\vartheta_k \right) \int_0^\infty \mathrm{d}|\varkappa| \, \frac{|\varkappa|^{D-1}}{\varkappa^2 + m_\Psi^2} \\
&= \frac{2\pi^{D/2}}{\Gamma\left(\frac{D}{2}\right)} \frac{1}{(2\pi)^D} \int_0^\infty \mathrm{d}|\varkappa| \, \frac{|\varkappa|^{D-1}}{\varkappa^2 + m_\Psi^2} \\
&= \frac{2\pi^{D/2}}{\Gamma\left(\frac{D}{2}\right)} \frac{m_\Psi^{D-2}}{2(2\pi)^D} \int_0^\infty \mathrm{d}y \, y^{\frac{1}{2}D-1} (y+1)^{-1} \\
&= \frac{m_\Psi^{D-2}}{2^D \pi^{D/2}} \frac{\Gamma\left(\frac{D}{2}\right) \Gamma\left(1 - \frac{D}{2}\right)}{\Gamma\left(\frac{D}{2}\right) \Gamma(1)} \\
&= \frac{m_\Psi^{D-2}}{2^D \pi^{D/2}} \Gamma\left(1 - \frac{D}{2}\right). \qquad \text{(B.22)}
\end{aligned}$$

At the first equality sign, we switched to spherical coordinates. At the third, we substituted $|\varkappa| =: y m_\Psi^2$. The three-dimensional integral thus takes the value

$$\int \frac{\mathrm{d}^3 \varkappa}{(2\pi)^3} \frac{1}{\varkappa^2 + m_\Psi^2} = \frac{\pi^{3/2}}{8\pi^3} m_\Psi \Gamma\left(-\frac{1}{2}\right) = -\frac{m_\Psi}{4\pi}. \qquad \text{(B.23)}$$

In total, we have

$$S(\lambda) = \left(m_\Psi^2 - \frac{\lambda^2}{4}\right) \left(\frac{1}{8\pi m_\Psi} - \frac{\lambda^2}{96\pi m_\Psi^3}\right) - \frac{m_\Psi}{8\pi} = -\frac{\lambda^2}{24\pi m_\Psi} \qquad \text{(B.24)}$$

and

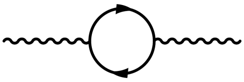

$$\begin{aligned}
&= iJ^2 \alpha_\mu(\lambda) \alpha_\nu(-\lambda) \left[\varepsilon_{\mu\rho\nu} m_\Psi \lambda_\rho I(\lambda) + S(\lambda) P_{\mu\nu}(\lambda)\right] \\
&= iJ^2 \alpha_\mu(\lambda) \alpha_\nu(-\lambda) \left[\frac{\varepsilon_{\mu\rho\nu} \lambda_\rho}{8\pi} - \frac{\lambda^2}{24\pi m_\Psi} P_{\mu\nu}(\lambda)\right] + \mathcal{O}\left(\lambda^3\right). \qquad \text{(B.25)}
\end{aligned}$$

The $\tilde{m}_z$-$\tilde{m}_z$ diagram leads to identical integrals and can now easily be calculated:

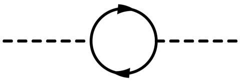

$$
\begin{aligned}
&= iJ^2 \int \frac{\mathrm{d}^3\varkappa}{(2\pi)^3}\, \tilde{m}_z(\lambda)\tilde{m}_z(-\lambda) \frac{m_\Psi^2 - \varkappa\cdot(\varkappa-\lambda)}{(\varkappa^2+m_\Psi^2)((\varkappa-\lambda)^2+m_\Psi^2)} \\
&= iJ^2 \int \frac{\mathrm{d}^3\varkappa}{(2\pi)^3}\, \tilde{m}_z(\lambda)\tilde{m}_z(-\lambda) \\
&\quad \frac{2m_\Psi^2 + \frac{1}{2}\lambda^2 - \frac{1}{2}[(\varkappa^2+m_\Psi^2) + (\varkappa-\lambda)^2 + m_\Psi^2]}{(\varkappa^2+m_\Psi^2)((\varkappa-\lambda)^2+m_\Psi^2)} \\
&= iJ^2 \tilde{m}_z(\lambda)\tilde{m}_z(-\lambda) \left[\left(2m_\Psi^2 + \frac{1}{2}\lambda^2\right) I(\lambda) - \int \frac{\mathrm{d}^3\varkappa}{(2\pi)^3}\, \frac{1}{\varkappa^2+m_\Psi^2}\right] \\
&= iJ^2 \tilde{m}_z(\lambda)\tilde{m}_z(-\lambda) \left[\frac{m_\Psi}{4\pi} - \frac{\lambda^2}{48\pi m_\Psi} + \frac{\lambda^2}{16\pi m_\Psi} + \frac{m_\Psi}{4\pi}\right] + \mathcal{O}\left(\lambda^3\right) \\
&= iJ^2 \tilde{m}_z(\lambda)\tilde{m}_z(-\lambda) \left[\frac{m_\Psi}{2\pi} + \frac{\lambda^2}{24\pi m_\Psi}\right] + \mathcal{O}\left(\lambda^3\right) \qquad \text{(B.26)}
\end{aligned}
$$

The two mixed diagrams are

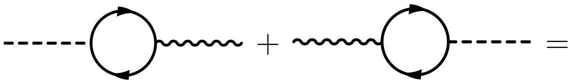

$$
\begin{aligned}
iJ^2 \int \frac{\mathrm{d}^3\varkappa}{(2\pi)^3} \Bigg[& \tilde{m}_z(\lambda)\alpha_\mu(-\lambda) \frac{-im_\Psi(2\varkappa_\mu - \lambda_\mu) + i\varepsilon_{\rho\nu\mu}\varkappa_\rho(\varkappa_\nu - \lambda_\nu)}{(\varkappa^2+m_\Psi^2)((\varkappa-\lambda)^2+m_\Psi^2)} \\
& + \alpha_\mu(\lambda)\tilde{m}_z(-\lambda) \frac{-im_\Psi(2\varkappa_\mu - \lambda_\mu) - i\varepsilon_{\rho\nu\mu}\varkappa_\rho(\varkappa_\nu - \lambda_\nu)}{(\varkappa^2+m_\Psi^2)((\varkappa-\lambda)^2+m_\Psi^2)} \Bigg]
\end{aligned}
\qquad \text{(B.27)}
$$

which can be split in two integrals as follows:

$$
\begin{aligned}
& m_\Psi W(\lambda) \int \frac{\mathrm{d}^3\varkappa}{(2\pi)^3}\, \frac{2\varkappa_\mu - \lambda_\mu}{(\varkappa^2+m_\Psi^2)((\varkappa-\lambda)^2+m_\Psi^2)} \\
& -W(\lambda) \int \frac{\mathrm{d}^3\varkappa}{(2\pi)^3}\, \frac{(\varkappa\times\lambda)_\mu}{(\varkappa^2+m_\Psi^2)((\varkappa-\lambda)^2+m_\Psi^2)}
\end{aligned}
\qquad \text{(B.28)}
$$

where $W(\lambda) = J^2\left[\tilde{m}_z(\lambda)\alpha_\mu(-\lambda) + \alpha_\mu(\lambda)\tilde{m}_z(-\lambda)\right]$ for brevity. The first integral can be solved using the same steps as in Eqs. (B.17) and (B.19) for $I(\lambda)$. After the variable transformation to σ and τ one arrives at

$$\begin{aligned} \ldots &= \frac{\lambda_\mu}{(2\sqrt{\pi})^3}\int_0^1 \mathrm{d}\tau\,(1-2\tau)\int_0^\infty \mathrm{d}\sigma\,\frac{e^{-[m_\Psi^2\sigma+\lambda^2\tau(1-\tau)\sigma]}}{\sqrt{\sigma}} \\ &= \frac{\lambda_\mu}{8\pi}\int_0^1 \mathrm{d}\tau\,\frac{1-2\tau}{\sqrt{m_\Psi^2+\lambda^2\tau(1-\tau)}} \\ &= \frac{\lambda_\mu}{4\pi\lambda^2}\left[\sqrt{m_\Psi^2+\lambda^2\tau(1-\tau)}\right]_{\tau=0}^{\tau=1} = 0. \end{aligned} \tag{B.29}$$

In the second integral of Eq. (B.28), $\varkappa$ can be transformed to cylindrical coordinates with respect to the direction of λ. It is then easy to check that the angular integration cancels the components of $\varkappa$ orthogonal to λ in the numerator. The remainder of $\varkappa$ is parallel to λ and therefore the cross product yields zero. In total, both mixed diagrams vanish.

Collecting the results from all diagrams, we have

$$\begin{aligned} \delta S &= \frac{iJ^2}{8\pi}\int\frac{\mathrm{d}^3\lambda}{(2\pi)^3}\left[\alpha_\mu(\lambda)\left(\varepsilon_{\mu\rho\nu}\lambda_\rho - \frac{\delta_{\mu\nu}\lambda^2-\lambda_\mu\lambda_\nu}{3m_\Psi}\right)\alpha_\nu(-\lambda)\right. \\ &\quad \left. + \tilde{m}_z(\lambda)\left(4m_\Psi + \frac{\lambda^2}{3m_\Psi}\right)\tilde{m}_z(-\lambda) + \mathcal{O}\left(\lambda^3\right)\right] \end{aligned} \tag{B.30}$$

Upon transformation to real space and time, this yields Eq. (4.16).

Appendix C

Critical angle: explicit solution

As discussed in Sec. 5.4.3, we can write the characteristic polynomial $p_k(\varepsilon)$ of the BdG Hamiltonian for the Majorana nanowire at zero energy, $\varepsilon = 0$, as a bi-quartic polynomial in momentum

$$p(\varkappa) = \varkappa^4 + a\varkappa^3 + b\varkappa^2 + c\varkappa + d, \tag{C.1}$$

with $\varkappa = k^2$. With the auxiliary quantities

$$\begin{aligned} M &= \frac{2m}{\hbar^2}, &\text{(C.2)}\\ S &= \frac{\hbar^2\mu}{m} + \alpha^2, &\text{(C.3)}\\ T &= \mu^2 + \Delta^2 - E_{\text{Zee}}^2, &\text{(C.4)} \end{aligned}$$

the coefficients in Eq. (C.1) read

$$\begin{aligned} a &= -2M^2S &\text{(C.5)}\\ b &= M^2(2T + M^2S^2) &\text{(C.6)}\\ c &= M^4[4\alpha^2(\Delta^2 - E_{\text{Zee}}^2\cos\vartheta) - 2ST] &\text{(C.7)}\\ d &= T^2M^4 &\text{(C.8)} \end{aligned}$$

The critical angle ϑ_c can be derived from the condition that the discriminant δ of $p(\varkappa)$ vanishes (see main text). In our case, the discriminant as a function of c (which is linear in $\cos\vartheta$) is the quartic polynomial

$$\delta(c) = c^4 + Ac^3 + Bc^2 + Cc + D, \tag{C.9}$$

with the coefficients

$$\begin{aligned}
A &= \frac{2}{3}a\left(\frac{2}{9}a^2 - b\right) && \text{(C.10)}\\
B &= \frac{2}{27}(2b^3 + 27a^2d - 72bd) + \frac{1}{9}a^2b^2 - \frac{4}{27}a^2(b^2 + 12d) && \text{(C.11)}\\
C &= \frac{2}{81}a\left[2(b^2 + 12d)^2 - b(2b^3 + 27a^2d - 72bd)\right] && \text{(C.12)}\\
D &= \frac{1}{3^6}\left[(2b^3 + 27a^2d - 72bd)^2 - 4(b^2 + 12d)^3\right] && \text{(C.13)}
\end{aligned}$$

The four solutions of $\delta(c) = 0$ can be found using the general solution formula [181] for quartic equations. It can be written in the form

$$c_{\rho\sigma} = -\frac{A}{4} + \rho\frac{W}{2} + \sigma\frac{1}{2}\sqrt{\frac{A^2}{2} - \frac{4B}{3} - \frac{F}{3L} - \frac{L}{3} + \rho\frac{-A^3 + 4AB - 8C}{4W}} \tag{C.14}$$

with $\rho, \sigma = \pm 1$ and

$$\begin{aligned}
E &= 2B^3 - 9ABC + 27C^2 + 27A^2D - 72BD && \text{(C.15)}\\
F &= B^2 - 3AC + 12D && \text{(C.16)}\\
K &= E + \sqrt{-4F^3 + E^2} && \text{(C.17)}\\
L &= \sqrt[3]{\frac{K}{2}} && \text{(C.18)}\\
W &= \sqrt{\frac{A^2}{4} - \frac{2B}{3} + \frac{F}{3L} + \frac{L}{3}} && \text{(C.19)}
\end{aligned}$$

One of the solutions $c_{\rho\sigma}$ is exactly equivalent to the condition $\cos\vartheta_c = \Delta/E_{\mathrm{Zee}}$. As the explicit intermediate expressions become unreasonably lengthy, the equivalence has been checked to `double` precision by implementing the solution formula in `python`.

Bibliography

[1] S. Rex, F. S. Nogueira, and A. Sudbø, Phys. Rev. B **93**, 014404 (2016)

[2] S. Rex, F. S. Nogueira, and A. Sudbø, Phys. Rev. B **94**, 020404(R) (2016)

[3] S. Rex, F. S. Nogueira, and A. Sudbø, Phys. Rev. B **95**, 155430 (2017)

[4] S. Rex and A. Sudbø, Phys. Rev. B **90**, 115429 (2014)

[5] C. Timm, S. Rex, and P. M. R. Brydon, Phys. Rev. B **91**, 180503(R) (2015)

[6] M. Z. Hasan and C. L. Kane, Rev. Mod. Phys. **82**, 3045 (2010)

[7] X.-L. Qi and S.-C. Zhang, Rev. Mod. Phys. **83**, 1057 (2011)

[8] D. Tong, *The Quantum Hall Effect* (2016), arXiv:1606.06687v2

[9] A. P. Schnyder and P. M. R. Brydon, J. Phys.: Condens. Matter **27**, 243201 (2015)

[10] Nobelprize.org, *The Nobel Prize in Physics 2016.* Https://www.nobelprize.org/nobel_prizes/physics/laureates/2016/

[11] M. Nakahara, *Geometry, Topology, and Physics.* Graduate Student Series in Physics, Taylor & Francis, 2$^{\text{nd}}$ ed. (2003), ISBN 978-0-7503-0606-5

[12] C. Nash and S. Sen, *Topology and Geometry for Physicists.* Dover Publications (2011), ISBN 978-0-486-47852-4, originally published 1983 by Academic Press

[13] K. von Klitzing, G. Dorda, and M. Pepper, Phys. Rev. Lett. **45**, 494 (1980)

[14] Z.-C. Gu and X.-G. Wen, Phys. Rev. B **80**, 155131 (2009)

[15] T. Senthil, Annu. Rev. Condens. Matter Phys. **6**, 299 (2015)

[16] C.-K. Chiu, J. C. Y. Teo, A. P. Schnyder, and S. Ryu, Rev. Mod. Phys. **88**, 035005 (2016)

[17] X. Wan, A. M. Turner, A. Vishwanath, and S. Y. Savrasov, Phys. Rev. B **83**, 205101 (2011)

[18] L. Fu, Phys. Rev. Lett. **106**, 106802 (2011)

[19] W. A. Benalcazar, B. A. Bernevig, and T. L. Hughes, Science **357**, 61 (2017)

[20] S. Sachdev, *Topological order in insulators and metals* (2016/17), lectures at the 34th Jerusalem Winter School

[21] D. C. Tsui, H. L. Stormer, and A. C. Gossard, Phys. Rev. Lett. **48**, 1559 (1982)

[22] R. Moessner and S. L. Sondhi, Phys. Rev. Lett. **86**, 1881 (2001)

[23] S. Yan, D. A. Huse, and S. R. White, Science **332**, 1173 (2011)

[24] N. Nagaosa and Y. Tokura, Nature Nanotech. **8**, 899 (2013)

[25] E. Kröner and K. H. Anthony, Annu. Rev. Mat. Sc. **5**, 43 (1975)

[26] R. B. Laughlin, Phys. Rev. B **23**, 5632 (1981)

[27] D. J. Thouless, M. Kohmoto, M. P. Nightingale, and M. den Nijs, Phys. Rev. Lett. **49**, 405 (1982)

[28] A. P. Schnyder, S. Ryu, A. Furusaki, and A. W. W. Ludwig, Phys. Rev. B **78**, 195125 (2008)

[29] S. Ryu, A. P. Schnyder, A. Furusaki, and A. W. W. Ludwig, New J. Phys. **12**, 065010 (2010)

[30] A. Altland and M. R. Zirnbauer, Phys. Rev. B **55**, 1142 (1997)

[31] E. P. Wigner, Ann. Math. **67**, 325 (1958)

[32] F. J. Dyson, J. Math. Phys. **3**, 140 (1962)

[33] E. Cartan, J. Math. Pures Appl. **6**, 1 (1927)

[34] A. Kitaev, AIP Conf. Proc. **1134**, 22 (2009)

[35] M. Berry, Proc. R. Soc. A **392**, 45 (1984)

[36] J. Anandan, Nature **360**, 307 (1992)

[37] F. Schwabl, *Quantenmechanik*. Springer, 7th ed. (2007, 1st ed. 1988), ISBN 978-3-540-73674-5

[38] F. Bloch, Zeitschrift für Physik **52**, 555 (1929)

[39] R. Jackiw and C. Rebbi, Phys. Rev. D **13**, 3398 (1976)

[40] E. Witten, Adv. Theor. Math. Phys. **2**, 253 (1998)

[41] S. S. Gubser, I. R. Klebanov, and A. M. Polyakov, Phys. Lett. B **428**, 105 (1998)

[42] S. N. Solodukhin, Nucl. Phys. B **539**, 403 (1999)

[43] J. C. Y. Teo and C. L. Kane, Phys. Rev. B **82**, 115120 (2010)

[44] A. M. Essin and V. Gurarie, Phys. Rev. B **84**, 125132 (2011)

[45] R. S. K. Mong and V. Shivamoggi, Phys. Rev. B **83**, 125109 (2011)

[46] W. P. Su, J. R. Schrieffer, and A. J. Heeger, Phys. Rev. B **22**, 2099 (1980)

[47] J. K. Asbóth, L. Oroszlány, and A. Pályi, *A Short Course on Topological Insulators*, Lecture Notes in Physics, vol. 919. Springer International Publishing (2016)

[48] E. H. Hall, Am. J. Math. **2**, 287 (1879)

[49] K. S. Novoselov, Z. Jiang, Y. Zhang, S. V. Morozov, H. L. Stormer, U. Zeitler, J. C. Maan, G. S. Boebinger, P. Kim, and A. K. Geim, Science **315**, 1379 (2007)

[50] M. A. Paalanen, D. C. Tsui, and A. C. Gossard, Phys. Rev. B **25**, 5566 (1982)

[51] C. Timm, *Vielteilchentheorie kondensierter Materie.* Lecture notes, version 2015

[52] D. R. Hofstadter, Phys. Rev. B **14**, 2239 (1976)

[53] F. D. M. Haldane, Phys. Rev. Lett. **61**, 2015 (1988)

[54] M. König, S. Wiedmann, C. Brüne, A. Roth, H. Buhmann, L. W. Molenkamp, X.-L. Qi, and S.-C. Zhang, Science **318**, 766 (2007)

[55] C. L. Kane and E. J. Mele, Phys. Rev. Lett. **95**, 226801 (2005)

[56] B. A. Bernevig and S.-C. Zhang, Phys. Rev. Lett. **96**, 106802 (2006)

[57] B. A. Bernevig, T. L. Hughes, and S.-C. Zhang, Science **314**, 1757 (2006)

[58] C. L. Kane and E. J. Mele, Phys. Rev. Lett. **95**, 146802 (2005)

[59] M. Knig, H. Buhmann, L. W. Molenkamp, T. Hughes, C.-X. Liu, X.-L. Qi, and S.-C. Zhang, J. Phys. Soc. Jpn. **77**, 031007 (2008)

[60] Z. Zhu, Y. Cheng, and U. Schwingenschlögl, Phys. Rev. B **85**, 235401 (2012)

[61] H. Zhang, C.-X. Liu, X.-L. Qi, X.-Y. Deng, X. Dai, and S.-C. Zhang, Nature Phys. **5**, 438 (2009)

[62] D. Hsieh, D. Qian, L. Wray, Y. Xia, Y. S. Hor, R. J. Cava, and M. Z. Hasan, Nature **452**, 970 (2008)

[63] A. H. Castro Neto, F. Guinea, N. M. R. Peres, K. S. Novoselov, and A. K. Geim, Rev. Mod. Phys. **81**, 109 (2009)

[64] H. Nielsen and M. Ninomiya, Nucl. Phys. B **185**, 20 (1981)

[65] H. Nielsen and M. Ninomiya, Phys. Lett. B **130**, 389 (1983)

[66] L. Susskind, J. Math. Phys. **36**, 6377 (1995)

[67] Y. Xia, D. Qian, D. Hsieh, L. Wray, A. Pal, H. Lin, A. Bansil, D. Grauer, Y. S. Hor, R. J. Cava, and M. Z. Hasan, Nature Phys. **5**, 398 (2009)

[68] Y. L. Chen, J. G. Analytis, J.-H. Chu, Z. K. Liu, S.-K. Mo, X. L. Qi, H. J. Zhang, D. H. Lu, X. Dai, Z. Fang, S. C. Zhang, I. R. Fisher, Z. Hussain, and Z.-X. Shen, Science **325**, 178 (2009)

[69] D. Hsieh, Y. Xia, D. Qian, L. Wray, F. Meier, J. H. Dil, J. Osterwalder, L. Patthey, A. V. Fedorov, H. Lin, A. Bansil, D. Grauer, Y. S. Hor, R. J. Cava, and M. Z. Hasan, Phys. Rev. Lett. **103**, 146401 (2009)

[70] Y. Fan, P. Upadhyaya, X. Kou, M. Lang, S. Takei, Z. Wang, J. Tang, L. He, L.-T. Chang, M. Montazeri, G. Yu, W. Jiang, T. Nie, R. N. Schwartz, Y. Tserkovnyak, and K. L. Wang, Nature Mat. **13**, 699 (2014)

[71] A. Bansil, H. Lin, and T. Das, Rev. Mod. Phys. **88**, 021004 (2016)

[72] L. Fu and C. L. Kane, Phys. Rev. B **74**, 195312 (2006)

[73] L. Fu and C. L. Kane, Phys. Rev. B **76**, 045302 (2007)

[74] L. Fu, C. L. Kane, and E. J. Mele, Phys. Rev. Lett. **98**, 106803 (2007)

[75] A. Cayley, Cambridge and Dublin Math. J. **VII**, 40 (1852)

[76] X.-L. Qi, T. L. Hughes, and S.-C. Zhang, Phys. Rev. B **78**, 195424 (2008)

[77] S.-C. Zhang, Int. J. Mod. Phys. B **6**, 25 (1992)

[78] Z. Wang, X.-L. Qi, and S.-C. Zhang, Phys. Rev. Lett. **105**, 256803 (2010)

[79] S.-C. Zhang and J. Hu, Science **294**, 823 (2001)

[80] F. Wilczek, Phys. Rev. Lett. **58**, 1799 (1987)

[81] A. M. Essin, J. E. Moore, and D. Vanderbilt, Phys. Rev. Lett. **102**, 146805 (2009)

[82] E. J. König, P. M. Ostrovsky, I. V. Protopopov, I. V. Gornyi, I. S. Burmistrov, and A. D. Mirlin, Phys. Rev. B **90**, 165435 (2014)

[83] M. Mulligan and F. J. Burnell, Phys. Rev. B **88**, 085104 (2013)

[84] H.-G. Zirnstein and B. Rosenow, Phys. Rev. B **88**, 085105 (2013)

[85] E. J. König, P. M. Ostrovsky, I. V. Protopopov, I. V. Gornyi, I. S. Burmistrov, and A. D. Mirlin, Phys. Rev. B **88**, 035106 (2013)

[86] Y. L. Chen, J.-H. Chu, J. G. Analytis, Z. K. Liu, K. Igarashi, H.-H. Kuo, X. L. Qi, S. K. Mo, R. G. Moore, D. H. Lu, M. Hashimoto, T. Sasagawa, S. C. Zhang, I. R. Fisher, Z. Hussain, and Z. X. Shen, Science **329**, 659 (2010)

[87] Y. Okada, C. Dhital, W. Zhou, E. D. Huemiller, H. Lin, S. Basak, A. Bansil, Y.-B. Huang, H. Ding, Z. Wang, S. D. Wilson, and V. Madhavan, Phys. Rev. Lett. **106**, 206805 (2011)

[88] P. Wei, F. Katmis, B. A. Assaf, H. Steinberg, P. Jarillo-Herrero, D. Heiman, and J. S. Moodera, Phys. Rev. Lett. **110**, 186807 (2013)

[89] Q. I. Yang, M. Dolev, L. Zhang, J. Zhao, A. D. Fried, E. Schemm, M. Liu, A. Palevski, A. F. Marshall, S. H. Risbud, and A. Kapitulnik, Phys. Rev. B **88**, 081407 (2013)

[90] J. Maciejko, X.-L. Qi, H. D. Drew, and S.-C. Zhang, Phys. Rev. Lett. **105**, 166803 (2010)

[91] L. Wu, M. Salehi, N. Koirala, J. Moon, S. Oh, and N. P. Armitage, Science **354**, 1124 (2016)

[92] V. Dziom, A. Shuvaev, A. Pimenov, G. V. Astakhov, C. Ames, K. Bendias, J. Böttcher, G. Tkachov, E. M. Hankiewicz, C. Brüne, H. Buhmann, and L. W. Molenkamp, Nature Comm. **8**, 15197 (2017)

[93] A. G. Mal'shukov, H. Skarsvåg, and A. Brataas, Phys. Rev. B **88**, 245122 (2013)

[94] X.-L. Qi, R. Li, J. Zang, and S.-C. Zhang, Science **323**, 1184 (2009)

[95] J. D. Jackson, *Classical Electrodynamics*. Wiley (1962), ISBN 0-471-43131-1

[96] K. Nomura and N. Nagaosa, Phys. Rev. B **82**, 161401 (2010)

[97] I. Žutić, J. Fabian, and S. Das Sarma, Rev. Mod. Phys. **76**, 323 (2004)

[98] T. Yokoyama, J. Zang, and N. Nagaosa, Phys. Rev. B **81**, 241410 (2010)

[99] Y. G. Semenov, X. Duan, and K. W. Kim, Phys. Rev. B **86**, 161406 (2012)

[100] I. Garate and M. Franz, Phys. Rev. Lett. **104**, 146802 (2010)

[101] Y. Tserkovnyak and D. Loss, Phys. Rev. Lett. **108**, 187201 (2012)

[102] J. Linder, Phys. Rev. B **90**, 041412 (2014)

[103] Y. Ferreiros and A. Cortijo, Phys. Rev. B **89**, 024413 (2014)

[104] Y. Ferreiros, F. J. Buijnsters, and M. I. Katsnelson, Phys. Rev. B **92**, 085416 (2015)

[105] L. Landau and E. Lifshitz, Phys. Z. Sowj. **8**, 153 (1935)

[106] F. S. Nogueira and I. Eremin, Phys. Rev. Lett. **109**, 237203 (2012)

[107] F. S. Nogueira and I. Eremin, Phys. Rev. B **88**, 085126 (2013)

[108] F. S. Nogueira and I. Eremin, Phys. Rev. B **90**, 014431 (2014)

[109] F. Katmis, V. Lauter, F. S. Nogueira, B. A. Assaf, M. E. Jamer, P. Wei, B. Satpati, J. W. Freeland, I. Eremin, D. Heiman, P. Jarillo-Herrero, and J. S. Moodera, Nature **533**, 513 (2016)

[110] J. W. Negele and H. Orland, *Quantum Many-Particle Systems.* Advanced Book Classics, Westview Press (1988), ISBN 0-7382-0052-2

[111] A. Altland and B. Simons, *Condensed Matter Field Theory.* Cambridge University Press, 2$^{\text{nd}}$ ed. (2010)

[112] W. Liu, L. He, Y. Xu, K. Murata, M. C. Onbasli, M. Lang, N. J. Maltby, S. Li, X. Wang, C. A. Ross, P. Bencok, G. van der Laan, R. Zhang, and K. L. Wang, Nano Lett. **15**, 764 (2015)

[113] Y. Kubota, K. Murata, J. Miyawaki, K. Ozawa, M. C. Onbasli, T. Shirasawa, B. Feng, S. Yamamoto, R.-Y. Liu, S. Yamamoto, S. K. Mahatha, P. Sheverdyaeva, P. Moras, C. A. Ross, S. Suga, Y. Harada, K. L. Wang, and I. Matsuda, J. Phys.: Condens. Matter **29**, 055002 (2017)

[114] Q. L. He, X. Kou, A. J. Grutter, G. Yin, L. Pan, X. Che, Y. Liu, T. Nie, B. Zhang, S. M. Disseler, B. J. Kirby, W. Ratcliff II, Q. Shao, K. Murata, X. Zhu, G. Yu, Y. Fan, M. Montazeri, X. Han, J. A. Borchers, and K. L. Wang, Nature Mat. **16**, 94 (2017)

[115] T. Jungwirth, X. Marti, P. Wadley, and J. Wunderlich, Nature Nanotech. **11**, 231 (2016)

[116] J. R. Schrieffer, *Theory Of Superconductivity.* Advanced Book Classics, Perseus Books, revised ed. (1999), ISBN 978-0738201207, originally published by Westview Press in 1964

[117] W. Meissner and R. Ochsenfeld, Naturwissenschaften **21**, 787 (1933)

[118] H. Kamerlingh Onnes, Leiden Communications 120b (1911)

[119] J. Bardeen, L. N. Cooper, and J. R. Schrieffer, Phys. Rev. **106**, 162 (1957)

[120] J. Bardeen, L. N. Cooper, and J. R. Schrieffer, Phys. Rev. **108**, 1175 (1957)

[121] Y. Nambu, Phys. Rev. **117**, 648 (1960)

[122] R. Balian and N. R. Werthamer, Phys. Rev. **131**, 1553 (1963)

[123] L. P. Gor'kov and E. I. Rashba, Phys. Rev. Lett. **87**, 037004 (2001)

[124] R. Roy, *Topological superfluids with time reversal symmetry* (2008), arXiv:0803.2868

[125] N. Read and D. Green, Phys. Rev. B **61**, 10267 (2000)

[126] A. P. Mackenzie and Y. Maeno, Rev. Mod. Phys. **75**, 657 (2003)

[127] Y. Maeno, S. Kittaka, T. Nomura, S. Yonezawa, and K. Ishida, J. Phys. Soc. Jpn. **81**, 011009 (2012)

[128] G. E. Volovik, JETP Lett. **90**, 587 (2009)

[129] L. Fu and C. L. Kane, Phys. Rev. Lett. **100**, 096407 (2008)

[130] J. Linder, Y. Tanaka, T. Yokoyama, A. Sudbø, and N. Nagaosa, Phys. Rev. Lett. **104**, 067001 (2010)

[131] J. Alicea, Rep. Prog. Phys. **75**, 076501 (2012)

[132] M. Leijnse and K. Flensberg, Semiconductor Science and Technology **27**, 124003 (2012)

[133] E. Majorana, Il Nuovo Cimento **14**, 171 (1937)

[134] F. T. Avignone, S. R. Elliott, and J. Engel, Rev. Mod. Phys. **80**, 481 (2008)

[135] A. Gando *et al.* (KamLAND-Zen Collaboration), Phys. Rev. Lett. **117**, 082503 (2016)

[136] M. Agnostini *et al.* (GERDA Collaboration), Nature **544**, 47 (2017)

[137] A. Y. Kitaev, Physics-Uspekhi **44**, 131 (2001)

[138] C. Nayak, S. H. Simon, A. Stern, M. Freedman, and S. Das Sarma, Rev. Mod. Phys. **80**, 1083 (2008)

[139] D. A. Ivanov, Phys. Rev. Lett. **86**, 268 (2001)

[140] J. M. Leinaas and J. Myrheim, Nuovo Cimento B **37**, 1 (1977)

[141] A. Stern, Nature **464**, 187 (2010)

[142] G. Moore and N. Read, Nucl. Phys. B **360**, 362 (1991)

[143] R. Verresen, R. Mössner, and F. Pollmann, *One-Dimensional Symmetry Protected Topological Phases and their Transitions* (2017), arXiv:1707.05787

[144] R. M. Lutchyn, J. D. Sau, and S. Das Sarma, Phys. Rev. Lett. **105**, 077001 (2010)

[145] Y. Oreg, G. Refael, and F. von Oppen, Phys. Rev. Lett. **105**, 177002 (2010)

[146] J. D. Sau, S. Tewari, R. M. Lutchyn, T. D. Stanescu, and S. Das Sarma, Phys. Rev. B **82**, 214509 (2010)

[147] J. Alicea, Phys. Rev. B **81**, 125318 (2010)

[148] L. Fu and C. L. Kane, Phys. Rev. B **79**, 161408 (2009)

[149] S. Nadj-Perge, I. K. Drozdov, B. A. Bernevig, and A. Yazdani, Phys. Rev. B **88**, 020407 (2013)

[150] S. Estévez Hernández, M. Akabori, K. Sladek, C. Volk, S. Alagha, H. Hardtdegen, M. G. Pala, N. Demarina, D. Grützmacher, and T. Schäpers, Phys. Rev. B **82**, 235303 (2010)

[151] I. van Weperen, B. Tarasinski, D. Eeltink, V. S. Pribiag, S. R. Plissard, E. P. A. M. Bakkers, L. P. Kouwenhoven, and M. Wimmer, Phys. Rev. B **91**, 201413 (2015)

[152] E. J. Johnson and D. H. Dickey, Phys. Rev. B **1**, 2676 (1970)

[153] B. D. McCombe and R. J. Wagner, Phys. Rev. B **4**, 1285 (1971)

[154] A. F. Andreev, Sov. Phys. JETP **19**, 1228 (1964)

[155] K. T. Law, P. A. Lee, and T. K. Ng, Phys. Rev. Lett. **103**, 237001 (2009)

[156] K. Flensberg, Phys. Rev. B **82**, 180516 (2010)

[157] H.-J. Kwon, K. Sengupta, and V. M. Yakovenko, Europ. Phys. J. B **37**, 349 (2004)

[158] B. Josephson, Phys. Lett. **1**, 251 (1962)

[159] V. Mourik, K. Zuo, S. M. Frolov, S. R. Plissard, E. P. A. M. Bakkers, and L. P. Kouwenhoven, Science **336**, 1003 (2012)

[160] M. T. Deng, C. L. Yu, G. Y. Huang, M. Larsson, P. Caroff, and H. Q. Xu, Nano Lett. **12**, 6414 (2012)

[161] A. Das, Y. Ronen, Y. Most, Y. Oreg, M. Heiblum, and H. Shtrikman, Nature Phys. **8**, 887 (2012)

[162] H. O. H. Churchill, V. Fatemi, K. Grove-Rasmussen, M. T. Deng, P. Caroff, H. Q. Xu, and C. M. Marcus, Phys. Rev. B **87**, 241401 (2013)

[163] A. D. K. Finck, D. J. Van Harlingen, P. K. Mohseni, K. Jung, and X. Li, Phys. Rev. Lett. **110**, 126406 (2013)

[164] S. M. Albrecht, A. P. Higginbotham, M. Madsen, F. Kuemmeth, T. S. Jespersen, J. Nygrd, P. Krogstrup, and C. M. Marcus, Nature **531**, 206 (2016)

[165] M. T. Deng, S. Vaitiekenas, E. B. Hansen, J. Danon, M. Leijnse, K. Flensberg, J. Nygård, P. Krogstrup, and C. M. Marcus, Science **354**, 1557 (2016)

[166] E. J. H. Lee, X. Jiang, R. Aguado, G. Katsaros, C. M. Lieber, and S. De Franceschi, Phys. Rev. Lett. **109**, 186802 (2012)

[167] C.-H. Lin, J. D. Sau, and S. Das Sarma, Phys. Rev. B **86**, 224511 (2012)

[168] E. Prada, P. San-Jose, and R. Aguado, Phys. Rev. B **86**, 180503 (2012)

[169] J. S. Lim, L. Serra, R. López, and R. Aguado, Phys. Rev. B **86**, 121103 (2012)

[170] B. Nijholt and A. R. Akhmerov, Phys. Rev. B **93**, 235434 (2016)

[171] J. Osca and L. Serra, Phys. Rev. B **91**, 235417 (2015)

[172] J. Liu, A. C. Potter, K. T. Law, and P. A. Lee, Phys. Rev. Lett. **109**, 267002 (2012)

[173] T. D. Stanescu, R. M. Lutchyn, and S. Das Sarma, Phys. Rev. B **90**, 085302 (2014)

[174] F. Pientka, G. Kells, A. Romito, P. W. Brouwer, and F. von Oppen, Phys. Rev. Lett. **109**, 227006 (2012)

[175] R. Thomale, S. Rachel, and P. Schmitteckert, Phys. Rev. B **88**, 161103 (2013)

[176] D. Aasen, M. Hell, R. V. Mishmash, A. Higginbotham, J. Danon, M. Leijnse, T. S. Jespersen, J. A. Folk, C. M. Marcus, K. Flensberg, and J. Alicea, Phys. Rev. X **6**, 031016 (2016)

[177] F. Nichele, A. C. C. Drachmann, A. M. Whiticar, E. C. T. O'Farrell, H. J. Suominen, A. Fornieri, T. Wang, G. C. Gardner, C. Thomas, A. T. Hatke, P. Krogstrup, M. J. Manfra, K. Flensberg, and C. M. Marcus, *Scaling of Majorana Zero-Bias Conductance Peaks* (2017), arXiv:1706.07033

[178] J. Osca, D. Ruiz, and L. Serra, Phys. Rev. B **89**, 245405 (2014)

[179] J. Liang and Y. Lyanda-Geller, Phys. Rev. B **95**, 201404 (2017)

[180] E. L. Rees, Am. Math. Mon. **29**, 51 (1922)

[181] B. L. van der Werden, *Modern Algebra*, vol. 1. Springer (1991), ISBN 0-387-97424-5

[182] G. E. Blonder, M. Tinkham, and T. M. Klapwijk, Phys. Rev. B **25**, 4515 (1982)

[183] M. Sato, Phys. Rev. B **73**, 214502 (2006)

[184] A. P. Schnyder and S. Ryu, Phys. Rev. B **84**, 060504 (2011)

[185] A. P. Schnyder, P. M. R. Brydon, and C. Timm, Phys. Rev. B **85**, 024522 (2012)

[186] P. M. R. Brydon, A. P. Schnyder, and C. Timm, Phys. Rev. B **84**, 020501 (2011)

[187] B. Béri, Phys. Rev. B **81**, 134515 (2010)

[188] E. Bauer, G. Hilscher, H. Michor, C. Paul, E. W. Scheidt, A. Gribanov, Y. Seropegin, H. Noël, M. Sigrist, and P. Rogl, Phys. Rev. Lett. **92**, 027003 (2004)

[189] Y. Yanase and M. Sigrist, J. Phys. Soc. Jpn. **77**, 124711 (2008)

[190] P. A. Frigeri, D. F. Agterberg, A. Koga, and M. Sigrist, Phys. Rev. Lett. **92**, 097001 (2004)

[191] D. Scalapino, Phys. Rep. **250**, 329 (1995)

[192] C. C. Tsuei and J. R. Kirtley, Rev. Mod. Phys. **72**, 969 (2000)

[193] R. Joynt and L. Taillefer, Rev. Mod. Phys. **74**, 235 (2002)

[194] P. Goswami and A. H. Nevidomskyy, Phys. Rev. B **92**, 214504 (2015)

[195] A. P. Schnyder, C. Timm, and P. M. R. Brydon, Phys. Rev. Lett. **111**, 077001 (2013)

[196] M. Matsumoto and H. Shiba, J. Phys. Soc. Jpn. **64**, 3384 (1995)

[197] M. Matsumoto and H. Shiba, J. Phys. Soc. Jpn. **64**, 4867 (1995)

[198] M. Fogelström, D. Rainer, and J. A. Sauls, Phys. Rev. Lett. **79**, 281 (1997)

[199] M. Covington, M. Aprili, E. Paraoanu, L. H. Greene, F. Xu, J. Zhu, and C. A. Mirkin, Phys. Rev. Lett. **79**, 277 (1997)

[200] A. C. Potter and P. A. Lee, Phys. Rev. Lett. **112**, 117002 (2014)

[201] Y. Wang and L. Fu, *Topological phase transitions in multi-component superconductors* (2017), arXiv:1703.06880

[202] C. Itzykson and J.-B. Zuber, *Quantum Field Theory*. Dover books on Physics, Dover Publications (2005), ISBN 0486445682, originally published in 1980 by McGraw-Hill (New York)

Paper [1]

Stefan Rex, Flavio S. Nogueira, and Asle Sudbø

Nonlocal topological magnetoelectric effect by Coulomb interaction at a topological insulator-ferromagnet interface

Physical Review B **93**, 014404 (2016)

PHYSICAL REVIEW B **93**, 014404 (2016)

Nonlocal topological magnetoelectric effect by Coulomb interaction at a topological insulator-ferromagnet interface

Stefan Rex,[1] Flavio S. Nogueira,[2,3] and Asle Sudbø[1]
[1]*Department of Physics, Norwegian University of Science and Technology, N-7491 Trondheim, Norway*
[2]*Institute for Theoretical Solid State Physics, IFW Dresden, PF 270116, 01171 Dresden, Germany*
[3]*Institut für Theoretische Physik III, Ruhr-Universität Bochum, Universitätsstraße 150, DE-44801 Bochum, Germany*

(Received 14 October 2015; published 6 January 2016)

The interface between a topological insulator and a ferromagnetic insulator exhibits an interesting interplay of topological Dirac electrons and magnetism. As has been shown recently, the breaking of time-reversal invariance by magnetic order generates a Chern-Simons term in the action, that in turn leads to a Berry phase and a magnetoelectric effect of topological origin. Here, we consider the system in the presence of a long-range Coulomb interaction between the Dirac electrons, and find that the magnetoelectric effect of the fluctuating electric field becomes nonlocal. We derive a Landau-Lifshitz equation for the fluctuation-induced magnetization dynamics and the Euler-Lagrange equation of the Coulomb field by explicit one-loop calculations. Via the Coulomb interaction, divergences in the in-plane magnetization affect the magnetization dynamics over large distances in a topologically protected way.

DOI: 10.1103/PhysRevB.93.014404

I. INTRODUCTION

In a topological insulator (TI), the bulk band structure gives rise to gapless surface states that are protected by symmetry via a bulk-boundary correspondence [1,2]. These conducting states have a linear dispersion (Dirac electrons) arising mainly due to strong spin-orbit coupling. In addition, spin-momentum locking makes surface currents on a TI a promising tool for spintronics applications [3,4]. However, not all materials that feature a Dirac dispersion and a strong spin-orbit coupling are TIs. For instance, pure bismuth is a Dirac-like material featuring a strong spin-orbit coupling, which is not a TI, since its surface states are not protected by symmetry. The protecting symmetry in most TIs is time-reversal invariance (TRI).

In three-dimensional (3D) TIs, the electromagnetic response is characterized by a magnetoelectric term in the Lagrangian [5,6]. Unlike the magnetoelectric term arising in other materials, for example, multiferroics, the magnetoelectric term in TI electrodynamics is intrinsically topological, both due to the topological properties in reciprocal lattice space and in real space. This can be seen by applying an external magnetic field perpendicular to the surface of a 3D TI of thickness L. A computation of the vacuum polarization of two-dimensional Dirac fermions in the presence of an external field for each TI surface yields the action [7,8]

$$S_{\text{vpol}} = \frac{e^2}{8\pi}\int dt \int dx\, dy\, \varepsilon_{\mu\nu\lambda} \times (A^\mu \partial^\nu A^\lambda|_{z=L} - A^\mu \partial^\nu A^\lambda|_{z=0}), \tag{1}$$

where A^μ is the gauge potential corresponding to the external field and we have adopted a covariant notation. In the above equation $z = 0$ and $z = L$ correspond to the lower and upper surfaces, respectively. We work in units where $c = 1$ and $\hbar = 1$. The above action yields the difference between Chern-Simons (CS) terms generated by the vacuum polarization on both surfaces. It can rewritten as the integral of a total derivative,

$$S_{\text{vpol}} = \frac{e^2}{16\pi}\int dt \int dx\, dy \int_0^L dz\, \partial_z(\varepsilon_{\mu\nu\lambda} A^\mu F^{\lambda\nu}) = \frac{e^2}{32\pi}\int d^4x\, \varepsilon_{\mu\nu\lambda\rho} F^{\mu\nu} F^{\lambda\rho}, \tag{2}$$

where $F^{\mu\nu} = \partial^\mu A^\nu - \partial^\nu A^\mu$, and in passing from the first to the second line, the expression has been made fully covariant by introducing an additional spacetime index (ρ) to accommodate the third spatial coordinate in the covariant notation. The above equations follow from the assumption that the Fermi level of each surface state lies precisely at zero, i.e., at the Dirac point of the Dirac spectrum. Moreover, spin-momentum locking implies that the Dirac fermions at the upper surface have a helicity opposite to the lower ones. Thus, we have obtained a magnetoelectric term that is overall time-reversal invariant. A more general form is given by

$$S_{\text{vpol}} = \frac{e^2\theta}{32\pi^2}\int d^4x\, \varepsilon^{\mu\nu\sigma\tau} F_{\mu\nu} F_{\sigma\tau}, \tag{3}$$

where θ is given by [5]

$$\theta = \frac{1}{8\pi}\int d^3k \operatorname{tr}\left[\mathbf{a}(\mathbf{k}) \wedge \mathbf{f}(\mathbf{k}) - \frac{2}{3}\mathbf{a}(\mathbf{k}) \wedge \mathbf{a}(\mathbf{k}) \wedge \mathbf{a}(\mathbf{k})\right], \tag{4}$$

where the 2-form $\mathbf{f}(\mathbf{k})$ yields the Berry curvature,

$$\mathbf{f}(\mathbf{k}) = \mathrm{d}\mathbf{a}(\mathbf{k}) + i\mathbf{a}(\mathbf{k}) \wedge \mathbf{a}(\mathbf{k}), \tag{5}$$

with

$$\mathbf{a}_{\alpha\beta}(\mathbf{k}) = -i\langle \alpha,\mathbf{k}|\nabla_{\mathbf{k}}|\beta,\mathbf{k}\rangle, \tag{6}$$

being the non-Abelian Berry vector potential associated with the Bloch state $|\alpha,\mathbf{k}\rangle$. Thus, the electromagnetic response of 3D TIs yields an interesting interplay between the differential geometry of the Bloch states and the topology of electromagnetic gauge fields in the form of a so-called axionic [9] term, Eq. (3), with θ representing a uniform axion field. The axion is periodic and we find that for $\theta = \pi$ TRI holds, since under a time-reversal transformation $\theta \to -\theta$ [5].

In terms of electric and magnetic field components, the axion term (3) becomes

$$S_{\text{vpol}} = \frac{e^2\theta}{4\pi^2}\int d^4x\, \mathbf{E}\cdot\mathbf{B}. \tag{7}$$

This magnetoelectric contribution is a topological term in real space, as it is more easily seen from the covariant writing, Eq. (3), which clearly exhibits its independence of the metric. Furthermore, in view of Eq. (4) it is also topological in Bloch momentum space due to the induced gauge structure in the Hilbert space of Bloch states.

If TRI at the TI surface is broken in the presence of a magnetically ordered phase, then $\mathbf{B} = \mathbf{H} + 4\pi\mathbf{M}$, and a topological magnetoelectric effect (TME) has been predicted [5,6]. This has inspired many proposals of magnetic TI devices [10–17]. In the TME, an electric field causes a magnetic polarization in the same direction as the field. The TME is the consequence of a CS term generated via the vacuum polarization due to proximity with a ferromagnetic insulator (FMI). If the FMI is epitaxially grown on only one of the TI surfaces, there is only one CS term, in contrast to Eq. (1). The CS term yields an additional Berry phase that modifies the dynamics of the magnetization [13,14].

While previous studies have focused on the magnetic polarization generated by an externally applied electric field, in this paper we address a different important consequence of the TME, namely, its interplay with long-range Coulomb interaction among the Dirac electrons. The Coulomb interaction will generate a fluctuating electric field that interacts with the magnetization. Consequently, a nonlocal TME emerges that significantly impacts on the magnetization dynamics by an effective coupling over large distances.

Taking a similar approach as in Ref. [14], we will carry out explicit calculations of the vacuum polarization contributions to the effective action at zero temperature to leading order in the quantum fluctuations (one-loop diagrams) to derive the dynamics of both the magnetization and the Coulomb electric field at the TI/FMI interface.

II. MODEL SYSTEM

We consider the interface between a FMI layer on top of a TI, as shown in Fig. 1, which we assume to lie in the xy plane. As a starting point, we use on the one hand the Lagrangian density of a bulk FMI,

$$\mathcal{L}_{\text{FMI}} = \mathbf{b}\cdot\partial_t\mathbf{n} - \frac{\kappa}{2}[(\nabla\mathbf{n})^2 + (\partial_z\mathbf{n})^2] - \frac{m^2}{2}\mathbf{n}^2 - \frac{u}{24}(\mathbf{n}^2)^2, \tag{8}$$

where $\mathbf{n}$ is the magnetization, $\mathbf{b}$ is the Berry connection, $m^2 < 0$ for temperatures below the critical temperature of the magnetically ordered phase in the bulk, and κ, u are positive constants. Note that throughout this paper, $\nabla = (\partial_x, \partial_y, 0)$.

On the other hand, the topological Dirac electrons on the surface of a TI are described by

$$\mathcal{L}_{\text{TI}} = \Psi^\dagger(\mathbf{r})[i\partial_t - iv_F(\sigma_y\partial_x - \sigma_x\partial_y) + J\boldsymbol{\sigma}\cdot\mathbf{n}(\mathbf{r})]\Psi(\mathbf{r}), \tag{9}$$

where $\Psi^\dagger(\mathbf{r})$ creates an electron at position $\mathbf{r}$ in the xy plane, v_F is the Fermi velocity, $\boldsymbol{\sigma} = (\sigma_x, \sigma_y, \sigma_z)$ is the vector of Pauli matrices, and $J > 0$ is the strength of the coupling of the electron spin to the magnetization $\mathbf{n}$ at $z = 0$.

In addition, we account for long-range Coulomb interaction between the Dirac electrons at the interface,

$$V = \frac{1}{2}\sum_{\mathbf{q}} \rho(\mathbf{q}) v_{\text{Cou}}(\mathbf{q}) \rho(-\mathbf{q}), \tag{10}$$

where the summation is over the two-dimensional momentum $\mathbf{q}$, the density operator is $\rho(\mathbf{q}) = \sum_{\mathbf{k},s}\Psi^\dagger_{\mathbf{k}+\mathbf{q},s}\Psi_{\mathbf{k},s}$, with spin denoted s, and $v_{\text{Cou}}(\mathbf{q})$ is the Fourier transform of the Coulomb potential $v_{\text{Cou}}(\mathbf{r} - \mathbf{r}') = e^2/|\mathbf{r} - \mathbf{r}'|$ for two electrons at positions $\mathbf{r}$ and $\mathbf{r}'$, where e is the elementary charge and the dielectric constant is $1/(4\pi)$ in Gaussian units. In two dimensions, the potential in reciprocal space takes the form

$$v_{\text{Cou}}(\mathbf{q}) = \frac{2\pi e^2}{|\mathbf{q}|}. \tag{11}$$

The interaction can be made linear in electron density by a Hubbard-Stratonovich decoupling. With an auxiliary scalar field φ, that we define to have the unit of an electric potential, one finds the decoupled Lagrangian

$$\mathcal{L}_{\text{Cou}} = \sum_{\mathbf{q}}\left[e\varphi(\mathbf{q})\rho(\mathbf{q}) - \frac{1}{4\pi}\varphi(-\mathbf{q})|\mathbf{q}|\varphi(\mathbf{q})\right], \tag{12}$$

which combined with Eq. (9) gives the complete real-space Lagrangian density of conduction electrons at the interface,

$$\begin{aligned}\mathcal{L}_{\text{c}} = {} & \Psi^\dagger[i\partial_t + iv_F\hat{\mathbf{e}}_z\cdot(\boldsymbol{\sigma}\times\nabla) + J\boldsymbol{\sigma}\cdot\mathbf{n} + e\varphi]\Psi \\ & -\frac{1}{8\pi^2}[\nabla_{\mathbf{r}}\varphi(\mathbf{r})]\cdot\int d^2r'\,\frac{\nabla_{\mathbf{r}'}\varphi(\mathbf{r}')}{|\mathbf{r} - \mathbf{r}'|}.\end{aligned} \tag{13}$$

where v_F is the Fermi velocity. In total, the bilayer system is described by $\mathcal{L} = \mathcal{L}_{\text{c}} + \mathcal{L}_{\text{FMI}}$.

III. FLUCTUATION EFFECTS

In this section, the quantum fluctuations will be evaluated to leading order by integrating out the electrons. First, we rewrite the fermionic part $\mathcal{L}_{\text{c}}^{\text{f}}$ of $\mathcal{L}_{\text{c}}$ in a form reminiscent of quantum electrodynamics [14]. With the definitions $\boldsymbol{\gamma} = (\gamma^0, \gamma^1, \gamma^2) = (\sigma_0, -i\sigma_x, -i\sigma_y)$, $\mathbf{a} = (\frac{e}{J}\varphi, n_y, -n_x)$, $\partial = (\partial_t, v_F\nabla)$, and the common notations $\overline{\Psi} = \Psi^\dagger\gamma^0$ and $\not{A} = \gamma^\mu A_\mu$, we get

$$\mathcal{L}_{\text{c}}^{\text{f}} = \overline{\Psi}[i\not{\partial} + J(n_z - \not{a})]\Psi. \tag{14}$$

The mean-field value $\mathbf{n}_{\text{MF}} = \sigma_0\hat{\mathbf{e}}_z$ of the magnetization leads to an effective mass $m_\Psi = J\sigma_0$ of the fermion field, while $\tilde{\sigma} = n_z - \sigma_0$ describes the out-of-plane fluctuations. Integrating out the fermions in the standard way [18] then leads to the action

$$S_{\text{c}} = S_{\text{MF}} - \frac{J^2}{2}\text{Tr}[G(\tilde{\sigma} - \not{a})]^2 \tag{15}$$

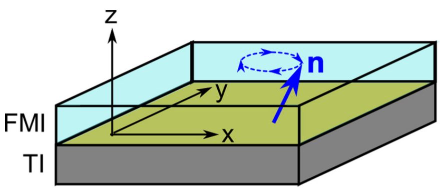

FIG. 1. Magnetization **n** at the interface of a TI and a FMI.

with the propagator $G = (i\not{\partial} + m_\Psi)^{-1}$. We relinquish an analysis of the mean-field action S_{MF}, which has been discussed in detail in Ref. [14], and focus instead on the fluctuation effects. These are contained in the second term δS of Eq. (15), where we have already restricted ourselves to leading order. The operation Tr implies integration over space-.time and tracing out all quantum numbers. Diagrammatically, δS contains four contributions to the vacuum polarization:

$$\delta S = \int \frac{\mathrm{d}^3\lambda}{(2\pi)^3}$$

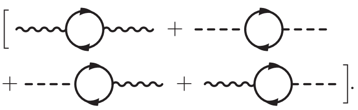

(16)

The fields Ψ, a, and $\tilde{\sigma}$ are represented by solid, wiggly, and dashed lines, respectively, and λ comprises both frequency and momentum. Some details of the calculation of the diagrams can be found in the Appendix. Each of the mixed diagrams in the second line vanishes, and the remaining processes yield in the long-wavelength limit

$$\delta S = \frac{J^2}{8\pi}\int dt \int d^2r \times\left[(\mathbf{a}\times\partial)\cdot\mathbf{a} - \frac{(\partial\times\mathbf{a})^2}{3m_\Psi} - 4m_\Psi\tilde{\sigma}^2 + \frac{(\partial\tilde{\sigma})^2}{3m_\Psi}\right]. \tag{17}$$

Note that scalar products are to be taken in Minkowski space, with signature $(+,-,-)$. As has been discussed earlier [13,14], the term $(\mathbf{a}\times\partial)\cdot\mathbf{a}$ is a fluctuation-induced CS term. In total, we arrive at the following effective Lagrangian for the coupled FMI-TI bilayer system:

$$\begin{aligned}\mathcal{L}_{\mathrm{eff}} = &-\frac{\sigma_{xy}}{2v_F^2}(\mathbf{n}\times\partial_t\mathbf{n})\cdot\hat{\mathbf{e}}_z + \frac{\sigma_{xy}e}{v_F J}\mathbf{n}\cdot\nabla\varphi\\ &-\frac{NJ^2}{24\pi m_\Psi}[(\nabla\cdot\mathbf{n})^2 + (\nabla n_z)^2] + \frac{NJ^2}{24\pi v_F^2 m_\Psi}(\partial_t\mathbf{n})^2\\ &+\frac{Ne^2}{24\pi m_\Psi}(\nabla\varphi)^2 - \frac{NJe}{12\pi v_F m_\Psi}[(\nabla\varphi)\times(\partial_t\mathbf{n})]\cdot\hat{\mathbf{e}}_z\\ &-\frac{NJ^2 m_\Psi}{2\pi v_F^2}n_z^2 + \frac{NJm_\Psi^2}{\pi v_F^2}n_z\\ &+\mathcal{L}_{\mathrm{FMI}} - \frac{1}{8\pi^2}[\nabla_{\mathbf{r}}\varphi(\mathbf{r})]\cdot\int d^2r'\,\frac{\nabla_{\mathbf{r}'}\varphi(\mathbf{r}')}{|\mathbf{r}-\mathbf{r}'|},\end{aligned} \tag{18}$$

where $\hat{\mathbf{e}}_z$ is the unit vector in the z direction. Furthermore, we assumed N orbital degrees of freedom of the Dirac electrons and defined the Hall conductance $\sigma_{xy} = NJ^2/(4\pi)$ in the two contributions from the CS term. The first one describes a Berry phase that adds up with the FMI Berry phase, while the second one leads to the TME. Derivatives of $\tilde{\sigma}$ have been replaced by derivatives of n_z, since σ_0 is constant.

Applying the Euler-Lagrange formalism on $\mathcal{L}_{\mathrm{eff}}$ yields the Landau-Lifshitz equation (LLE) for the magnetization at the interface and the equation of motion for the fluctuating Coulomb potential φ. We arrange the LLE such that all first-order time derivatives of the magnetization are on the left side, such that it takes the form $A\cdot\partial_t\mathbf{n} = \mathbf{d}$ with a matrix A and a vector $\mathbf{d}$ that depends on φ and any other instance of $\mathbf{n}$. Since A then collects precisely the Berry phase terms, it is antisymmetric and we can rewrite $A\cdot\partial_t\mathbf{n} = \mathbf{v}\times\partial_t\mathbf{n}$, where we find

$$\mathbf{v} = \frac{\mathbf{n}}{\mathbf{n}^2} + \frac{\sigma_{xy}}{v_F^2}\hat{\mathbf{e}}_z. \tag{19}$$

The first term stems from the FMI Berry connection $\mathbf{b}$, which satisfies the condition $\partial_{\mathbf{n}}\times\mathbf{b} = -\mathbf{n}/\mathbf{n}^2$. The second term originates with the CS term and enhances the overall Berry phase. If the magnetization is strong, the Berry phase may even be dominated by this topologically protected term. By taking the cross product with $\mathbf{n}$ in both sides of the equation $\mathbf{v}\times\partial_t\mathbf{n} = \mathbf{d}$, we obtain

$$\frac{\mathbf{v}}{2}\partial_t\mathbf{n}^2 - (\mathbf{n}\cdot\mathbf{v})\partial_t\mathbf{n} = \mathbf{n}\times\mathbf{d}. \tag{20}$$

Assuming that $\mathbf{n}^2$ is time independent, Eq. (20) becomes

$$\partial_t\mathbf{n} = \frac{\mathbf{d}\times\mathbf{n}}{1 + \frac{\sigma_{xy}}{v_F^2}(\mathbf{n}\cdot\mathbf{e}_z)}. \tag{21}$$

We split $\mathbf{d} = \mathbf{d}_{\mathbf{n}} + \mathbf{d}_\varphi$ into the magnetization-dependent part

$$\begin{aligned}\mathbf{d}_{\mathbf{n}} = &\rho_s\cdot\nabla^2\mathbf{n} + \frac{NJ^2}{12\pi m_\Psi}\left[\frac{\partial_t^2\mathbf{n}}{v_F^2} + \nabla(\nabla\cdot\mathbf{n})\right]\\ &+\frac{NJm_\Psi}{\pi v_F^2}(Jn_z - m_\Psi)\hat{\mathbf{e}}_z + \left(m^2 + \frac{u}{6}\mathbf{n}^2\right)\mathbf{n},\end{aligned} \tag{22}$$

where the stiffness matrix is $\rho_s = \kappa\mathbb{1} + (NJ^2/12\pi m_\Psi)\mathrm{diag}(0,0,1)$, and the contribution from the Coulomb interaction

$$\mathbf{d}_\varphi = -\frac{\sigma_{xy}e}{v_F J}\nabla\varphi - \frac{NJe}{12\pi v_F m_\Psi}\hat{\mathbf{e}}_z\times\partial_t\nabla\varphi. \tag{23}$$

In addition, we obtain the Euler-Lagrange equation for the field φ. To make the physics more transparent, we write it in terms of the fluctuating electric field $\mathbf{E} = -\nabla\varphi$,

$$\begin{aligned}0 = &\frac{2\pi\sigma_{xy}e}{v_F J}\mathbf{n}_\shortparallel + \frac{Ne}{6m_\Psi}\left(e\mathbf{E} - \frac{J}{v_F}\partial_t\mathbf{n}\times\hat{\mathbf{e}}_z\right)\\ &-\frac{1}{4\pi}\int d^2r'\,\frac{\mathbf{E}(\mathbf{r}')}{|\mathbf{r}-\mathbf{r}'|},\end{aligned} \tag{24}$$

where $\mathbf{n}_\shortparallel$ denotes the in-plane part of the magnetization. This is an explicit form of the fluctuation-induced TME, where the electric field will be aligned with the magnetization, up to a dynamical correction depending on $\partial_t\mathbf{n}$. For the net field and magnetization this correction is irrelevant, since the time average of $\partial_t\mathbf{n}$ vanishes. The first terms in Eqs. (23) and (24) stem from the contribution proportional to $\mathbf{n}\cdot\mathbf{E}$ in the Lagrangian, Eq. (18), representing the usual TME, which is a local effect. In contrast, the last term in Eq. (24) is a direct consequence of the long-range Coulomb interaction, and clearly makes the TME nonlocal by integration over the field at each point in the plane.

The motion of the magnetization becomes more clear when the bosonic field φ in Eq. (18) is integrated out as well. The part of the Lagrangian density that depends on the Coulomb interaction then becomes

$$\mathcal{L}_\varphi(\mathbf{r},t) = \frac{1}{2}\rho_{\mathbf{n}}(\mathbf{r},t)\int d^2r'\,\frac{\rho_{\mathbf{n}}(\mathbf{r}',t)}{|\mathbf{r}-\mathbf{r}'|}, \tag{25}$$

with the induced magnetic charge density,

$$\rho_{\mathbf{n}}(\mathbf{r},t) = \frac{\sigma_{xy} e}{v_F J} \boldsymbol{\nabla} \cdot \mathbf{n}(\mathbf{r},t) - \frac{NJe}{12\pi v_F m_\Psi} [\nabla \times \partial_t \mathbf{n}(\mathbf{r},t)] \cdot \hat{\mathbf{e}}_z. \tag{26}$$

Note that to leading order in momentum, the term involving $(\nabla\varphi)^2$ is negligible compared to the last term in Eq. (18). We observe that the fluctuation-induced magnetic charge contains an additional contribution besides the usual one. Typically, the magnetic charge density is proportional to $\nabla \cdot \mathbf{n}$ and usually arises in studies of magnetic skyrmions [19]. We also obtain a contribution $\sim(\nabla \times \partial_t \mathbf{n}) \cdot \hat{\mathbf{e}}_z$, which does not have a topological origin. From the continuity equation we derive also the magnetic current density,

$$\begin{aligned}\mathbf{j}_{\mathbf{n}} = &-\frac{\sigma_{xy}}{v_F} \partial_t \mathbf{n} \\ &+ \frac{NJe}{24\pi^2 v_F m_\Psi} \int d^2 r' \frac{\mathbf{r} - \mathbf{r}'}{|\mathbf{r} - \mathbf{r}'|^2} [\nabla_{\mathbf{r}'} \times \partial_t \mathbf{n}(\mathbf{r}',t)] \cdot \hat{\mathbf{e}}_z.\end{aligned} \tag{27}$$

The magnetization dynamics is now determined by the integro-differential equation

$$\partial_t \mathbf{n} = \frac{\mathbf{D}_{\mathbf{n}} \times \mathbf{n}}{1 + \frac{\sigma_{xy}}{v_F^2} (\mathbf{n} \cdot \mathbf{e}_z)}, \tag{28}$$

where

$$\mathbf{D}_{\mathbf{n}} = \mathbf{d}_{\mathbf{n}} + \frac{\sigma_{xy} e}{2 v_F J} \mathbf{E} + \frac{NJe}{24\pi v_F m_\Psi} \hat{\mathbf{e}}_z \times \partial_t \mathbf{E}, \tag{29}$$

and the electric field is now given explicitly by

$$\mathbf{E}(\mathbf{r}) = -\int d^2 r' \, \rho_{\mathbf{n}}(\mathbf{r}',t) \frac{(\mathbf{r} - \mathbf{r}')}{|\mathbf{r} - \mathbf{r}'|^3}. \tag{30}$$

The equation of motion can be simplified by an approximation of $\rho_{\mathbf{n}}$. Namely, in the low-frequency regime we can expect the second term in Eq. (26) to be small compared to the first term. Consequently, we find that the Coulomb interaction mainly acts via the CS term. The induced electric field is then independent of $\partial_t \mathbf{n}$, and the equation can be brought into an explicit form similar to Eq. (21).

An important consequence of Eqs. (26) and (28) is that the Coulomb interaction does not directly couple the magnetizations at different points in the plane. Rather, it is the *divergence* of the magnetization that enters into the magnetization dynamics over long distances. This can be understood by the duality of magnetic and electric charges on the surface of a TI [20], where $\nabla \cdot \mathbf{n}$ is equivalent to an electric charge of the magnetic texture. This charge generates a Coulomb field. In the case of a uniform magnetization, where both $\rho_{\mathbf{n}}$ and $\mathbf{E}$ are absent, the Coulomb interaction will thus not affect the magnetization dynamics. We are then left with the LLE (21) with $\mathbf{d} = \mathbf{d}_{\mathbf{n}}$, where also in $\mathbf{d}_{\mathbf{n}}$, all spatial derivatives vanish. From the remaining terms, we simply obtain a precession of the magnetization around the z axis by Eq. (21).

To illustrate how the long-range Coulomb interaction affects the dynamics, we turn to a simple example of a nonuniform magnetization. Assume that the system is prepared with a magnetic texture, where the phase of the precession changes within a narrow region about $x = 0$. The divergence of $\mathbf{n}$ will then be nonzero within that region. The corresponding terms in $\mathbf{d}_{\mathbf{n}}$ will locally alter the magnetization dynamics, trying to align the magnetization at neighboring sites. This will smoothen the transition at $x = 0$ and evoke spin waves spreading in both half planes. However, via the Coulomb interaction, there is an instantaneous impact on the magnetization even far from the texture. For large x, we can assume $\rho_{\mathbf{n}} = \rho_{\mathbf{n},0}\delta(x)$, where $\rho_{\mathbf{n},0}$ oscillates with the precession frequency at $x = 0$, and one readily verifies that $\mathbf{E} = 2\hat{\mathbf{e}}_x \rho_{\mathbf{n},0}/x$. The second and third terms in Eq. (29) lead to in-plane components of the effective field of precession in the x and y directions, respectively, where the latter can be neglected in the low-frequency limit. Thus, the effective field at arbitrary x is already tilted away from the z direction before the spin waves due to the local stiffness terms arrive.

As a final remark, we note that only the in-plane inhomogeneities of the magnetization participate in the Coulomb driven dynamics, while the out-of-plane magnetization does not enter. Therefore, we can expect a similar nonlocal effect if we replace the texture discussed above by a domain wall, as long as the rotation of the magnetization within the transition region happens in a way that involves an in-plane divergence. Apart from evoking Coulomb terms in the magnetization dynamics, the presence of a domain wall in a magnetic layer on a TI also leads to other effects, e.g., chiral currents, that we have not discussed in this paper, but have been subject to a number of previous studies [11,16,21–23].

IV. CONCLUSION

We have analytically studied a TI-FMI interface in the presence of long-range Coulomb interaction and derived the fluctuation-induced dynamics of both the magnetization and the electric field mediating Coulomb interactions, to second order in gradients and fields. We have found that, as a result of long-range interactions, the TME becomes nonlocal, such that the magnetization is coupled to the electric field anywhere in the plane. The CS term in the effective action enhances the overall Berry phase and thus modifies the magnitude of the effective field of the magnetization precession. Magnetic textures involving a divergence of the in-plane magnetization tilt the effective field of the precession in a nonlocal way.

ACKNOWLEDGMENTS

A.S. and S.R. acknowledge support from the Norwegian Research Council, Grants No. 205591/V20 and No. 216700/F20. F.S.N. acknowledges support from the Collaborative Research Center SFB 1143 “Correlated Magnetism: From Frustration to Topology” of the German Research Foundation (DFG).

APPENDIX: CALCULATION OF THE DIAGRAMS

In this Appendix, we present the zero-temperature calculation that leads to Eq. (17). From Eq. (15), we have

$$\delta S = -\frac{J^2}{2} \int dt \int d^2 x \sum_{\varkappa} \langle \varkappa | \mathrm{tr}[G(\tilde{\sigma} - \not{a})]^2 | \varkappa \rangle, \tag{A1}$$

where the trace tr is taken in spin space, $\varkappa$ denotes all other quantum numbers, and the propagator is

$$G = \frac{-i\slashed{\partial} + m_\Psi}{\partial^2 + m_\Psi^2}. \tag{A2}$$

We go to imaginary time by the Wick rotation, $\tau = it$, which makes space-time Euclidean. The Dirac γ matrices are then identical to the Pauli matrices. We find $i\slashed{\partial} \to -\slashed{\partial}$ and $\slashed{\alpha} \to \slashed{\alpha}$, where we defined $\alpha = (a^0, ia^1, ia^2)$. Furthermore, δS is transformed to reciprocal space and the sum over electron quantum numbers is carried out in a basis of plane-wave states, $\varkappa = (\omega, \mathbf{k})$, with frequency ω and two-dimensional momentum $\mathbf{k}$. The frequency and momentum of the bosonic fields α and $\tilde{\sigma}$ in reciprocal space are denoted as $\lambda = (\Omega, \mathbf{q})$. We get

$$\delta S = \frac{iJ^2}{2}\int\frac{d^3\lambda}{(2\pi)^3}\int\frac{d^3\varkappa}{(2\pi)^3}\,\frac{\mathrm{tr}[(m_\Psi + i\slashed{\varkappa})(-\slashed{\alpha}(\lambda) + \tilde{\sigma}(\lambda))(m_\Psi + i(\slashed{\varkappa} - \slashed{\lambda}))(-\slashed{\alpha}(-\lambda) + \tilde{\sigma}(-\lambda))]}{\left(\varkappa^2 + m_\Psi^2\right)\left((\varkappa - \lambda)^2 + m_\Psi^2\right)}, \tag{A3}$$

and the matrix structure inside the remaining trace is now determined by products of Dirac matrices. As one can easily verify by using the commutation and anticommutation relations of the Euclidean Dirac matrices [24,25], $\mathrm{tr}(\gamma_\mu\gamma_\nu) = 2\delta_{\mu\nu}$, $\mathrm{tr}(\gamma_\mu\gamma_\nu\gamma_\lambda) = 2i\varepsilon_{\mu\nu\lambda}$, and $\mathrm{tr}(\gamma_\mu\gamma_\nu\gamma_\lambda\gamma_\rho) = 2(\delta_{\mu\nu}\delta_{\lambda\rho} - \delta_{\mu\lambda}\delta_{\nu\rho} + \delta_{\mu\rho}\delta_{\nu\lambda})$. Inserting these formulas into the numerator of the integrand in Eq. (A3) yields

$$\begin{aligned}
&\mathrm{tr}[\ldots] = \\
&2\alpha_\mu(\lambda)\alpha_\nu(-\lambda)\big[m_\Psi\varepsilon_{\mu\rho\nu}\lambda_\rho + \delta_{\mu\nu}\big(m_\Psi^2 + \varkappa\cdot(\varkappa - \lambda)\big) \\
&\qquad -2\varkappa_\mu\varkappa_\nu + \varkappa_\nu\lambda_\mu + \varkappa_\mu\lambda_\nu\big] \\
&+2\tilde{\sigma}(\lambda)\tilde{\sigma}(-\lambda)\big[m_\Psi^2 - \varkappa\cdot(\varkappa - \lambda)\big] \\
&+2i\tilde{\sigma}(\lambda)\alpha_\mu(-\lambda)[-m_\Psi(\varkappa_\mu - \lambda_\mu) - m_\Psi\varkappa_\mu \\
&\qquad +\varepsilon_{\rho\nu\mu}\varkappa_\rho(\varkappa_\nu - \lambda_\nu)] \\
&+2i\alpha_\mu(\lambda)\tilde{\sigma}(-\lambda)[-m_\Psi(\varkappa_\mu - \lambda_\mu) - m_\Psi\varkappa_\mu \\
&\qquad +\varepsilon_{\rho\mu\nu}\varkappa_\rho(\varkappa_\nu - \lambda_\nu)],
\end{aligned} \tag{A4}$$

corresponding to the four diagrams in Eq. (16). Let these diagrams be called $D_1, \ldots, D_4$, in the same order as in Eq. (16). Next, the integral over $\varkappa$ will be carried out. As has been discussed in Appendix of Ref. [25], one can rewrite the first diagram to take the form

$$\begin{aligned}
D_1(\lambda) = iJ^2a_\mu(\lambda)a_\nu(-\lambda)\Big[&\varepsilon_{\mu\rho\nu}m_\Psi\lambda_\rho I_1(\lambda) \\
&+ P_{\mu\nu}(\lambda)\Big(m_\Psi I_1(\lambda) - \frac{\lambda^2}{4}I_1(\lambda) + \frac{1}{2}I_2\Big)\Big],
\end{aligned} \tag{A5}$$

with the projector $P_{\mu\nu}(\lambda) = \delta_{\mu\nu} - \lambda_\mu\lambda_\nu/\lambda^2$ and the integrals

$$\begin{aligned}
I_1(\lambda) &= \int\frac{d^3\varkappa}{(2\pi)^3}\,\frac{1}{\left(\varkappa^2 + m_\Psi^2\right)\left[(\varkappa - \lambda)^2 + m_\Psi^2\right]} \\
&= \frac{1}{4\pi|\lambda|}\arctan\left(\frac{|\lambda|}{2m_\Psi}\right),
\end{aligned} \tag{A6}$$

$$I_2 = \int\frac{d^3\varkappa}{(2\pi)^3}\,\frac{1}{\varkappa^2 + m_\Psi^2} = -\frac{m_\Psi}{4\pi}, \tag{A7}$$

with the result

$$D_1(\lambda) = iNJ^2\alpha_\mu(\lambda)\alpha_\nu(-\lambda)\left[\frac{\varepsilon_{\mu\rho\nu}\lambda_\rho}{8\pi} - \frac{\lambda^2P_{\mu\nu}(\lambda)}{24\pi m_\Psi}\right] \tag{A8}$$

to second order in λ. Note that I_2 requires dimensional regularization [24], since it is formally divergent. By simple manipulations, one can reduce the second diagram to the same integrals:

$$\begin{aligned}
D_2(\lambda) &= iNJ^2\tilde{\sigma}(\lambda)\tilde{\sigma}(-\lambda)\left[\left(2m_\Psi^2 + \frac{1}{2}\lambda^2\right)I_1(\lambda) - I_2\right] \\
&= iNJ^2\tilde{\sigma}(\lambda)\tilde{\sigma}(-\lambda)\left[\frac{m_\Psi}{2\pi} + \frac{\lambda^2}{24\pi m_\Psi}\right] + \mathcal{O}(\lambda^3).
\end{aligned} \tag{A9}$$

In the two diagrams mixing α and $\tilde{\sigma}$, performing the $\varkappa$ integration leads to $D_3(\lambda) = D_4(\lambda) = 0$. Summing up the contributions from D_1 and D_2 and transforming back to real space and real time finally yields Eq. (17).

[1] M. Z. Hasan and C. Kane, Rev. Mod. Phys **82**, 3045 (2010).

[2] X.-L. Qi and S.-C. Zhang, Rev. Mod. Phys **83**, 1057 (2011).

[3] X.-L. Qi, T. L. Hughes, and S.-C. Zhang, Nat. Phys. **4**, 273 (2008).

[4] T. Yokoyama, Y. Tanaka, and N. Nagaosa, Phys. Rev. B **81**, 121401(R) (2010).

[5] X.-L. Qi, T. L. Hughes, and S.-C. Zhang, Phys. Rev. B **78**, 195424 (2008).

[6] A. M. Essin, J. E. Moore, and D. Vanderbilt, Phys. Rev. Lett. **102**, 146805 (2009).

[7] A. J. Niemi and G. W. Semenoff, Phys. Rev. Lett. **51**, 2077 (1983).

[8] A. N. Redlich, Phys. Rev. D **29**, 2366 (1984).

[9] F. Wilczek, Phys. Rev. Lett. **58**, 1799 (1987).

[10] I. Garate and M. Franz, Phys. Rev. Lett. **104**, 146802 (2010).

[11] Y. Tserkovnyak and D. Loss, Phys. Rev. Lett. **108**, 187201 (2012).

[12] Y. G. Semenov, X. Duan, and K. W. Kim, Phys. Rev. B **86**, 161406(R) (2012).

[13] T. Yokoyama, J. Zang, and N. Nagaosa, Phys. Rev. B **81**, 241410(R) (2010).

[14] F. S. Nogueira and I. Eremin, Phys. Rev. Lett. **109**, 237203 (2012).

[15] J. Wang, B. Lian, X.-L. Qi, and S.-C. Zhang, Phys. Rev. B **92**, 081107(R) (2015).

[16] Y. Ferreiros, F. J. Buijnsters, and M. I. Katsnelson, Phys. Rev. B **92**, 085416 (2015).

[17] T. Morimoto, A. Furusaki, and N. Nagaosa, Phys. Rev. B **92**, 085113 (2015).

[18] J. W. Negele and H. Orland, *Quantum Many-Particle Systems* (Addison-Wesley, Reading, MA, 1988).

[19] N. Nagaosa and Y. Tokura, Nat. Nanotech. **8**, 899 (2013).

[20] K. Nomura and N. Nagaosa, Phys. Rev. B **82**, 161401(R) (2010).

[21] J. Linder, Phys. Rev. B **90**, 041412(R) (2014).

[22] Y. Ferreiros and A. Cortijo, Phys. Rev. B **89**, 024413 (2014).

[23] C. Wickles and W. Belzig, Phys. Rev. B **86**, 035151 (2012).

[24] C. Itzykson and J.-B. Zuber, *Quantum Field Theory* (McGraw-Hill College, Singapore, 1980).

[25] F. S. Nogueira and I. Eremin, Phys. Rev. B **88**, 085126 (2013).

Paper [2]

Stefan Rex, Flavio S. Nogueira, and Asle Sudbø

Topological magnetic dipolar interaction and nonlocal electric magnetization control in topological insulator heterostructures

Physical Review B **94**, 020404(R) (2016)

RAPID COMMUNICATIONS

PHYSICAL REVIEW B **94**, 020404(R) (2016)

Topological magnetic dipolar interaction and nonlocal electric magnetization control in topological insulator heterostructures

Stefan Rex,[1] Flavio S. Nogueira,[2,3] and Asle Sudbø[1]

[1]*Department of Physics, Norwegian University of Science and Technology, N-7491 Trondheim, Norway*
[2]*Institute for Theoretical Solid State Physics, IFW Dresden, PF 270116, 01171 Dresden, Germany*
[3]*Institut für Theoretische Physik III, Ruhr-Universität Bochum, Universitätsstraße 150, DE-44801 Bochum, Germany*

(Received 2 March 2016; revised manuscript received 12 May 2016; published 7 July 2016)

The magnetoelectric effect predicted in topological insulators makes heterostructures that combine magnetic materials and such insulators promising candidates for spintronics applications. Here, we theoretically consider a setup that exhibits two well-separated interfaces between a topological insulator and a ferromagnetic insulator. We show that there is a topological magnetic dipole-dipole interaction stemming from long-range Coulomb interactions. We analytically derive the magnetization dynamics at the two interfaces and discuss how the long-range coupling can be applied to nonlocally induce the formation of a magnetic texture at one interface by suitably gating the other interface.

DOI: 10.1103/PhysRevB.94.020404

Topological insulators (TIs) represent a fascinating and novel state of matter, namely a combined bulk insulator and surface metal with the additional property that the gapless current-carrying surface states are protected from scattering by particle number conservation and time-reversal symmetry [1,2]. When TIs coexist with magnetic order, the magnetization opens a gap in the surface Dirac cone on the topological insulator. This leads to an anomalous quantum Hall effect with a half-integer quantized conductance of $\sigma_{xy}^0 = e^2/(2h)$ [1,3] and a topological magnetoelectric effect (TME) [4] whereby an electric field induces a magnetic polarization in the same direction and vice versa. The latter can be understood from a field theoretic description of the Dirac fermions, which resembles axion electrodynamics [5]. Namely, the TME is evoked by a contribution proportional to $\theta \boldsymbol{E} \cdot \boldsymbol{B}$ in the Lagrangian, where θ is the axion field. This term is of a topological origin and quantized, as only the two values $\theta = 0,\pi$ are allowed by time-reversal symmetry (TRS) of the TI bulk.

Even though conclusive direct evidence of the TME is still pending, the tantalizing idea of magnetization control by electric fields in a topologically protected way has led to intense research. For instance, heterostructures of TIs and ferromagnets have recently attracted much attention as a highly promising platform for spintronics in both theory [6–15] and experiment [16–22]. The strong spin-orbit coupling required to invert the band structure in a TI enables strong spin-orbit torques, and the spin-momentum locking provided by the topological Dirac fermions offers unique possibilities for magnetization control by electrical currents. Envisioned devices based on the TME aim at, for instance, electrically controlled domain wall motion [23–25] and qubits [26] and even indicate a route to topological transistors [27].

Importantly, the TME is a generic feature involving *any* electric field that is present, not only external fields. The setup we propose in this Rapid Communication differs from most previous suggestions in that it takes into account the fluctuating electric field stemming from long-range Coulomb interaction and its impact on the magnetization dynamics in the presence of the TME [6,7]. This is crucial, as the Coulomb interaction always will be present in a real system. For instance, electrostatic coupling between TI surfaces has been reported [28]. We show that Coulomb interactions lead to a topological magnetic dipole-dipole interaction whereby it gives rise to a magnetic anisotropy. Furthermore, we suggest a spintronics nanodevice where this long-range interaction is exploited to couple two otherwise completely independent interfaces between TIs and ferromagnetic insulators (FMIs). A magnetic texture at one interface can then be switched on and off by applying a voltage at the other interface. Measuring this effect would not only serve as a clear evidence of the TME, since no other coupling mechanism exists in the system we consider. It might also inspire device architectures for electric magnetization control where the applied field and the desired response are locally separated in the device.

In Fig. 1, we show a possible TI/FMI multilayer heterostructure for our approach featuring two parallel magnetoelectrically active interfaces. We emphasize that these two interfaces belong to different TI layers and that these two layers are separated by FMI and nonmagnetic insulator layers in a way that no electron hopping or direct magnetic coupling is present. In the following, we will first employ the framework of quantum field theory to obtain the effective Lagrangian of the system in the low-frequency regime after integrating out all quantum fluctuations and show that it contains a topologically protected magnetic dipolar interaction. Then, we derive the Landau-Lifshitz equation (LLE) for magnetization dynamics. Finally, we argue how nonlocal electric magnetization control is possible with a suitable gate placement at one of the interfaces. We work in natural and Gaussian units and assume that the TI and FMI layers are made of the same material, respectively, such that any material constants are the same at the two interfaces. We use the symbol $\boldsymbol{\nabla}$ to denote the two-dimensional differential operator.

We begin by considering the Coulomb interaction, which plays a key role for our results. The well-known three-dimensional r^{-1} potential is acting on charge carriers that are restricted to a plane. A two-dimensional Fourier transformation yields the intraplane potential $2\pi e^2/|\mathbf{q}|$ and the interplane potential $2\pi e^2 \exp(-d|\mathbf{q}|)/|\mathbf{q}|$. Here, e is the

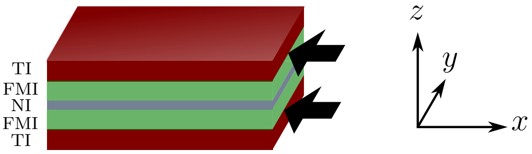

FIG. 1. The structure of the nanodevice: a top and a bottom TI layer sandwich two FMI layers that are separated by a nonmagnetic insulator (NI). At the two interfaces indicated by arrows, the magnetization opens a gap in the TI surface state dispersion, leading to the TME. The interfaces are well separated and interact only via Coulomb interactions. The coordinate system is chosen such that the z axis is pointing out of plane.

elementary charge, $\mathbf{q}$ is the momentum in two dimensions, and d denotes the distance between the two interfaces. The overlap integral of electron orbitals from different interfaces will be zero, since they belong to different TI bulks and are well separated. The only contribution from the Coulomb interaction acting between the interfaces will thus be a density-density interaction, while exchange interactions vanish. To facilitate handling the two-particle interaction, we write it as a single-particle term by introducing the scalar Hubbard-Stratonovich fields φ_i with units of an electric potential. With the operator $\rho_i(\mathbf{q})$ of electron density at interface $i = 1,2$, the potential then has the two contributions $\sum_{i,\mathbf{q}} e\varphi_i(\mathbf{q})\rho_i(\mathbf{q})$ and $\frac{1}{2}\sum_{i,j,\mathbf{q}} \varphi_i(-\mathbf{q})B_{ij}(\mathbf{q})\varphi_j(\mathbf{q})$, where the matrix B now contains the Coulomb-mediated coupling of the interfaces. The matrix entries can be derived from the intra- and interplane potential.

In the low-energy regime, the conduction electrons at the two interfaces can be described by a Lagrangian

$$\mathcal{L}_i = \Psi_i^\dagger[i\partial_t + iv_F(\boldsymbol{\sigma} \times \nabla)\cdot\hat{\mathbf{e}}_z + e(\varphi_i + \phi_i) + J\boldsymbol{\sigma}\cdot\mathbf{n}_i]\Psi_i, \tag{1}$$

with the second-quantized fermion operators $\Psi_i^\dagger, \Psi_i$. It contains the Dirac-cone dispersion proportional to the Fermi velocity v_F, which is typical for TI surface states. As explained above, the electric potential φ_i from the Coulomb interaction enters. In addition, we allow for an externally applied electric field $\mathbf{E}_i = -\nabla\phi_i$. Proximity to an FMI layer induces a magnetization $\mathbf{n}_i$ at each interface that couples to the electron spin with a coupling strength J. The three Pauli matrices are included in the vector $\boldsymbol{\sigma}$. In the anomalous quantum Hall regime, the uniform mean-field magnetization will be orthogonal to the plane and give rise to a mass $m_\Psi = J\langle n_{1z}\rangle = J\langle n_{2z}\rangle$ of the fermion field, thus opening a gap in the Dirac cone. We assume that the Fermi level, ϵ_F, lies inside the gap, either by doping or gating. Thus, there is no loss of generality in considering $\epsilon_F = 0$. Furthermore, note that since φ_i are fluctuating fields, any nonzero ϵ_F can be absorbed into φ_i. The situation is different in the metallic regime where the Fermi level lies outside the gap, in which case Friedel oscillations are expected to occur in the Coulomb interacting system [29].

To account for the ferromagnetism of the bulk FMI layers, we add

$$\mathcal{L}_{\mathrm{FMI,i}} = \mathbf{b}_i\cdot\partial_t\mathbf{n}_i - \frac{\kappa}{2}[(\nabla\mathbf{n}_i)^2 + (\partial_z\mathbf{n}_i)^2], \tag{2}$$

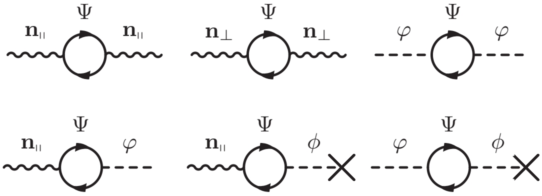

FIG. 2. The topologically distinct one-loop diagrams of vacuum polarization that contribute to the effective action upon integrating out the fermions. Here, $\mathbf{n}_{\|}$ and $\mathbf{n}_{\perp}$ denote the magnetization fluctuations in plane and out of plane, respectively, Ψ is the fermion field, φ is the fluctuating Coulomb potential, and ϕ is the electric potential that is fixed by the externally applied field (indicated with a cross). Diagrams that mix in-plane and out-of-plane fluctuations vanish, and we skipped the ϕ-ϕ diagram, which yields a constant. Magnetoelectric effects are due to the first two diagrams in the second line.

where $(\partial_{\mathbf{n}_i} \times \mathbf{b}_i)\mathbf{n}_i^2 = -\mathbf{n}_i$ and $\kappa > 0$ is the coefficient of exchange energy. Recall that ∇ is two dimensional. We assume that the magnitude of the magnetization is fixed at constant temperature. In total, the model Lagrangian including Coulomb interactions is

$$\begin{aligned}\mathcal{L}_{\mathrm{tot}}(\mathbf{r}) = &\sum_{i=1,2}[\mathcal{L}_i(\mathbf{r}) + \mathcal{L}_{\mathrm{FMI},i}(\mathbf{r})]\\ &+\frac{1}{4\pi}\sum_{i,j=1,2}\sum_{\mathbf{q}}[\nabla\varphi_i(\mathbf{r})]\cdot\int d^2r'\frac{e^{i(\mathbf{r}-\mathbf{r}')\cdot\mathbf{q}}}{|\mathbf{q}|(1-e^{-2|\mathbf{q}|d})}\\ &\times[\delta_{ij} - (1-\delta_{ij})e^{-|\mathbf{q}|d}][\nabla'\varphi_j(\mathbf{r}')].\end{aligned} \tag{3}$$

Since our analysis will mainly focus the magnetoelectric dynamics of the magnetization at the interface, the physics is effectively two dimensional. Furthermore, we will perform the calculations at zero temperature. However, it must be noted that the results obtained here are of relevance for finite-temperature analysis, provided $T \ll m_\Psi$. Due to the proximity coupling to the Dirac fermions at the interface, the system overcomes the Mermin-Wagner theorem so that a finite Curie temperature exists. To see this it is enough to consider a mean-field theory where the dynamics of the magnetization is simply given by $\partial_t\mathbf{n} = \mathbf{n} \times (\mathbf{H}_{\mathrm{eff}} + J\langle\Psi^\dagger\boldsymbol{\sigma}\Psi\rangle)$, where $\mathbf{H}_{\mathrm{eff}} = -\delta\mathcal{H}_{\mathrm{FM}}/\delta\mathbf{n}$, with $\mathcal{H}_{\mathrm{FM}}$ being the Hamiltonian of the ferromagnet. In this case it is easy to show that the magnon spectrum is given by $\omega(q) = m_\Psi[(\kappa/J)q^2 + 1]$, which clearly does not have any infrared singularity.

We now integrate out the fermions, keeping only leading-order terms. More precisely, we consider the one-loop diagrams of vacuum polarization. The relevant topologically distinct diagrams are shown in Fig. 2. The breaking of TRS by the magnetization generates a Chern-Simons (CS) term in the resulting action [4] that leads to the TME $\sim(\mathbf{n} \times \partial_t\mathbf{n})$ and a Berry phase. Since the two interfaces so far are decoupled in the fermion sector, to this point the calculation is identical for $i = 1$ and 2. The field-theoretic treatment of a single interface can be found in Ref. [7]. Next, we proceed to integrate out the Hubbard-Stratonovich fields to unravel the effective magnetic interaction. The Lagrangian for the fields $\mathbf{n}_i(\mathbf{r})$ is then given by

$$
\begin{aligned}
\mathcal{L}(\mathbf{r}) = \sum_{i=1,2} \Bigg(& \mathcal{L}_{\mathrm{FMI},i}(\mathbf{r}) - \frac{\sigma_{xy}}{2v_F^2}[\mathbf{n}_i(\mathbf{r}) \times \partial_t \mathbf{n}_i(\mathbf{r})] \cdot \hat{\mathbf{e}}_z \\
& - \frac{NJ^2}{24\pi m_\Psi}\left\{[\nabla \cdot \mathbf{n}_i(\mathbf{r})]^2 + [\nabla n_{i,z}(\mathbf{r})]^2\right\} \\
& - \frac{NJ^2 m_\Psi}{2\pi v_F^2} n_{i,z}^2(\mathbf{r}) + \frac{NJm_\Psi^2}{\pi v_F^2} n_{i,z}(\mathbf{r}) \\
& - \frac{\sigma_{xy} e}{J v_F}\mathbf{n}_i(\mathbf{r}) \cdot \mathbf{E}_i(\mathbf{r}) \Bigg) + \sum_{i,j=1,2} \frac{\sigma_{xy} e}{2Jv_F}[\nabla \cdot \mathbf{n}_i(\mathbf{r})] \\
& \times \int \frac{d^2r' \rho_j(\mathbf{r}')}{\sqrt{(\mathbf{r}-\mathbf{r}')^2 + (1-\delta_{ij})d^2}} \qquad (4)
\end{aligned}
$$

Here, $\sigma_{xy} = \sigma_{xy}^0 NJ^2/e^2$ is the induced Hall conductivity, assuming N electron orbital degrees of freedom. We have neglected several further terms that are constant or contain time derivatives that are not of leading order in the low-frequency regime. Although we have not included any intrinsic axial anisotropy in the Lagrangian of the FMI proximate to the TI, we note that such an anisotropy has been dynamically generated by Dirac fermion quantum fluctuations, in the form of a term $\sim n_{iz}^2$. Thus, if an intrinsic axial anisotropy is already present in the FMI, the TI surface states will necessarily enhance it. In the last term, ρ_j denotes the effective charge density, which appears in the presence of in-plane divergences of the magnetization and the applied electric field. This is because the electric charge at a TI/FMI interface coincides with the magnetic charge [30]. The charge density is given by

$$
\rho_i = \frac{\sigma_{xy} e}{2v_F J}\nabla \cdot \mathbf{n}_i - \frac{Ne^2}{24\pi m_\Psi}\nabla \cdot \mathbf{E}_i, \qquad (5)
$$

where the first term is of topological origin. Remarkably, the contribution from this topological term to Eq. (4) can be rewritten by partial integrations over both $\mathbf{r}$ and $\mathbf{r}'$ to read

$$
\begin{aligned}
\mathcal{L}_{\mathrm{dipolar}}(\mathbf{r}) = -\left(\frac{\sigma_{xy} e}{2Jv_F}\right)^2 & \sum_{i,j=1,2} \int \frac{d^2r'}{[(\mathbf{r}-\mathbf{r}')^2 + (1-\delta_{ij})d^2]^{3/2}} \\
& \times \left\{ 3\frac{[\mathbf{n}_i^{\parallel}(\mathbf{r}) \cdot (\mathbf{r}-\mathbf{r}')][\mathbf{n}_j^{\parallel}(\mathbf{r}') \cdot (\mathbf{r}-\mathbf{r}')]}{(\mathbf{r}-\mathbf{r}')^2 + (1-\delta_{ij})d^2} \right. \\
& \left. - \mathbf{n}_i^{\parallel}(\mathbf{r}) \cdot \mathbf{n}_j^{\parallel}(\mathbf{r}') \right\}, \qquad (6)
\end{aligned}
$$

where $\mathbf{n}_i^{\parallel} = (n_{ix}, n_{iy}, 0)$. Thus, we have found a magnetic dipole-dipole interaction having an intrinsic topological origin. We note from the effective magnetic field, $\mathbf{H}_{\mathrm{eff}}^{(i)} = -\partial\mathcal{H}/\partial\mathbf{n}_i$, that it is the dipolar interaction that connects the two interfaces via the in-plane magnetization. Here $\mathcal{H}$ is the Hamiltonian associated to the effective Lagrangian (4), i.e., by removing the Berry phase terms.

Typically, dipolar interactions generate a magnetic anisotropy, turning the susceptibility nondiagonal. Indeed, it is easy to see from Eqs. (4) and (6) that the susceptibilities for the spin-wave modes in the interfaces and across them feature transverse and longitudinal components, and have the form $\chi_{\alpha\beta}^{ii}(\omega,\mathbf{q}) = \chi_T^{ii}(\omega,q)(\delta_{\alpha\beta} - q_\alpha q_\beta/q^2) + \chi_L^{ii}(\omega,q)q_\alpha q_\beta/q^2$, $\chi_{\alpha\beta}^{12}(\omega,\mathbf{q}) = \chi_{\alpha\beta}^{21}(\omega,\mathbf{q}) = \chi_T^{12}(\omega,q)(\delta_{\alpha\beta} - q_\alpha q_\beta/q^2) + \chi_L^{12}(\omega,q)q_\alpha q_\beta/q^2$, where $\alpha,\beta = x,y$ and $\chi_{zz}^{ii}(\omega,q)$ describes the gapped, longitudinal (in field space) mode. The spin-wave mode across the interfaces decays exponentially with the thickness in momentum space. Moreover, there is no longitudinal field mode propagating between the interfaces. Dipolar interactions are normally considerably smaller than exchange interactions. However, they are known to be as large as exchange interactions in some ferromagnetic insulators, such as europium monochalcogenides [31]. The dipolar interaction (6) is quantized due to the TME. An estimate can be given based on recent experiments on $\mathrm{Bi_2Se_3}$-EuS heterostructures [16,21]. Using $\hbar v_F = 2.17$ eV Å and assuming that $J \approx 90$ meV, we estimate a dipolar interaction roughly having a strength $\sim$1 meV. Note how the prefactor in Eq. (6) is independent of the fermionic gap m_Ψ. Thus, the topologically induced dipolar term is expected to play a role also above the Curie temperature of the system. In principle, the anisotropy in the susceptibility can be probed in the static limit via polarized neutron scattering techniques, similar to the one used in Ref. [32] to probe the dynamics of longitudinal and transverse fluctuations in EuS. Since Eq. (6) involves only the planar components of the magnetization, it is particularly sensitive to polarized neutron reflectometry (PNR) experiments, since PNR only measures the in-plane components of the magnetization. In the context of TI heterostructures, PNR has recently been successfully used to probe the magnetization for a wide range of temperatures near the interface between $\mathrm{Bi_2Se_3}$ and EuS in a TI/FMI bilayer structure [21]. The same method can in principle be used to find evidence of a dipolar magnetic anisotropy arising from TME.

From Eq. (4), we derive the LLE at interface i,

$$
\left(\frac{\mathbf{n}_i}{\mathbf{n}_i^2} + \frac{\sigma_{xy}}{v_F^2}\hat{\mathbf{e}}_z\right) \times \partial_t \mathbf{n}_i = \mathbf{d}_{\mathbf{n},i} + \mathbf{d}_{\mathbf{E},i} + \mathbf{d}_{\mathrm{Cou},i}, \qquad (7)
$$

which describes precession around an effective field $\mathbf{d}_i$. The second term inside the parentheses stems from the additional Berry phase generated by the CS term. The effective field consists of three contributions: $\mathbf{d}_{\mathbf{n},i}$ describes the local spin dynamics and is given by

$$
\begin{aligned}
\mathbf{d}_{\mathbf{n},i} = \rho_{\mathrm{s}} \cdot (\nabla^2 \mathbf{n}_i) + \frac{NJ^2}{12\pi m_\Psi}\nabla(\nabla \cdot \mathbf{n}_i) \\
+ \frac{NJm_\Psi}{\pi v_F^2}(Jn_{i,z} - m_\Psi)\hat{\mathbf{e}}_z, \qquad (8)
\end{aligned}
$$

with the spin-stiffness matrix $\rho_{\mathrm{s}} = \mathrm{diag}[\kappa,\kappa,\kappa + NJ^2/(12\pi m_\Psi)]$. The last line reflects the dynamically generated axial anisotropy and leads to precession around the out-of-plane axis even if the magnetization is uniform. The vectors $\mathbf{d}_{\mathbf{E},i} = \sigma_{xy}e/(Jv_F)\mathbf{E}_i$ and $\mathbf{d}_{\mathrm{Cou},i} = \sigma_{xy}e/(Jv_F)\mathbf{E}_{\mathrm{Cou},i}$ are due to the TME involving the external field and the Coulomb field of the charge density Eq. (5), respectively. Thus, $\mathbf{d}_{\mathrm{Cou},i}$ is nonlocal and contains both in-plane and interplane interactions. The Coulomb field at interface i is given by

$$
\mathbf{E}_{\mathrm{Cou},i}(\mathbf{r}) = -\sum_{j=1,2}\int d^2r' \frac{(\mathbf{r}-\mathbf{r}')\rho_j(\mathbf{r}')}{[(\mathbf{r}-\mathbf{r}')^2 + (1-\delta_{ij})d^2]^{3/2}}. \qquad (9)
$$

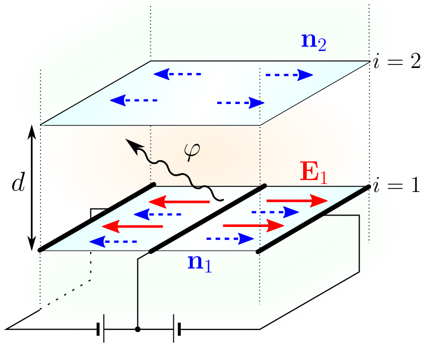

FIG. 3. Schematic depiction of the mechanism for a specific gate placement: At interface 1, a voltage between the middle and edge gates (bold black lines) leads to an electric field $\mathbf{E}_1$ (solid red arrows) with an in-plane divergence. By the TME, the in-plane component of the magnetization (dashed blue arrows) $\mathbf{n}_1$ aligns with the field, resulting in a charged texture that gives rise to a Coulomb potential φ. The Coulomb field causes the magnetization $\mathbf{n}_2$ at interface 2 to develop a magnetic texture as well.

Equations (5) and (9) describe the effective nonlocal interaction between magnetic moments in the system. We find that a charge density at *one* interface leads to a net in-plane magnetic texture at *both* interfaces.

Based on this topological coupling mechanism, we propose a spintronics device for nonlocal electric magnetization control, where we adopt the following strategy: One of the magnetoelectrically active interfaces is gated such that the electric field will have an in-plane divergence. By the TME, the magnetization at the same interface will develop a net in-plane component that is aligned with the field. Thus, a charge density according to Eq. (5) is induced and creates a field, cf. Eq. (9), that finally causes a magnetic texture to emerge at the other interface. A specific gate geometry is shown in Fig. 3, where we consider the impact of an applied electric field at $i=1$ on the magnetic texture at $i=2$. We place three gates, where the two outer ones lie at the same potential, and a voltage is applied between them and the middle gate such that the electric field will have opposite orientation in the two half-planes. Consequently, a charge density emerges along the middle gate, where $\nabla\cdot\mathbf{E}_1$ and $\nabla\cdot\mathbf{n}_1$ become large. Due to the Coulomb field, the net magnetization at interface 2 will develop an opposite in-plane component in the two half-planes. Thus, we obtain a magnetic texture without any local manipulations. This texture can be switched on and off by means of the voltage applied at the first interface. We note that in principle any setup where the applied field has a divergence would work.

Besides applications for electric magnetization control, measuring the magnetic texture at interface 2 would also be an intriguing demonstration of the TME. The interplane coupling mechanism is topologically protected. Namely, the TME that translates the diverging field into a magnetic charge density at interface 1, the correspondence of magnetic and electric charge, and the TME with the Coulomb field at interface 2 are all topologically protected. Furthermore, the device is constructed in such a way that other long-range interactions are excluded. One could think of a seemingly simpler heterostructure than the one shown in Fig. 1, where a single TI layer is coated with FMI layers on both sides, such that the active interfaces are opposite surfaces of the same TI bulk. In that case, however, the electric field could, at least close to the sample edges, directly leak around the topological side surfaces onto the other interface and interfere with the magnetization there, circumventing the desired long-range coupling of purely topological origin. The nonmagnetic insulator layer in our setup also prevents spin waves from traveling from one interface to the other.

In conclusion, we have analytically derived a topological magnetic dipole-dipole interaction that emerges from long-range Coulomb interactions in the presence of the TME. It generates a magnetic anisotropy that could, e.g., be probed by PNR. We presented analytical results for the magnetization dynamics in a heterostructure with two well-separated parallel TI/FMI interfaces and demonstrated that the long-range interactions enable nonlocal electric control of a magnetic texture at one interface by applying a voltage at the other interface. We believe that these results are experimentally accessible with the existing technology.

S.R. and A.S. acknowledge support by the Norwegian Research Council, Grants No. 205591/V20 and No. 216700/F20. F.S.N. would like to thank the Collaborative Research Center SFB 1143 “Correlated Magnetism: From Frustration to Topology” for the financial support.

[1] M. Z. Hasan and C. L. Kane, Rev. Mod. Phys. **82**, 3045 (2010).
[2] X.-L. Qi and S.-C. Zhang, Rev. Mod. Phys. **83**, 1057 (2011).
[3] Y. Zheng and T. Ando, Phys. Rev. B **65**, 245420 (2002).
[4] X.-L. Qi, T. L. Hughes, and S.-C. Zhang, Phys. Rev. B **78**, 195424 (2008).
[5] F. Wilczek, Phys. Rev. Lett. **58**, 1799 (1987).
[6] F. S. Nogueira and I. Eremin, Phys. Rev. Lett. **109**, 237203 (2012).
[7] S. Rex, F. S. Nogueira, and A. Sudbø, Phys. Rev. B **93**, 014404 (2016).
[8] I. Garate and M. Franz, Phys. Rev. Lett. **104**, 146802 (2010).
[9] T. Yokoyama, J. Zang, and N. Nagaosa, Phys. Rev. B **81**, 241410 (2010).
[10] Y. G. Semenov, X. Duan, and K. W. Kim, Phys. Rev. B **86**, 161406 (2012).
[11] C. Wickles and W. Belzig, Phys. Rev. B **86**, 035151 (2012).
[12] F. S. Nogueira and I. Eremin, Phys. Rev. B **88**, 085126 (2013).
[13] A. G. Mal’shukov, H. Skarsvåg, and A. Brataas, Phys. Rev. B **88**, 245122 (2013).
[14] J. Wang, B. Lian, X.-L. Qi, and S.-C. Zhang, Phys. Rev. B **92**, 081107(R) (2015).

[15] Y. Ferreiros, F. J. Buijnsters, and M. I. Katsnelson, Phys. Rev. B **92**, 085416 (2015).

[16] P. Wei, F. Katmis, B. A. Assaf, H. Steinberg, P. Jarillo-Herrero, D. Heiman, and J. S. Moodera, Phys. Rev. Lett. **110**, 186807 (2013).

[17] Q. I. Yang, M. Dolev, L. Zhang, J. Zhao, A. D. Fried, E. Schemm, M. Liu, A. Palevski, A. F. Marshall, S. H. Risbud, and A. Kapitulnik, Phys. Rev. B **88**, 081407(R) (2013).

[18] Y. Fan, P. Upadhyaya, X. Kou, M. Lang, S. Takei, Z. Wang, J. Tang, L. He, L.-T. Chang, M. Montazeri, G. Yu, W. Jiang, T. Nie, R. N. Schwartz, Y. Tserkovnyak, and K. L. Wang, Nat. Mat. **13**, 699 (2014).

[19] A. R. Mellnik, J. S. Lee, A. Richardella, J. L. Grab, P. J. Mintun, M. H. Fischer, A. Vaezi, A. Manchon, E.-A. Kim, N. Samarth, and D. C. Ralph, Nature (London) **511**, 449 (2014).

[20] M. Li, C.-Z. Chang, B. J. Kirby, M. E. Jamer, W. Cui, L. Wu, P. Wei, Y. Zhu, D. Heiman, J. Li, and J. S. Moodera, Phys. Rev. Lett. **115**, 087201 (2015).

[21] F. Katmis, V. Lauter, F. S. Nogueira, B. A. Assaf, M. E. Jamer, P. Wei, B. Satpati, J. W. Freeland, I. Eremin, D. Heiman, P. Jarillo-Herrero, and J. S. Moodera, Nature (London) **533**, 513 (2016).

[22] Y. Wang, P. Deorani, K. Banerjee, N. Koirala, M. Brahlek, S. Oh, and H. Yang, Phys. Rev. Lett **114**, 257202 (2015).

[23] Y. Tserkovnyak and D. Loss, Phys. Rev. Lett. **108**, 187201 (2012).

[24] Y. Ferreiros and A. Cortijo, Phys. Rev. B **89**, 024413 (2014).

[25] J. Linder, Phys. Rev. B **90**, 041412(R) (2014).

[26] G. J. Ferreira and D. Loss, Phys. Rev. Lett. **111**, 106802 (2013).

[27] J. Liu, T. H. Hsieh, P. Wei, W. Duan, J. Moodera, and L. Fu, Nat. Mat. **13**, 178 (2014).

[28] V. Fatemi, B. Hunt, H. Steinberg, S. L. Eltinge, F. Mahmood, N. P. Butch, K. Watanabe, T. Taniguchi, N. Gedik, R. C. Ashoori, and P. Jarillo-Herrero, Phys. Rev. Lett. **113**, 206801 (2014).

[29] Absorbing ϵ_F into φ_i does not make the Fermi level irrelevant, since in this case the Fermi momentum is given by $k_F^2 = \sqrt{\epsilon_F^2 - m_\Psi^2}$.

[30] K. Nomura and N. Nagaosa, Phys. Rev. B **82**, 161401(R) (2010).

[31] A. Kasuya and M. Tachiki, Phys. Rev. B **8**, 5298 (1973).

[32] P. Böni, D. Görlitz, J. Kötzler, and J. L. Martínez, Phys. Rev. B **43**, 8755(R) (1991).

Paper [3]

Stefan Rex, Flavio S. Nogueira, and Asle Sudbø

Topological staggered field electric effect with bipartite magnets

Physical Review B **95**, 155430 (2017)

PHYSICAL REVIEW B **95**, 155430 (2017)

Topological staggered field electric effect with bipartite magnets

Stefan Rex,[1] Flavio S. Nogueira,[2,3] and Asle Sudbø[1]
[1] *Department of Physics, Norwegian University of Science and Technology, N-7491 Trondheim, Norway*
[2] *Institute for Theoretical Solid State Physics, IFW Dresden, PF 270116, D-01171 Dresden, Germany*
[3] *Institut für Theoretische Physik III, Ruhr-Universität Bochum, Universitätsstraße 150, D-44801 Bochum, Germany*

(Received 21 February 2017; published 19 April 2017)

We study the interface physics of bipartite magnetic materials deposited on a topological insulator. Our study comprises antiferromagnets as well as ferrimagnets and ferromagnets with multiple magnetic moments per unit cell. If an energy gap is induced in the Dirac states on the topological surface, a topological magnetoelectric effect has been predicted. Here, we show that this effect can act in opposite directions on the two components of the magnet in a certain parameter region. Consequently, an electric field will mainly generate a staggered field rather than a net magnetization in the plane. This result is relevant for current attempts to detect the magnetoelectric effect experimentally, as well as for possible applications. We take a field-theoretic approach that includes the quantum fluctuations of both the Dirac fermions on the topological surface and the fermions in the surface layer of the magnet in an analytically solvable model. The effective Lagrangian and the Landau-Lifshitz equation describing the interfacial magnetization dynamics are derived.

DOI: 10.1103/PhysRevB.95.155430

I. INTRODUCTION

Since their discovery, topological insulators (TIs) [1,2] have attracted much attention due to their unique surface properties. In three-dimensional TIs, every surface exhibits linearly dispersing conducting states inside the bulk band gap. These can be described as Dirac fermions and exhibit spin-momentum locking. If time-reversal symmetry (TRS) at the surface is broken by an orthogonal net magnetization, the Dirac states become massive; that is, a gap opens in their energy dispersion. It has been shown that this generates a Chern-Simons (CS) term in the effective field theory which imposes a topological magnetoelectric (TME) effect [3,4] on the surface, where an electric field induces a net in-plane magnetization. This distinct response to an electromagnetic field is a hallmark of the TI phase.

Magnetic order on the TI surface can be established by doping with $3d$ transition metals [5–11], proximity coupling to a magnetic insulator in bilayer structures [12–16], or a combination of both [17]. In [15], a magnetization orthogonal to the surface was realized even at room temperature in EuS-Bi_2Se_3 bilayers. In theoretical works, a broad range of potential applications of such heterojunctions combining ferromagnetic insulators (FMIs) and TIs has been suggested, e.g., related to spintronics [18–28], and several further implications of the TME effect have been discussed, including the formation of magnetic monopoles [29] and the interplay with long-range Coulomb interaction [28,30,31].

So far, not much focus has been directed at more general classes of magnetic materials. Mostly, it is assumed that the TME effect will occur in the same way as long as a net magnetization is present. However, several technologically relevant materials do not have a simple ferromagnetic (FM) structure and are instead ferrimagnets (FiMs) or antiferromagnets (AFMs). For instance, one of the most prominent materials for spintronics devices is yttrium iron garnet (YIG), a FiM with a complicated crystal structure [32,33]. In YIG, an enhancement of the magnetization has recently been observed in a bilayer structure YIG-Bi_2Se_3, where Bi_2Se_3 is doped with Cr [16]. It is thus natural to ask if and how the topological effects will manifest in multicomponent FMIs, FiMs, or AFM insulators. In AFMs, there is no net magnetization (except in some cases for special surface orientations [34]). However, a gap can still be opened at the Dirac points, as in the FM and FiM cases, by means of magnetic doping in the TI. Such a system has recently been realized experimentally [35].

In the present paper, we study a bilayer heterostructure consisting of a bipartite magnetic insulator (BMI) and a TI. We show that, depending on the microscopic parameters of the BMI, the TME effect can take the opposite sign on the two sublattices, turning the overall electric-field response from a TME effect into a topological staggered-field-electric (TSE) effect. Our calculation is to be understood as a proof of principle, as the model we employ is simplified and may not suffice to make quantitative predictions. On the other hand, we are able to obtain fully analytic solutions within a field-theoretic approach that accounts for the fermionic quantum fluctuations on both the BMI and TI surfaces. We will derive the effective Lagrangian, revealing the structure of the magnetoelectric response, and the Landau-Lifshitz equation (LLE) of the interfacial magnetization dynamics. We work in Gaussian units and set $\hbar = 1$. All calculations are done at zero temperature. This is justified as long as the Fermi level is tuned to lie in the induced energy gap, for instance. by gating of the interface.

The model we use is described in the following section. We discuss the nontopological fluctuation effects originating with the electrons on the BMI surface in Sec. III, and then we move on to the topological effects that are revealed upon integrating out the Dirac states in Sec. IV. We summarize our results in Sec. V.

II. MODEL SYSTEM

Describing the heterostructure, one has to account for the contributions from the bulk of the BMI, the surfaces of the BMI and the TI, hopping across the interface due to proximity, and Coulomb interactions between the Dirac electrons at the

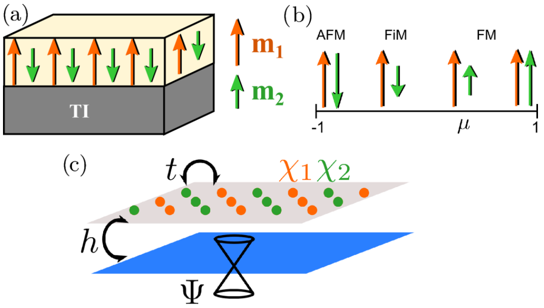

FIG. 1. The model system: (a) Bilayer heterostructure consisting of a bipartite magnetic insulator (BMI) deposited on a topological insulator (TI). (b) By means of the parameter $\mu = \overline{m}_2/\overline{m}_1$, the magnet can be tuned to be in an antiferromagnetic (AFM), ferrimagnetic (FiM), or ferromagnetic (FM) configuration at mean field. (c) The model involves fermionic fields Ψ and $\chi_{1,2}$ on the surfaces of both the TI (blue plane) and the BMI (gray plane), respectively, which are coupled by the amplitudes h (hopping across the interface) and t (local coupling of the two sublattices).

interface. The bulk of the TI is required to guarantee the existence of the topological surface states but does not appear explicitly. The model system is illustrated in Fig. 1.

We start with the surface of the TI which is chosen to be the (x,y) plane and is described by the Dirac Lagrangian,

$$\mathcal{L}_{\rm D} = \Psi^\dagger[i\partial_t - iv_F(\sigma_y\partial_x - \sigma_x\partial_y) + e(\varphi + \phi)]\Psi, \qquad (1)$$

where $\Psi = [\psi_\uparrow\psi_\downarrow]^T$ are the surface Dirac fermions, v_F is the Fermi velocity, φ is the fluctuating potential of Coulomb interactions among the Dirac fermions, and ϕ is any externally applied electric potential. A term quadratic in φ describes the Coulomb interaction in the plane [28,30,31]:

$$\mathcal{L}_{\rm Cou}(\mathbf{r}) = -\frac{1}{8\pi^2}[\nabla_\parallel\varphi(\mathbf{r})]\cdot\int d^2r'\frac{\nabla'_\parallel\varphi(\mathbf{r}')}{|\mathbf{r}-\mathbf{r}'|}, \qquad (2)$$

where $\nabla_\parallel = (\partial_x,\partial_y)$ denotes the in-plane gradient operator.

We model the bulk bipartite magnetic material as two interpenetrating FMs (denoted by indices $i = 1,2$) that are coupled by an exchange interaction, $\mathcal{L}_{\rm bulk} = \mathcal{L}_1 + \mathcal{L}_2 + \mathcal{L}_{\rm ex}$, where

$$\mathcal{L}_i = -\mathbf{b}(\mathbf{m}_i)\cdot\partial_t\mathbf{m}_i - \frac{\kappa}{2}(\nabla\mathbf{m}_i)^2 \qquad (3)$$

and

$$\mathcal{L}_{\rm ex}(\mathbf{r}) = -\lambda\mathbf{m}_1(\mathbf{r})\cdot\mathbf{m}_2(\mathbf{r}). \qquad (4)$$

Here, $\mathbf{b}$ is the Berry connection, which satisfies $\nabla_{\mathbf{m}_i}\times\mathbf{b}(\mathbf{m}_i) = \mathbf{m}_i/m_i^2$, $\kappa > 0$ is the FM exchange energy, and $\lambda > 0$ (< 0) for AFM (FM) coupling of the two components. In the bulk model, we ignore anisotropy terms. It turns out that the system intrinsically contains anisotropy, and additional bulk contributions would not qualitatively alter the physics.

In order to describe the surface Berry phases associated with the two sublattices, we introduce fermionic fields $\chi_i = [\chi_{i\uparrow}\chi_{i\downarrow}]^T$, $i = 1,2$, representing sublattice indices, which when integrated out generate the desired surface Berry phases. This procedure to generate Berry phases is well known in the literature [36,37] and is very useful in our case because it permits coupling the underlying sublattice fermions to the Dirac surface states. The surface layer of the bipartite magnetic insulator is thus described by the Hamiltonian,

$$\mathcal{H}_{\rm surf} = -t(\chi_1^\dagger\chi_2 + \chi_2^\dagger\chi_1) - J\sum_{i=1,2}\mathbf{m}_i\cdot\chi_i^\dagger\boldsymbol{\sigma}\chi_i, \qquad (5)$$

where J is the strength of the exchange coupling to the respective magnetization $\mathbf{m}_i(z=0)$, $\boldsymbol{\sigma}$ are the Pauli matrices, and t is a parameter coupling the surface fermions of the BMI on different sublattices. It will be crucial in obtaining a TSE effect and also leads to mixed Berry phase terms originating on the different sublattices. When $t = 0$, the surface Berry phases decouple and just correspond to a shift of the Berry phases already present in Eq. (3). Note that the Lagrangian accounts only for coupling of fermions χ_1 and χ_2 within one unit cell, thus being momentum independent in the continuum limit. Further electron dynamics (gradient terms) is neglected. This rough approximation is valid as long as the magnet is a strong insulator and the gap is much larger than the induced gap in the Dirac states. It does not spoil the generation of the surface Berry phases, however. Furthermore, the lattice model of the surface of the magnet does not explicitly include nearest-neighbor exchange interactions, which are already captured by the Lagrangian of the magnetic bulk. The chemical potential is set to zero for the electrons on both surfaces because the Fermi level is assumed to be tuned to lie in the gap.

If the surfaces of the TI and the AFM or FiM are in proximity to each other, there is also an amplitude h that couples the surface fermions of the magnetic insulator to the surface fermions of the topological insulator,

$$\mathcal{L}_{\rm int} = h[\Psi^\dagger(\chi_1 + \chi_2) + (\chi_1^\dagger + \chi_2^\dagger)\Psi]. \qquad (6)$$

Our calculation amounts to integrating out all fermionic fields in order to obtain an effective theory of the magnetization.

III. QUANTUM FLUCTUATIONS OF THE SUBLATTICE FERMIONS

We start by integrating out the fermions χ_i of the BMI surface to obtain an effective model for the Dirac fermions Ψ. We assume that the mean-field direction of the magnetization is orthogonal to the interface, such that a mass in the Dirac states can be induced. We write $\mathbf{m}_i^{\rm mf} = \overline{m}_i\hat{\mathbf{e}}_z$ and define the dimensionless parameter $\mu = \overline{m}_2/\overline{m}_1$, where without loss of generality $|\mu| \leqslant 1$. Then, $\mu > 0$ describes a FM, $-1 < \mu < 0$ describes a FiM, and $\mu = -1$ describes an AFM [Fig. 1(b)]. We also introduce $\tau = t^2/J^2\overline{m}_1^2$, which will be useful later. From Eq. (5), we define a matrix

$$A = \begin{pmatrix} i\partial_t + J\mathbf{m}_1\cdot\boldsymbol{\sigma} & t \\ t & i\partial_t + J\mathbf{m}_2\cdot\boldsymbol{\sigma}\end{pmatrix}, \qquad (7)$$

such that the action of the surface of the magnetic insulator is symbolically written as $\mathcal{S}_{\rm surf} = \chi^\dagger A\chi$, where $\chi^\dagger = (\chi_1^\dagger,\chi_2^\dagger)$. The integral over space-time is implicit in this symbolic representation. We use a spinor $\tilde{\Psi}^\dagger = (\Psi^\dagger,\Psi^\dagger)$ that contains the same Dirac fermion twice to write $\mathcal{L}_{\rm int} = h\chi^\dagger\tilde{\Psi} + {\rm H.c.}$ We next proceed by integrating out the magnetic surface fermions χ,

$$\begin{aligned}\mathcal{Z} &= \int D[\overline{\chi},\chi]\, e^{i\int dt \int d^2r(\mathcal{L}_{\rm surf}+\mathcal{L}_{\rm int})} \\ &= \int D[\overline{\chi},\chi]\, e^{i(\chi^\dagger A\chi - h\chi^\dagger\tilde{\Psi} - h\tilde{\Psi}^\dagger\chi)} \\ &= \exp(i\mathrm{Tr}\,\ln A + ih^2\tilde{\Psi}^\dagger A^{-1}\tilde{\Psi}). \qquad (8)\end{aligned}$$

Note that the notation Tr contains the integration over the quantum numbers in addition to the matrix trace. We will discuss the two terms in the last line separately in the following sections.

A. Surface corrections to the bulk terms

The term Tr ln A in Eq. (8) is independent of the topological Dirac states. It leads to the Berry phases mentioned previously and renormalizes the magnetic bulk terms at the surface. Details of the calculation and complete analytical expressions can be found in Appendix A. We finally obtain

$$\begin{aligned}&\delta\mathcal{L}_{\rm mag}(\mathbf{r},t)\\ &\quad= -2J^2\mathbf{m}_1\cdot\mathrm{diag}(T^{00}-T^{zz},T^{00}-T^{zz},T^{00}+T^{zz})\cdot\mathbf{m}_2\\ &\qquad+2J^2\sum_{i=1,2}\{[(D_i^{00}+D_i^{zz})\overline{m}_i+(T^{00}+T^{zz})\overline{m}_{3-i}]m_{iz}\\ &\qquad-D_i^{zz}m_{iz}^2+\mathcal{D}_i^{0z}\hat{\mathbf{e}}_z\cdot[\mathbf{m}_i(\mathbf{r},t)\times\partial_t\mathbf{m}_i(\mathbf{r},t)]\}\\ &\qquad+2J^2\mathcal{T}^{0z}\hat{\mathbf{e}}_z\cdot[\mathbf{m}_1(\mathbf{r},t)\times\partial_t\mathbf{m}_2(\mathbf{r},t)\\ &\qquad+\mathbf{m}_2(\mathbf{r},t)\times\partial_t\mathbf{m}_1(\mathbf{r},t)], \qquad (9)\end{aligned}$$

where $D_i^{00},D_i^{zz},\mathcal{D}_i^{0z},T^{00},\mathcal{T}^{0z}$, and T^{zz} are functions of $t,J,\overline{m}_i$, and the lattice spacing a. The Berry phases are represented by the cross-product terms. The terms proportional to $\mathcal{D}_i^{0z}$ shift the Berry phases introduced in Eq. (3), while the term proportional to $\mathcal{T}^{0z}$ is a mixed Berry phase term. We remark that $\mathcal{T}^{0z}\propto t$; thus, no mixed Berry phase appears if $t=0$.

Furthermore, the coupling of $\mathbf{m}_1$ and $\mathbf{m}_2$ given by Eq. (4) is renormalized by the first line in Eq. (9) and becomes anisotropic. This leads to in-plane and out-of-plane effective exchange couplings given by

$$\lambda_{\rm eff}^{\parallel} = \lambda + 2J^2(T^{00}-T^{zz}), \qquad (10)$$

$$\lambda_{\rm eff}^{\perp} = \lambda + 2J^2(T^{00}+T^{zz}). \qquad (11)$$

An evaluation of our analytic expressions (Appendix A) reveals that the dynamically generated coupling favors AFM alignment of the two magnetic components. Indeed, using Eqs. (A19) and (A21) of Appendix A, we obtain

$$T^{00}-T^{zz} = \frac{t^2\left[2|t^2-J^2\overline{m}_1\overline{m}_2|+2t^2+J^2\left(\overline{m}_1^2+\overline{m}_2^2\right)\right]}{2a^2|t^2-J^2\overline{m}_1\overline{m}_2|(M_+ + M_-)^3}, \qquad (12)$$

$$T^{00}+T^{zz} = \frac{t^2[1+\mathrm{sgn}(t^2-J^2\overline{m}_1\overline{m}_2)]}{a^2(M_+ + M_-)^3}, \qquad (13)$$

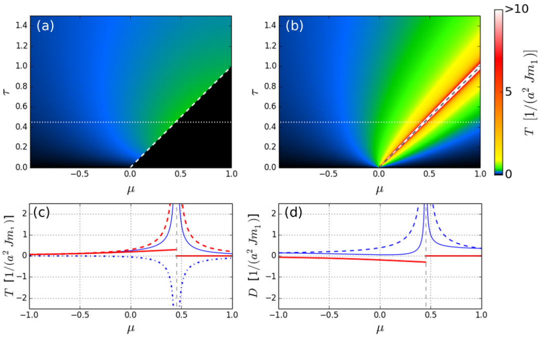

FIG. 2. The anisotropic fluctuation-induced antiferromagnetic exchange coupling of $\mathbf{m}_1$ and $\mathbf{m}_2$ at the surface, which renormalizes the exchange coupling induced from the bulk. (a) In the component along the mean-field direction, the coupling constant is given by $T^{00}+T^{zz}$ (see main text) and shows a finite discontinuity at $\mu=\tau$ (dashed line). (b) In the component orthogonal to the mean-field direction, the AFM coupling $T^{00}-T^{zz}$ diverges at the discontinuity. The color scale is identical in both plots. (c) The quantities T^{00} (thin solid blue line), T^{zz} (dash-dotted blue line), $T^{00}+T^{zz}$ (bold solid red line), and $T^{00}-T^{zz}$ (dashed red line) as a function of μ for a specific value of τ ($\tau=0.45$), which is indicated by the thin white dotted lines in (a) and (b). (d) The anisotropy terms D_1^{zz} (thin solid blue line), D_2^{zz} (dashed blue line), and $D_i^{00}+D_i^{zz}$ (bold solid red line, identical for $i=1,2$) behave similarly, showing a discontinuity at $\tau=\mu$. The vicinity of this line is excluded from the further analysis.

where

$$M_\pm^2 = \frac{J^2}{2}\left(\overline{m}_1^2+\overline{m}_2^2\right)+t^2 \pm\frac{J^2}{2}|\overline{m}_1+\overline{m}_2|\sqrt{(\overline{m}_1-\overline{m}_2)^2+\left(\frac{2t}{J}\right)^2}. \qquad (14)$$

The coupling constants show a discontinuity at $t^2=J^2\overline{m}_1\overline{m}_2$ or, equivalently, $\tau=\mu$, as shown in Fig. 2. Indeed, we see that Eq. (12) diverges for $t^2=J^2\overline{m}_1\overline{m}_2$, while (13) vanishes when $t^2<J^2\overline{m}_1\overline{m}_2$. This divergence obviously does not occur when $\overline{m}_1\overline{m}_2<0$, corresponding to the AFM case, further corroborating the favoring of the AFM alignment. Physically, the divergence for $\tau=\mu$ implies the vanishing of the in-plane susceptibility.

The remaining terms in Eq. (9) describe a z-axis anisotropy in both magnetizations. As we mentioned in Sec. II, our model does not account for possible anisotropy contributions originating with the bulk of the magnet. Such terms would simply be renormalized by the corresponding coefficients in Eq. (9) without changing the physical picture.

Our view of the dynamically generated surface terms as corrections to the bulk values will hold as long as the surface effects are not too large. As can be seen from Fig. 2, within our model some surface terms are divergent at the discontinuity at $\mu=\tau$. Therefore, the vicinity of this line in parameter space will be excluded in our further analysis.

As a side remark, the fluctuation effects discussed in this section can easily be generalized to account for magnetizations that are, at mean field, tilted relative to the surface. We have checked that Eq. (9) remains valid when the z components are replaced by mean-field components in an arbitrary direction.

B. Effective Dirac Lagrangian

The term $h^2\tilde{\Psi}^\dagger A^{-1}\tilde{\Psi}$ in Eq. (8) may now be added to Eq. (1) to yield an effective action for the Dirac fermions,

$$\mathcal{S}_{\text{eff}} = \int dt \int d^2r \mathcal{L}_{\text{eff}} = \int dt \int d^2r \big(\mathcal{L}_{\text{D}} + h^2\tilde{\Psi}^\dagger A^{-1}\tilde{\Psi}\big). \tag{15}$$

Multiplying out $\tilde{\Psi}^\dagger A^{-1}\tilde{\Psi}$ into single-fermion operators again, we find the effective Lagrangian of the Dirac electrons at the coupled surfaces,

$$\begin{aligned}\mathcal{L}_{\text{eff}} = \mathcal{L}_{\text{D}} + \gamma\Psi^\dagger\left(\frac{t^2}{J^2} - \mathbf{m}_1\cdot\mathbf{m}_2\right)\Psi \\ + \Psi^\dagger(J_1\mathbf{m}_1\cdot\boldsymbol{\sigma} + J_2\mathbf{m}_2\cdot\boldsymbol{\sigma})\Psi,\end{aligned} \tag{16}$$

where we have defined the constant

$$\gamma = \frac{2th^2J^2}{\det A} \tag{17}$$

and the effective magnetic coupling constants for the two sublattices

$$J_i = \frac{h^2J}{\det A}\big(J^2\mathbf{m}_{3-i}^2 - t^2\big), \tag{18}$$

where

$$\begin{aligned}\det A = \big(-\partial_t^2 - t^2\big)^2 + J^2\partial_t^2\big(\mathbf{m}_1^2 + \mathbf{m}_2^2\big) \\ + J^2\big(J^2\mathbf{m}_1^2\mathbf{m}_2^2 - 2t^2\mathbf{m}_1\cdot\mathbf{m}_2\big).\end{aligned} \tag{19}$$

In $\det A$, the fluctuations in $\mathbf{m}_{1,2}$ are not of leading order. Therefore, we will approximate the determinant in the Dirac Lagrangian by its mean-field value $\det A^{\text{mf}} = t^4 + J^2[J^2\overline{m}_1^2\overline{m}_2^2 - 2t^2\overline{m}_1\overline{m}_2]$, whereby we also neglected higher-order time derivatives in the low-frequency limit. Furthermore, we assume that the coupling h of the surface fermions χ and Ψ at the interface is small compared to the internal energy scales of the magnet, t and $J\overline{m}_i$. Otherwise, one obtains a renormalization of the time scale. It is interesting to note that the term $\propto \gamma$ in Eq. (16) contributes to the chemical potential of Ψ. The chemical potential may be tuned by adjusting ϕ appearing in Eq. (1), and the mean-field part of the second term in Eq. (16) may thus always be adjusted away. We will keep the remainder only to linear order in the fluctuations.

Note that the sign of J_i in Eq. (18) depends on the parameter t appearing in Eq. (5), as well as the magnitude of the magnetic moments. This is a key observation that we will return to when discussing the topological effects in the next section.

IV. TOPOLOGICAL MAGNETOELECTRIC EFFECTS

Now, we express the effective Lagrangian equation (16) as

$$\mathcal{L}_{\text{eff}} = \overline{\Psi}(i\not{\partial} + m_\Psi)\Psi + \overline{\Psi}(\tilde{\sigma} - \not{a})\Psi, \tag{20}$$

where the first term is the mean-field part, with $\partial = (\partial_t, v_F\boldsymbol{\nabla}_\parallel)$ and $m_\Psi = J_1\overline{m}_1 + J_2\overline{m}_2$, whereas the second term contains the fluctuating fields $\tilde{\sigma} = J_1\tilde{m}_{1z} + J_2\tilde{m}_{2z}$ and

$$\mathbf{a} = \begin{pmatrix} -e(\varphi + \phi) + \gamma(\overline{m}_1\tilde{m}_{2z} + \overline{m}_2\tilde{m}_{1z}) \\ J_1\tilde{m}_{1y} + J_2\tilde{m}_{2y} \\ -J_1\tilde{m}_{1x} - J_2\tilde{m}_{2x} \end{pmatrix}. \tag{21}$$

From this representation, one can see that the out-of-plane fluctuations of the magnetization contribute to the effective electric potential at the interface. This is a result of the fluctuations in the chemical potential that we have observed in Eq. (16). To obtain an effective field theory for the magnetizations that contains the proximity effects induced by the topological insulator, we also have to integrate out the remaining fermions Ψ and the fluctuating Coulomb potential φ. Equation (20) is formally equivalent to the field theory studied in Refs. [30,31], given that the mass term m_Ψ is nonzero. This is naturally the case for FMs and FiMs (except at $\mu = \tau$, which we already excluded), while it might be enforced by doping in the case of an AFM.

Integrating out Ψ yields the fluctuation-induced Lagrangian to one-loop order in the vacuum polarization diagrams [30,31],

$$\delta\mathcal{L}_{\text{eff}} = \frac{\epsilon_{\mu\nu\lambda}a^\mu\partial^\nu a^\lambda}{8\pi} - \frac{(\epsilon_{\mu\nu\lambda}\partial^\nu a^\lambda)^2}{24\pi m_\Psi} - \frac{m_\Psi\tilde{\sigma}^2}{2\pi} + \frac{(\partial\tilde{\sigma})^2}{24\pi m_\Psi}. \tag{22}$$

The first term is the CS term that is responsible for all topologically protected contributions to the Lagrangian. The other terms correspond to a Maxwell term and out-of-plane anisotropy.

Besides these dynamical terms, a term describing the energy at mean field is produced after all fermionic fields have been integrated out. This term can be expanded into a Landau theory for the mean-field magnetizations at the BMI-TI interface. The Landau expansion can be found in Appendix B, where we find that the quadratic term is always negative. This serves as a check that our model, where we treated $\overline{m}_{1,2}$ as parameters, is consistent with the existence of a magnetic phase.

Reinserting $\mathbf{a}$, we can separate $\delta\mathcal{L}_{\text{eff}}$ into a Coulomb-interaction (φ-dependent) part $\mathcal{L}_\varphi$ and the remaining dynamically generated terms $\mathcal{L}_{\text{dyn}}$. After integrating out φ, the Coulomb contributions become

$$\mathcal{L}_\varphi(\mathbf{r},t) = 2\rho(\mathbf{r},t)\int d^2r' \frac{\rho(\mathbf{r}',t)}{|\mathbf{r} - \mathbf{r}'|}, \tag{23}$$

with the charge density

$$\begin{aligned}\rho = \frac{e}{8\pi v_F}\boldsymbol{\nabla}_\parallel\cdot(J_1\mathbf{m}_1 + J_2\mathbf{m}_2) + \frac{e^2}{24\pi m_\Psi}\boldsymbol{\nabla}_\parallel\mathbf{E}_{\text{ext}} \\ - \frac{e}{24\pi m_\Psi v_F}[\boldsymbol{\nabla}_\parallel \times \partial_t(J_1\mathbf{m}_1 + J_2\mathbf{m}_2)]\cdot\hat{\mathbf{e}}_z \\ + \frac{\gamma e}{24\pi m_\Psi}(\boldsymbol{\nabla}_\parallel)^2(\overline{m}_1 m_{2z} + \overline{m}_2 m_{1z}),\end{aligned} \tag{24}$$

where $\mathbf{E}_{\text{ext}} = -\boldsymbol{\nabla}\phi$ is the externally applied electric field. We also define the Coulomb field induced by the charge density,

$$\mathbf{E}_{\text{Cou}}(\mathbf{r}) = -\int d^2r' \frac{\mathbf{r} - \mathbf{r}'}{|\mathbf{r} - \mathbf{r}'|^3}\rho(\mathbf{r}'). \tag{25}$$

For low frequency and momentum, the last two terms in Eq. (24) will be negligible compared to the first two terms.

The part of the Lagrangian that is due to the nontrivial topology (i.e., stemming from the CS term), where we write $\mathbf{M} = J_1\mathbf{m}_1 + J_2\mathbf{m}_2$ for brevity, can be expressed explicitly as

$$\mathcal{L}_{\text{topol}} = \frac{e}{4\pi v_F}\mathbf{M}_\parallel \cdot (\mathbf{E}_{\text{ext}} + \mathbf{E}_{\text{Cou}}) - \frac{1}{8\pi v_F^2}(\mathbf{M} \times \partial_t \mathbf{M}) \cdot \hat{\mathbf{e}}_z + \frac{\gamma}{4\pi v_F}\mathbf{M} \cdot \nabla_\parallel(\overline{m}_1 m_{2z} + \overline{m}_2 m_{1z}). \tag{26}$$

The first term represents the magnetoelectric coupling, involving both the external field and the fluctuation-induced Coulomb field. The second term is a Berry phase. Unlike the Berry phase generated by the fluctuations of χ, this expression always includes mixed terms, regardless of the parameter t. Finally, we also obtain a topological coupling of the magnetic in-plane and out-of-plane fluctuations.

At this point, we can discuss how the system will respond to an electric field. This is the main result of our paper. As we can see from Eq. (26), the electric field is coupled to $\mathbf{M}$ in the same way as it couples to the magnetic polarization in the usual TME effect. Now, let us write $\mathbf{M}$ in terms of the net magnetization $\mathbf{m} = \mathbf{m}_1 + \mathbf{m}_2$ and the staggered field $\mathbf{l} = \mathbf{m}_1 - \mathbf{m}_2$,

$$\mathbf{M} = \tfrac{1}{2}(J_1 + J_2)\mathbf{m} + \tfrac{1}{2}(J_1 - J_2)\mathbf{l}. \tag{27}$$

Obviously, if J_1 and J_2 have the same sign, an electric field will mainly generate a net in-plane magnetization, while the coupling to the staggered field is small. Overall, the system will behave as one would expect for a simple FM. However, if J_1 and J_2 have opposite signs, an electric field will mainly induce a staggered field in the plane, while the response in the net magnetization will be weak. This is because the usual TME effect takes place on both sublattices, but with opposite direction. Going back to Eq. (18), it is easy to find the parameter region where this TSE effect can be found. In terms of the dimensionless model parameters, the condition for J_1 and J_2 having opposite signs is $\mu^2 < \tau < 1$ (see Fig. 3). A purely TSE response is expected if $J_1 = -J_2$, which is the case if $\tau = \frac{1}{2}(1 + \mu^2)$. Remarkably, the predominantly TSE response can appear even in a FM material ($\mu > 0$) if it consists of multiple magnetic components per unit cell with different magnitudes and a suitable parameter t. Thus, it is possible that experiments fail to detect the usual TME effect even when a decent gap opening occurs. In contrast, a purely AFM material ($\mu = -1$) would not show any coupling to the staggered field, even in the presence of a mass term m_Ψ by magnetic doping, because $J_1 = J_2$ for equally strong magnetic moments on the two sublattices. Our model of the BMI is quite simple, and for a real material it might be much harder to find the parameter regions that allow for the observation of the TME or TSE effect. However, it is a remarkable finding that the overall topological response in a BMI-TI heterostructure can depend dramatically on microscopic details of the magnet.

A restriction on our findings is imposed by the discontinuity discussed in the previous section. Due to divergent terms, our results on the TSE effect will not be applicable for parameters in the vicinity of the line $\mu = \tau$ in Fig. 3.

Previous work has found a Coulomb-mediated magnetic dipolar interaction [28]. The Coulomb interaction in the present work will lead to the same effect within each sublattice. Moreover, there will be a dipolar interaction between the sublattices. Again, for a system in the TSE regime, we will get an effect in the opposite direction. Thus, the intercomponent dipolar interaction will favor counteralignment instead of alignment of $\mathbf{m}_{1,\parallel}$ and $\mathbf{m}_{2,\parallel}$.

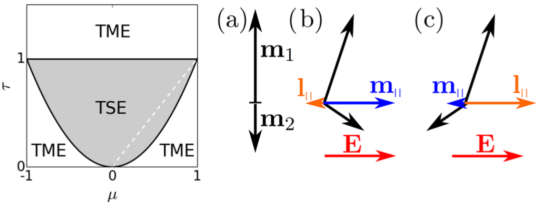

FIG. 3. Left: parameter regions of the bipartite magnet where the topological response to an electric field has the same (white area) or opposite (gray area) direction on the two sublattices, corresponding to a predominantly magnetoelectric (TME) or staggered field electric (TSE) effect, respectively. Here, τ is the dimensionless amplitude of the coupling of the fermions on the two sublattices, and μ is the ratio of the mean-field values of the magnetizations on the sublattices. Close to the dashed line at $\mu = \tau$, our results may not be applicable. Right: illustration of the topological effects for a FiM. (a) Both magnetizations $\mathbf{m}_1$ and $\mathbf{m}_2$ (black) pointing in their mean-field directions. (b) TME effect: if the topological response to the electric field $\mathbf{E}$ (red) has the same sign on both sublattices, an in-plane net magnetization $\mathbf{m}_\parallel$ (blue) is generated, while the induced in-plane staggered field $\mathbf{l}_\parallel$ (orange) is small. (c) TSE effect: if the topological response to $\mathbf{e}$ has opposite signs for $\mathbf{m}_1$ and $\mathbf{m}_2$, an in-plane staggered field is generated, while $\mathbf{m}_\parallel$ is small. The overall sign of these effects depends on the sign of the mass term m_Ψ.

Our model also reveals a topological coupling of the in-plane components of the magnetic moments and the gradient in the out-of-plane component as described by the last term in Eq. (26), which can be understood as an anomalous spin-stiffness term. This term has not been considered in previous studies and can lead to a spin canting effect if the magnetization is not homogeneous, as in the presence of spin waves or domain walls. For the observation of the electromagnetic response it will, however, not be important.

The full Lagrangian describing the magnetic moments in the system is now given by

$$\mathcal{L}_{\text{tot}} = \mathcal{L}_{\text{bulk}} + \mathcal{L}_\varphi + \mathcal{L}_{\text{dyn}} + \delta\mathcal{L}_{\text{mag}}, \tag{28}$$

from which the coupled LLEs for the motion of $\mathbf{m}_1$ and $\mathbf{m}_2$ at the interface can be derived. The LLE takes the form takes the form

$$\partial_t \begin{pmatrix} \mathbf{m}_1 \\ \mathbf{m}_2 \end{pmatrix} = \Xi^{-1} \begin{pmatrix} \mathbf{m}_1 \times \mathbf{d}_1 \\ \mathbf{m}_2 \times \mathbf{d}_2 \end{pmatrix}. \tag{29}$$

For details, we refer to Appendix C. The (6×6) matrix Ξ contains all Berry phase terms. In particular, there are off-diagonal terms that stem from the fluctuation-induced mixed Berry phases. Such terms are generated by the fermions χ_i (if $t \neq 0$) as well as the Dirac fermions Ψ. The contribution by the fluctuations of Ψ is of topological origin, as it stems from the CS term. The effective fields $\mathbf{d}_i$ contain, in addition to spin-stiffness and anisotropy terms, a topological part,

$$\mathbf{d}^{i}_{\text{topol}} = \frac{eJ_i}{4\pi v_F}\mathbf{E}_{\text{Cou}} + \frac{eJ_i}{4\pi v_F}\mathbf{E}_{\text{ext}} - \frac{\gamma \overline{m}_{3-i}}{4\pi v_F}(\nabla_{\parallel}\cdot\mathbf{M})\hat{\mathbf{e}}_z - \frac{\gamma J_i}{4\pi v_F}\nabla_{\parallel}(\overline{m}_1 m_{2z} + \overline{m}_2 m_{1z}), \tag{30}$$

corresponding to Eq. (26). The first two terms show explicitly how the external electric field and the Coulomb field affect the magnetization dynamics as a consequence of the magnetoelectric effects discussed above.

V. CONCLUSION

We have studied the topological effects at the interface of a TI and a BMI within an analytically accessible model that accounts for the fermionic quantum fluctuations at the surfaces of both materials. We have demonstrated that the TME effect that is known for magnetic TI surfaces can take the opposite sign for the different magnetic components, depending on microscopic details of the material. This leads to an overall TSE response to an electric field, while the induced net magnetization in the plane can be weak even in the presence of a stable energy gap in the Dirac dispersion. Thus, experiments that aim at detecting the TME effect might also look for a response in the staggered field. A response in the magnetization can be absent even when a FM insulator is used if there are multiple magnetic components with different magnitudes. In addition to the TSE effect, we have derived several dynamically generated Berry phases, including terms mixing $\mathbf{m}_1$ and $\mathbf{m}_2$. We also found a topological coupling of in-plane and out-of-plane magnetic components which is present for nonhomogeneous magnetization. The fluctuations of the fermions on the magnets' surface cause discontinuity in our model, close to which our results are not applicable.

ACKNOWLEDGMENTS

S.R. and A.S. acknowledge funding from the Norwegian Research Council, Grants No. 205591/V20 and No. 216700/F20.

APPENDIX A: DERIVATION OF THE SURFACE CORRECTIONS

Here, we derive the magnetic surface terms discussed in Sec. III A that are generated by Tr ln A in the Gaussian integral, Eq. (8). Splitting $A = A^{\text{mf}} + A^{\text{fl}}$ into the mean-field part and the quantum fluctuations,

$$A^{\text{mf}} = \begin{pmatrix} i\partial_t + J\overline{m}_1\sigma_z & t \\ t & i\partial_t + J\overline{m}_2\sigma_z \end{pmatrix}, \tag{A1}$$

$$A^{\text{fl}} = \begin{pmatrix} J\tilde{\mathbf{m}}_1\cdot\boldsymbol{\sigma} & 0 \\ 0 & J\tilde{\mathbf{m}}_2\cdot\boldsymbol{\sigma} \end{pmatrix}, \tag{A2}$$

we obtain the usual expansion

$$\text{Tr}\ \ln A = \text{Tr}\ \ln A^{\text{mf}} - \tfrac{1}{2}\text{Tr}(GA^{\text{fl}})^2, \tag{A3}$$

where the first term is a constant corresponding to the ground-state energy that will be dealt with in Appendix B, while the second term describes the dynamics close to equilibrium to leading order. The propagator G is given by $(A^{\text{mf}})^{-1}$. In reciprocal space and imaginary time, G depends only on the frequency ω and not on momentum because the hopping terms in our model are momentum independent. For all momentum integrals, we use π/a as a cutoff value, where a is the lattice spacing. The propagator can be written in the form

$$G = \frac{1}{\det A^{\text{mf}}}\begin{pmatrix} D_1^0 + D_1^z\sigma_z & T^0 + T^z\sigma_z \\ T^0 + T^z\sigma_z & D_2^0 + D_2^z\sigma_z \end{pmatrix}, \tag{A4}$$

where the components are

$$D_1^0(\omega) = i\omega^3 + i\omega J^2\overline{m}_2^2 + i\omega t^2, \tag{A5}$$

$$D_2^0(\omega) = i\omega^3 + i\omega J^2\overline{m}_1^2 + i\omega t^2, \tag{A6}$$

$$D_1^z(\omega) = J\overline{m}_1\omega^2 + J^3\overline{m}_2^2\overline{m}_1 - t^2J\overline{m}_2, \tag{A7}$$

$$D_2^z(\omega) = J\overline{m}_2\omega^2 + J^3\overline{m}_1^2\overline{m}_2 - t^2J\overline{m}_1, \tag{A8}$$

$$T^0(\omega) = t\omega^2 + t^3 - tJ^2\overline{m}_1\overline{m}_2, \tag{A9}$$

$$T^z(\omega) = -it\omega J(\overline{m}_1 + \overline{m}_2), \tag{A10}$$

and the determinant is

$$\det A^{\text{mf}}(\omega) = \left[\omega^2 + \frac{J^2}{2}\left(\overline{m}_1^2 + \overline{m}_2^2\right) + t^2\right]^2 - \frac{J^4}{4}\left(\overline{m}_1^2 - \overline{m}_2^2\right)^2 - t^2J^2(\overline{m}_1 + \overline{m}_2)^2. \tag{A11}$$

Performing the trace in Eq. (A3) at $T = 0$ then leads to the Lagrangian

$$\begin{aligned}\delta\mathcal{L}_{\text{mag}}(\Omega) = -J^2\sum_{i=1,2}\Big\{&\big[D_i^{00}(\Omega) - D_i^{zz}(\Omega)\big]\tilde{\mathbf{m}}_i(\Omega)\cdot\tilde{\mathbf{m}}_i(-\Omega)\\ &+2D_i^{zz}(\Omega)\tilde{m}_{i,z}(\Omega)\tilde{m}_{i,z}(-\Omega)\\ &+i\big[D_i^{z0}(\Omega) - D_i^{0z}(\Omega)\big]\hat{\mathbf{e}}_z\cdot[\tilde{\mathbf{m}}_i(\Omega)\times\tilde{\mathbf{m}}_i(-\Omega)]\Big\}\\ &-J^2[T^{00}(\Omega) - T^{zz}(\Omega)][\tilde{\mathbf{m}}_1(\Omega)\cdot\tilde{\mathbf{m}}_2(-\Omega)\\ &+\tilde{\mathbf{m}}_1(-\Omega)\cdot\tilde{\mathbf{m}}_2(\Omega)] - iJ^2[T^{z0}(\Omega) - T^{0z}(\Omega)]\\ &\times\hat{\mathbf{e}}_z\cdot[\tilde{\mathbf{m}}_1(\Omega)\times\tilde{\mathbf{m}}_2(-\Omega) + \tilde{\mathbf{m}}_2(\Omega)\times\tilde{\mathbf{m}}_1(-\Omega)]\\ &-2J^2T^{zz}(\Omega)[\tilde{m}_{1z}(\Omega)\tilde{m}_{2z}(-\Omega)\\ &+\tilde{m}_{1z}(-\Omega)\tilde{m}_{2z}(\Omega)],\end{aligned} \tag{A12}$$

with frequency Ω, containing the integrals

$$D_i^{\alpha\beta}(\Omega) = \frac{1}{a^2}\int\frac{d\omega}{2\pi}\,\frac{D_i^{\alpha}(\omega)D_i^{\beta}(\omega-\Omega)}{[\det A^{\text{mf}}(\omega)][\det A^{\text{mf}}(\omega-\Omega)]} \tag{A13}$$

and

$$T^{\alpha\beta}(\Omega) = \frac{1}{a^2}\int\frac{d\omega}{2\pi}\,\frac{T^{\alpha}(\omega)T^{\beta}(\omega-\Omega)}{[\det A^{\text{mf}}(\omega)][\det A^{\text{mf}}(\omega-\Omega)]}, \tag{A14}$$

with $\alpha,\beta\in\{0,z\}$ and $i = 1,2$. These integrals can be solved exactly by partial fraction decomposition since the zeros of the denominator are known: $\det A^{\text{mf}}(\omega) = 0$ if $\omega^2 = N^{\pm}$, with

$$N^{\pm} = \pm J\sqrt{\frac{J^2}{4}\left(\overline{m}_1^2 - \overline{m}_2^2\right)^2 + t^2(\overline{m}_1 + \overline{m}_2)^2} - \frac{1}{2}J^2\left(\overline{m}_1^2 + \overline{m}_2^2\right) - t^2, \tag{A15}$$

where $N^- < 0$ and $N^+ \leqslant 0$. Namely, $N^+ = 0$ if $t^2 = J^2\overline{m}_1\overline{m}_2$, i.e., in terms of the dimensionless parameters, if $\tau = \mu$. This is where the discontinuity which is discussed in Sec. III A is located. In the integrals, we neglect terms of order Ω^2 or higher in the long-wavelength limit and obtain

$$\begin{aligned} D_1^{00}(\Omega) = {} & \frac{1}{4a^2\sqrt{-N^+}(N^+ - N^-)^3}\big\{-(N^+)^3 + 5(N^+)^2N^- \\ & + 2\left(J^2\overline{m}_2^2 + t^2\right)[(N^+)^2 + 3N^+N^-] \\ & + \left(J^2\overline{m}_2^2 + t^2\right)^2(3N^+ + N^-)\big\} \\ & + (\text{same with } N^+ \leftrightarrow N^-) + O(\Omega^2), \end{aligned} \tag{A16}$$

$$\begin{aligned} D_i^{0z}(\Omega) = {} & \frac{i\Omega}{16a^2N^+\sqrt{-N^+}(N^- - N^+)^3} \\ & \times \big[J\overline{m}_1(N^+)^2\left(2N^+ + 9N^-\right) \\ & + J\overline{m}_1\left(J^2\overline{m}_2^2 + t^2\right)N^+(N^+ - 5N^-) \\ & + J\overline{m}_2\left(J^2\overline{m}_2^2 + t^2\right)(J^2\overline{m}_1\overline{m}_2 - t^2) \\ & \times (10N^+ - 2N^-)\big] \\ & + (\text{same with } N^+ \leftrightarrow N^-) + O(\Omega^3), \end{aligned} \tag{A17}$$

$$\begin{aligned} D_1^{zz}(\Omega) = {} & \frac{-J^2}{4a^2N^+\sqrt{-N^+}(N^+ - N^-)^3} \\ & \times \big[\overline{m}_1^2(N^+)^2(N^+ + 3N^-) \\ & + 2\overline{m}_1\overline{m}_2(J^2\overline{m}_1\overline{m}_2 - t^2)N^+(3N^+ + N^-) \\ & + \overline{m}_2^2(J^2\overline{m}_1\overline{m}_2 - t^2)^2(5N^+ - N^-)\big] \\ & + (\text{same with } N^+ \leftrightarrow N^-) + O(\Omega^2), \end{aligned} \tag{A18}$$

$$\begin{aligned} T^{00}(\Omega) = {} & \frac{-t^2(J^2\overline{m}_1\overline{m}_2 - t^2 - N^+)}{a^2\sqrt{-N^+}(N^+ - N^-)^2} \\ & \times \left[1 + \frac{(5N^+ - N^-)(J^2\overline{m}_1\overline{m}_2 - t^2 - N^+)}{4N^+(N^+ - N^-)}\right] \\ & + (\text{same with } N^+ \leftrightarrow N^-) + O(\Omega^2), \end{aligned} \tag{A19}$$

$$\begin{aligned} T^{0z}(\Omega) = {} & \frac{i\Omega t^2(\overline{m}_1 + \overline{m}_2)}{16a^2N^+\sqrt{-N^+}(N^- - N^+)^3} \\ & \times [(t^2 - J^2\overline{m}_1\overline{m}_2)(10N^+ + 2N^-) \\ & - 7(N^+)^2 + N^+N^-] \\ & + (\text{same with } N^+ \leftrightarrow N^-) + O(\Omega^3), \end{aligned} \tag{A20}$$

$$\begin{aligned} T^{zz}(\Omega) = {} & \frac{t^2J^2(\overline{m}_1 + \overline{m}_2)^2(3N^+ + N^-)}{4a^2\sqrt{-N^+}(N^+ - N^-)^3} \\ & + (\text{same with } N^+ \leftrightarrow N^-) + O(\Omega^2). \end{aligned} \tag{A21}$$

Expressions for $D_2^{00}(\Omega)$, $D^{0z}(\Omega)$, and $D_2^{zz}(\Omega)$ can be obtained from Eqs. (A16), (A17), and (A18), respectively, by exchanging $\overline{m}_1 \leftrightarrow \overline{m}_2$. It turns out that $D_1^{00} + D_1^{zz} = D_2^{00} + D_2^{zz} = -(T^{00} + T^{zz})$. Furthermore, $D_i^{z0}(\Omega) = D_i^{0z}(-\Omega) = -D_i^{0z}(\Omega)$ and $T^{z0}(\Omega) = T^{0z}(-\Omega) = -T^{0z}(\Omega)$. These relations follow by substituting $\omega \to (\omega + \Omega)$ in Eqs. (A13) and (A14) and from the fact that only odd powers of Ω appear in Eqs. (A17) and (A20). For ease of notation, we write $D_i^{0z}(\Omega) = i\Omega\mathcal{D}_i^{0z}$ and $T^{0z}(\Omega) = i\Omega\mathcal{T}^{0z}$, where $\mathcal{D}_i^{0z}$ and $\mathcal{T}_i^{0z}$ are frequency independent.

The effective magnetic surface Lagrangian that is evoked by the fermionic fluctuations, Eq. (A12), is, in real space and time, given by

$$\begin{aligned} \delta\mathcal{L}_{\text{mag}}(\mathbf{r},t) = {} & -J^2\sum_{i=1,2}\big\{\left(D_i^{00} - D_i^{zz}\right)\tilde{\mathbf{m}}_i^2(\mathbf{r},t) + 2D_i^{zz}\tilde{m}_{i,z}^2(\mathbf{r},t) \\ & - 2\mathcal{D}_i^{0z}\hat{\mathbf{e}}_z \cdot [\tilde{\mathbf{m}}_i(\mathbf{r},t) \times \partial_t\tilde{\mathbf{m}}_i(\mathbf{r},t)]\big\} \\ & - 2J^2(T^{00} - T^{zz})\tilde{\mathbf{m}}_1(\mathbf{r},t) \cdot \tilde{\mathbf{m}}_2(\mathbf{r},t) \\ & + 2J^2\mathcal{T}^{0z}\hat{\mathbf{e}}_z \cdot [\tilde{\mathbf{m}}_1(\mathbf{r},t) \times \partial_t\tilde{\mathbf{m}}_2(\mathbf{r},t) + \tilde{\mathbf{m}}_2(\mathbf{r},t) \\ & \times \partial_t\tilde{\mathbf{m}}_1(\mathbf{r},t)] - 4J^2T^{zz}\tilde{m}_{1z}(\mathbf{r},t)\tilde{m}_{2z}(\mathbf{r},t). \end{aligned} \tag{A22}$$

Equation (9) in Sec. III A follows by writing the Lagrangian in terms of $\mathbf{m}_i = \overline{m}_i\hat{\mathbf{e}}_z + \tilde{\mathbf{m}}_i$ again, where constant terms are discarded. The meaning of the different contributions is discussed in the main text.

In the special case of a pure AFM, where $\overline{m}_1 = -\overline{m}_2$, a mathematical subtlety arises. Namely, the solution of the integrals $D_i^{\alpha\beta}(\Omega)$ and $T^{\alpha\beta}(\Omega)$ by partial fraction decomposition requires a different ansatz because the zeros of the denominator are degenerate: $N^+ = N^- = -J^2\overline{m}_1^2 - t^2$. The integrals are notably easier as a consequence of multiple cancellations, and we find, again to leading order in Ω in the low-frequency regime,

$$D_{1,\text{AFM}}^{00}(\Omega) = D_{2,\text{AFM}}^{00}(\Omega) = -\frac{1}{4a^2\sqrt{J^2\overline{m}_1^2 + t^2}} + O(\Omega^2), \tag{A23}$$

$$D_{1,\text{AFM}}^{0z}(\Omega) = -D_{2,\text{AFM}}^{0z}(\Omega) = \frac{i\Omega J\overline{m}_1}{8a^2\left(J^2\overline{m}_1^2 + t^2\right)^{3/2}} + O(\Omega^3), \tag{A24}$$

$$D_{1,\text{AFM}}^{zz}(\Omega) = D_{2,\text{AFM}}^{zz}(\Omega) = \frac{J^2\overline{m}_1^2}{4a^2\left(J^2\overline{m}_1^2 + t^2\right)^{3/2}} + O(\Omega^2), \tag{A25}$$

$$T_{\text{AFM}}^{00}(\Omega) = \frac{t^2}{4a^2\left(J^2\overline{m}_1^2 + t^2\right)^{3/2}} + O(\Omega^2), \tag{A26}$$

$$T_{\text{AFM}}^{0z}(\Omega) = T_{\text{AFM}}^{zz}(\Omega) = 0. \tag{A27}$$

We have checked that these expressions are identical to the continuous limit $\overline{m}_2 \to -\overline{m}_1$ of the integrals in the general case. Notably, no mixed Berry phase term is generated for the AFM. The fluctuation-induced Lagrangian takes the simplified form

$$\begin{aligned} & \delta\mathcal{L}_{\text{mag}}^{\text{AFM}} \\ & = \frac{J^2\left[t^2\mathbf{m}_1 \cdot \mathbf{m}_2 + 2t^2\overline{m}_1(m_{1z} - m_{2z}) + J^2\overline{m}_1^2\left(m_{1z}^2 + m_{2z}^2\right)\right]}{-2a^2\left(J^2\overline{m}_1^2 + t^2\right)^{3/2}} \\ & \quad + \frac{J^3\overline{m}_1}{4a^2\left(J^2\overline{m}_1^2 + t^2\right)}\hat{\mathbf{e}}_z \cdot (\mathbf{m}_1 \times \partial_t\mathbf{m}_1 - \mathbf{m}_2 \times \partial_t\mathbf{m}_2). \end{aligned} \tag{A28}$$

APPENDIX B: FLUCTUATION-INDUCED LANDAU THEORY

In this appendix, we present the Landau expansion of the energy in terms of the mean-field magnetizations at the interface. Here, we allow arbitrary directions of the magnetizations. Thus, the Landau theory is still valid if $\mathbf{m}_1$ and $\mathbf{m}_2$ are not aligned with each other or the z axis at mean field. For simplicity, we drop the overline notation indicating mean-field values in this appendix.

The energy contains two contributions, namely, (i) one from the term $\det A$ in Eq. (A3) originating with the quantum fluctuations of the sublattice fermions and (ii) one from a similar term $\det B$ generated by the quantum fluctuations of the Dirac fermions, where B is defined such that Eq. (16) can be written as $\mathcal{L}_{\text{eff}} = \Psi^\dagger B \Psi$. The energy density is then given by

$$\mathcal{E} = -\int \frac{d\omega}{2\pi} \int \frac{d^2k}{2\pi} (\ln\det A + \ln\det B), \tag{B1}$$

where we use the cutoff value π/a in divergent momentum integrals. We did not include Landau terms for the bulk in Eq. (3); however, any bulk contributions would simply add up with the interface terms shown here. We obtain the following expansion to fourth order, where $\perp$ indicates the component orthogonal to the interface and $\|$ indicates the in-plane component:

$$\begin{aligned}\mathcal{E} = {} & J^2\bigg[\frac{-1}{4a^2|t|}(\mathbf{m}_1 - \mathbf{m}_2)^2 - t^2K_2(\mathbf{m}_1 + \mathbf{m}_2)_\perp^2 \\ & - \bigg(t^2K_2\big(1 - v_F^2\big) + \frac{5h^4}{128\pi v_F^2|t|^3}\bigg)(\mathbf{m}_1 + \mathbf{m}_2)_\|^2\bigg] \\ & + J^4\big[c_1\big(m_1^4 + m_2^4\big) + c_2 m_1^2 m_2^2 + c_3(\mathbf{m}_1\cdot\mathbf{m}_2)^2 \\ & + c_4\big(m_1^2 + m_2^2\big)\mathbf{m}_1\cdot\mathbf{m}_2 + c_5\big(m_1^2 m_{1\|}^2 + m_2^2 m_{2\|}^2\big) \\ & + c_6\big(m_1^2 m_{2\|}^2 + m_2^2 m_{1\|}^2\big) + c_7\big(\mathbf{m}_1^2 + \mathbf{m}_2^2\big)(\mathbf{m}_{1\|}\cdot\mathbf{m}_{2\|}) \\ & + c_8\big(m_{1\|}^2 + m_{2\|}^2\big)\mathbf{m}_1\cdot\mathbf{m}_2 + K_1(\mathbf{m}_{1\|} + \mathbf{m}_{2\|})^4 \\ & + 2c_8(\mathbf{m}_{1\|}\cdot\mathbf{m}_{2\|})(\mathbf{m}_1\cdot\mathbf{m}_2)\big].\end{aligned} \tag{B2}$$

The coefficients of the fourth-order terms are

$$c_1 = \frac{1}{64a^2|t|^3} + K_1 + K_3 - K_4, \tag{B3}$$

$$c_2 = \frac{-7}{64a^2|t|^3} + K_1 + K_2 + K_3 - K_4, \tag{B4}$$

$$c_3 = \frac{5}{16a^2|t|^3} + 4K_1 - 4K_4, \tag{B5}$$

$$c_4 = \frac{-1}{16a^2|t|^3} + 4K_1 + K_2 + 2K_3 - 4K_4, \tag{B6}$$

$$c_5 = \frac{7h^4}{1024\pi v_F^2|t|^5} - 2K_1 - v_F^2(K_3 - K_4), \tag{B7}$$

$$c_6 = \frac{237h^4}{1024\pi v_F^2|t|^5} - 2K_1 - v_F^2(K_2 + K_3 - K_4), \tag{B8}$$

$$c_7 = \frac{47h^4}{512\pi v_F^2|t|^5} - 4K_1 - v_F^2(K_2 + 2K_3 - 2K_4), \tag{B9}$$

$$c_8 = \frac{-63h^4}{512\pi v_F^2|t|^5} - 4K_1 + 2v_F^2K_4, \tag{B10}$$

and we have used the constants

$$K_1 = \frac{6435h^8}{2^{15}\pi v_F^2|t|^9}, \tag{B11}$$

$$K_2 = h^4\frac{92\pi^2v_F^2 + 108\pi v_F a|t| + 33a^2t^2}{48v_F|t|^5(2\pi v_F + a|t|)^3} + \frac{5h^4\ln\big(1 + \frac{2\pi v_F}{a|t|}\big)}{64\pi v_F^2|t|^5}, \tag{B12}$$

$$K_3 = h^4\frac{1408\pi^3v_F^3 + 2396\pi^2v_F^2a|t| + 1392\pi v_F a^2t^2 + 279a^3|t|^3}{384v_F|t|^5(2\pi v_F + a|t|)^4} + \frac{35h^4\ln\big(1 + \frac{2\pi v_F}{a|t|}\big)}{512\pi v_F^2|t|^5}, \tag{B13}$$

$$K_4 = h^4\frac{9008\pi^4v_F^4 + 20000\pi^3v_F^3a|t| + 16920\pi^2v_F^2a^2t^2 + 6500\pi v_F a^3|t|^3 + 965a^4t^4}{1280v_F|t|^5(2\pi v_F + a|t|)^5} + \frac{63h^4\ln\big(1 + \frac{2\pi v_F}{a|t|}\big)}{1024\pi v_F^2|t|^5}. \tag{B14}$$

It turns out that the second-order term is always negative, indicating a stable magnetic phase at the interface.

For the special cases of a FM, with $\mathbf{m}_1 = \mathbf{m}_2 = \mathbf{n}$, and an AFM, with $\mathbf{m}_1 = -\mathbf{m}_2 = \mathbf{n}$, the Landau theory can be simplified:

$$\begin{aligned}\mathcal{E}_{\text{FM}} = {} & -4J^2\bigg[t^2K_2n_\perp^2 + \bigg(t^2K_2\big(1 - v_F^2\big) + \frac{5h^4}{128\pi v_F^2|t|^3}\bigg)n_\|^2\bigg] + J^4\big[(16c_1 + c_2 + c_3 + 2c_4)n^4 \\ & + 2(c_5 + c_6 + c_7 + 2c_8)n_\|^2n^2 + 16K_1n_\|^4\big],\end{aligned} \tag{B15}$$

$$\mathcal{E}_{\text{AFM}} = -\frac{J^2n^2}{a^2|t|} + J^4\big[(16c_1 + c_2 + c_3 - 2c_4)n^4 + 2(c_5 + c_6 - c_7)n_\|^2n^2 + 16K_1n_\|^4\big]. \tag{B16}$$

APPENDIX C: LANDAU-LIFSHITZ EQUATION

Applying the Euler-Lagrange formalism in the total Lagrangian equation (28) leads to the two equations of motion (with $i = 1{,}2$ and $j = 3 - i$),

$$-\frac{\mathbf{m}_i}{\mathbf{m}_i^2} \times \partial_t \mathbf{m}_i + b\hat{\mathbf{e}}_z \times \partial_t \mathbf{m}_i + c\hat{\mathbf{e}}_z \times \partial_t \mathbf{m}_j = \mathbf{d}_i, \tag{C1}$$

with the coefficients

$$b = 4J^2 \mathcal{D}_i^{0z} - \frac{J_i^2}{4\pi v_F^2}, \tag{C2}$$

$$c = 4J^2 \mathcal{T}^{0z} - \frac{J_1 J_2}{4\pi v_F^2} \tag{C3}$$

and the effective field $\mathbf{d}_i = \mathbf{d}^i_{\text{topol}} + \mathbf{d}^i_{\text{non-top}}$, which consists of a part generated by the CS term,

$$\mathbf{d}^i_{\text{topol}} = \frac{eJ_i}{4\pi v_F}\mathbf{E}_{\text{Cou}} + \frac{eJ_i}{4\pi v_F}\mathbf{E}_{\text{ext}} - \frac{\gamma \overline{m}_j}{4\pi v_F}(\nabla_\parallel \cdot \mathbf{M})\hat{\mathbf{e}}_z - \frac{\gamma J_i}{4\pi v_F}\nabla_\parallel(\overline{m}_1 m_{2z} + \overline{m}_2 m_{1z}), \tag{C4}$$

and the remainder containing various spin-stiffness and anisotropy terms in addition to the renormalized magnetic coupling of the sublattices,

$$\begin{aligned}
\mathbf{d}^i_{\text{non-top}} = {} & -\kappa\left(\nabla_\parallel\right)^2 \mathbf{m}_i - \lambda \mathbf{m}_j - 4J^2 D_1^{zz} m_{1z}\hat{\mathbf{e}}_z - 2J^2 \text{diag}(T^{00} - T^{zz}, T^{00} - T^{zz}, T^{00} + T^{zz}) \cdot \mathbf{m}_j \\
& + 2J^2\left[\left(D_i^{00} + D_i^{zz}\right)\overline{m}_i + (T^{00} + T^{zz})\overline{m}_j\right]\hat{\mathbf{e}}_z + \frac{m_\Psi J_i}{\pi v_F^2}(J_1\overline{m}_1 + J_2\overline{m}_2 - M_z)\hat{\mathbf{e}}_z - \frac{J_i}{12\pi m_\Psi v_F^2}\partial_t^2 \mathbf{M} \\
& - \frac{J_i}{12\pi m_\Psi v_F}\partial_t\left[\gamma \nabla_\parallel(\overline{m}_1 m_{2z} + \overline{m}_2 m_{1z}) - e\mathbf{E}_{\text{ext}}\right] \times \hat{\mathbf{e}}_z - \frac{J_i}{12\pi m_\Psi}\nabla_\parallel\left(\nabla_\parallel \cdot \mathbf{M}\right) - \frac{\gamma \overline{m}_j}{12\pi m_\Psi v_F}\left[\partial_t(\nabla_\parallel \times \mathbf{M}) \cdot \hat{\mathbf{e}}_z\right]\hat{\mathbf{e}}_z \\
& + \frac{\gamma^2}{12\pi m_\Psi}\left(\nabla_\parallel\right)^2\left(\overline{m}_2^2 m_{1z} + \overline{m}_1^2 m_{2z}\right)\hat{\mathbf{e}}_z + \frac{\gamma e}{12\pi m_\Psi}(\nabla_\parallel \cdot \mathbf{E}_{\text{ext}})\hat{\mathbf{e}}_z - \frac{J_i}{12\pi m_\Psi}\left(\nabla_\parallel\right)^2 M_z \hat{\mathbf{e}}_z,
\end{aligned} \tag{C5}$$

with the shorthand notation $\mathbf{M} = J_1\mathbf{m}_1 + J_2\mathbf{m}_2$. The second and third terms in Eq. (C1) are due to the fluctuation-induced Berry phases. Taking the cross product with $\mathbf{m}_i$ in Eq. (C1), using $\partial_t \mathbf{m}_i^2 = 0$, one obtains

$$(1 - bm_i z)\partial_t \mathbf{m}_i - cm_{iz}\partial_t \mathbf{m}_j + c(\mathbf{m}_i \cdot \partial_t \mathbf{m}_j)\hat{\mathbf{e}}_z = \mathbf{m}_i \times \mathbf{d}_i. \tag{C6}$$

The equations of motion can now be rewritten in matrix form,

$$\Xi \cdot \begin{pmatrix} \partial_t \mathbf{m}_1 \\ \partial_t \mathbf{m}_2 \end{pmatrix} = \begin{pmatrix} \mathbf{m}_1 \times \mathbf{d}_1 \\ \mathbf{m}_2 \times \mathbf{d}_2 \end{pmatrix}, \tag{C7}$$

where the entries of the (6×6) matrix Ξ follow from Eq. (C6):

$$\Xi = \mathbb{1}_{(6\times 6)} + \begin{pmatrix} -bm_{1z} & 0 & 0 & -cm_{1z} & 0 & 0 \\ 0 & -bm_{1z} & 0 & 0 & -cm_{1z} & 0 \\ 0 & 0 & -bm_{1z} & cm_{1x} & cm_{1y} & 0 \\ -cm_{2z} & 0 & 0 & -bm_{2z} & 0 & 0 \\ 0 & -cm_{2z} & 0 & 0 & -bm_{2z} & 0 \\ cm_{1x} & cm_{2y} & 0 & 0 & 0 & -bm_{2z} \end{pmatrix}. \tag{C8}$$

[1] M. Z. Hasan and C. L. Kane, Rev. Mod. Phys. **82**, 3045 (2010).

[2] X.-L. Qi and S.-C. Zhang, Rev. Mod. Phys. **83**, 1057 (2011).

[3] X.-L. Qi, T. L. Hughes, and S.-C. Zhang, Phys. Rev. B **78**, 195424 (2008).

[4] A. M. Essin, J. E. Moore, and D. Vanderbilt, Phys. Rev. Lett. **102**, 146805 (2009).

[5] Y. S. Hor, P. Roushan, H. Beidenkopf, J. Seo, D. Qu, J. G. Checkelsky, L. A. Wray, D. Hsieh, Y. Xia, S.-Y. Xu, D. Qian, M. Z. Hasan, N. P. Ong, A. Yazdani, and R. J. Cava, Phys. Rev. B **81**, 195203 (2010).

[6] Y. L. Chen, J.-H. Chu, J. G. Analytis, Z. K. Liu, K. Igarashi, H.-H. Kuo, X. L. Qi, S. K. Mo, R. G. Moore, D. H. Lu, M. Hashimoto, T. Sasagawa, S. C. Zhang, I. R. Fisher, Z. Hussain, and Z. X. Shen, Science **329**, 659 (2010).

[7] X. Kou, L. He, M. Lang, Y. Fan, K. Wong, Y. Jiang, T. Nie, W. Jiang, P. Upadhyaya, Z. Xing, Y. Wang, F. Xiu, R. N. Schwartz, and K. L. Wang, Nano Lett. **13**, 4587 (2013).

[8] X. Kou, M. Lang, Y. Fan, Y. Jiang, T. Nie, J. Zhang, W. Jiang, Y. Wang, Y. Yao, L. He, and K. L. Wang, ACS Nano **7**, 9205 (2013).

[9] Y. Okada, C. Dhital, W. Zhou, E. D. Huemiller, H. Lin, S. Basak, A. Bansil, Y.-B. Huang, H. Ding, Z. Wang, S. D. Wilson, and V. Madhavan, Phys. Rev. Lett. **106**, 206805 (2011).
[10] C.-Z. Chang, J. Zhang, M. Liu, Z. Zhang, X. Feng, K. Li, L.-L. Wang, X. Chen, X. Dai, Z. Fang, X.-L. Qi, S.-C. Zhang, Y. Wang, K. He, X.-C. Ma, and Q.-K. Xue, Adv. Mater. **25**, 1065 (2013).
[11] M. Li, C.-Z. Chang, L. Wu, J. Tao, W. Zhao, M. H. W. Chan, J. S. Moodera, J. Li, and Y. Zhu, Phys. Rev. Lett. **114**, 146802 (2015).
[12] P. Wei, F. Katmis, B. A. Assaf, H. Steinberg, P. Jarillo-Herrero, D. Heiman, and J. S. Moodera, Phys. Rev. Lett. **110**, 186807 (2013).
[13] A. Kandala, A. Richardella, D. W. Rench, D. M. Zhang, T. C. Flanagan, and N. Samarth, Appl. Phys. Lett. **103**, 202409 (2013).
[14] Q. I. Yang, M. Dolev, L. Zhang, J. Zhao, A. D. Fried, E. Schemm, M. Liu, A. Palevski, A. F. Marshall, S. H. Risbud, and A. Kapitulnik, Phys. Rev. B **88**, 081407(R) (2013).
[15] F. Katmis, V. Lauter, F. S. Nogueira, B. A. Assaf, M. E. Jamer, P. Wei, B. Satpati, J. W. Freeland, I. Eremin, D. Heiman, P. Jarillo-Herrero, and J. S. Moodera, Nature (London) **533**, 513 (2016).
[16] W. Liu, L. He, Y. Xu, K. Murata, M. C. Onbasli, M. Lang, N. J. Maltby, S. Li, X. Wang, C. A. Ross, P. Bencok, G. van der Laan, R. Zhang, and K. L. Wang, Nano Lett. **15**, 764 (2015).
[17] M. Li, C.-Z. Chang, B. J. Kirby, M. E. Jamer, W. Cui, L. Wu, P. Wei, Y. Zhu, D. Heiman, J. Li, and J. S. Moodera, Phys. Rev. Lett. **115**, 087201 (2015).
[18] I. Garate and M. Franz, Phys. Rev. Lett. **104**, 146802 (2010).
[19] K. Nomura and N. Nagaosa, Phys. Rev. B **82**, 161401(R) (2010).
[20] T. Yokoyama, J. Zang, and N. Nagaosa, Phys. Rev. B **81**, 241410(R) (2010).
[21] Y. Tserkovnyak and D. Loss, Phys. Rev. Lett. **108**, 187201 (2012).
[22] Y. Ferreiros and A. Cortijo, Phys. Rev. B **89**, 024413 (2014).
[23] J. Linder, Phys. Rev. B **90**, 041412(R) (2014).
[24] Y. Ferreiros, F. J. Buijnsters, and M. I. Katsnelson, Phys. Rev. B **92**, 085416 (2015).
[25] Y. G. Semenov, X. Duan, and K. W. Kim, Phys. Rev. B **86**, 161406(R) (2012).
[26] Y. G. Semenov, X. Duan, and K. W. Kim, Phys. Rev. B **89**, 201405(R) (2014).
[27] X. Duan, X.-L. Li, Y. G. Semenov, and K. W. Kim, Phys. Rev. B **92**, 115429 (2015).
[28] S. Rex, F. S. Nogueira, and A. Sudbø, Phys. Rev. B **94**, 020404(R) (2016).
[29] X.-L. Qi, R. Li, J. Zang, and S.-C. Zhang, Science **323**, 1184 (2009).
[30] F. S. Nogueira and I. Eremin, Phys. Rev. Lett. **109**, 237203 (2012).
[31] S. Rex, F. S. Nogueira, and A. Sudbø, Phys. Rev. B **93**, 014404 (2016).
[32] V. Cherepanov, I. Kolokolov, and V. L'vov, Phys. Rep. **229**, 81 (1993).
[33] J. Barker and G. E. W. Bauer, Phys. Rev. Lett. **117**, 217201 (2016).
[34] W. Luo and X.-L. Qi, Phys. Rev. B **87**, 085431 (2013).
[35] Q. L. He, X. Kou, A. J. Grutter, G. Yin, L. Pan, X. Che, Y. Liu, T. Nie, B. Zhang, S. M. Disseler, B. J. Kirby, W. Ratcliff II, Q. Shao, K. Murata, X. Zhu, G. Yu, Y. Fan, M. Montazeri, X. Han, J. A. Borchers, and K. L. Wang, Nat. Mater. **16**, 94 (2017).
[36] M. Stone, Phys. Rev. D **33**, 1191 (1986).
[37] K. Fujikawa, Phys. Rev. D **72**, 025009 (2005).

Paper [4]

Stefan Rex and Asle Sudbø

Tilting of the magnetic field in Majorana nanowires: critical angle and zero-energy differential conductance

Physical Review B **90**, 115429 (2014)

PHYSICAL REVIEW B **90**, 115429 (2014)

Tilting of the magnetic field in Majorana nanowires: Critical angle and zero-energy differential conductance

Stefan Rex and Asle Sudbø

Department of Physics, Norwegian University of Science and Technology, N-7491 Trondheim, Norway

(Received 18 June 2014; revised manuscript received 10 September 2014; published 23 September 2014)

Semiconductor nanowires with strong spin-orbit coupling and proximity-induced s-wave superconductivity in an external magnetic field have been the most promising settings for approaches towards experimental evidence of topological Majorana zero modes. We investigate the effect of tilting the magnetic field relative to the spin-orbit coupling direction in a simple continuum model and provide an analytical derivation of the critical angle, at which the topological states disappear. We also obtain the differential conductance characteristic of a junction with a normal wire for different tilting angles and propose a qualitative change of the dependence of the zero-energy differential conductance on the tunnel barrier strength at the critical angle as a criterion for establishing the topological nature of the observed signal.

DOI: 10.1103/PhysRevB.90.115429 PACS number(s): 74.78.Na, 73.40.−c, 73.63.Nm

I. INTRODUCTION

Many decades after the prediction of Majorana fermions [1], with no direct and unequivocal experimental evidence for their existence, the possibility of finding emergent Majorana modes of a topological nature in condensed matter systems has evoked considerable interest in a number of systems [2–13], partly because of their expected non-Abelian braiding statistics [2,14,15]. Among the proposed systems, semiconductor nanowires [16] with strong spin-orbit coupling (SOC) and induced s-wave superconductivity in an external magnetic field (Majorana nanowires) have become the most prominent setting. Here, suspected signatures of Majorana zero modes have already been measured [17–23]. However, the experimental findings do not match the predictions precisely, and some predictions therefore have been made for more realistic nanowire models [24–28]. This includes, for instance, finite temperature, finite-size effects, and the three-dimensional wire geometry. Still, further distinguishing criteria for the existence of the topological states in experiment are desirable.

In the present paper, we go back to a simple and analytically accessible one-dimensional continuum model. We focus on the possibility of driving the topological phase transition by changing the direction of the magnetic field relative to the SOC direction, while the standard choice is taking them orthogonal. It is immediately clear that the Majorana zero modes cannot exist for arbitrary field directions. Some experiments have included a rotation of the external magnetic field, but there has been limited quantitative analysis [24,29] of the precise impact of the field direction on the Majorana zero modes and the measured quantity, namely the differential conductance in a junction of the Majorana nanowire with a normal lead.

In this paper, we carry out a detailed analysis of the effect of rotating the magnetic field, with particular emphasis on identifying features of the differential conductance directly connected to the the topological character of the zero-energy modes. In Sec. II, we formulate the Hamiltonian of the system. In Sec. III, we present a way to analytically derive the allowed field directions in terms of a critical angle, for which the system remains in the topological phase. Our analytical results confirm the numerically inspired results of Ref. [29]. In Sec. IV, we compute the differential conductance characteristics of a normal-Majorana nanowire junction for various angles of the Zeeman field relative to the spin-orbit coupling direction. In particular, we concentrate on the zero-energy differential conductance and propose one further criterion for testing the topological origin of the observed peak by varying the tunnel barrier strength while tilting the field across the critical angle. The main result is that below some critical tilting angle away from the direction where the Zeeman field and the SOC are orthogonal, the value of the zero-energy peak is quantized in units of $2\frac{e^2}{h}$, where e is the electron charge and h is Planck's constant, independent of the tunnel barrier of the junction, the value being protected by topology. Beyond a certain angle, this is no longer so, and the value of the zero-energy peak depends on the barrier potential. Conclusions are given in Sec. V.

II. MODEL HAMILTONIAN

We consider a one-dimensional semiconductor nanowire with SOC strength α and a proximity-induced s-wave superconducting gap Δ. Thermal effects can be taken into account in a simple way by taking into account the temperature dependence of the gap Δ in the standard way, at least for temperatures not too close to the superconducting transition temperature. In this paper, we choose the nanowire to be aligned with the x axis, with the SOC in the z direction. We express the external magnetic field $\boldsymbol{B}$ in spherical coordinates, with the polar angle ϑ measured from the z axis and the azimuthal angle φ measured from the x axis, and introduce the Zeeman energy $E_{\mathrm{Zee}} = \frac{1}{2} g \mu_{\mathrm{B}} B$. A sketch of the system and the chosen coordinates can be found in Fig. 1. The Bogoliubov-De Gennes (BdG) Hamiltonian acting on spinors $\psi = (u_\uparrow, u_\downarrow, v_\uparrow, v_\downarrow)^{\mathrm{T}}$, where u, v refer to the electron and hole part of a quasiparticle and $\uparrow, \downarrow$ to the spin in the z direction, respectively, reads [16]

$$H(k) = \begin{pmatrix} h_{\mathrm{n}}(k) & h_{\mathrm{sc}}(k) \\ h_{\mathrm{sc}}^{\dagger}(k) & -h_{\mathrm{n}}^{\mathrm{T}}(-k) \end{pmatrix}, \tag{1a}$$

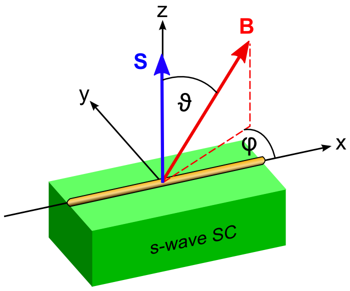

FIG. 1. (Color online) Schematic view of the system: The semiconductor nanowire (yellow) is placed on a bulk s-wave superconductor and defines the x axis of the coordinate system. The z axis is parallel to the SOC direction (labeled $\boldsymbol{S}$ in the figure). The direction of the magnetic field $\boldsymbol{B}$ is represented by the two angles ϑ (tilting relative to the SOC) and φ (azimuthal rotation in the xy plane).

with the normal part

$$h_{\mathrm{n}}(k) = \begin{pmatrix} \xi_k + E_{\mathrm{Zee}} \cos\vartheta + k\alpha & E_{\mathrm{Zee}} \sin\vartheta\, e^{-i\varphi} \\ E_{\mathrm{Zee}} \sin\vartheta\, e^{i\varphi} & \xi_k - E_{\mathrm{Zee}} \cos\vartheta - k\alpha \end{pmatrix} \tag{1b}$$

and s-wave pairing

$$h_{\mathrm{sc}}(k) = h_{\mathrm{sc}} = \begin{pmatrix} 0 & \Delta \\ -\Delta & 0 \end{pmatrix}, \tag{1c}$$

where $\xi_k = (\hbar k)^2/2m - \mu$, m is the effective electron mass, and μ the chemical potential.

III. CRITICAL ANGLE

It is well-known theoretically that the system harbors Majorana zero modes in the topological phase, $E_{\mathrm{Zee}} > \sqrt{\Delta^2 + \mu^2}$ [3,16,30], when $\boldsymbol{B}$ is orthogonal to the SOC direction ($\vartheta = \frac{\pi}{2}$). If the field is tilted, on the other hand, the Majorana modes disappear at a critical angle [24,29] ϑ_c, where the energy gap closes. Figure 2 illustrates the eigenenergies of the BdG Hamiltonian Eq. (1) for parallel and orthogonal field and at $\vartheta = \vartheta_c$. We note that level crossings happen only at $\vartheta = \pi$, thus the gap closes only indirectly at ϑ_c. The second angle φ only gives a phase factor in the eigenstates and is irrelevant for the eigenenergies and the discussion of topological states. The critical angle was observed to follow a rule equivalent to $\cos\vartheta_c = \Delta/E_{\mathrm{Zee}}$ in numerical calculations [29,31]. In this section, we provide the analytical derivation of this rule.

Technically, the task is to find the angle at which the low-energy band first reaches zero energy. The calculation of the eigenenergies is done via the characteristic polynomial, $p_k(E) = \det(H(k) - E)$, which is of order 8 in momentum. For $E = 0$, all odd powers of k vanish, leaving a biquartic equation. With the substitution $\varkappa = k^2$, it reads

$$p(\varkappa) = \left[\left(\frac{\hbar^2}{2m}\varkappa - \mu\right)^2 - \alpha^2\varkappa + \Delta^2 - E_{\mathrm{Zee}}^2\right]^2 + 4\alpha^2\left(\Delta^2 - E_{\mathrm{Zee}}^2 \cos^2\vartheta\right)\varkappa. \tag{2}$$

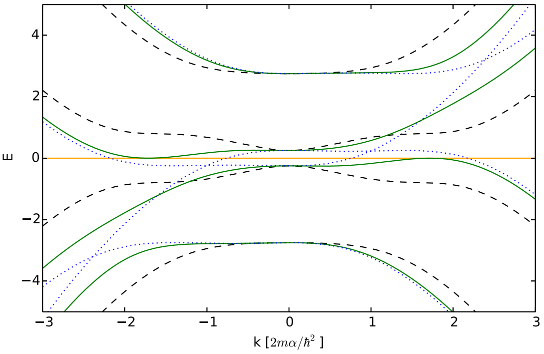

FIG. 2. (Color online) The four eigenenergies of the BdG Hamiltonian Eq. (1) as a function of momentum for $\vartheta = \frac{\pi}{2}$ (black dashed lines), at the critical angle (green solid lines), where the gap closes (here $\vartheta_c \approx 0.81\pi$), and at $\vartheta = \pi$ (blue dotted lines). The orange line indicates zero energy. Parameters: $m = 1, \Delta = 1.25, E_{\mathrm{Zee}} = 1.5, \alpha = \sqrt{1/2}, \mu = 0$.

As long as the band gap remains open, $p_k(0)$ will be solved only by complex momenta, whereas real solutions appear when $\boldsymbol{B}$ is tilted beyond the critical angle. The real solutions of $p_k(0)$ lead to non-negative solutions of $p(\varkappa)$. To derive the critical angle, we will exploit the special form of Eq. (2), being the square of a quadratic polynomial in $\varkappa$, with one additional $\varkappa$-linear term containing the dependence on ϑ. We analyze the quadratic expression first, and find its zeros

$$\varkappa_{1,2} = \frac{1}{2}\left(\frac{2m}{\hbar^2}\right)^2 \left[\frac{\hbar^2\mu}{m} + \alpha^2 \pm \sqrt{\left(\frac{\hbar^2\mu}{m} + \alpha^2\right)^2 - \left(\frac{\hbar^2}{m}\right)^2 \left(\mu^2 + \Delta^2 - E_{\mathrm{Zee}}^2\right)}\right]. \tag{3}$$

To allow for topological states at all, $(\mu^2 + \Delta^2 - E_{\mathrm{Zee}}^2)$ must necessarily be negative [3,16,30]. Thus, Eq. (3) always yields two real solutions, where $\varkappa_1 > 0$ and $\varkappa_2 < 0$. In the absence of the linear term, Eq. (2) is positive semidefinite and will have precisely the same solutions, just two-fold degenerate each. If, however, the $\varkappa$-linear term is present with positive (negative) coefficient, the point symmetry of $p(\varkappa)$ is lost and the solutions become nondegenerate, where the positive solution is split in two distinct complex (real) values, cf. Fig. 3. We conclude from Eq. (2) that the system is in the topological phase, when $\Delta^2 - E_{\mathrm{Zee}}^2 \cos^2\vartheta > 0$. Consequently, the critical angle satisfies

$$\cos\vartheta_c = \pm\frac{\Delta}{E_{\mathrm{Zee}}}. \tag{4}$$

Thus, we have analytically confirmed the numerical results obtained in Ref. [29]. As the angle ϑ is increased through the value ϑ_c, topologically trivial zero-energy states will appear with the momentum $\pm\sqrt{\varkappa_1}$. An alternative, but much more lengthy, derivation of the same result using the discriminant [32] of the fourth-order polynomial $p(\varkappa)$ is also possible.

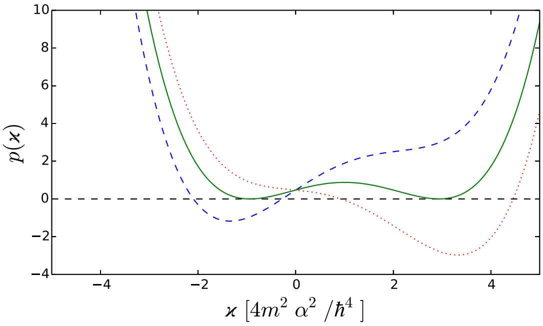

FIG. 3. (Color online) The characteristic polynomial $p(\varkappa)$ of the Hamiltonian at zero energy as a function of $\varkappa = k^2$ for the tilting angles $\vartheta = 0.74\pi$ (blue dashed line), the critical angle $\vartheta_c \approx 0.81\pi$ (green solid line), where positive solutions for $\varkappa$ appear first, and $\vartheta = 0.9\pi$. Parameters: $m = 1, \Delta = 1.25, E_{\mathrm{Zee}} = 1.5, \alpha = \sqrt{1/2}, \mu = 0$.

The angle-resolved topological phase diagram is shown in Fig. 4. If the Zeeman energy is just slightly larger than the superconducting gap, ϑ can be varied over a wide range without destroying the Majorana zero modes, whereas for large Zeeman energy the tilting angle is restricted to a narrow range about $\frac{\pi}{2}$. In that sense, a high field does not lead to a more stable topological phase, although $E_{\mathrm{Zee}} > \sqrt{\Delta^2 + \mu^2}$ is a necessary prerequisite [3,16,30]. This is readily seen, since this latter condition acts on the energy gap at zero momentum, which does not depend on the direction of the field. In contrast, if the phase transition is driven by ϑ, the gap closes near the Fermi momentum [29] at $\sqrt{\varkappa_1}$, cf. Fig. 2, where increasing the field strength pushes the low-energy band closer to zero.

IV. DIFFERENTIAL CONDUCTANCE CHARACTERISTICS

In the remainder of this paper, we focus on the differential conductance characteristics of a junction of the Majorana nanowire with a normal lead and the impact of tilting $\boldsymbol{B}$. The angular dependence of the differential conductance in such junctions was briefly discussed in Ref. [24] based on numerical studies of a tight-binding model. In contrast, we will analyze the current through the system in a simple continuum model. In the following, we will for simplicity set $\mu = 0$.

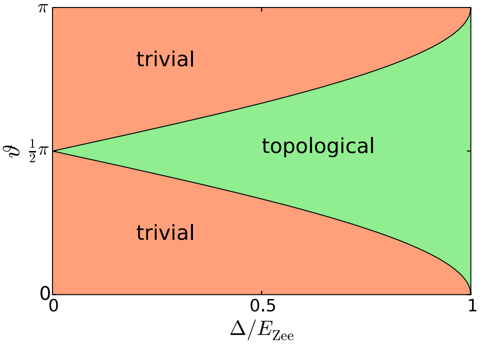

FIG. 4. (Color online) The angle-resolved topological phase diagram of the Majorana nanowire.

We assume infinite wire length and a tunnel barrier of strength V at the junction (located at $x = 0$). The normal ($x < 0$) and superconducting ($x > 0$) sections of the wire are modeled with the same Hamiltonian Eq. (1), where we just set $\Delta = 0$ in the normal state. For electrons impinging from the normal side onto the junction we investigate the coefficients of reflected and transmitted waves. To solve the scattering problem, we employ a Blonder-Tinkham-Klapwijk (BTK) formalism [33], i.e., matching of wave functions at the junction. The original BTK scheme is extended to account for the spin as well.

At a given energy E, we first obtain all possible momenta by solving $p_k(E) = 0$ for the normal and the superconducting wire. Exact diagonalization of Eq. (1) at each k (including complex) then yields plane-wave states $\Psi_k(x) = \psi_k e^{ikx}$ with four-component spinors ψ_k. The incident electron wave $\Psi^{\mathrm{in}}_{k_{\mathrm{in}}}$ is always chosen from the normal low-energy band. All other states that correspond to incoming waves are discarded. The scattering process comprises ordinary and Andreev reflection into the normal lead, and transmission without ($k > 0$) and with ($k < 0$) branch crossing into the superconducting lead. The corresponding scattering coefficients are denoted a_i, b_i, c_i, d_i, respectively, where $i \in \{1,2\}$ labels the pseudospin. The total wave functions on the normal and superconducting side of the junction are then

$$\Psi^{\mathrm{n}}(x < 0) = \Psi^{\mathrm{in}}_{k_{\mathrm{in}}} + \sum_{i=1,2} a_i \Psi_{k_{a,i}} + b_i \Psi_{k_{b,i}}, \tag{5}$$

$$\Psi^{\mathrm{sc}}(x > 0) = \sum_{i=1,2} c_i \Psi_{k_{c,i}} + d_i \Psi_{k_{d,i}}. \tag{6}$$

At the junction, we impose the boundary conditions

$$\Psi^{\mathrm{n}}(x \to 0^-) - \Psi^{\mathrm{sc}}(x \to 0^+) = 0 \tag{7}$$

$$\partial_x \Psi^{\mathrm{n}}(x \to 0^-) - \partial_x \Psi^{\mathrm{sc}}(x \to 0^+) = \frac{2mV}{\hbar^2} \Psi(0) \tag{8}$$

and solve the resulting linear system of equations to obtain all scattering coefficients. The probability current

$$J = \frac{\hbar}{m} \mathfrak{Im}(\Psi^\dagger \partial_x \tau_z \Psi) + \frac{\alpha}{\hbar} \Psi^\dagger \sigma_z \Psi \tag{9}$$

carried by each outgoing wave, where we have taken into account a contribution due to the SOC [34], is proportional to the square of the absolute value of the respective coefficient. Here, τ_z and σ_z denote Pauli matrices acting in particle-hole and spin space, respectively. In the subgap regime, where the Majorana modes reside, the system is effectively spinless, therefore we will relinquish the distinction of states with different pseudospin for the discussion of the scattering probabilities, denoted A, B, C, and D. Then, C, for instance, reads

$$C = \sum_{i=1,2} |c_i|^2 \frac{\left|\psi^\dagger_{k_{c,i}} \left(\mathfrak{Re}(k_{c,i})\tau_z + \frac{\alpha m}{\hbar^2}\sigma_z\right)\psi_{k_{c,i}}\right|}{\left|k_{\mathrm{in}} + \frac{\alpha m}{\hbar^2}\psi^\dagger_{\mathrm{in}}\sigma_z\psi_{\mathrm{in}}\right|}. \tag{10}$$

Note that for A and B the term $\psi^\dagger_k \tau_z \psi_k$ gives always just -1 (holes, Andreev reflection) or 1 (electrons, ordinary reflection),

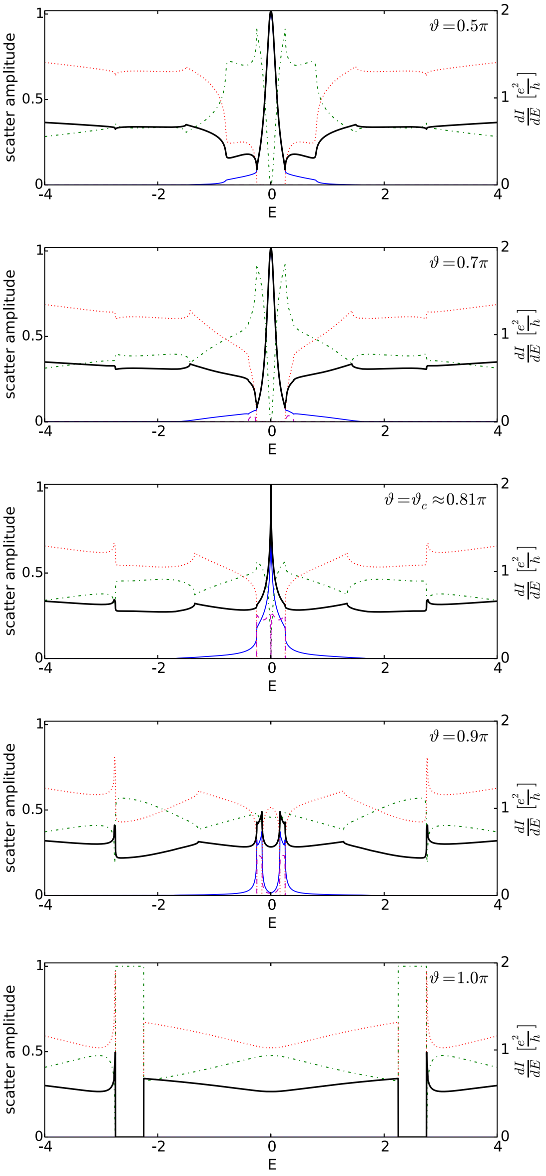

FIG. 5. (Color online) The energy-resolved scattering coefficients (left scale) and differential conductance characteristic (right scale) of a normal-Majorana nanowire junction at different tilting angles of the magnetic field: Andreev reflection A (blue solid line), ordinary reflection B (green dash-dotted line), transmission without branch crossing C (red dotted line), transmission with branch crossing D (purple dashed line), and differential conductance (black bold solid line). Parameters: $m = 1, \Delta = 1.25, E_{\mathrm{Zee}} = 1.5, \alpha = \sqrt{1/2}, V = 2.0$.

respectively. The differential conductance at E through the junction at zero temperature is finally given by [28,33] $\frac{dI}{dE} = 1 + A - B$ in units of $\frac{e^2}{h}$, and inside the gap, where $C = D = 0$, even simpler as $\frac{dI}{dE} = 2A$ by conservation of probability $(A + B + C + D = 1)$.

By this scheme, we obtain the scattering probabilities and the differential conductance profile $\frac{dI}{dV}(E)$ of the junction for different field directions, cf. Fig. 5. The scattering probability profiles indicate the features of the band structure at the respective angle, e.g., the gap width. In the topological phase, the conductance peak at zero energy that signals the existence of Majorana zero modes is clearly seen. The peak gets narrower as the tilting angle of the field approaches the critical angle and disappears in the trivial phase. As expected, the peak height exhibits the quantized value [35–38] of $2\frac{e^2}{h}$ due to resonant Andreev reflection.

Attempts at detecting emergent Majorana zero modes experimentally originally focused on the quantized value of the zero-energy differential conductance as the hallmark of such states. Under real conditions, however, only much smaller values are observed [17,24]. Other, more qualitative and more robust distinguishing criteria are required. We propose that sharp change in the zero-energy differential conductance peak at the critical tilting angle ϑ_c of the field provides an appropriate further qualitative criterion for examining the topological nature of measured signatures. In experiments, it may be difficult to record the full conductance profiles as in Fig. 5 with the required precision. Therefore, we propose to measure the zero-energy differential conductance for different tilting angles of the field while varying the tunnel barrier strength of the junction. The predicted behavior is shown in Fig. 6. A qualitative change of the dependence of $\frac{dI}{dE}(0)$ on V should be observed at the critical angle upon entering the trivial phase, where the conductance can be suppressed by increasing the tunnel barrier. In the topological state, the value of the zero-bias conductance peak is impervious to the change in barrier strength, being protected by topology.

At finite temperatures well below the superconducting transition temperature, the impact on the results in Fig. 5 is to slightly smear the sharp cusp at ϑ_c. The main change in qualitative behavior above and below ϑ_c is robust. The main effect on the critical angle itself can be accounted for by taking into account the temperature dependence of the gap in Eq. (4). Finite-size effects are also present, in principle. A finite length of the Majorana nanowire causes an overlap of the exponentially localized topological states at the ends

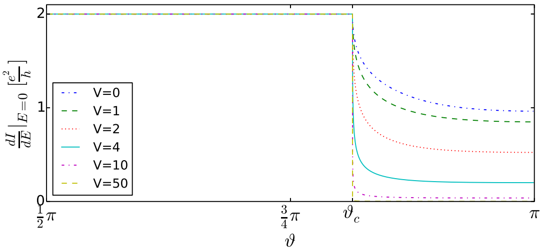

FIG. 6. (Color online) The differential conductance at zero energy as a function of the tilting angle of the field for different tunnel barrier strengths V. Parameters: $m = 1, \Delta = 1.25, E_{\mathrm{Zee}} = 1.5, \alpha = \sqrt{1/2}$.

of the wire [24]. Thus, the transition happens before the low-energy band reaches zero and the true topological regime is expected to be slightly narrower than predicted by ϑ_c. Numerical data from Ref. [29] indicate, however, that this effect is not important.

V. CONCLUSION

In this paper, we have studied semiconductor nanowires with SOC and s-wave superconductivity in an external magnetic field with arbitrary direction in an analytically accessible continuum model. We have derived the critical tilting angle ϑ_c of the field relative to the SOC direction, at which the topological (Majorana) zero modes disappear. Our result confirms recent numerical findings [29]. Furthermore, we have considered normal-Majorana nanowire junctions and obtained the differential conductance characteristics at various angles, where, as expected, a stable peak at zero energy with the quantized value of $2\frac{e^2}{h}$ occurs as long as the field is not tilted beyond the critical angle ϑ_c. The peak disappears for fields aligned too much in the direction of the SOC, and the value of the zero-energy differential conductance becomes strongly dependent on the tunnel barrier strength. We have pointed out the qualitative change of the dependence on the barrier strength at the critical angle and suggest it as further criterion to test the topological nature of the experimentally observable signals, even if the theoretical quantized peak value may not be reached under realistic conditions.

ACKNOWLEDGMENTS

A.S. and S.R. acknowledge support from the Norwegian Research Council, Grant Nos. 205591/V20 and 216700/F20. We thank Jacob Linder for helpful comments.

[1] E. Majorana, Nuovo Cimento **14**, 171 (1937).
[2] N. Read and D. Green, Phys. Rev. B **61**, 10267 (2000).
[3] A. Kitaev, Phys. Usp. **44**, 131 (2001).
[4] S. Das Sarma, C. Nayak, and S. Tewari, Phys. Rev. B **73**, 220502(R) (2006).
[5] Y. Tsutsumi, T. Kawakami, T. Mizushima, M. Ichioka, and K. Machida, Phys. Rev. Lett. **101**, 135302 (2008).
[6] V. Gurarie, L. Radzihovsky, and A. V. Andreev, Phys. Rev. Lett. **94**, 230403 (2005).
[7] L. Fu and C. L. Kane, Phys. Rev. Lett. **100**, 096407 (2008).
[8] F. Wilceck, Nat. Phys. **5**, 614 (2009).
[9] J. Linder, Y. Tanaka, T. Yokoyama, A. Sudbø, and N. Nagaosa, Phys. Rev. Lett. **104**, 067001 (2010).
[10] J. Alicea, Rep. Prog. Phys. **75**, 076501 (2012).
[11] Y. Tanaka, M. Sato, and N. Nagaosa, J. Phys. Soc. Jpn. **81**, 011013 (2012).
[12] S. Nakosai, J. C. Budich, Y. Tanaka, B. Trauzettel, and N. Nagaosa, Phys. Rev. Lett. **110**, 117002 (2013).
[13] Y. Asano and Y. Tanaka, Phys. Rev. B **87**, 104513 (2013).
[14] D. A. Ivanov, Phys. Rev. Lett. **86**, 268 (2001).
[15] A. Kiteav, Annals Phys. **303**, 2 (2003).
[16] R. M. Lutchyn, J. D. Sau, and S. Das Sarma, Phys. Rev. Lett. **105**, 077001 (2010).
[17] V. Mourik, K. Zuo, S. M. Frolov, S. R. Plissard, E. P. A. M. Bakkers, and L. P. Kouwenhoven, Science **336**, 1003 (2012).
[18] L. P. Rokhinson, X. Liu, and J. K. Furdyna, Nat. Phys. **8**, 795 (2012).
[19] A. Das, Y. Ronen, Y. Most, Y. Oreg, M. Heiblum, and H. Shtrikman, Nat. Phys. **8**, 887 (2012).
[20] A. D. K. Finck, D. J. Van Harlingen, P. K. Mohseni, K. Jung, and X. Li, Phys. Rev. Lett. **110**, 126406 (2013).
[21] M. T. Deng, C. L. Yu, G. Y. Huan, M. Larsson, and P. Caroff, Nano Lett. **12**, 6414 (2012).
[22] H. O. H. Churchill, V. Fatemi, K. Grove-Rasmussen, M. T. Deng, P. Caroff, H. Q. Xu, and C. M. Marcus, Phys. Rev. B **87**, 241401(R) (2013).
[23] E. J. H. Lee, X. Jiang, M. Houzet, R. Aguado, C. M. Lieber, and S. De Franceschi, Nat. Nanotechnol. **5**, 79 (2013).
[24] C.-H. Lin, J. D. Sau, and S. Das Sarma, Phys. Rev. B **86**, 224511 (2012).
[25] J. S. Lim, R. Lopez, and L. Serra, New J. Phys. **14**, 083020 (2012).
[26] J. S. Lim, R. Lopez, and L. Serra, Europhys. Lett. **103**, 37004 (2013).
[27] J. Osca and L. Serra, Phys. Rev. B **88**, 144512 (2013).
[28] E. Prada, P. San-Jose, and R. Aguado, Phys. Rev. B **86**, 180503(R) (2012).
[29] J. Osca, D. Ruiz, and L. Serra, Phys. Rev. B **89**, 245405 (2014).
[30] Y. Oreg, G. Refael, and F. von Oppen, Phys. Rev. Lett. **105**, 177002 (2010).
[31] With our choice of coordinates, the rule contains only one instead of two angles, and it appears with a cosine instead of a sine.
[32] E. L. Rees, Am. Math. Mon. **29**, 51 (1922).
[33] G. E. Blonder, M. Tinkham, and T. M. Klapwijk, Phys. Rev. B **25**, 4515 (1982).
[34] F. Bottegoni, H.-J. Drouhin, J.-E. Wegrowe, and G. Fishman, J. Appl. Phys. **111**, 07C305 (2012).
[35] K. Sengupta, I. Žutić, H.-J. Kwon, V. M. Yakovenko, and S. Das Sarma, Phys. Rev. B **63**, 144531 (2001).
[36] K. T. Law, P. A. Lee, and T. K. Ng, Phys. Rev. Lett. **103**, 237001 (2009).
[37] K. Flensberg, Phys. Rev. B **82**, 180516(R) (2010).
[38] M. Wimmer, A. R. Akhmerov, J. P. Dahlhaus, and C. W. J. Beenakker, New J. Phys. **13**, 053016 (2011).

Paper [5]

Carsten Timm, Stefan Rex, and Philip M. R. Brydon

Surface instability in nodal superconductors

Physical Review B **91**, 180503(R) (2015)

RAPID COMMUNICATIONS

PHYSICAL REVIEW B **91**, 180503(R) (2015)

Surface instability in nodal noncentrosymmetric superconductors

Carsten Timm,[1,*] Stefan Rex,[2] and P. M. R. Brydon[3,†]

[1]*Institute of Theoretical Physics, Technische Universität Dresden, 01062 Dresden, Germany*
[2]*Department of Physics, Norwegian University of Science and Technology, 7491 Trondheim, Norway*
[3]*Condensed Matter Theory Center and Joint Quantum Institute, University of Maryland, College Park, Maryland 20742, USA*

(Received 8 April 2015; revised manuscript received 29 April 2015; published 13 May 2015)

We study the stability of topologically protected zero-energy flat bands at the surface of nodal noncentrosymmetric superconductors, accounting for the alteration of the gap near the surface. Within a self-consistent mean-field theory, we show that the flat bands survive in a broad temperature range below the bulk transition temperature. There is a second transition at a lower temperature, however, below which the system spontaneously breaks time-reversal symmetry. The surface bands are shifted away from zero energy and become weakly dispersive. Simultaneously, a spin polarization and an equilibrium charge current develop in the surface region.

DOI: 10.1103/PhysRevB.91.180503 PACS number(s): 74.20.Rp, 73.20.At, 74.25.Ha, 74.25.Jb

Introduction. The topological properties of gapless electronic systems have recently attracted much attention [1–6]. Important examples are time-reversal-symmetric noncentrosymmetric superconductors (NCSs) [1,2,7–11], which are characterized by strong antisymmetric spin-orbit coupling (SOC) and a parity-mixed pairing state [12]. Many NCSs display evidence of gaps with line nodes [13–18]. This is exciting, as the line nodes of NCSs with dominant triplet pairing are topologically nontrivial defects in momentum space [1–4]. Zero-energy flat bands of Majorana fermions are predicted to appear within the projections of these nodal lines onto the surface Brillouin zone (BZ). Such flat bands have clear experimental signatures, such as sharp zero-bias peaks in tunneling spectra [2,11], equilibrium currents parallel to the interface between the NCS and a ferromagnet [19,20], and characteristic quasiparticle interference patterns [21].

The topological properties of NCSs and consequently the protection of the surface states are controlled by the superconducting gaps, which arise from interactions. Properly accounting for these interactions may qualitatively alter the surface physics. For example, a surface tends to suppress some gap components and enhance others [22–28]. This may change the conclusions of the aforementioned studies [1–6,9–11], which imposed unrealistic uniform gaps. Flat bands with their high density of states are particularly prone to instabilities. Indeed, the zero-energy flat bands at the (110) surface of d-wave superconductors with time-reversal symmetry (TRS) [29] are predicted to be unstable towards a time-reversal-symmetry-breaking (TRSB) state [22–28,30]. This has been supported by some tunneling and transport experiments [31–33] but was not seen in others [34–38]. d-wave superconductors are however qualitatively different from NCSs in that the zero-energy flat bands are degenerate in the first case but nondegenerate in the second.

In this Rapid Communication, we study the stability of the surface zero-energy flat bands of nodal NCSs by performing self-consistent mean-field (MF) calculations in real space for a slab of finite thickness. For concreteness, we consider a model with point group C_{4v}, which is realized for $\mathrm{CePt_3Si}$ [39], $\mathrm{CeRhSi_3}$ [40], and $\mathrm{CeIrSi_3}$ [41]. We show that an instability to a TRSB state can occur and study its signatures.

Model and mean-field theory. We start from a tight-binding Hamiltonian for an NCS with C_{4v} point group, $H = H_0 + H_{\mathrm{int}}$. The noninteracting part is

$$H_0 = -\mu \sum_j c_j^\dagger c_j - t \sum_{\langle ij\rangle} (c_i^\dagger c_j + c_j^\dagger c_i) + i\lambda \sum_{\langle ij\rangle} (\hat{\mathbf{z}} \times \hat{\mathbf{e}}_{ij}) \cdot \left(c_i^\dagger \frac{\boldsymbol{\sigma}}{2} c_j - c_j^\dagger \frac{\boldsymbol{\sigma}}{2} c_i \right), \tag{1}$$

with the chemical potential μ, the nearest-neighbor hopping amplitude t, and the Rashba SOC strength λ. The SOC term breaks inversion symmetry. The annihilation operator $c_j = (c_{j,\uparrow}, c_{j,\downarrow})^T$ is a two-component spinor, σ is the vector of Pauli matrices, and $\hat{\mathbf{e}}_{ij}$ is the unit vector pointing from site j to site i of a simple cubic lattice. Attractive interactions at the same site and between nearest neighbors in the xy plane are described by

$$H_{\mathrm{int}} = -U_s \sum_j c_{j\uparrow}^\dagger c_{j\downarrow}^\dagger c_{j\downarrow} c_{j\uparrow} - U_t \sum_{\langle ij\rangle \perp \hat{\mathbf{z}}} \sum_{\sigma\sigma'} c_{i\sigma}^\dagger c_{j\sigma'}^\dagger c_{j\sigma'} c_{i\sigma}. \tag{2}$$

The interaction is decoupled in the pairing channel. We define the singlet and triplet order parameters $\Delta_j^s \equiv (U_s/2)\langle c_j^T i\sigma^y c_j\rangle$ and $\boldsymbol{\Delta}_{ij}^t \equiv iU_t\langle c_j^T i\sigma^y \boldsymbol{\sigma} c_i\rangle$, respectively, where the site indices i,j in $\boldsymbol{\Delta}_{ij}^t$ are restricted to nearest-neighbor sites in the xy plane. The triplet vector order parameter is taken to be parallel to the effective SOC field, $\boldsymbol{\Delta}_{ij}^t = \Delta_{ij}^t \hat{\mathbf{z}} \times \hat{\mathbf{e}}_{ij}$. This choice avoids the triplet-pair-breaking effect of the SOC, and is therefore energetically favorable in the bulk [42].

We first consider the MF solution for an extended system, assuming spatially uniform gaps $\Delta_j^s = \Delta_s$ and $\Delta_{ij}^t = \Delta_t$. Details of the calculation are given in Sec. I of the Supplemental Material [43]. We find that the singlet and triplet gaps have the same phase, which can be set to zero, so that TRS is preserved. SOC splits the bands and thus also the Fermi surface according to the helicity of states [2]. Since the triplet order parameter is parallel to the SOC, pairing only occurs between states with the same helicity. We determine interaction strengths U_s, U_t that lead to flat zero-energy surface bands under the assumption of uniform gaps. The resulting surface states have been studied

---

[*] carsten.timm@tu-dresden.de
[†] pbrydon@umd.edu

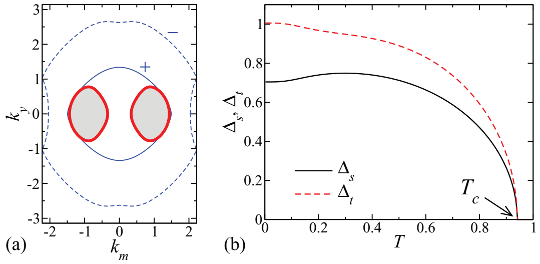

FIG. 1. (Color online) (a) Projection onto the (101) plane of the positive-helicity Fermi surface (thin solid line), the negative-helicity Fermi surface (dashed line), and the superconducting gap nodes on the former (heavy solid lines), for the bulk NCS. The gray areas denote the zero-energy flat bands predicted to exist at (101) surfaces under the assumption of uniform gaps [1,2]. The plot is restricted to momenta in the (101) surface BZ, where $k_m = (k_x - k_z)/\sqrt{2}$. The parameters are $t = 1$, $\lambda = 1.5$, $\mu = -3$, $U_s = 5.0$, $U_t = 5.4$, and $T = 0.0025$. (b) Mean-field gaps Δ_s (solid black) and Δ_t (dashed red) as functions of temperature T.

in detail in Refs. [2,11,44]. This is realized for the parameters $t = 1$ (hence, t is our unit of energy), $\lambda = 1.5$, $\mu = -3$, $U_s = 5.0$, $U_t = 5.4$ at the temperature $T = 0.0025$ (setting $k_B = 1$), giving bulk MF gaps $\Delta_s = 0.704$ and $\Delta_t = 1.006$. We consequently find a gap with line nodes on the (smaller) positive-helicity Fermi surface, but a full gap on the (larger) negative-helicity Fermi surface [45]. Figure 1(a) shows the projection of the two Fermi surfaces and the nodal lines onto the (101) plane. The topological argument from Refs. [1,2] predicts that a (101) surface hosts flat zero-energy bands within the region bounded by the projected nodal lines. In addition, there is an arc of zero-energy states connecting the two regions with flat bands [2,5,11]. Figure 1(b) shows the bulk gaps Δ_s and Δ_t as functions of temperature.

We next turn to the MF solution for a slab of thickness W with (101) surfaces. We introduce new coordinates $x = m + (l + l \bmod 2)/2$ and $z = -m + (l - l \bmod 2)/2$, where m is parallel to the surfaces and $l = 0, \ldots, W - 1$ is orthogonal to them. The geometry of one surface and our coordinate system are depicted in the inset of Fig. 2. Since translational symmetry in the normal direction is broken, the gaps depend on l. We define

$$\frac{U_s}{2}\langle c_j^T i\sigma^y c_j\rangle \equiv \Delta_l^s, \tag{3}$$

$$iU_t\langle c_j^T i\sigma^y \boldsymbol{\sigma} c_i\rangle \equiv \begin{cases} \Delta^x_{l+1/2}\,\hat{\mathbf{z}}\times\hat{\mathbf{e}}_{ij} & \text{for } x \text{ bonds},\\ \Delta^y_l\,\hat{\mathbf{z}}\times\hat{\mathbf{e}}_{ij} & \text{for } y \text{ bonds},\end{cases} \tag{4}$$

where the subscript l denotes the (identical) l coordinate of sites i and j, while $l + 1/2$ in $\Delta^x_{l+1/2}$ is the mean of the l coordinates of sites i and j. We Fourier transform in the directions parallel to the slab, introducing the two-dimensional momentum vector $\mathbf{k} = (k_m, k_y)$ in the surface BZ, defined by $-\pi < k_y \leqslant \pi$ and $-\pi/\sqrt{2} < k_m \equiv (k_x - k_z)/\sqrt{2} \leqslant \pi/\sqrt{2}$. The MF calculations are performed for a slab of thickness $W = 300$, using the same parameters as for the bulk calculation.

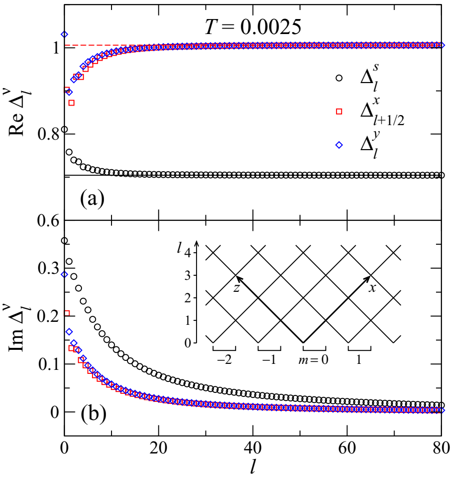

FIG. 2. (Color online) Self-consistent gaps Δ_l^s, $\Delta_{l+1/2}^x$, Δ_l^y for a slab of thickness $W = 300$ and parameters as in Fig. 1. (a) and (b) show the real and imaginary parts, respectively. The lines denote the bulk gaps Δ_s (solid black) and Δ_t (dashed red). Inset: Sketch of the bottom ($l = 0$) surface of a (101) slab, showing the coordinates l and m. The y axis points into the plane of the drawing.

Further details are presented in Sec. II of the Supplemental Material [43].

Spontaneous breaking of TRS. Our central results are summarized in Figs. 2 and 3: At sufficiently low temperatures, the singlet and triplet gaps develop imaginary components

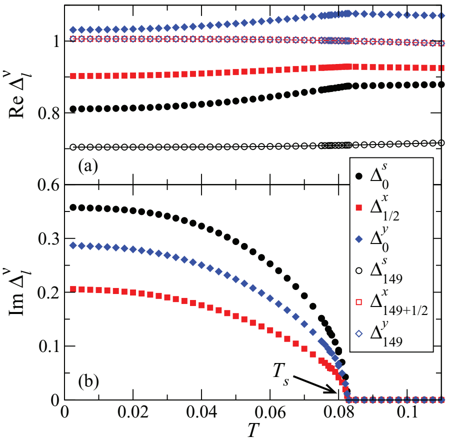

FIG. 3. (Color online) Self-consistent gaps Δ_l^s, $\Delta_{l+1/2}^x$, Δ_l^y for the surface layer ($l = 0$, solid symbols) and at the slab center ($l = W/2 - 1$, open symbols) as functions of temperature. The thickness is $W = 300$, and the parameters are as in Fig. 1. (a) and (b) show the real and imaginary parts, respectively. The imaginary parts for $l = W/2 - 1$ would be indistinguishable from zero and are omitted. The lines in (a) denote the bulk gaps Δ_s (solid black) and Δ_t (dashed red) from Fig. 1(b).

close to the surface, spontaneously breaking TRS. This solution is degenerate with a state with complex-conjugated gaps. In the limit $W \to \infty$, the two surfaces are decoupled and there are hence four degenerate TRSB solutions, differing in the signs of the imaginary parts of the gaps close to the surfaces.

The spatial variation of the gaps near the surface in the TRSB phase is shown in Fig. 2. While both the singlet and triplet gaps develop imaginary components near the surface, the real parts of the singlet and triplet gaps are enhanced above and suppressed below their bulk values, respectively. The suppression of the triplet gaps originates from the pair-breaking effect of the surface, which in turn enhances the singlet gap to compensate for the lost condensation energy. The reversal of the suppression of the triplet gaps in the outermost layer can be understood similarly: Since one of the triplet amplitudes is missing at the surface, the others are enhanced.

The gaps converge to their bulk values as we move away from the surface; the gaps at the center of the slab are within 0.01% of their bulk values. Note that the deviation of the imaginary parts from their bulk value (of zero) has a much longer range than that of the real parts. Indeed, close to the center of the slab, we find that $\mathrm{Im}\,\Delta_l^y \propto (l - W/2)$ [see Fig. 2(b)]. We have checked that the proportionality constant decreases more rapidly than $W^{-1/2}$ with W so that the gradient energy vanishes for $W \to \infty$. We attribute the slow spatial decay to the enhancement of length scales close to the bulk quantum phase transition to a nodeless singlet-dominated state. This transition can be reached by increasing U_s and decreasing U_t by only 0.067 (not shown).

The evolution of the TRSB state with temperature is shown in Fig. 3, where we plot the gaps Δ_l^s, $\Delta_{l+1/2}^x$, and Δ_l^y in the surface layer and at the slab center. Upon increasing the temperature, the gaps in the surface layer show a second-order transition at which the imaginary parts vanish and TRS is restored. This occurs at a temperature of $T_s \approx 0.083$, well below the bulk superconducting transition temperature $T_c \approx 0.942$.

Dispersion and density of states. In Fig. 4(a) we plot the dispersion for a cut through the surface BZ at $k_y = 0$ at temperatures below and above T_s. For $T > T_s$, the zero-energy flat band predicted in Refs. [2,11] is clearly visible for $0.5 \lesssim k_m \lesssim 1.5$; the zero-energy states at $k_m \lesssim 0.5$ form an arc connecting the projections of the nodal rings [2,11]. The TRSB for $T < T_s$ removes the topological protection of the zero-energy flat bands of the TRS state, which are consequently pushed away from zero energy, with a low-temperature energy shift on the order of T_s. Since the shift is weakly momentum dependent, the band obtains a nonzero velocity. Due to particle-hole symmetry, the dispersion is odd in $\mathbf{k}$. The zero-energy flat bands give a singular contribution to the surface density of states, which can be detected as a sharp zero-bias peak in the tunneling spectrum of an NCS–normal-metal junction [1,10,11]. The shift of the surface bands in the TRSB state causes a splitting of this peak, as shown in Fig. 4(b). This splitting is a key experimental signature of TRSB. Indeed, the observed splitting of the zero-bias peak for tunneling into the (110) surface of the cuprates is important evidence for TRSB in this system [31,32].

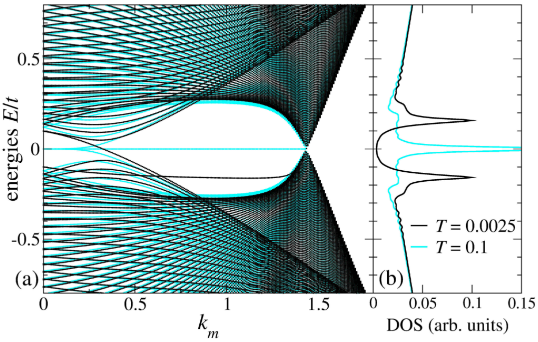

FIG. 4. (Color online) (a) Dispersion for a cut through the surface BZ at $k_y = 0$, for $W = 300$ and the same parameters as in Fig. 1. The black points refer to $T = 0.0025 \ll T_s$ in the TRSB state, whereas the cyan (light gray) points in the background refer to $T = 0.1 > T_s$ with restored TRS. The dispersion is odd in k_m, and only points for $k_m \geqslant 0$ are shown. (b) Surface DOS in the $l = 0$ layer at the same temperatures. An artificial broadening of $\eta = 0.01$ was used.

Spin polarization. Broken TRS is also manifested by a nonzero spin polarization near the surface, which is directed along the y axis. A polarization in other directions is forbidden by mirror symmetry in the xz plane. Figure 5(a) shows the spatial variation of the layer-resolved spin contributions $\langle s_l^y \rangle$; explicit expressions for the spin operator $\mathbf{s}_l$ in layer l and its thermal average are given in Sec. III of the Supplemental Material [43]. It is interesting to examine how states at different $\mathbf{k}$ contribute to the spin polarization: Due to the strong polarization of the flat-band surface states in the TRS state [44,46], one might expect that the spin polarization largely originates from the shifted flat bands. To check this, we plot in Fig. 5(b) the momentum-resolved contribution to the spin polarization of the half slab defined by $0 \leqslant l < W/2$ [43]. Surprisingly, the spin polarization is not primarily carried by the shifted flat bands but rather by bulk and perhaps dispersing surface states [2,11] from the region between the projected nodal rings.

Equilibrium currents. Furthermore, the absence of TRS permits a nonzero equilibrium surface current [22,24,26]. Indeed, we expect such a current since the surface bands become dispersive and the dispersion is odd in k_m; a similar modification of the electronic structure at an interface with a ferromagnet does result in a surface current [19,20]. Explicit expressions for the current operator $\mathbf{j}_l$ in layer l and its thermal average are given in Sec. IV of the Supplemental Material [43]. Although charge is not conserved in the superconducting MF state, one can account for the pairing potentials by adding so-called source terms to the continuity equation [47]. For self-consistently calculated gaps, however, the thermal average of the source terms vanishes, and charge conservation is retained [47]. This implies that the current perpendicular to the slab's surface, i.e., in the l direction, must vanish. Mirror symmetry in the xz plane forbids a current along the y axis [43], leaving only the current along the m direction, defined as $\langle j_{l+1/2}^m \rangle = (\langle j_{l+1/2}^x \rangle - \langle j_{l+1/2}^z \rangle)/\sqrt{2}$. $\langle j_{l+1/2}^m \rangle$ is indeed nonzero in the TRSB state: In Fig. 5(a) we plot the current as a function of the layer index l, which shows that it is bound to the

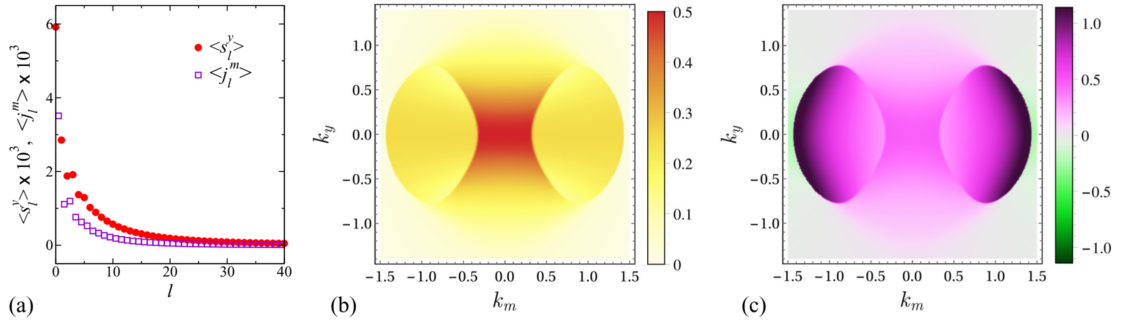

FIG. 5. (Color online) (a) Spin polarization $\langle s_l^y \rangle$ (solid circles) and current $\langle j_l^m \rangle$ (open squares) as functions of l, for $W = 300$ and the same parameters as in Fig. 1. Both quantities are given in units of their value at the surface. The layer indices of $\langle j_l^m \rangle$ are given as half integers to indicate that the current flows between two layers (see the inset of Fig. 2). (b) Momentum-resolved contributions to the y component of the total spin polarization of half the slab ($0 \leqslant l < W/2$) in the surface BZ. (c) Momentum-resolved contributions to the m component of the current in half the slab ($0 \leqslant l < W/2$). The momentum-space plots in (b) and (c) are restricted to a region just enclosing the projection of the positive-helicity Fermi surface.

surface with a spatial profile similar to the spin polarization. In contrast to the spin polarization, the main contribution to the current stems from surface states within the projected nodal rings, as shown by the momentum-resolved current in a half slab plotted in Fig. 5(c). We have also studied the contributions to the vanishing components $\langle j_l^l \rangle$ and $\langle j_l^y \rangle$, shown in the Supplemental Material [43]. Interestingly, $\langle j_l^l \rangle$ cancels only in the sum over the full surface BZ, showing that bulk states must be included to satisfy charge conservation. Note that the sign of both the spin polarization and the current is reversed for the degenerate solution with complex-conjugated gaps.

The coupling to the electromagnetic field, which is not included here, leads to additional screening currents that exactly balance the spontaneous surface current in the limit $W \rightarrow \infty$. However, these currents build up on the length scale of the magnetic penetration depth λ, which in typical NCSs is much larger than the decay length of the surface current, on the order of the coherence length ξ [12]. In samples with thickness smaller than the penetration depth but larger than the coherence length, it should thus be possible to detect the surface current.

Summary and conclusions. We have studied the stability of zero-energy flat bands at the surface of an NCS within self-consistent MF theory. We find that the flat bands are indeed recovered by the self-consistent calculation within a broad temperature range below the bulk transition temperature T_c. TRS is spontaneously broken at a much lower temperature T_s, which is signaled by a nonuniform phase of the gaps. This destroys the topological protection for the flat bands, shifting them away from zero energy and giving them finite velocity. Figure 4 shows that at low temperatures the flat bands are displaced by an energy on the order of T_s, which is significantly smaller than the bulk gaps of order T_c. The free-energy gain due to the shift of the flat bands is likely a major driver of the TRSB state, and ultimately limits T_s as the free-energy gain from the shift is reduced by the broadening of the Fermi function.

The TRSB state leads to clear experimental signatures: a splitting of the zero-bias peak in the tunneling spectrum, a nonvanishing spin polarization at the surface, and a nonvanishing equilibrium charge current parallel to the surface. The latter two effects show that the TRSB state found here is qualitatively different from that predicted for the (110) surface of cuprate superconductors [22–26,30].

We thank A. P. Schnyder, R. Quieroz, and T. Neupert for helpful discussions. C.T. gratefully acknowledges support by the Deutsche Forschungsgemeinschaft through Research Training Group GRK 1621 and Collaborative Research Center SFB 1143. S.R. was supported by the Norwegian Research Council, Grants No. 205591/V20 and No. 216700/F20. P.M.R.B. acknowledges support from Microsoft Station Q, LPS-CMTC, and JQI-NSF-PFC.

[1] A. P. Schnyder and S. Ryu, Phys. Rev. B **84**, 060504(R) (2011).
[2] A. P. Schnyder, P. M. R. Brydon, and C. Timm, Phys. Rev. B **85**, 024522 (2012).
[3] Y. X. Zhao and Z. D. Wang, Phys. Rev. Lett. **110**, 240404 (2013).
[4] S. Matsuura, P.-Y. Chang, A. P. Schnyder, and S. Ryu, New J. Phys. **15**, 065001 (2013).
[5] S. A. Yang, H. Pan, and F. Zhang, Phys. Rev. Lett. **113**, 046401 (2014).
[6] A. P. Schnyder and P. M. R. Brydon, arXiv:1502.03746.
[7] M. Sato, Phys. Rev. B **73**, 214502 (2006).
[8] B. Béri, Phys. Rev. B **81**, 134515 (2010).
[9] Y. Tanaka, Y. Mizuno, T. Yokoyama, K. Yada, and M. Sato, Phys. Rev. Lett. **105**, 097002 (2010).
[10] M. Sato, Y. Tanaka, K. Yada, and T. Yokoyama, Phys. Rev. B **83**, 224511 (2011); K. Yada, M. Sato, Y. Tanaka, and T. Yokoyama, *ibid.* **83**, 064505 (2011); M. Sato and S. Fujimoto, Phys. Rev. Lett. **105**, 217001 (2010).

[11] P. M. R. Brydon, A. P. Schnyder, and C. Timm, Phys. Rev. B **84**, 020501(R) (2011).

[12] *Non-Centrosymmetric Superconductors: Introduction and Overview*, edited by E. Bauer and M. Sigrist, Lecture Notes in Physics Vol. 847 (Springer, Berlin, 2012).

[13] K. Izawa, Y. Kasahara, Y. Matsuda, K. Behnia, T. Yasuda, R. Settai, and Y. Onuki, Phys. Rev. Lett. **94**, 197002 (2005).

[14] H. Q. Yuan, D. F. Agterberg, N. Hayashi, P. Badica, D. Vandervelde, K. Togano, M. Sigrist, and M. B. Salamon, Phys. Rev. Lett. **97**, 017006 (2006).

[15] M. Nishiyama, Y. Inada, and G.-Q. Zheng, Phys. Rev. Lett. **98**, 047002 (2007).

[16] H. Mukuda, T. Fujii, T. Ohara, A. Harada, M. Yashima, Y. Kitaoka, Y. Okuda, R. Settai, and Y. Onuki, Phys. Rev. Lett. **100**, 107003 (2008).

[17] I. Bonalde, R. L. Robeiro, W. Bramer-Escamilla, C. Rojas, E. Bauer, A. Prokofiev, Y. Haga, T. Yasuda, and Y. Onuki, New J. Phys. **11**, 055054 (2009).

[18] G. Eguchi, D. C. Peets, M. Kriener, S. Yonezawa, G. Bao, S. Harada, Y. Inada, G.-q. Zheng, and Y. Maeno, Phys. Rev. B **87**, 161203(R) (2013).

[19] P. M. R. Brydon, C. Timm, and A. P. Schnyder, New J. Phys. **15**, 045019 (2013).

[20] A. P. Schnyder, C. Timm, and P. M. R. Brydon, Phys. Rev. Lett. **111**, 077001 (2013).

[21] J. S. Hofmann, R. Queiroz, and A. P. Schnyder, Phys. Rev. B **88**, 134505 (2013).

[22] M. Matsumoto and H. Shiba, J. Phys. Soc. Jpn. **64**, 3384 (1995); **64**, 4867 (1995).

[23] M. Fogelström, D. Rainer, and J. A. Sauls, Phys. Rev. Lett. **79**, 281 (1997).

[24] M. Sigrist, Prog. Theor. Phys. **99**, 899 (1998).

[25] J.-X. Zhu, B. Friedman, and C. S. Ting, Phys. Rev. B **59**, 3353 (1999).

[26] C. Honerkamp, K. Wakabayashi, and M. Sigrist, Europhys. Lett. **50**, 368 (2000).

[27] S. Kashiwaya and Y. Tanaka, Rep. Prog. Phys. **63**, 1641 (2000).

[28] A. M. Black-Schaffer, D. S. Golubev, T. Bauch, F. Lombardi, and M. Fogelström, Phys. Rev. Lett. **110**, 197001 (2013).

[29] Y. Tanaka and S. Kashiwaya, Phys. Rev. Lett. **74**, 3451 (1995).

[30] A. C. Potter and P. A. Lee, Phys. Rev. Lett. **112**, 117002 (2014).

[31] M. Covington, M. Aprili, E. Paraoanu, L. H. Greene, F. Xu, J. Zhu, and C. A. Mirkin, Phys. Rev. Lett. **79**, 277 (1997).

[32] R. Krupke and G. Deutscher, Phys. Rev. Lett. **83**, 4634 (1999).

[33] D. Gustafsson, D. Golubev, M. Fogelström, T. Claeson, S. Kubatkin, T. Bauch, and F. Lombardi, Nat. Nanotechnol. **8**, 25 (2013).

[34] J. Y. T. Wei, N.-C. Yeh, D. F. Garrigus, and M. Strasik, Phys. Rev. Lett. **81**, 2542 (1998).

[35] A. Biswas, P. Fournier, M. M. Qazilbash, V. N. Smolyaninova, H. Balci, and R. L. Greene, Phys. Rev. Lett. **88**, 207004 (2002).

[36] H. Kashiwaya, S. Kashiwaya, B. Prijamboedi, A. Sawa, I. Kurosawa, Y. Tanaka, and I. Iguchi, Phys. Rev. B **70**, 094501 (2004).

[37] B. Chesca, M. Seifried, T. Dahm, N. Schopohl, D. Koelle, R. Kleiner, and A. Tsukada, Phys. Rev. B **71**, 104504 (2005); B. Chesca, D. Doenitz, T. Dahm, R. P. Huebener, D. Koelle, R. Kleiner, Ariando, H. J. H. Smilde, and H. Hilgenkamp, *ibid.* **73**, 014529 (2006); B. Chesca, H. J. H. Smilde, and H. Hilgenkamp, *ibid.* **77**, 184510 (2008).

[38] M. Wagenknecht, D. Koelle, R. Kleiner, S. Graser, N. Schopohl, B. Chesca, A. Tsukada, S. T. B. Goennenwein, and R. Gross, Phys. Rev. Lett. **100**, 227001 (2008).

[39] E. Bauer, G. Hilscher, H. Michor, C. Paul, E. W. Scheidt, A. Gribanov, Y. Seropegin, H. Noël, M. Sigrist, and P. Rogl, Phys. Rev. Lett. **92**, 027003 (2004).

[40] N. Kimura, K. Ito, K. Saitoh, Y. Umeda, H. Aoki, and T. Terashima, Phys. Rev. Lett. **95**, 247004 (2005).

[41] I. Sugitani, Y. Okuda, H. Shishido, T. Yamada, A. Thamizhavel, E. Yamamoto, T. D. Matsuda, Y. Haga, T. Takeuchi, R. Settai, and Y. Ōnuki, J. Phys. Soc. Jpn. **75**, 043703 (2006).

[42] P. A. Frigeri, D. F. Agterberg, A. Koga, and M. Sigrist, Phys. Rev. Lett. **92**, 097001 (2004).

[43] See Supplemental Material at http://link.aps.org/supplemental/10.1103/PhysRevB.91.180503 for details on the MF theory and on the calculation of the spin per site and the charge current.

[44] P. M. R. Brydon, A. P. Schnyder, and C. Timm, New J. Phys. **17**, 013016 (2015).

[45] Note that the sign of the SOC is inverted compared to Refs. [11, 2, 44].

[46] R. Queiroz and A. P. Schnyder, Phys. Rev. B **89**, 054501 (2014).

[47] A. Furusaki and M. Tsukada, Solid State Commun. **78**, 299 (1991).

Supplemental Material for
Surface instability in nodal noncentrosymmetric superconductors

Carsten Timm, Stefan Rex, and P. M. R. Brydon

I. MEAN-FIELD THEORY FOR THE BULK

In this section we sketch the MF theory for the bulk NCS. We assume spatially uniform pairing potentials $\Delta^s_j = \Delta_s$ and $\Delta^t_{ij} = \Delta_t$. Using this ansatz to decouple the interaction Hamiltonian H_{int}, we obtain the Bogoliubov-de Gennes (BdG) Hamiltonian [S1]

$$H_{\text{MF}} = \frac{1}{2} \sum_{\mathbf{k}} \Phi^\dagger_{\mathbf{k}} \mathcal{H}(\mathbf{k}) \Phi_{\mathbf{k}} + N\, \frac{\Delta_s^2}{U_s} + N\, \frac{\Delta_t^2}{U_t}, \tag{S1}$$

with the number of sites, N, and the block matrix

$$\mathcal{H}(\mathbf{k}) = \begin{pmatrix} h(\mathbf{k}) & \Delta(\mathbf{k}) \\ \Delta^\dagger(\mathbf{k}) & -h^T(-\mathbf{k}) \end{pmatrix} \tag{S2}$$

written in terms of $h(\mathbf{k}) = \xi_{\mathbf{k}}\sigma^0 - \lambda\, \mathbf{l}_{\mathbf{k}} \cdot \boldsymbol{\sigma}$, $\Delta(\mathbf{k}) = (\Delta_s \sigma^0 + \Delta_t\, \mathbf{l}_{\mathbf{k}} \cdot \boldsymbol{\sigma})\, i\sigma^y$, $\xi_{\mathbf{k}} = -2t\,(\cos k_x + \cos k_y + \cos k_z) - \mu$, $\mathbf{l}_{\mathbf{k}} = \hat{\mathbf{x}}\, \sin k_y - \hat{\mathbf{y}}\, \sin k_x$, and the Nambu spinor $\Phi_{\mathbf{k}} = (c_{\mathbf{k}\uparrow}, c_{\mathbf{k}\downarrow}, c^\dagger_{-\mathbf{k},\uparrow}, c^\dagger_{-\mathbf{k},\downarrow})^T$. Here, σ^0 is the 2×2 identity matrix. The dispersion $E_{\mathbf{k}\nu}$, $\nu = 1, \ldots, 4$ is obtained by diagonalizing $\mathcal{H}(\mathbf{k})$. Δ_s and Δ_t are then obtained by minimizing the free energy

$$F_{\text{MF}} = -k_B T \sum_{\mathbf{k}\nu}{}' \ln\left(2 \cosh \frac{\beta E_{\mathbf{k}\nu}}{2}\right) + N\, \frac{\Delta_s^2}{U_s} + N\, \frac{\Delta_t^2}{U_t}, \tag{S3}$$

where the momentum sum is over half the BZ, $k_m > 0$. This restriction of the sum makes use of particle-hole symmetry, which relates the Hamiltonian in Eq. (S2) at $\mathbf{k}$ and $-\mathbf{k}$ by [S1] $\mathcal{U}_C\, \mathcal{H}^T(-\mathbf{k})\, \mathcal{U}_C^\dagger = -\mathcal{H}(\mathbf{k})$ with the unitary matrix $\mathcal{U}_C = \sigma^x \otimes \sigma^0$.

II. MEAN-FIELD THEORY FOR THE SLAB

We now set up the MF Hamiltonian for the (101) slab and describe the determination of the gap parameters Δ^s_l, $\Delta^x_{l+1/2}$, and Δ^y_l in the MF approximation. After Fourier transformation in the directions parallel to the surfaces, the MF Hamiltonian reads

$$\begin{aligned} H_{\text{MF}} = {} & \frac{1}{2} \sum_{\mathbf{k}} \sum_{l=0}^{W-1} \Phi^\dagger_{\mathbf{k}l} \mathcal{H}_{ll}(\mathbf{k}) \Phi_{\mathbf{k}l} + \frac{1}{2} \sum_{\mathbf{k}} \sum_{l=0}^{W-2} \Phi^\dagger_{\mathbf{k},l+1} \mathcal{H}_{l+1,l}(\mathbf{k}) \Phi_{\mathbf{k}l} + \frac{1}{2} \sum_{\mathbf{k}} \sum_{l=1}^{W-1} \Phi^\dagger_{\mathbf{k},l-1} \mathcal{H}_{l-1,l}(\mathbf{k}) \Phi_{\mathbf{k}l} \\ & + \frac{N_\parallel}{U_s} \sum_{l=0}^{W-1} |\Delta^s_l|^2 + \frac{N_\parallel}{2U_t} \sum_{l=0}^{W-2} |\Delta^x_{l+1/2}|^2 + \frac{N_\parallel}{2U_t} \sum_{l=0}^{W-1} |\Delta^y_l|^2, \end{aligned} \tag{S4}$$

where $N_\parallel$ is the number of unit cells of the slab and $\Phi_{\mathbf{k}l} = (c_{\mathbf{k}l\uparrow}, c_{\mathbf{k}l\downarrow}, c^\dagger_{-\mathbf{k},l,\uparrow}, c^\dagger_{-\mathbf{k},l,\downarrow})^T$ is the partially Fourier-transformed Nambu spinor. The sums over l containing $\Phi^\dagger_{\mathbf{k},l\pm 1}$ are restricted in such a way that $l \pm 1 \in \{0, \ldots, W-1\}$. The coefficient matrices appearing in H_{MF} are

$$\mathcal{H}_{ll}(\mathbf{k}) = \begin{pmatrix} -2t\cos k_y - \mu & -\lambda \sin k_y & -\Delta^y_l \sin k_y & \Delta^s_l \\ -\lambda \sin k_y & -2t\cos k_y - \mu & -\Delta^s_l & \Delta^y_l \sin k_y \\ -\Delta^{y*}_l \sin k_y & -\Delta^{s*}_l & 2t\cos k_y + \mu & -\lambda \sin k_y \\ \Delta^{s*}_l & \Delta^{y*}_l \sin k_y & -\lambda \sin k_y & 2t\cos k_y + \mu \end{pmatrix}, \tag{S5}$$

$$\mathcal{H}_{l\pm 1,l}(\mathbf{k}) = \begin{pmatrix} -2t\cos(k_m/\sqrt{2}) & \pm(\lambda/2)\, e^{\mp i k_m/\sqrt{2}} & \pm(\Delta^x_{l\pm 1/2}/2)\, e^{\mp i k_m/\sqrt{2}} & 0 \\ \mp(\lambda/2)\, e^{\mp i k_m/\sqrt{2}} & -2t\cos(k_m/\sqrt{2}) & 0 & \pm(\Delta^x_{l\pm 1/2}/2)\, e^{\mp i k_m/\sqrt{2}} \\ \mp(\Delta^{x*}_{l\pm 1/2}/2)\, e^{\mp i k_m/\sqrt{2}} & 0 & 2t\cos(k_m/\sqrt{2}) & \mp(\lambda/2)\, e^{\mp i k_m/\sqrt{2}} \\ 0 & \mp(\Delta^{x*}_{l\pm 1/2}/2)\, e^{\mp i k_m/\sqrt{2}} & \pm(\lambda/2)\, e^{\mp i k_m/\sqrt{2}} & 2t\cos(k_m/\sqrt{2}) \end{pmatrix}. \tag{S6}$$

We next construct the $4W \times 4W$ block matrix

$$\mathcal{H}(\mathbf{k}) \equiv \begin{pmatrix} \mathcal{H}_{00}(\mathbf{k}) & \mathcal{H}_{01}(\mathbf{k}) & 0 & \cdots \\ \mathcal{H}_{10}(\mathbf{k}) & \mathcal{H}_{11}(\mathbf{k}) & \mathcal{H}_{12}(\mathbf{k}) & \cdots \\ 0 & \mathcal{H}_{21}(\mathbf{k}) & \mathcal{H}_{22}(\mathbf{k}) & \cdots \\ \vdots & \vdots & \vdots & \ddots \end{pmatrix} \tag{S7}$$

and denote its eigenvalues by $E_{\mathbf{k}\nu}$, $\nu = 1, \dots, 4W$ and the corresponding eigenvectors by $|\mathbf{k}\nu\rangle$. The MF Hamiltonian satisfies particle-hole symmetry [S1], $\mathcal{U}_C\, \mathcal{H}^T(-\mathbf{k})\,\mathcal{U}_C^\dagger = -\mathcal{H}(\mathbf{k})$ with the unitary matrix $\mathcal{U}_C = \mathbb{1}_W \otimes \sigma^x \otimes \sigma^0$, where $\mathbb{1}_W$ is the $W \times W$ identity matrix. This symmetry again allows to restrict the momentum sums to half the BZ. The free energy can then be written as

$$F_{\mathrm{MF}} = -k_B T {\sum_{\mathbf{k}\nu}}' \ln\left(2\cosh\frac{\beta E_{\mathbf{k}\nu}}{2}\right) + \frac{N_\parallel}{U_s}\sum_{l=0}^{W-1} |\Delta^s_l|^2 + \frac{N_\parallel}{2U_t}\sum_{l=0}^{W-2} |\Delta^x_{l+1/2}|^2 + \frac{N_\parallel}{2U_t}\sum_{l=0}^{W-1} |\Delta^y_l|^2, \tag{S8}$$

where the momentum sum is restricted to half the BZ, $k_m > 0$. Minimization of F_{MF} gives the gaps Δ^s_l, $\Delta^x_{l+1/2}$, and Δ^y_l. The derivatives of F_{MF} with respect to the complex conjugate gaps can be calculated with the help of the Hellmann-Feynman theorem, for example

$$\frac{\partial F_{\mathrm{MF}}}{\partial \Delta^{s*}_l} = -\frac{1}{2} {\sum_{\mathbf{k}\nu}}' \tanh\frac{\beta E_{\mathbf{k}\nu}}{2}\, \langle \mathbf{k}\nu| \frac{\partial \mathcal{H}(\mathbf{k})}{\partial \Delta^{s*}_l} |\mathbf{k}\nu\rangle + \frac{N_\parallel}{U_s}\, \Delta^s_l. \tag{S9}$$

The momentum sums are performed on a 50×50 mesh, referring to the full surface BZ. Quadrupling the number of points in the mesh to 100×100 leads to changes in the MF gaps on the order of only 0.1%.

Solving the resulting MF equations by iteration turns out to be prohibitively slow for the required W, essentially because the minimum of F_{MF} is very shallow in some directions in the high-dimensional space of gap parameters. On the other hand, numerical minimization making use of the explicitly known gradient is reasonably efficient. We use the Broyden-Fletcher-Goldfarb-Shanno method implemented in Numerical Recipes [S2]. It requires an initial guess for the inverse Hessian. When we scan over ranges of temperatures, we use not only the converged values of the gaps but also the best approximate inverse Hessian from one step as starting values for the next, which significantly speeds up the convergence. We assume that the method has converged when no real or imaginary part of any gap parameter changes by more than (double) machine precision in the last step.

For certain parameter values, we find nonvanishing gradients of the phases of the order parameters in the l direction, normal to the surfaces. Specifically, we find four metastable solutions, which are mapped onto each other by inverting the phase gradients at one or both surfaces. In the limit $W \to \infty$, the four solutions are degenerate. For finite W, they split into two degenerate pairs with phase gradients that are even and odd, respectively, under reflection at the center of the slab. We here choose a solution with even phase gradients since then the selfconsistent solution ensures that the phases of Δ^s_l, $\Delta^x_{l+1/2}$, and Δ^y_l become equal at the center of the slab; equal phases of all gaps at the center are expected since the bulk MF solution has equal phases. By a global phase change we can then make the phase of all gaps zero at the center. The phases and imaginary parts of the gaps are then odd under reflection at the center. Finally, of the two remaining solutions differing in the sign of the imaginary parts of the gaps, we select the solution with $\mathrm{Im}\,\Delta^s_0 \geq 0$ for definiteness. The other solution leads to inverted spin polarizations and currents.

III. SPIN POLARIZATION

Here, we present expressions for the spin polarization. The operator of the spin per site, averaged over the directions parallel to the surfaces, is

$$\mathbf{s}_l = \frac{1}{N_\parallel} \sum_{\mathbf{k}} c^\dagger_{\mathbf{k}l}\, \frac{\boldsymbol{\sigma}}{2}\, c_{\mathbf{k}l}. \tag{S10}$$

Using particle-hole symmetry, the thermal spin average can be written as

$$\langle \mathbf{s}_l \rangle = -\frac{1}{4N_\parallel} {\sum_{\mathbf{k}\nu}}' \tanh\frac{\beta E_{\mathbf{k}\nu}}{2}\, \langle \mathbf{k}\nu| P_{ll} \otimes \begin{pmatrix} \boldsymbol{\sigma} & 0 \\ 0 & -\boldsymbol{\sigma}^T \end{pmatrix} |\mathbf{k}\nu\rangle, \tag{S11}$$

where $P_{ll'}$ is a $W \times W$ matrix with the components $(P_{ll'})_{nn'} = \delta_{ln}\delta_{l'n'}$. We also consider the momentum-dependent contributions to the spin polarization of the half slab defined by $0 \leq l < W/2$. These contributions are obtained by summing $\langle \mathbf{s}_l \rangle$ over $l = 0, \dots, W/2 - 1$ and removing the factor $1/N_\parallel$ and the momentum sum.

IV. EQUILIBRIUM CURRENT

The second observable of interest is the current. The operators j_{ij}^{α} denote the *electron-number* current from site j to its nearest neighbor i in the $\alpha = x, y, z$ direction. They can be read off from H_0 in Eq. (1) in the main text,

$$j_{ij}^{x} = -i\, c_i^{\dagger} \begin{pmatrix} -t & \lambda/2 \\ -\lambda/2 & -t \end{pmatrix} c_j + i\, c_j^{\dagger} \begin{pmatrix} -t & -\lambda/2 \\ \lambda/2 & -t \end{pmatrix} c_i, \tag{S12}$$

$$j_{ij}^{y} = -i\, c_i^{\dagger} \begin{pmatrix} -t & -i\lambda/2 \\ -i\lambda/2 & -t \end{pmatrix} c_j + i\, c_j^{\dagger} \begin{pmatrix} -t & i\lambda/2 \\ i\lambda/2 & -t \end{pmatrix} c_i, \tag{S13}$$

$$j_{ij}^{z} = -i\, c_i^{\dagger} \begin{pmatrix} -t & 0 \\ 0 & -t \end{pmatrix} c_j + i\, c_j^{\dagger} \begin{pmatrix} -t & 0 \\ 0 & -t \end{pmatrix} c_i. \tag{S14}$$

The interaction term H_{int} conserves charge locally and therefore does not contribute to the current operator. After the MF decoupling, the anomalous terms do not conserve charge—they describe creation or annihilation of two electrons either at the same site or at neighboring sites. Such processes do not lead to currents but do introduce a source term, which is discussed in the main text. We average the current over layers parallel to the surface, taking into account that j_{ij}^{x} and j_{ij}^{z} connect adjacent layers, whereas j_{ij}^{y} describes a current within a single layer. We then obtain the thermal averages, again using particle-hole symmetry,

$$\langle j_{l+1/2}^{x} \rangle = -\frac{1}{2N_{\|}} \sum_{\mathbf{k}\nu}{}' \tanh \frac{\beta E_{\mathbf{k}\nu}}{2}\, \langle \mathbf{k}\nu | \left\{ i\, e^{-ik_m/\sqrt{2}}\, P_{l+1,l} \otimes \begin{pmatrix} t & -\lambda/2 & 0 & 0 \\ \lambda/2 & t & 0 & 0 \\ 0 & 0 & t & -\lambda/2 \\ 0 & 0 & \lambda/2 & t \end{pmatrix} + \text{H.c.} \right\} | \mathbf{k}\nu \rangle, \tag{S15}$$

$$\langle j_{l}^{y} \rangle = -\frac{1}{N_{\|}} \sum_{\mathbf{k}\nu}{}' \tanh \frac{\beta E_{\mathbf{k}\nu}}{2}\, \langle \mathbf{k}\nu |\, P_{ll} \otimes \begin{pmatrix} t \sin k_y & -(\lambda/2)\cos k_y & 0 & 0 \\ -(\lambda/2)\cos k_y & t \sin k_y & 0 & 0 \\ 0 & 0 & t \sin k_y & (\lambda/2)\cos k_y \\ 0 & 0 & (\lambda/2)\cos k_y & t \sin k_y \end{pmatrix} | \mathbf{k}\nu \rangle, \tag{S16}$$

$$\langle j_{l+1/2}^{z} \rangle = -\frac{1}{2N_{\|}} \sum_{\mathbf{k}\nu}{}' \tanh \frac{\beta E_{\mathbf{k}\nu}}{2}\, \langle \mathbf{k}\nu | \left\{ i\, e^{ik_m/\sqrt{2}}\, P_{l+1,l} \otimes \begin{pmatrix} t & 0 & 0 & 0 \\ 0 & t & 0 & 0 \\ 0 & 0 & t & 0 \\ 0 & 0 & 0 & t \end{pmatrix} + \text{H.c.} \right\} | \mathbf{k}\nu \rangle, \tag{S17}$$

where $\langle j_{l+1/2}^{x,z} \rangle$ denotes currents connecting layers l and $l+1$. The components with respect to the slab coordinates are

$$\langle j_{l+1/2}^{l} \rangle = \frac{\langle j_{l+1/2}^{x} \rangle + \langle j_{l+1/2}^{z} \rangle}{\sqrt{2}}, \qquad \langle j_{l+1/2}^{m} \rangle = \frac{\langle j_{l+1/2}^{x} \rangle - \langle j_{l+1/2}^{z} \rangle}{\sqrt{2}}. \tag{S18}$$

We note that $\langle j_{l}^{y} \rangle$ vanishes for any choice of gap parameters for our model, even non-selfconsistent ones. This is based on mirror symmetry in the xz plane. The current in the y direction changes sign under this symmetry operation and thus vanishes.

The momentum-dependent contributions to the current in the half slab $0 \le l < W/2$ are obtained by summing $\langle \mathbf{j}_l \rangle$ over $l = 0, \ldots, W/2-1$ and removing the factor $1/N_{\|}$ and the momentum sum. The momentum-resolved m component, which sums to a nonzero current, is shown in Fig. 5(c) in the main text. We present the momentum-resolved y and l components in Fig. S1. The y components chancel by symmetry, as noted above. The cancelation of the l components, which is required by charge conservation, is only ensured for selfconsistent gaps [S3]. Large positive contributions from bulk states within the projected (small) positive-helicity Fermi surface are canceled by small negative contributions from the flat bands and from bulk states within the projected (large) negative-helicity Fermi surface. This shows that the bulk states must be included to satisfy charge conservation.

[S1] A. P. Schnyder, P. M. R. Brydon, and C. Timm, Phys. Rev. B **85**, 024522 (2012).

[S2] W. H. Press, S. A. Teukolsky, W. T. Vetterling, and B. P. Flannery, *Numerical Recipes: The Art of Scientific Computing*, 3rd edition (Cambridge University Press, New York, 2007).

[S3] A. Furusaki and M. Tsukada, Solid State Commun. **78**, 299 (1991).

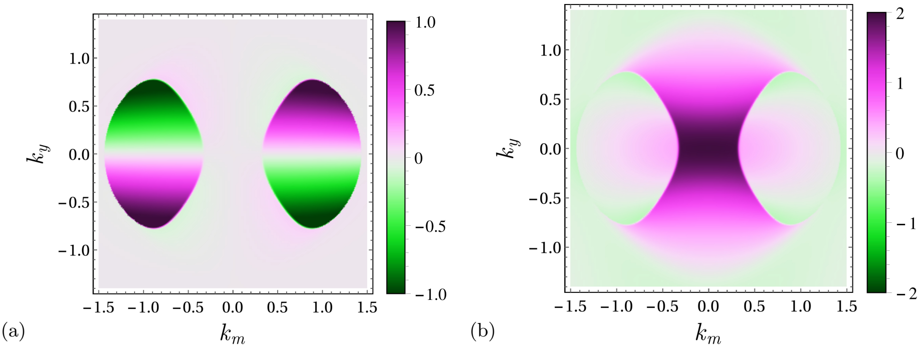

FIG. S1. Momentum-resolved contributions to (a) the y component and (b) the l component of the current in half the slab ($0 \leq l < W/2$).